DEVELOPMENT OF A NUMERICAL TOOL TO PREDICT HYDRODYNAMICS, TEMPERATURE AND TDG IN HYDROPOWER FLOWS

by

Yushi Wang

A thesis submitted in partial fulfillment
of the requirements for the Doctor of
Philosophy degree in Civil and Environmental Engineering
in the Graduate College of
The University of Iowa

December 2013

Thesis Supervisors: Adjunct Associate Professor Marcela Politano
Professor Larry Weber

Graduate College
The University of Iowa
Iowa City, Iowa

CERTIFICATE OF APPROVAL

_____

PH.D. THESIS

_____

This is to certify that the Ph.D. thesis of

Yushi Wang

has been approved by the Examining Committee
for the thesis requirement for the Doctor of Philosophy
degree in Civil and Environmental Engineering at the December 2013
graduation.

Thesis Committee: _____
Marcela Politano, Thesis Supervisor

_____
Larry Weber, Thesis Supervisor

_____
Jacob Odgaard

_____
Pablo Carrica

_____
George Constantinescu

_____
Shaun Parkinson

ACKNOWLEDGMENTS

First and foremost, I wish to express my deepest gratitude to my supervisors, Dr. Marcela Politano and Larry Weber, for their encouragement, guidance, and support throughout this research. I am extremely thankful and appreciative of all the effort and time Dr. Politano has spent helping me to expand my knowledge of fluid mechanics and numerical modeling. She and Dr. Weber have been greater teachers, wonderful mentors, and best role models to me. I consider myself very fortunate to have had the opportunity to learn from them.

I would also like to thank the Hydro Research Foundation and the U.S. Department of Energy for providing me with a fellowship to fund this research. Their support made this work possible.

I am deeply grateful for the time and expertise of the other members of my thesis committee, Dr. Pablo Carrica, Dr. Jacob Odgaard, Dr. George Constantinescu, and Dr. Shaun Parkinson. Their review and input of my thesis provided valuable feedback and was very much appreciated.

Thank you also to my friends and colleagues at IIHR for the assistant they have provided towards the completion of my research. Special thanks go to my friend Yuwei Li for the many discussions, suggestions and help along the way.

Last but not least, I would like to thank my parents and family in China for always believing in me, encouraging me, and strengthening me. I also want to thank my lovely wife Yue; she has always been there to support me through the entire process. It has meant more to me than I can ever express.

ABSTRACT

Hydropower is the most important renewable energy source on the planet. Though it provides abundant benefits to society, it also has environmental and ecological consequences. Dam construction significantly alters natural flow conditions. Fish numbers decline and other aquatic life may be adversely affected, especially during migration and reproduction cycles, due to degradation of their natural habitat. High summer water temperatures in hydropower reservoirs and elevated total dissolved gas (TDG) concentrations in downstream tailrace regions can increase mortality rates of fish passing through the dam.

This study proposes to develop a numerical model to improve the prediction of hydrodynamics and water-quality parameters in hydropower flows. The main focus is to simulate temperature dynamics and TDG distribution in the McNary Dam forebay and tailrace. Existing numerical temperature and TDG models, developed by Politano et al. (2008, 2009c), were improved and implemented into the open-source CFD code OpenFOAM. These newly developed models can be used to evaluate the efficiency of operational changes or structural modifications to reduce the negative environmental impacts of hydropower facilities.

The forebay temperature model was based on the incompressible Reynolds-Averaged Navier-Stokes (RANS) equations with the Boussinesq approximation. Turbulence was modeled with an improved realizable $k-\varepsilon$ model taking into account wind turbulence generation at the free surface. A thermal model incorporating solar radiation and convective heat transfer at the free surface was employed. The model was validated against field data collected on August 18th, 2004 at McNary Dam. Observed vertical and lateral temperature distributions and dynamics in the forebay were captured by the model. The incorporation of the atmospheric heat flux, solar radiation, and wind-induced turbulence improved the temperature predictions near the free surface.

The multi-phase TDG model utilized the Volume of Fluid (VOF) method combined with a Detached Eddy Simulation (DES) approach to calculate hydrodynamics. A one-way coupling approach was used to incorporate a TDG model, which includes the transport and dissolution of bubbles entrained in the spillway and takes into account bubble size change caused by dissolution and compression. The capability of the present model to predict spillway flow regimes was evaluated against observations in a reduced scale laboratory model. Simulation results demonstrated that flow regimes downstream of a spillway can be adequately reproduced by the numerical model. The capability of the model to quantify dissolved gas exchanges and TDG distribution was evaluated using a tailrace sectional model. The model captured TDG production and observed longitudinal TDG reduction under different flow regimes. Disparities between predicted and measured average TDG values fell within 4%. The model developed in this study is an effective predictive numerical tool to identify flow regimes and quantify TDG production under various flow conditions in near dam regions when lateral flows are not important.

TABLE OF CONTENTS

LIST OF TABLES

LIST OF FIGURES

CHAPTER I

INTRODUCTION

1.1 Background and Motivation

Hydropower is the most widely used form of renewable energy in the world and the global installed capacity has grown rapidly over the past several decades. Hydropower is renowned for its low costs, low environmental impact, flexibility, and reliability. The hydropower capacity of United States has remained relatively stable in recent decades since most large dams were built before 1980. Today, more than 7% of the total U.S. electricity supply is generated by hydropower. According to the U.S. Department of Energy (DOE), about 40% of all U.S. hydropower originates in the Columbia River Basin. Up to 70% of the electricity in the Pacific Northwest is generated by hydropower.

Despite these benefits, hydropower does have negative impacts on local habitats and ecosystems as free flowing rivers become impounded reaches. The large dams and reservoirs required for the operation of hydroelectric power stations change natural flow conditions, pool elevations, and channel morphologies. They also block spatial connections and historic fish migration pathways in rivers (Braatne et al. 2008). Many aquatic species numbers have significantly declined due to the installation of hydropower facilities. Fish are especially vulnerable during migration and reproduction cycles due to compromised migration routes and habitat loss. With more than 400 dams in the Columbia River and Snake River Basin, fish passage at dams has been a major problem for nearly as long as dams have been built in the basin (Lichatowich 1999). Many aquatic organisms in this region are listed as endangered or threatened by the U.S. Fish and Wildlife Service (USFWS). Federal and State governments have been passing legislation to mitigate negative impacts of hydropower since the 1890s.

One of the negative impacts of hydropower is the elevation of summer water temperatures in the reservoir upstream of dams. Hydroelectric projects impound water into reservoirs, disrupting natural temperature dynamics and distribution. High summer temperatures

warm surface layers in the reservoir and can cause thermal stratification (Zhao et al. 2011). A strong vertical thermal gradient (thermocline) can be observed in the reservoirs. In the water column, a high temperature water layer forms near the surface. A cold, low dissolved oxygen water layer forms at the bottom. Vertical mixing between these layers is inhibited. This phenomenon imposes adverse impacts on the environment and local eco-systems near dams. The drinking water quality may also be affected. Recreational resource may be limited by excessive plankton growth. Fish populations may decrease due to thermal stress (Zeng and Rasmussen 2005; Lackey and Holmes 1972).

In addition to changes in the forebay area, tailrace water quality can also be affected by dams. Particularly, dissolved gas content in the water may increase from pre-construction conditions. Spillway operations significantly impact the amount of dissolved gases in the tailrace of hydraulic dams (Beeman and Maule 2006). Fish migrating through hydropower dams exposed to high levels of total dissolved gas (TDG) can suffer gas-bubble disease. Currently, dissolved oxygen and TDG levels upstream and downstream of dams are major environmental concerns in building a new dam and re-licensing of existing hydropower projects.

Many efforts have been made to reduce fish fatalities when traveling through dams. To facilitate diadromous fishes' natural migration, fish ladders have been installed on most dams occupying salmon habitats, to enable access to upstream spawning grounds (Fryer et al. 2010). Fish-friendly turbines (Robb 2011) and efficient downstream passage systems (Katopodis and Williams 2011) are active areas of research to mitigate potential hazards to fish migrating downstream.

Many studies have focused on optimizing operations and structural modifications to reduce environmental impacts and improve water quality without detriment to electrical production (Strain et al. 2008, Ferrari et al. 2009). Such studies require a deep understanding and accurate modeling of the physical processes that impact fish and other aquatic organisms. Advances in computer technology have made the use of Computational Fluid Dynamics (CFD) modeling possible to analyze abatement options and to complement the laboratory models

traditionally employed by the hydropower community. CFD models have emerged as economical and efficient tools for hydropower studies (Teklemariam et al. 2002). The development of numerical tools to model various problems encountered by hydraulic projects has benefited both the hydropower community and the environment.

The goal of this thesis is to improve existing temperature and TDG prediction models, and to implement these models in an efficient open-source CFD tool. These numerical models can provide reliable results and impact engineering decisions on designs and operations of large scale hydraulic structures. Given the computational limitations as well as time constraints, computational resources are focused to critical regions to resolve key flow characteristics. Hydrodynamic details that do not strongly affect the large scale flow patterns and distribution of water quality parameters are not the main focus of this study.

1.2 Study Area

McNary Dam is a concrete, gravity-type hydroelectric dam that spans the main stem of the Columbia River. It is about 2.25 km long, climbing to 56 m above the streambed, and located at river kilometer (rkm) 470 upriver from the mouth of the Columbia in Astoria, Oregon. Construction of McNary Dam began in 1947 and was completed, with all generating units operating, in 1957. It is operated by the U.S. Army Corps of Engineers (USACE) Walla Walla District and is one of the largest hydroelectric power facilities in the Pacific Northwest. The dam is composed of twenty-two spillways with an overall length of 400 m, and a powerhouse that contains fourteen 70,000 kilowatt hydroelectric generator units that can generate 980 megawatts at maximum capacity. To protect and enhance fish migration across the dam, two fish passage facilities were constructed on both north (Washington) and south (Oregon) shores of the dam. These facilities consist of fish ladders for adult migrating salmon and steelhead. Two spillway weirs were installed in 2007 to create a surface-oriented route for downstream juvenile salmon passage at the dam.

The reservoir created by McNary Dam (Lake Wallula) extends 98 rkm upstream to the Hanford Reach on the Columbia River, and 16 rkm up the Snake River until reaching Ice Harbor Dam. When at full pool, Lake Wallula's elevation is about 103.6 m above sea level. Downstream of McNary Dam, the river is impounded by John Day Dam located 123 rkm downstream of McNary Dam and forms Lake Umatilla, which is a 166 km long reservoir with a full-pool elevation of about 81.7 m. The study area for this thesis encompasses 5.2 km, extending from 4.1 km upstream of McNary Dam to about 1.1 km downstream of the dam. Figure 1.1 shows the location of McNary dam and the area of study. An aerial view of the McNary Dam forebay and tailrace is shown in Figure 1.2.

1.3 Approach

The models introduced in this study are implemented based on the CFD code OpenFOAM (Open Source Field Operation and Manipulation). OpenFOAM is an open source CFD software programmed in C++. The code was designed to meet requirements for both research uses as well as industrial applications. As an open source toolbox, it provides a flexible and programmable environment that allows researchers to implement complex and coupled physical models extending current numerical modeling capabilities. Its high modularity and object oriented features also enable seamless transition from a model development framework to industrial application by representing differential equations in their natural way in the software as closely as possible.

For a system of equations governing the problem of interest, OpenFOAM offers the user an unrestricted choice to specify numerical schemes to solve different terms in the equations, such as derivatives and interpolations. Continuum equations are discretized and matrix equations are constructed using the finite volume method applied to cells of any shape. Matrix equations are then solved segregated within an iterative sequence and coupled using well-known algorithms such as SIMPLE or PISO.

OpenFOAM was first released in 2004 and has been continuously developed in recent years. A large set of individual solvers that addresses a specific problem in fluid dynamics or other engineering mechanics has been developed. For example, *interFoam* is a transient solver developed to solve two incompressible, isothermal immiscible fluids using a VOF (volume of fluid) phase-fraction based interface capturing approach. One of the most important features of OpenFOAM is that the user can write their own solvers for specific simulation conditions. In order to create an efficient practical tool, a solid understanding of physics and numerical method is required. Other customized objects, such as boundary conditions or turbulence models, can be created to work with existing solvers without having to modify or recompile the existing source code. Another advantage OpenFOAM has is that the code is parallelized at a fundamental level allowing user customized solvers to easily run in parallel.

A large number of peer-reviewed scientific and engineering papers and studies have been conducted using OpenFOAM and validated against field/experimental data or other CFD software (e.g. Karvinen and Ahlstedt 2008; Carneiro et al. 2008; Mahmoodi et al. 2012 among others). Recently, there has been increasing interest in conducting numerical studies related to environment hydraulics and open channel flows. OpenFOAM has been proven to be efficient and accurate in carrying out studies in many relevant research areas (Panara et al. 2006; Pasiok and Stilger-Szydlo 2010; Sinha et al. 2012).

Standard solvers available in OpenFOAM include heat transfer and multi-phase flow capabilities, and provide a promising starting point for development of more complex models. OpenFOAM release version 2.0 was used for the work presented in this study.

1.4 Goals and Objectives

The main goals of this thesis are:

1) Develop an unsteady, three-dimensional CFD model capable of predicting the hydrodynamics and temperature dynamics in the forebay of a dam within an order of days.

2) Validate the forebay model by comparing the predicted temperature profiles with measurements collected in McNary Dam.
3) Develop an unsteady, three-dimensional, multi-phase numerical model capable of predicting spillway flow regimes under different spillway flowrates and tailrace elevations, and TDG distribution in the tailrace.
4) Validate the multi-phase model against flow regimes observed in a reduced-scale sectional model that includes two spillway bays, deflectors, and a portion of the tailrace of McNary Dam.
5) Compare TDG predictions in a portion of the McNary tailrace against field data.

1.5 Outline of the Thesis

The outline of this thesis is as follows:

Chapter II describes development of the forebay numerical model. A literature review of temperature modeling in deep reservoirs is provided. Mathematical and computational methodologies for the numerical model developed in this chapter are explained in detail. The numerical results are discussed and validated using field measurements in McNary Dam.

Chapter III focuses on the development of the multi-phase numerical model to predict spillway flow regimes and TDG distribution in the tailrace of a dam. Relevant literature is reviewed. Governing equations and computational methodology for the three-dimensional hydrodynamics and TDG model are described in detail. Effects of grid size density on the predicted flow field are evaluated and discussed. Predicted flow regimes under different flow conditions are discussed and compared against observations from a reduced scale laboratory model study of McNary Dam. Predicted TDG distributions under different flow conditions are discussed and compared against field measurements.

In chapter IV, summaries of research findings and recommendations for future work are presented.

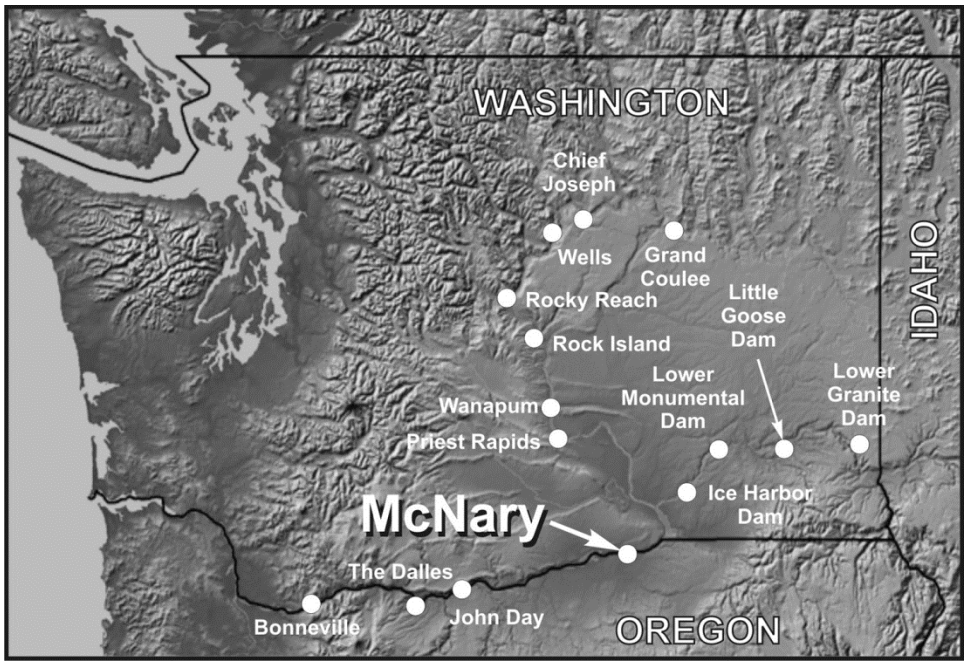

Figure 1.1 Map of the Columbia River Basin showing the location of McNary Dam

Figure 1.2 Aerial view of McNary Dam forebay and tailrace (Source: Google Earth)

CHAPTER II

MCNARY DAM FOREBAY MODEL

The temperature dynamics in the impounded reservoir upstream of a hydropower dam do not follow the pre-construction temperature seasonal cycles due to changes in flow condition. Vertical profiles and spatial distributions of water temperature in river reaches and reservoirs are crucial parameters that strongly affect water quality. High temperature is an environmental and ecological issue that affects water bodies. Water temperature changes of a few degrees can dramatically impact chemical and biological reaction rates and alter dissolved oxygen levels. These changes can harm aquatic organisms, since most have enzyme systems that operate optimally in a narrow temperature range. Juvenile fish are particularly vulnerable to elevated temperatures during summer months in forebays and tailraces at hydropower dams in the Columbia River Basin.

High summer water temperatures at McNary forebay have, for several decades, been considered a principal cause of juvenile fish mortality in the fish bypass facilities. Severe fish mortality in July 1994 was reported, believed to be primarily a result of elevated water temperatures. Daily fish mortality ranged from approximately 3% to 8% from July 10 to 12, 1998, coincident with fish facility water temperatures above 21 ℃ (Smith et al. 2000). The McNary Dam operator, USACE Walla Walla District, has conducted several field and laboratory studies collecting water temperature, atmospheric and climatic data, to address and actively attempt to solve the problem. Numerical models capable of predicting temperature dynamics and distributions in the reservoir were developed to better understand the main mechanisms leading to high temperatures, and ultimately reduce impacts of high local temperature on fish.

2.1 Goals and Objectives

The main goals of this chapter are:

1) Develop an unsteady, three-dimensional CFD model capable of predicting the hydrodynamics and temperature distribution in the forebay region of a dam.

2) Validate the thermal model against field data collected at McNary Dam.

2.2 Outline of this Chapter

The outline of this chapter is as follows: Section 2.3 is a literature review of temperature modeling and effects of water temperature on fish. In Section 2.4, mathematical and computational methodologies for the forebay numerical model are described in detail. Boundary and simulation conditions are explained. Section 2.5 presents simulation results. Modeled hydrodynamics and temperature dynamics are discussed. Predicted vertical temperature profiles are compared against field measurements for selected data stations. Section 2.6 provides a summary of the results.

2.3 Previous and Related Studies

2.3.1 Thermal Stratification

Hydropower dams decelerate rivers and usually store a large body of water in upstream reservoirs. During summers, solar radiation and air convection warm the uppermost layers of the reservoir. Warmer and lighter waters rise above cooler and denser waters, causing thermal stratification. Thermal-stratified reservoirs are composed of three layers. The epilimnion, the top-most layer, consists of well-mixed, high temperature water. The hypolimnion, or bottom layer, remains dense and cold due to extinction of solar radiation. A thin but distinct layer in between the epilimnion and hypolimnion, the metalimnion, contains large temperature gradients and may change in depth in response to seasonal and/or daily weather variations.

Stratification in a reservoir acts as a barrier, preventing mixing of water temperatures, dissolved substances, and nutrients within the water column. Due to the insufficient irradiance for photosynthesis, the hypolimnion usually contains low levels of dissolved oxygen which can cause anoxia, in turn leading to significant increases in the release of undesirable substances, such as methane, carbon dioxide, and hydrogen sulphide (Bellanger et al. 2004), and an overall

degradation of water quality. This condition can harm fish, such as lake trout, that need cold water to survive.

Hydropower dam operations may impose additional adverse impacts on water quality in the tailrace and ecological systems. When water from a stratified reservoir is released for power generation or to maintain a given river flow, temperatures, dissolved oxygen, and dissolved nutrients from exiting turbines or spillways are not consistent with downstream, well mixed river flows. This phenomenon can disrupt life-cycles of certain aquatic species. It may bring about declines in fish and snail populations due to water quality degradation and incompatible spawning temperatures (Hurford et al. 2010).

Previous field and numerical studies for the temperature distribution at McNary Dam reveal noticeable vertical temperature profiles in the reservoir during summer. However, owing to the relatively shallow water and high velocity, the stable stratified water column with distinct layers was not observed in the reservoir.

2.3.2 Temperature and Fish

Cold blooded fish, such as juvenile salmon, cannot control their body temperatures. Their metabolism is strongly influenced by temperatures in their surrounding environment. Effects of water temperature on juvenile salmon and other species have been extensively studied since the 1950s (Brett 1952). The influence of temperature on fish tolerance, performance, metabolism, food consumption, growth, reproduction, and aggregation continues to this day as a subject of intense research. In general, increased water temperature imposes additional stresses and higher mortality risk on fish.

In a thermal-stratified reservoir, dissolved oxygen amounts vary with water temperature and other factors. In general, warmer water holds less oxygen. Aquatic organisms need to breathe rapidly and swim near the free surface in the highly oxygenated water layers. This process requires additional energy and may exhaust juvenile fish traveling downstream. The thermal stratification and resultant partitioned nutrient-poor epilimnion and nutrient-rich

hypolimnion also have adverse consequences on fish survival and reproduction. A very high negative correlation was found between thermal stratification and monthly fish yields (Mtada 1987). Laboratory and field investigations have been conducted to improve the survival rate of migrating fish at hydropower dams (Somero and DeVries 1967; Lessard and Hayes 2003). Complementing experimental studies, numerical models were developed to predict water temperature under diverse flowrates and atmospheric conditions (Politano et al. 2008).

2.3.3 Wind-Induced Turbulence

The surface boundary layer (SBL) is the most dynamic zone in a lake or reservoir. Exchanges of physical and chemical properties, including momentum, kinetic energy, heat, gas, and others in the SBL are driven by wind and heat flux induced turbulence. Thermal energy from the atmosphere is absorbed by surface waters and redistributed in the SBL by turbulence. Among these two main mechanisms, wind induced turbulence is the dominant mixing mechanism in the SBL (Etemad-Shahidi et al. 2010).

The turbulence characteristic near the surface is complex (Craig and Banner 1994). Total input surface shear stress generated by wind is used to create waves at the very top of the water column and maintain currents in the SBL. At large scales, it is commonly assumed that wind creates a boundary-layer close to the upper surface. In this boundary layer, shear stress is assumed constant, resulting in a vertical velocity profile following the Law-of-the-Wall. The production of turbulent kinetic energy in this logarithmic region can be estimated by the vertical gradient of energy flux, expressed as a function of wind velocity and water depth (Batchelor 1953).

In large-scale environmental and fluid dynamics modeling, assumption of this log-layer near the surface has been widely accepted. Verdier-Bonnet et al. (1999) investigated three-dimensional effects of different $k-\varepsilon$ models on coastal circulations. Wind generated shear stress at the surface was treated as the origin of coastal turbulence. Their simulation results agreed with similar previous studies. Pringle (2007) estimated wind-driven turbulence in the

upper ocean by comparing observations of turbulence avoidance in zooplankton. The author evaluated a turbulence threshold level prompting plankton to move deeper to avoid wind-driven turbulence near the surface. The dissipation of turbulence kinetic energy, ε, was used to indicate turbulence intensity. Chen et al. (2009) simulated the vertical movement of buoyancy regulating cyanobacteria in wind-driven currents. They found that wind driven turbulence affected velocity fields contributing to vertical cyanobacteria migration. An isotropic $k-\varepsilon$ model was applied, taking into account wind-induced turbulence near the free surface. Model results revealed a relationship between wind speed over the water surface and cyanobacteria intensity.

2.3.4 Temperature Models

Temperature models employing a one-dimensional approach have been constructed over the last few decades. Stefan and Ford (1975) developed a deterministic, process-oriented, unsteady, one-dimensional lake water quality model. The model used a one-dimensional vertical transport equation to predict temperature as a function of depth and time. The authors successfully applied the model to several lakes (Stefan et al. 1980; Ford and Stefan 1980). A later study by Hondzo and Stefan (1993) generalized the temperature model for a wide range of lake classes and meteorological conditions. Surface wind mixing, vertical turbulent diffusion, convective heat transfer, and heat flux from solar radiation were incorporated into the model through regression analysis of field data. A recent study by Kirillin (2010) coupled a global climate model with a one-dimensional lake temperature model to evaluate impacts of global warming on lakes. The model revealed relationships between daily and monthly mean air and water temperature. This one-dimensional approach fails when the horizontal advective term cannot be neglected. Another commonly used one-dimensional approach assumes a well-mixed temperature for any cross-section. Gooseff et al. (2005) used this approach to evaluate climate change effects on water temperature in the lower Madison River. This approach, unfortunately, cannot be used to predict thermal stratification in reservoirs.

Multi-dimensional models accounting for both vertical and longitudinal temperature distributions have been extensively applied. Lei and Patterson (2002) used two-dimensional Navier-Stokes and energy equations with the Boussinesq approximation to study natural convection in a reservoir sidearm subject to solar radiation. Bednarz et al. (2009) used a similar approach to investigate transient flow responses to periodic water surface temperature changes in a reservoir model. Their two-dimensional reservoir model consisted of a sloping bottom region and a uniform water depth region. Unsteady flow patterns and stable stratification obtained in the numerical simulations were validated by experiments (Bednarz et al. 2008). Fan et al. (2009) used a three-dimensional model to simulate lateral and vertical water temperature distributions in the Fenhe Reservoir. Parameters of the model were calibrated with field data, and simulation results were consistent with measurements. Liu and Chen (2012) used the three-dimensional circulation model developed by Zhang and Baptista (2008) to simulate water temperature dynamics at a buoy station in Yuan-Yang Lake in north-central Taiwan. Water temperature measured at different depths was used to calibrate and validate the model. Temporal and spatial temperature distributions were satisfactorily predicted by the model.

A fully three-dimensional model, assuming a non-hydrostatic approach, was used to predict hydrodynamics and temperature distribution at McNary Dam by Politano et al. (2008). Heat flux due to short and long wave radiation at the free surface were included through user-defined functions (UDFs). Heat convection at the water-air interface was incorporated into the model considering the air temperature and effects of wind. Good agreement was obtained between the numerical results and field data measured on August 18, 2004, except near the water surface. This model improved the temperature prediction in large-scale flows.

For this study, a three-dimensional numerical model was developed extending the approach of Politano et al. (2008) using the open-source code OpenFOAM. The model aims to more accurately simulate temperature dynamics and distribution, particularly near the water surface. Wind shear stress effects on temperature distribution have been proven negligible (Politano et al. 2006) and therefore are not considered in this study. Turbulence production due

to wind was included into the realizable $k-\varepsilon$ model to account for temperature mixing near the free surface. Simulation results were compared with field data collected on August 18, 2004 at McNary Dam.

2.4 Mathematical and Numerical Models

2.4.1 Mathematical Model

The river hydrodynamics is solved using the incompressible RANS equations with the Boussinesq approximation:

$$\nabla \cdot \boldsymbol{U} = 0 \tag{2.1}$$

$$\rho_0 \frac{\partial \boldsymbol{U}}{\partial t} + \rho_0 \nabla \cdot (\boldsymbol{U}\boldsymbol{U}) = -\nabla p + \nabla \cdot \left(\mu_{eff} \left(\nabla \boldsymbol{U} + \nabla \boldsymbol{U}^{\boldsymbol{T}} \right) \right) + \rho_0 \boldsymbol{g} \left[1 - \beta (T - T_0) \right] \tag{2.2}$$

where $\boldsymbol{U}$ represents the velocity, p the pressure, T the water temperature, $\boldsymbol{g}$ the acceleration due to gravity, β the thermal expansion coefficient, ρ_0 the water density at reference temperature $T_0 = 25$ ℃, and $\mu_{eff} = \mu + \mu_t$ is the effective viscosity, with μ and μ_t denoting molecular and eddy viscosity, respectively.

Studies have shown that the realizable $k-\varepsilon$ model provides better results than the standard or other traditional $k-\varepsilon$ models in many cases involving complex secondary flow (Shih et al. 1995). In this model, the turbulent kinetic energy k and the turbulent dissipation rate ε are obtained from:

$$\frac{\partial}{\partial t}(\rho_0 k) + \nabla (\rho_0 k \boldsymbol{U}) = \nabla \left[\left(\mu + \frac{\mu_t}{\sigma_k} \right) \nabla k \right] + G_k + G_b - \rho_0 \varepsilon + S_k \tag{2.3}$$

$$\frac{\partial}{\partial t}(\rho_0 \varepsilon) + \nabla (\rho_0 \varepsilon \boldsymbol{U}) = \nabla \left[\left(\mu + \frac{\mu_t}{\sigma_\varepsilon} \right) \nabla \varepsilon \right] + \rho_0 C_1 S \varepsilon - C_2 \rho_0 \frac{\varepsilon^2}{k + \sqrt{\nu \varepsilon}} + C_{1\varepsilon} \frac{\varepsilon}{k} C_{3\varepsilon} G_b + S_\varepsilon \tag{2.4}$$

where G_k and G_b are the productions of turbulence kinetic energy by the mean velocity gradients and buoyancy, respectively. ν is the turbulent kinematic viscosity, $C_{3\varepsilon} = \tanh \left| \frac{v}{u} \right|$ where v and u are the velocity components parallel and perpendicular to the gravity, respectively.

$\sigma_k = 1.0$ and $\sigma_\varepsilon = 1.2$ are the turbulent Prandtl numbers for k and ε, respectively. The coefficient C_1 is evaluated as $C_1 = max\left[0.43, \frac{\eta}{\eta+5}\right]$ with $\eta = S\frac{k}{\varepsilon}$, $S = \sqrt{2S_{ij}S_{ij}}$, and $S_{ij} = \frac{1}{2}\left(\frac{\partial u_j}{\partial x_i} + \frac{\partial u_i}{\partial x_j}\right)$. The realizable $k-\varepsilon$ model constants are $C_{1\varepsilon} = 1.44$ and $C_2 = 1.9$. S_k and S_ε are the source terms for k and ε, respectively.

In a reservoir, turbulence produced by wind can be critical. The momentum input at the water surface can be caused by skin friction directly onto the water lid as well as by wave-induced pressure fluctuations and wave and drift-related current interactions (Anis and Moum 1995). The extremely complex nature of this wave-affected layer precludes consideration of the effects of this thin zone (typically less than 1 m) on temperature in the present study. Below the wave-affected surface layer, the steady-state vertical profiles of the horizontal velocity follow the law-of–the-wall. The classical logarithmic-layer characteristic is thus applicable (Craig and Banner 1994). Wind effects on k and ε can be included as source terms in Equations (2.3) and (2.4) following Wüest and Lorke (2003):

$$S_k = \frac{u_*^3}{k_k z^*} \tag{2.5}$$

$$S_\varepsilon = C_{1\varepsilon}\frac{\varepsilon}{k}S_k \tag{2.6}$$

where k_k is the Von Kármán constant and z^* the vertical distance from the free surface. The friction velocity u_* is given as $u_* = \sqrt{\frac{\tau_0}{\rho_0}}$.

The wind stress is determined as $\tau_0 = \rho_a D_w U_w^2$, where ρ_a is air density, U_w the wind speed, and D_w the wind drag coefficient calculated following Wüest and Lorke (2003):

$$D_w \approx 0.0044 U_w^{-1.15} \tag{2.7}$$

Notice that the wind drag coefficient is strongly affected by the state of the surface wave development. Waves produce additional roughness, increasing friction at the free surface and enhancing momentum flux transferred from air to water. Observations found that young and

underdeveloped waves are shorter, steeper, and of higher frequencies and therefore appear rougher and produce more turbulence than more mature waves. Due to the limited extent of the McNary reservoir, the wave field typically stays underdeveloped. The above approximation under-predicts the wind-induce turbulence because it is based on a fully developed wave field.

In the realizable $k-\varepsilon$ model, the turbulent viscosity is given by

$$\mu_t = \rho_0 C_\mu \frac{k^2}{\varepsilon} \tag{2.8}$$

with the coefficient C_μ calculated from

$$C_\mu = \frac{1}{A_0 + A_s \frac{kU^*}{\varepsilon}} \tag{2.9}$$

where U^* is defined as $\sqrt{S_{ij}S_{ij} + \overline{\Omega}_{ij}\overline{\Omega}_{ij}}$ with $\overline{\Omega}_{ij}$ being the mean rate-of-rotation tensor. The constants $A_0 = 4.0$ and $A_s = \sqrt{6}cos\phi$, where $\phi = \frac{1}{3}cos^{-1}\left(\sqrt{6}W\right)$, $W = \frac{S_{ij}S_{jk}S_{ki}}{S^3}$, and $S = \sqrt{S_{ij}S_{ij}}$.

The production of turbulence kinetic energy by the mean velocity gradient is evaluated with the Boussinesq hypothesis:

$$G_k = \mu_t S^2 \tag{2.10}$$

The buoyancy-induced production of both k and ε is given by

$$G_b = \beta \boldsymbol{g} \frac{\mu_t}{Pr_t} \nabla T \tag{2.11}$$

where $Pr_t = 0.85$ is the turbulent Prandtl number for energy. This term tends to suppress turbulence if stratification is established, as in the case of this study.

Modeling of the energy budget and reservoir temperature cycles requires incorporation of short and long wave radiation and heat convection at the free surface. The incident solar radiation can be included as a positive energy source in the energy conservation equation while the other heat fluxes are considered at the free surface as boundary conditions. In this study it is

assumed that the heat flux to the underlying soil is negligible. Water temperature T can be calculated from the energy conservation equation for incompressible flows:

$$\rho_0 C_p \frac{\partial T}{\partial t} + \rho_0 C_p \nabla \cdot (\boldsymbol{U} T) = \nabla \cdot \alpha_{eff} (\nabla T) + S_{rad} \quad (2.12)$$

where C_p is the specific heat and $\alpha_{eff} = \alpha + \alpha_t$ is effective thermal conductivity, with α and α_t, the molecular and turbulent thermal conductivity, respectively. Pressure work, energy source due to viscous dissipation, and kinetic energy are not considered. S_{rad} represents energy source due to solar radiation, which is calculated following Beer's law as:

$$S_{rad} = S_0 \varphi exp(-\varphi z^*) \quad (2.13)$$

with S_0 the incident radiation and z^* the vertical distance from the free surface. φ is the absorption coefficient, or attenuation coefficient that describes the reduction of solar radiation intensity as it passes through the water body. A typical range for φ in a reservoir is from 0.02 to 0.2 m^{-1} (Smith and Baker 1981). Politano et al. (2006) performed a sensitivity study of this parameter and demonstrated that a value of $\varphi = 0.5\ m^{-1}$ matched the field data. In this study, $\varphi = 0.5\ m^{-1}$ was used.

2.4.2 Computational Grid

The McNary Dam forebay (Figure 2.1) was meshed with multi-block grids containing only hexahedral elements using the commercial grid generator Gridgen. The main features of the dam, including the powerhouse units, spillway bays, fish collection facilities, and the navigation lock were meshed with approximately 1.7 million grid points (Figure 2.2). Nodes were clustered near the free surface to resolve the flow field and capture temperature distributions in the most dynamic zone. Grids at the reservoir bottom were created conforming to measured bathymetric data. Figure 2.2 shows grid details. Sections A, B, and C on the lower left show cross-sections of the grid at the inflow section, middle section, and near the structures, respectively. Since the focus of this study is to evaluate temperature dynamics in the McNary Dam forebay area, detailed structures within the powerhouse units were simplified or not included. Adequacy of the

grids was tested by comparing results obtained with two grids: an original grid and a fine grid refined $2^{0.5}$ times in all directions. Temperature profiles obtained with these grids were almost identical (Wang et al. 2013a).

2.4.3 Simulation Conditions

Water temperature measurements were available from the USACE for 43 of 46 stations along 6 transects at 15 minute intervals for the summer of 2004. Station nomenclature employs a two-character transect identifier (T1-T6), and a two-character point identifier (e.g. P1) indicating the sampling station location in the river cross-section direction. For example, station T2P3 refers to the third monitoring station starting from the Oregon shore on the second transect. Figure 2.3 illustrates data collection stations along with bathymetric information in the study domain. The model extended about 4100 m upstream of the dam to minimize influences of the boundary conditions. Weather conditions, including air temperature, longwave radiation, incident shortwave radiation, and wind magnitude, were collected every 10 minutes as provided by the Walla Walla District/OA Systems Weather Station.

In this study, atmospheric and operational conditions on August 18, 2004 were used to simulate the flow field and temperature dynamics in the McNary Dam forebay. Hourly water temperature data collected at T6 was interpolated and imposed at the inflow boundary. Figure 2.4 shows inlet temperature contours at 6 AM, 12 PM, 6 PM, and 12 AM. On the simulated day, the average river flow was 4380 m^3/s. As illustrated in Figure 2.5, the measured river discharge indicated a nearly constant flow condition from 6 AM to 5 PM. Transient flows were observed before and after this period due to turbine operation variations. Since inclusion of a variable flowrate requires a much smaller time step, a constant flow condition was assumed as in Politano et al. (2008). Effects of this simplification are discussed in Section 2.5. The incident radiation S_0 was calculated as the difference between measured incoming and reflected solar radiation (Figure 2.6). Data collected between 9 AM and 5 PM was distributed in a scattered manner due to reflection and absorption effects of clouds.

2.4.4 Boundary Conditions

Free Surface: the water surface is modeled with a rigid-lid approach, assuming a flat surface with zero shear stress. Water surface elevation is obtained from field data provided by the USACE. Heat flux at the free surface, q, is modeled as a linear function of the difference between water and air temperatures (Edinger et al. 1968):

$$q = h\left(T - T_a\right) \tag{2.14}$$

where T_a is the air temperature, and h is the heat transfer coefficient calculated as in Ahsan and Blumberg (1999):

$$h = C\left(6.9 + 0.345\left|U_w\right|^2\right) \tag{2.15}$$

where C is the Bowen coefficient, and $C = 0.62\,\text{mb/℃}$, which relates the wind effect on sensible heat flux to that on latent heat flux. In this study an average measured wind speed on August 18, 2004 of 1.74 m/s is used.

Air temperature data collected in the field is fitted with a quadratic sinusoidal function to represent temporal temperature variations at the free surface.

$$T_a = 10\sin^2\left(\frac{\pi\left(t-5\right)}{24}\right) + 21.4 \tag{2.16}$$

where t is the time in hours. Figure 2.7 shows the function used to adjust the air temperature on August 18, 2004. Energy balance at the free surface corresponds to a mixed boundary condition. In OpenFOAM, the temperature at the boundary face T_{face} is determined using (Vilums 2011):

$$T_{face} = fTa + \left(1 - f\right)T_{center} \tag{2.17}$$

with T_{center} the temperature at the cell center, and $f = \left(1 + \frac{k_{eff}}{h\delta}\right)^{-1}$. δ is the distance from the cell center to the face, and k_{eff} is the effective thermal conductivity. This condition was implemented in OpenFOAM using the utility groovyBC.

Walls and River Bed: a non-slip condition and zero heat flux are used for all walls, river banks, and the river bed. Standard wall functions available in OpenFOAM are used.

Outflows: the powerhouse, spillways, and fishways are modeled as outflows with a specified outflow discharge. Zero temperature gradients are imposed on the outflows.

Inflow: a given total river flow and measured temperature, provided by USACE, are specified at the upstream inflow section. Velocity is assumed to be uniformly distributed. Turbulent variables are assumed to be zero at the upstream end of the study domain.

2.4.5 Numerical Method

The mathematical model described in the preceding section was implemented in the control-volume open-source code OpenFOAM. OpenFOAM uses a co-located methodology. The PIMPLE algorithm, which is a mixture of the PISO (Pressure Implicit with Splitting of Operators) and SIMPLE (Semi-Implicit Method for Pressure-Linked Equations) algorithms, was used to couple pressure and velocity. The Euler blended Crank-Nicholson method was used to discretize the temporal term. This is a first-order, bounded implicit method. Convective terms were discretized using Gauss limited Linear (Gauss refers to the standard finite volume discretization of Gaussian integration). Lapacian terms used Gauss linear corrected interpolation to calculate values from cell centers to face centers. Due to the transient nature of the problem, an adaptive time-stepping technique based on the Courant number was employed. A maximum Courant number of 0.5 was used for this study. Numerical tests using Courant numbers of 1 and 1.5 were also performed (Wang et al. 2013a). Temperature profiles for these Courant numbers were almost identical. The model, however, becomes more unstable as the Courant number increases.

Unsteady atmospheric conditions observed on August 18, 2004 were applied repeatedly over many diurnal cycles. The model was run with a constant initial uniform temperature of 22 ℃ until a periodic solution was obtained. Figure 2.8 shows the temperature evolution at the powerhouse exits.

2.5 Numerical Results

Daily flow pattern and temperature dynamics in the McNary forebay on August 18, 2004 were obtained with the model. The predicted flow field in the forebay is unsteady and highly three-dimensional due to the influence of the dam structures, reservoir bathymetry, and dynamic atmospheric conditions. Note that the flow is coupled with energy and therefore temperature changes can result in unsteady velocity distributions. Predicted velocity vectors (black vectors) for a horizontal plane 1 meter beneath the free surface at 6 AM, 12 PM, 6 PM, and 12 AM, are shown in Figure 2.9. Velocity vectors near the river bed (20 meters below the water surface, area colored in gray) are plotted in the same figure as red vectors. Since the spillway was not operating on the simulated day, river flow exits at powerhouse units in the central area of the forebay. A high velocity zone is observed near the powerhouse region. The influence zone of powerhouse intakes extends up to 1000 meters upstream of the structures. The predicted vertical velocity profile is not uniformly distributed. Flows in the upper water column are entrained toward the powerhouse region and move away from the Washington shore. On the other hand, flows near the bottom tend to follow the bathymetry. Low velocity eddies are observed near the navigation lock in response to the structure and relatively shallow waters close to the bank. This phenomenon decreases local temperature mixing with the main channel and increases residence time in this region.

The spatial and temporal temperature cycles are a consequence of both convective heat transfer from the river upstream and periodic heating/cooling of the atmosphere (Figures 2.6 and 2.7). Positive heat flux during the day warms the water body. Longwave radiation along with lower air temperatures cools the surface layer after sunset. Figure 2.10 shows the predicted temperatures near the water surface at various times during the simulated day. The lag between air and water temperatures results in the lowest and highest predicted temperatures being observed at around 7 AM and 5 PM, respectively. Due to the non-uniform vertical velocity field (Figure 2.9), warm surface waters are transported towards the Oregon side, while cooler waters at the bottom migrated to the Washington shore. An overall higher temperature is predicted near

the Oregon side of the reservoir. Predicted temperatures around the navigation lock is about 1 to 2 ℃ lower than the water temperature through the powerhouse. This low temperature zone greatly benefits the Washington Fishway. Shallow waters with strong mixing, as predicted by the model, raise temperatures near the Oregon Fishway.

Predicted and measured temperatures at 0.5 meter beneath the free surface for sampling stations along transect 4 are shown in Figure 2.11. The x-axis denotes distance from the Oregon shore. Data points in this figure, from left to right, represent stations T4P1 to T4P6. As illustrated, the predicted temperature evolution in the lateral direction agrees quantitatively with field data. Higher general temperatures are predicted near the Oregon shore, consistent with field observations. Field data does show a higher variability than the model at around 6 PM. This phenomenon may be attributed to transient flow conditions during this period (Figure 2.6). Since in the current study, the flowrate is assumed constant, this effect is not captured by the model.

Figure 2.12 shows predicted temperature distributions through powerhouse unit 7 at 6 AM, 12 PM, 6 PM, and 12 AM. The daily thermal cycle is predicted by the model. The nearly uniform vertical velocity in the McNary forebay gradually accelerates approaching the powerhouse intake. Average gatewell temperatures increases as warm waters are entrained from the free surface. As seen in this figure, water in the surface layer, heated after sunrise by short wave radiation and air convection, is transported to the gatewells imposing risk of additional stress to fish traveling towards the gatewells.

Predicted temperature dynamics in the simulation domain are compared with field measurements and discussed in detail for four stations, T1P4, T2P4, T3P4, and T4P3, to demonstrate the capability of the model to represent temperature dynamics in the forebay. These selected data points are located in the main stream, where temperature distribution is strongly affected by the flow convection and heating/cooling of the atmosphere. Comparison between predicted and measured temperature profiles for other stations can be found in Figures 2.15 to 2.24. Notice that the capability of the model to predict the forebay temperature dynamics focuses on agreement between field data and predictions in several stations at different times. The model

is validated by determining the accuracy of predictions of forebay temperature dynamics from the perspective of the intended use of the model. It is important to note that the model validity is confined to the area of study and restrained by inputs and parameters used. This limits the use of the model to this dam. Its application to any other dam would require re-validation.

Figure 2.13 shows vertical temperature profiles at 6-hour intervals predicted by the model (solid lines), along with field data (symbols) for stations T1P4, T2P4, T3P4, and T4P3. Good agreement between predicted and measured data is obtained. The measured temperature profile is captured by the numerical model. Below 15 m from the water surface, an undisturbed, well mixed temperature profile is predicted for all stations. Predicted temperatures in this layer match quantitatively well with field measurements. Differences between the numerical and field data fall within 0.5 ℃.

Water temperature in the top layer is more sensitive to the meteorological conditions. A strong temperature gradient in the first 5 m beneath the free surface is predicted by the model. Although deviations between modeled and measured temperature profiles in this layer are relatively large, general trends and daily temperature fluctuations due to heat transfer are reasonably reproduced by the model. Incorporation of the wind-induced turbulent diffusion and clouds albedo help to distribute thermal energy uniformly in this layer. Differences between the numerical and field data are less than 1℃ for all four stations. In most cases, predicted temperature profiles near the free surface with the present model are closer to the measured data than those obtained by Politano et al. (2008) (Wang et al. 2013b). Note that measured surface temperature mixing is stronger near dam structures (T1P4 and T2P4) than in the forebay region (T3P4 and T4P3) at 6 AM. This can be attributed to the transient flows before 6 AM (Figure 2.6) not captured by the current model. Errors in field measurements near the free surface may be attributed to difficulties in data acquisition under strong vertical temperature gradients. Evaluation of the model prediction accuracy is difficult since uncertainty analysis of the field data is not provided. However, the overall agreement between numerical results and field measurements is satisfactory at all stations

Figure 2.14 shows the effect of each of the thermal processes on the predicted vertical temperature distributions at station T4P1. Vertical temperature profiles predicted without solar radiation, convective heat transfer at the free surface, and wind induced turbulence are plotted in the first column of Figure 2.14. The free surface was assumed to be adiabatic in this case. The above mentioned processes were included in sequence and the resulting temperature profiles are illustrated in the second, third, and fourth columns, respectively. Field data is represented in the plots as symbols. Temperature distributions near the forebay bottom are not affected by the applied thermal and turbulence models. Influence of the models can only be seen in the surface layer. As illustrated in the figure, the solar radiation, which is a positive energy source, increases surface water layer temperatures during the day. Temperature profiles predicted with solar radiation at 12 PM and 6 PM are closer to the field data than model predictions without radiation. However, surface water temperatures at night (6 AM and 12 AM) are over predicted due to an absence of cooling mechanisms. Long wave radiation and heat transfer between water and air enhance cooling process at night. An improvement of temperature prediction at 6 AM and 12 AM is observed with incorporation of the atmospheric convection and long wave radiation. Incorporation of the wind-induced turbulence results in a more smoothly distributed thermal energy near the free surface. In general, incorporation of thermal and turbulence models better represents heat transfer and mixing processes in the reservoir and improves overall prediction near the water surface.

2.6 Summary

An unsteady three-dimensional numerical model was developed to predict hydrodynamics and temperature dynamics in the forebay of a hydropower dam. The model is based on the open-source code OpenFOAM, and solves the incompressible RANS equations with the Boussinesq approximation. Turbulence was modeled with a realizable k-ε model with wall functions. Solar radiation and convective heat transfer at the free surface were incorporated into the model. Wind-induced turbulence was modeled by assuming a logarithmic boundary

layer beneath the free surface. Simulation results were compared against field data collected in McNary Dam for a typical summer day. The main conclusions are:

1) The model captures the observed spatial and temporal temperature fluctuation.
2) The flow pattern in the forebay of McNary Dam is highly three-dimensional and coupled with temperature.
3) Incorporation of solar radiation, atmospheric convection, and wind-induced turbulence improves the temperature predictions near the free surface.
4) The presented computational fluid dynamics model can be used to evaluate operational conditions or structural modifications to improve fish survival in the dam.

Figure 2.1 Aerial view of McNary dam forebay (source: Google Earth)

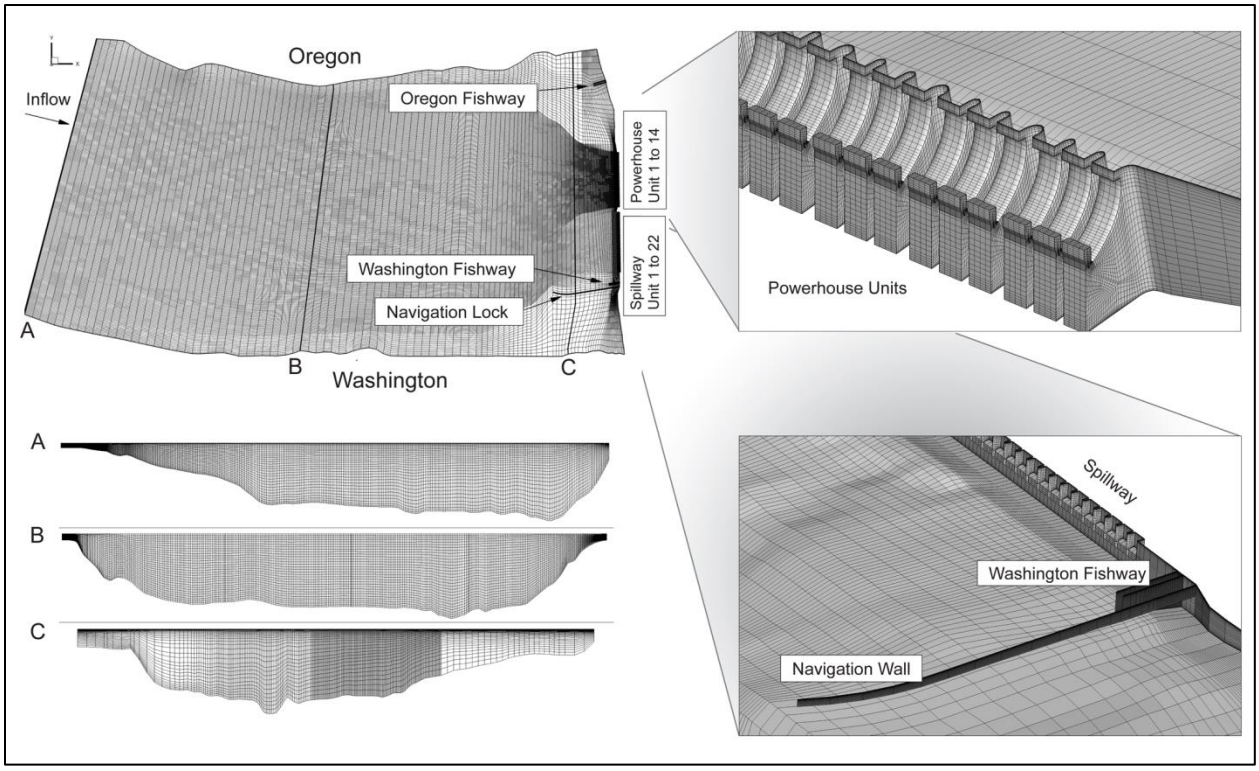

Figure 2.2 Numerical grid of McNary forebay and dam structures with details

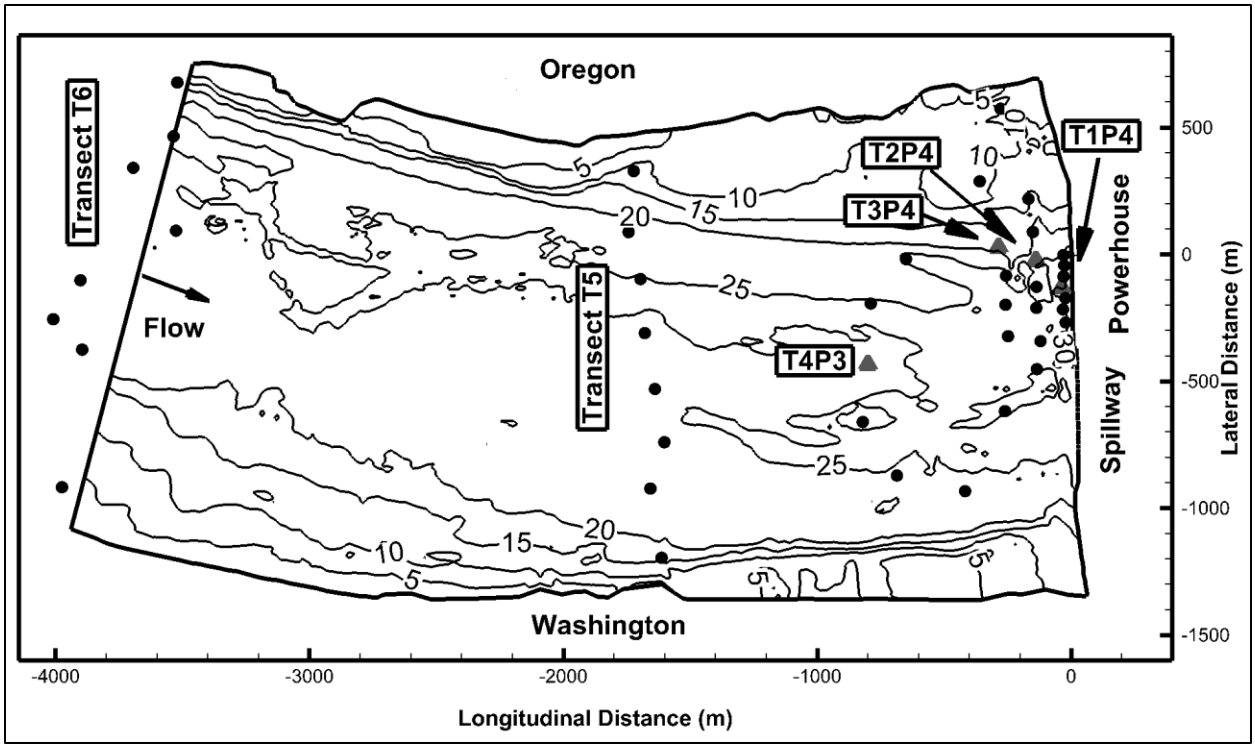

Figure 2.3 McNary reservoir bathymetry and data collection sites

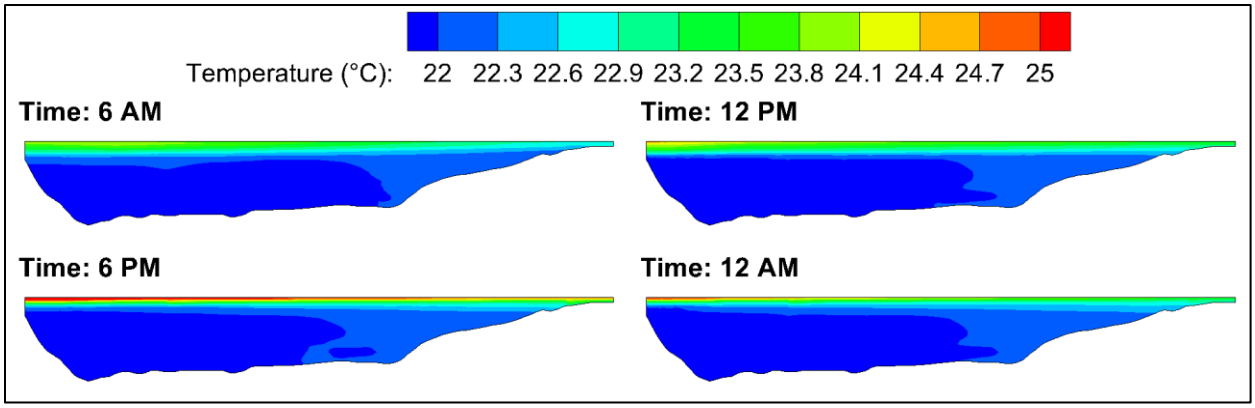

Figure 2.4 Inlet boundary temperature contours

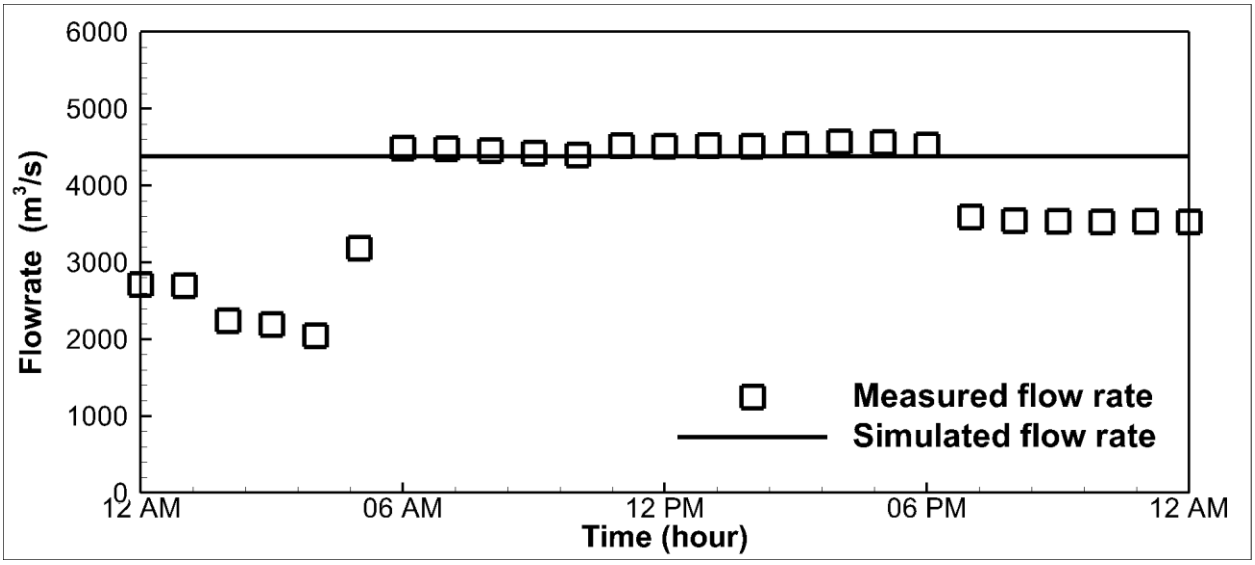

Figure 2.5 Measured and simulated flow rate

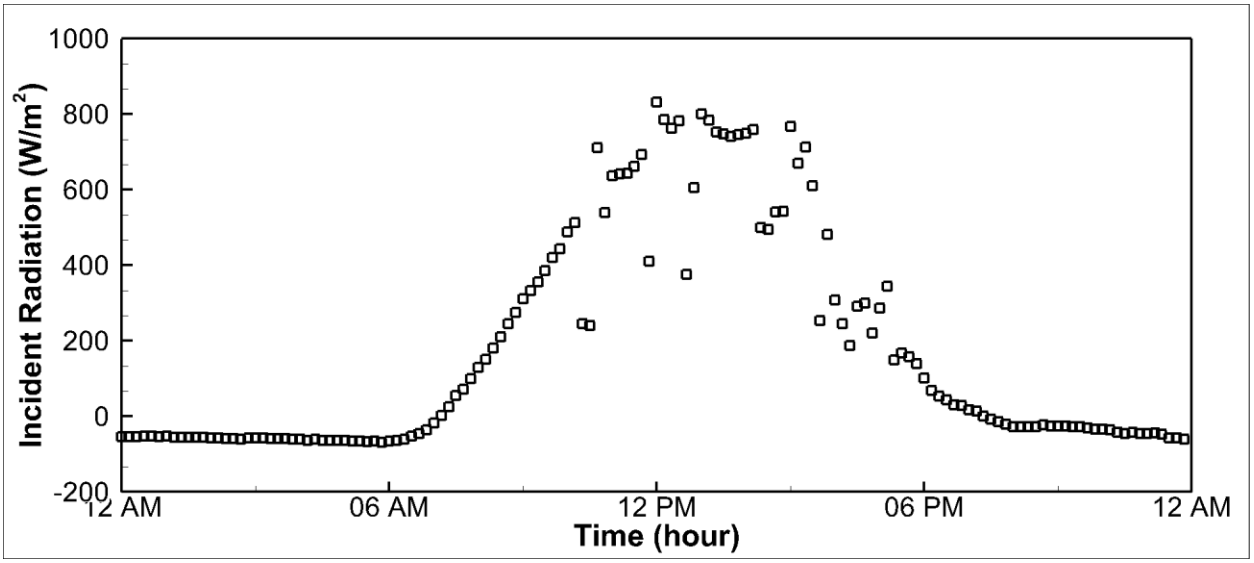

Figure 2.6 Net radiation as a function of time

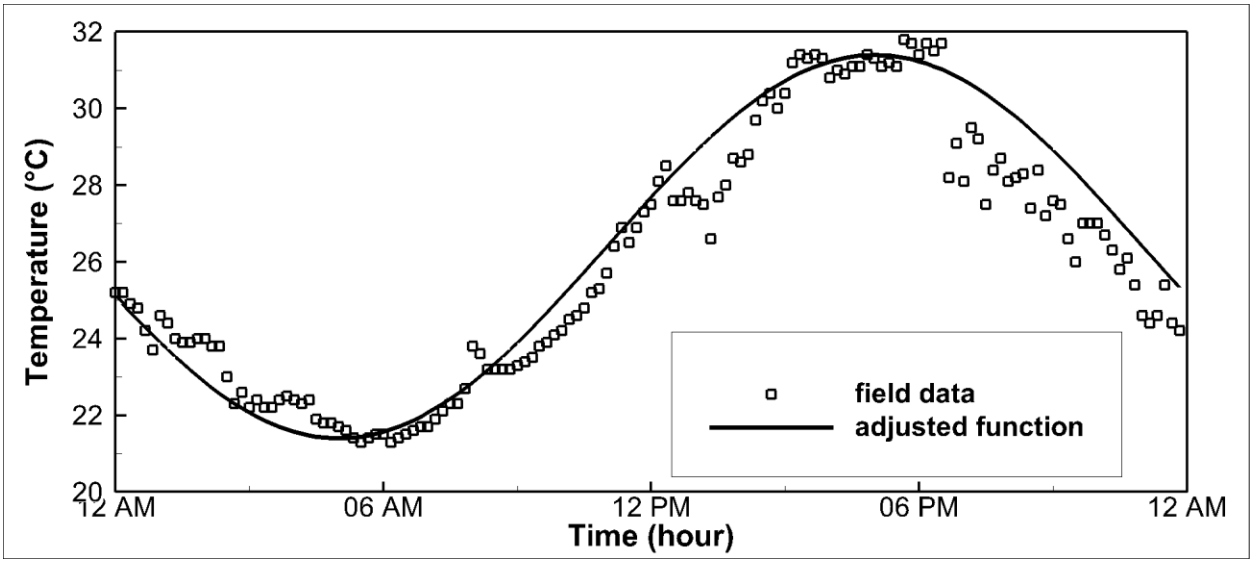

Figure 2.7 Measured air temperature and adjusted function as function of time

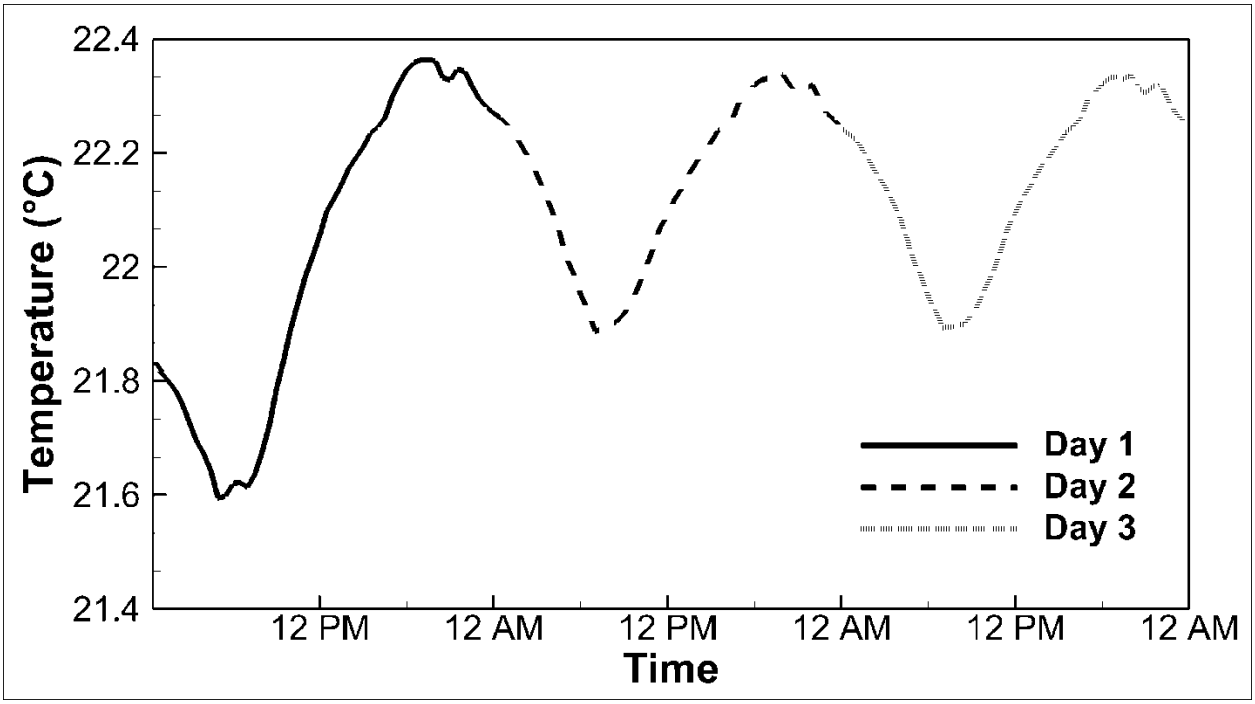

Figure 2.8 Predicted temperature evolution at powerhouse units

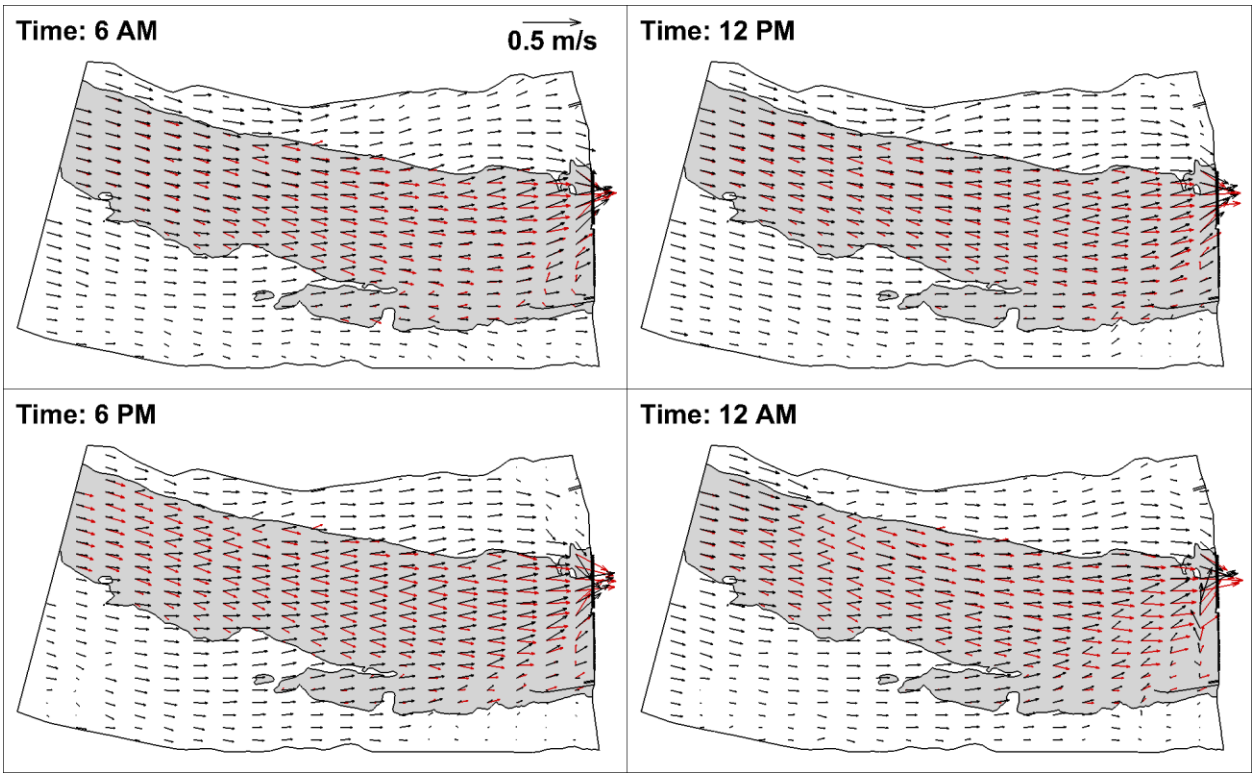

Figure 2.9 Predicted velocity distribution at 1 m (black vectors) and 20 m (red vectors) beneath the free surface

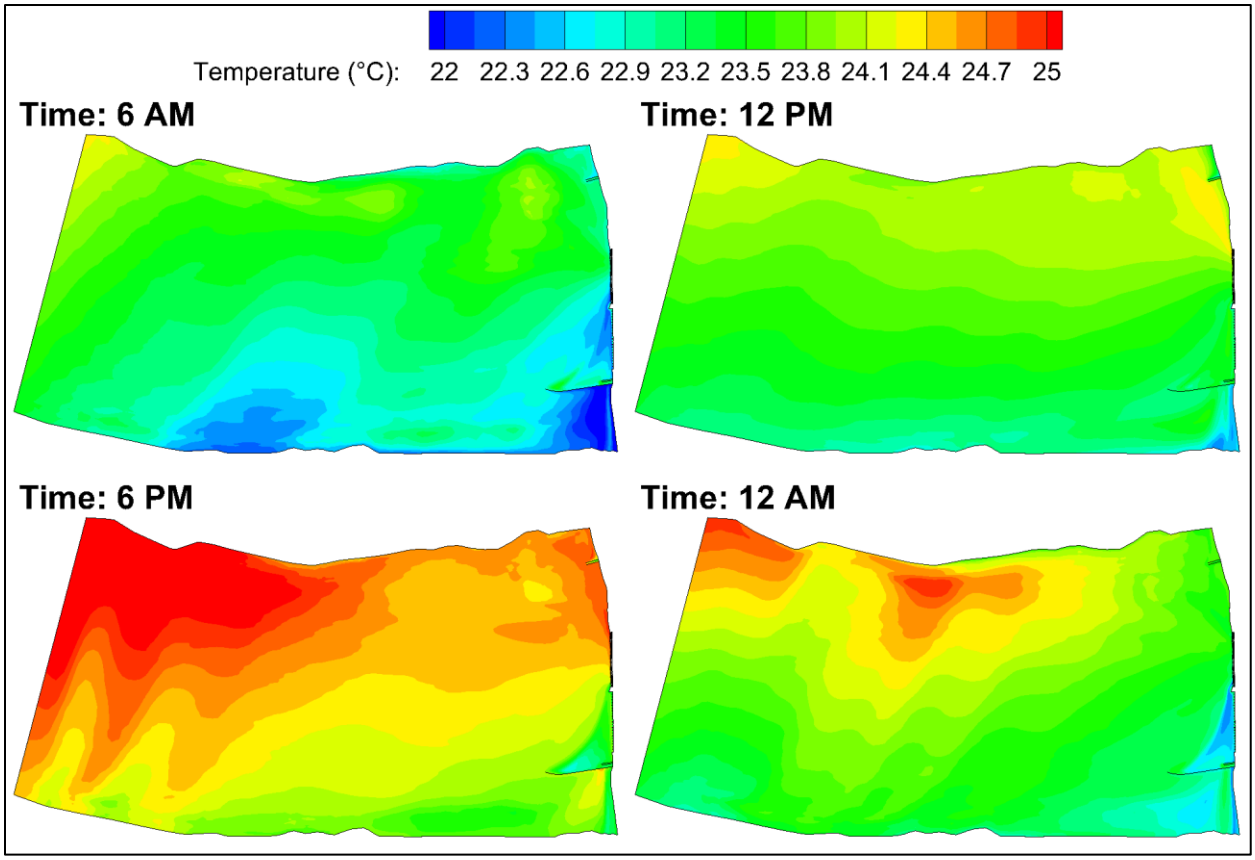

Figure 2.10 Predicted temperature contours at 1 m beneath the free surface

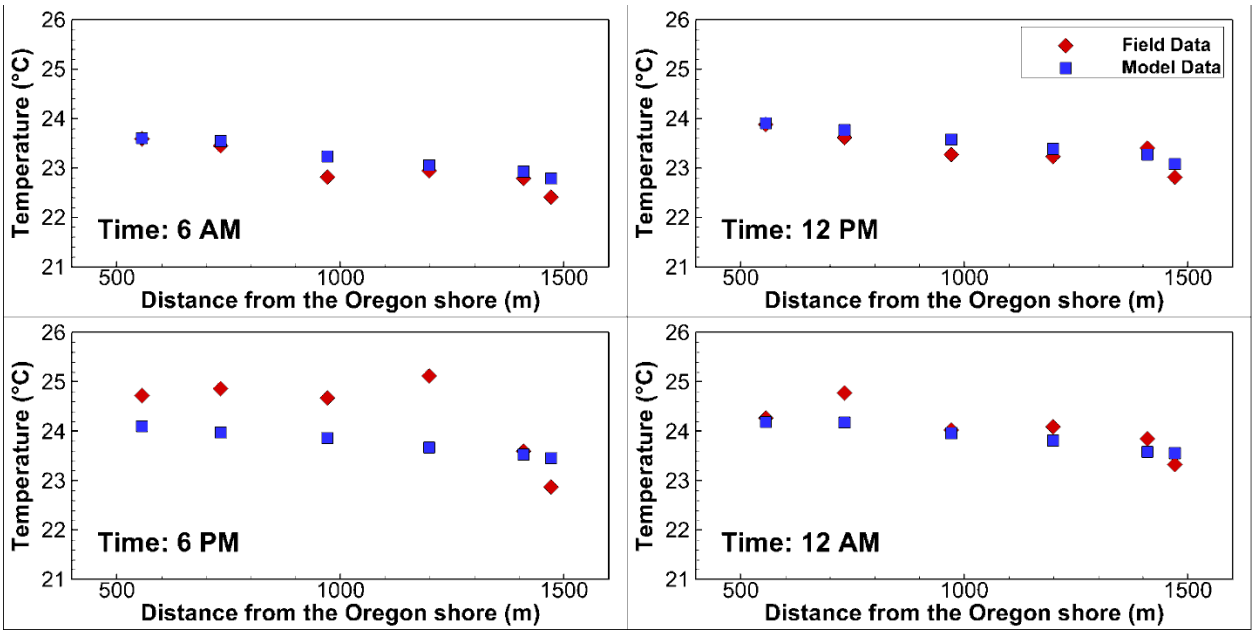

Figure 2.11 Predicted and measured temperature at Transect 4 as a function of the distance from the Oregon shore

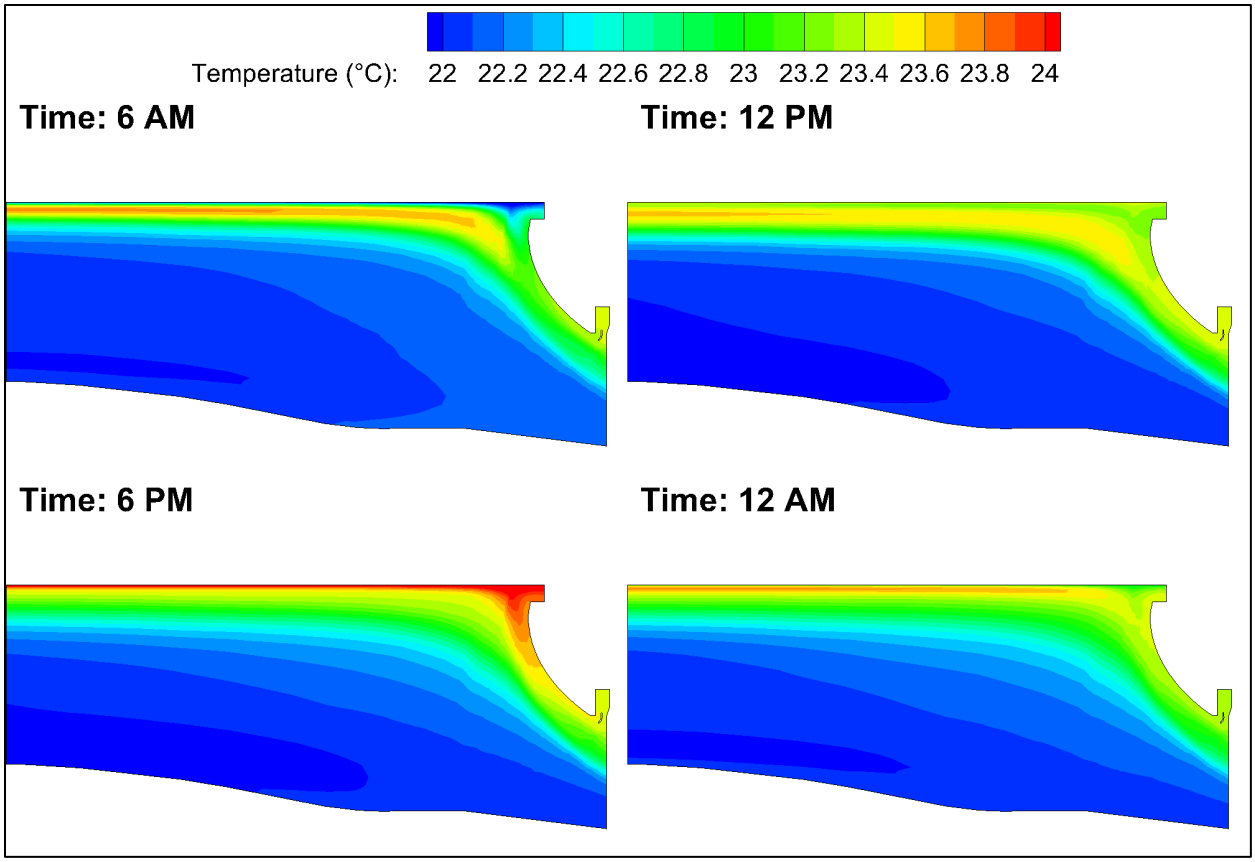

Figure 2.12 Predicted vertical temperature contours through powerhouse unit 7

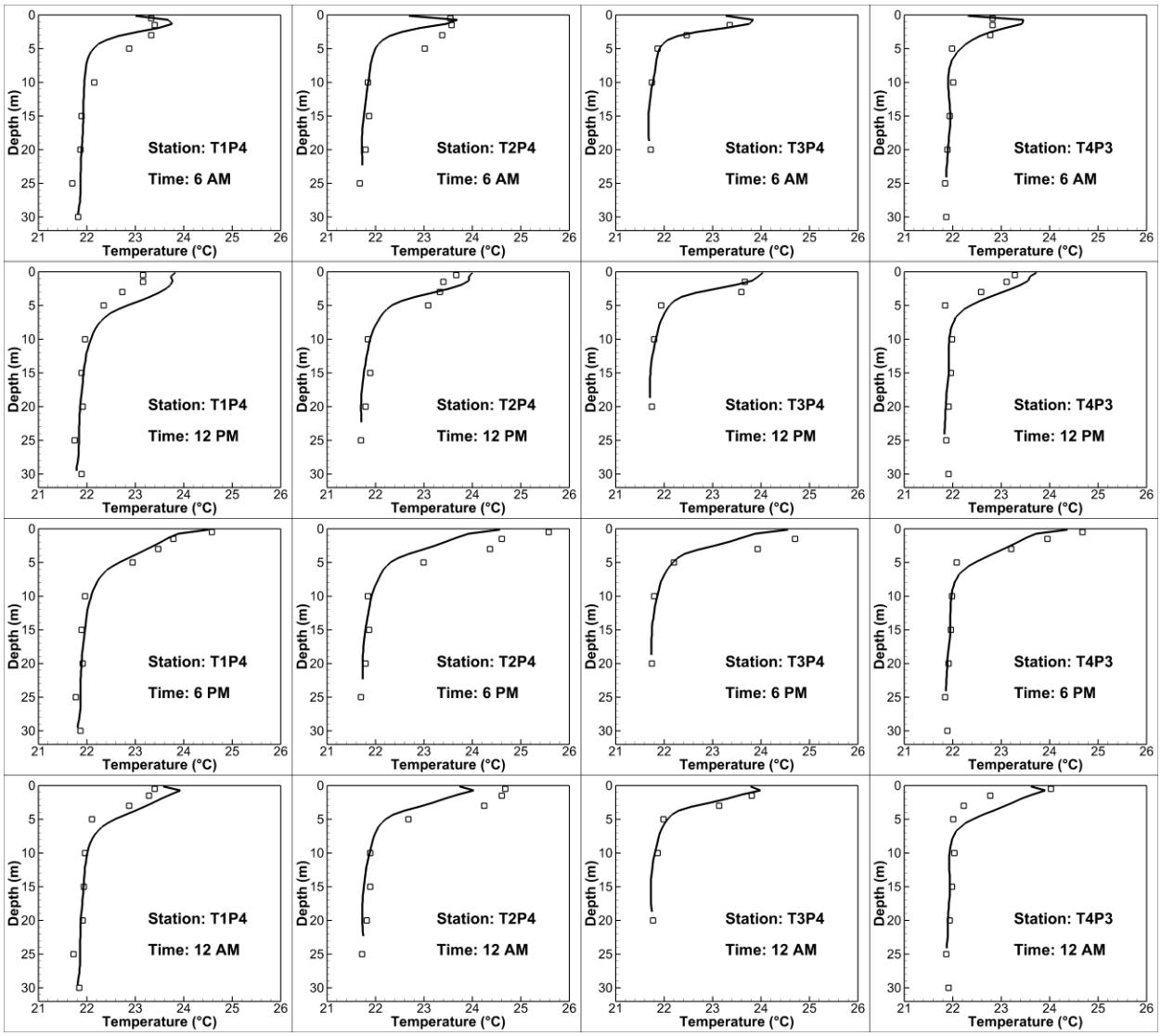

Figure 2.13 Predicted and measured temperature profiles at 6 AM, 12 PM, 6 PM, and 12 AM at stations T1P4, T2P4, T3P4, and T4P3

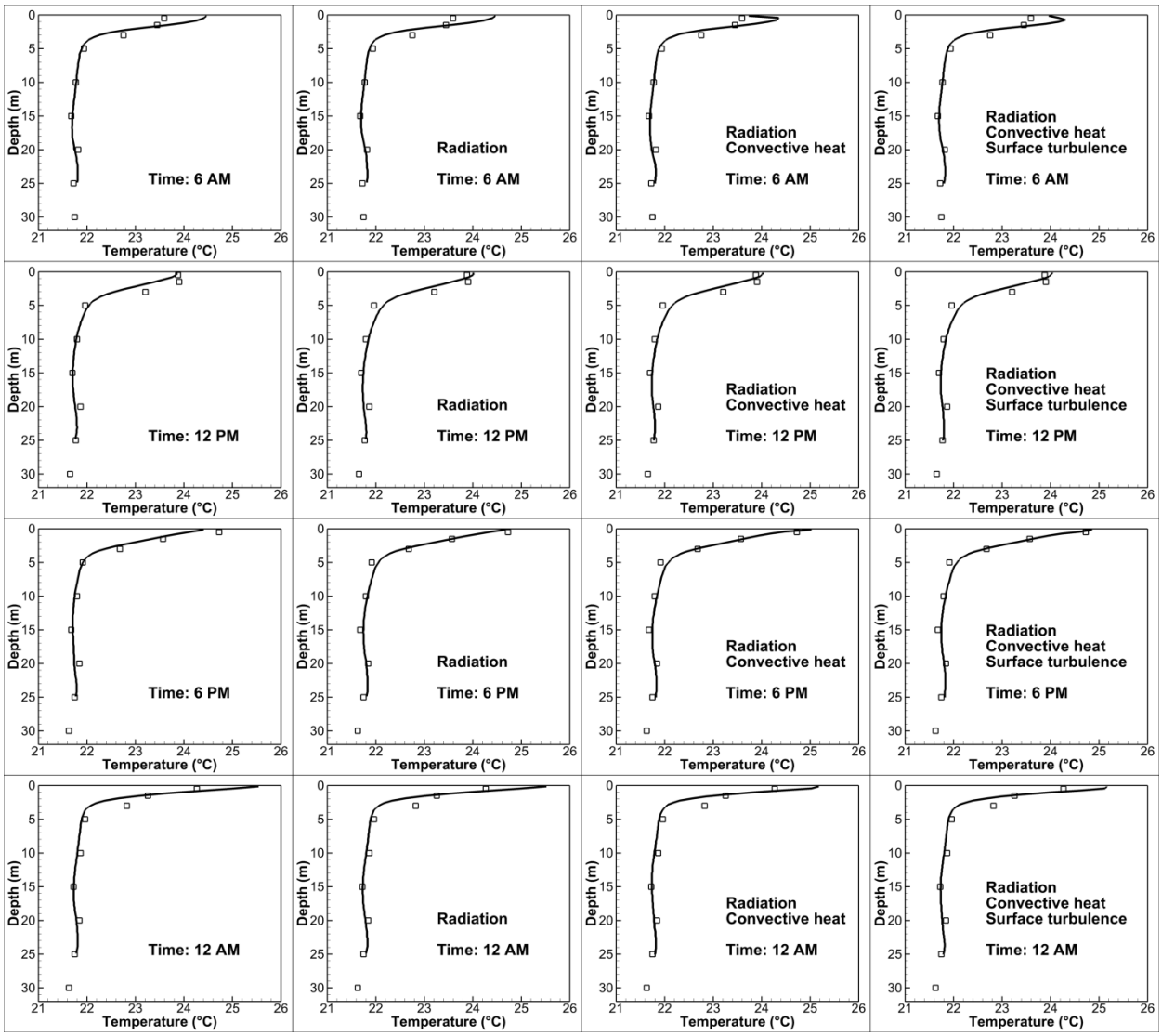

Figure 2.14 Predicted temperature profiles with adiabatic free surface (first column), solar radiation model (second column), convective heat transfer (third column), and wind induced turbulence (last column).

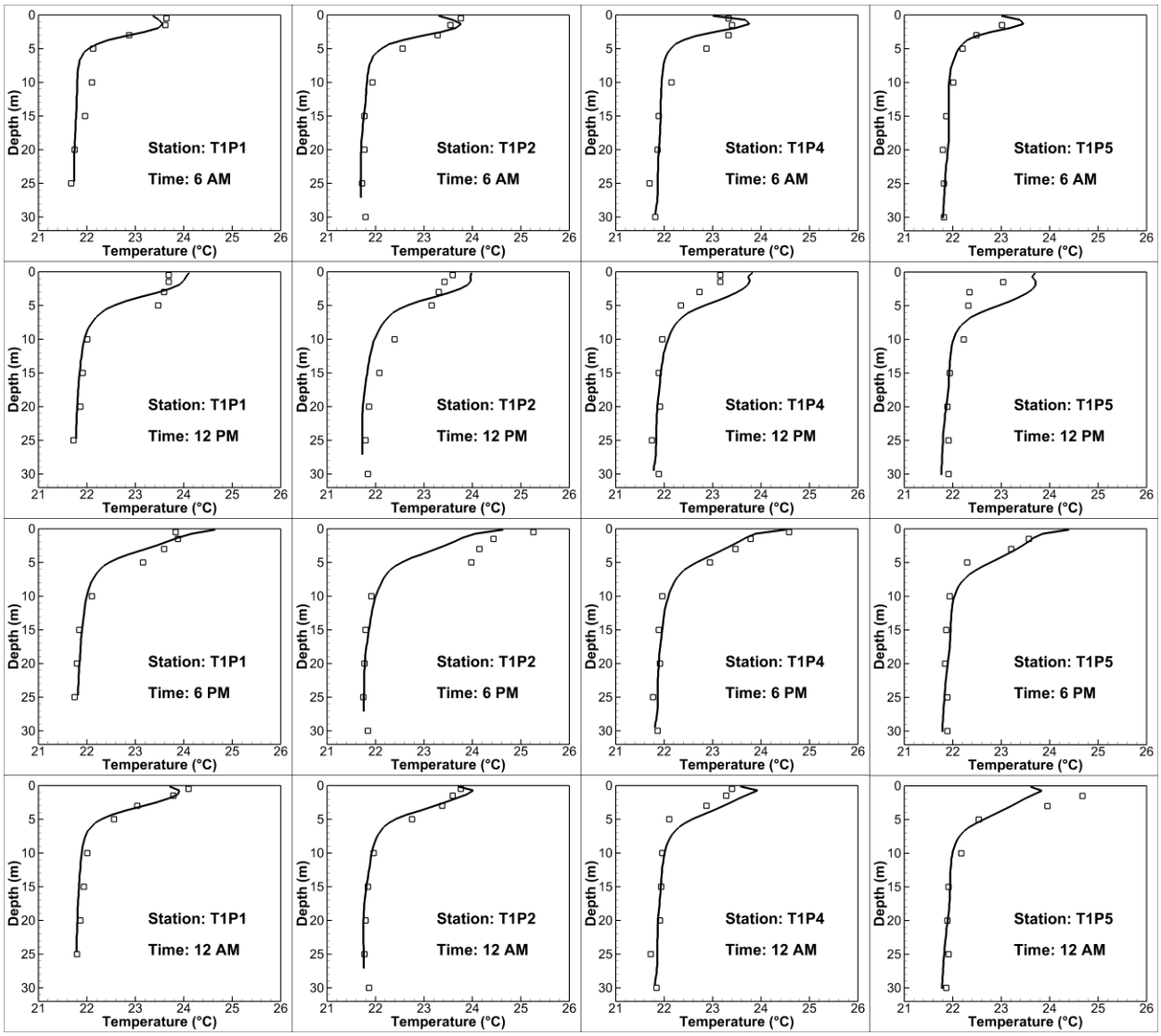

Figure 2.15 Predicted and measured temperature profiles at 6 AM, 12 PM, 6 PM, and 12 AM at stations T1P1, T1P2, T1P4, and T1P5

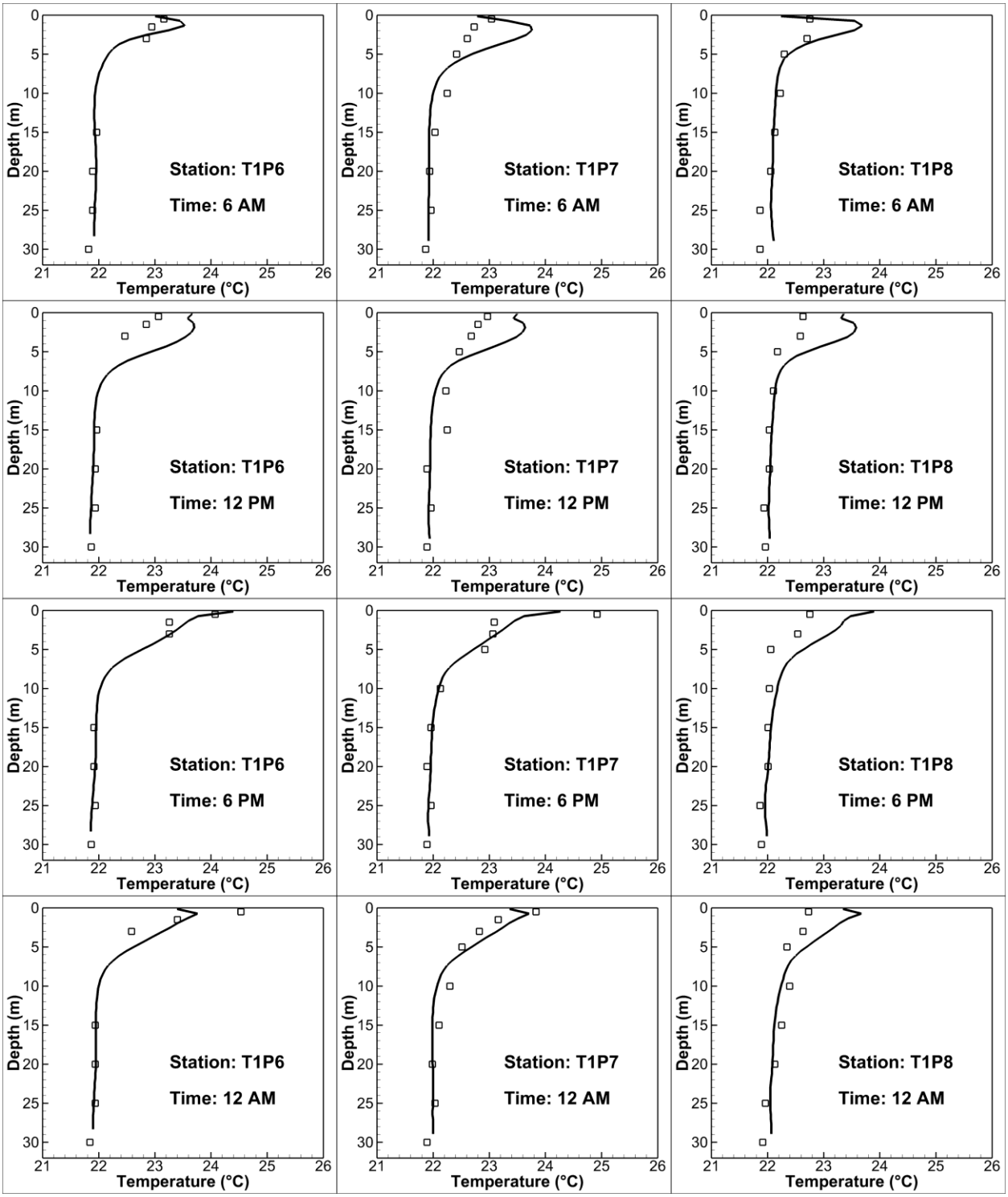

Figure 2.16 Predicted and measured temperature profiles at 6 AM, 12 PM, 6 PM, and 12 AM at stations T1P6, T1P7, and T1P8

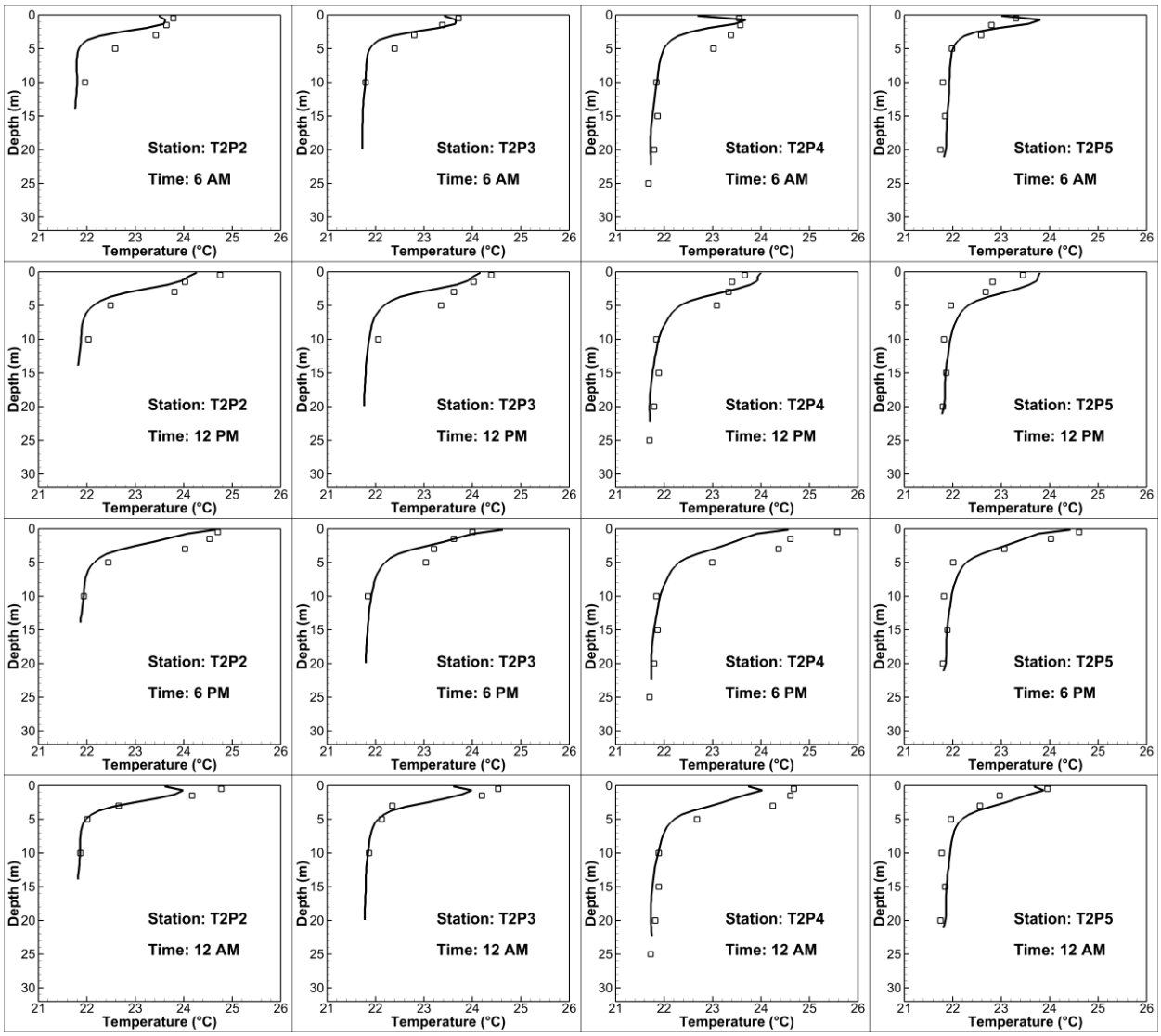

Figure 2.17 Predicted and measured temperature profiles at 6 AM, 12 PM, 6 PM, and 12 AM at stations T2P2, T2P3, T2P4, and T2P5

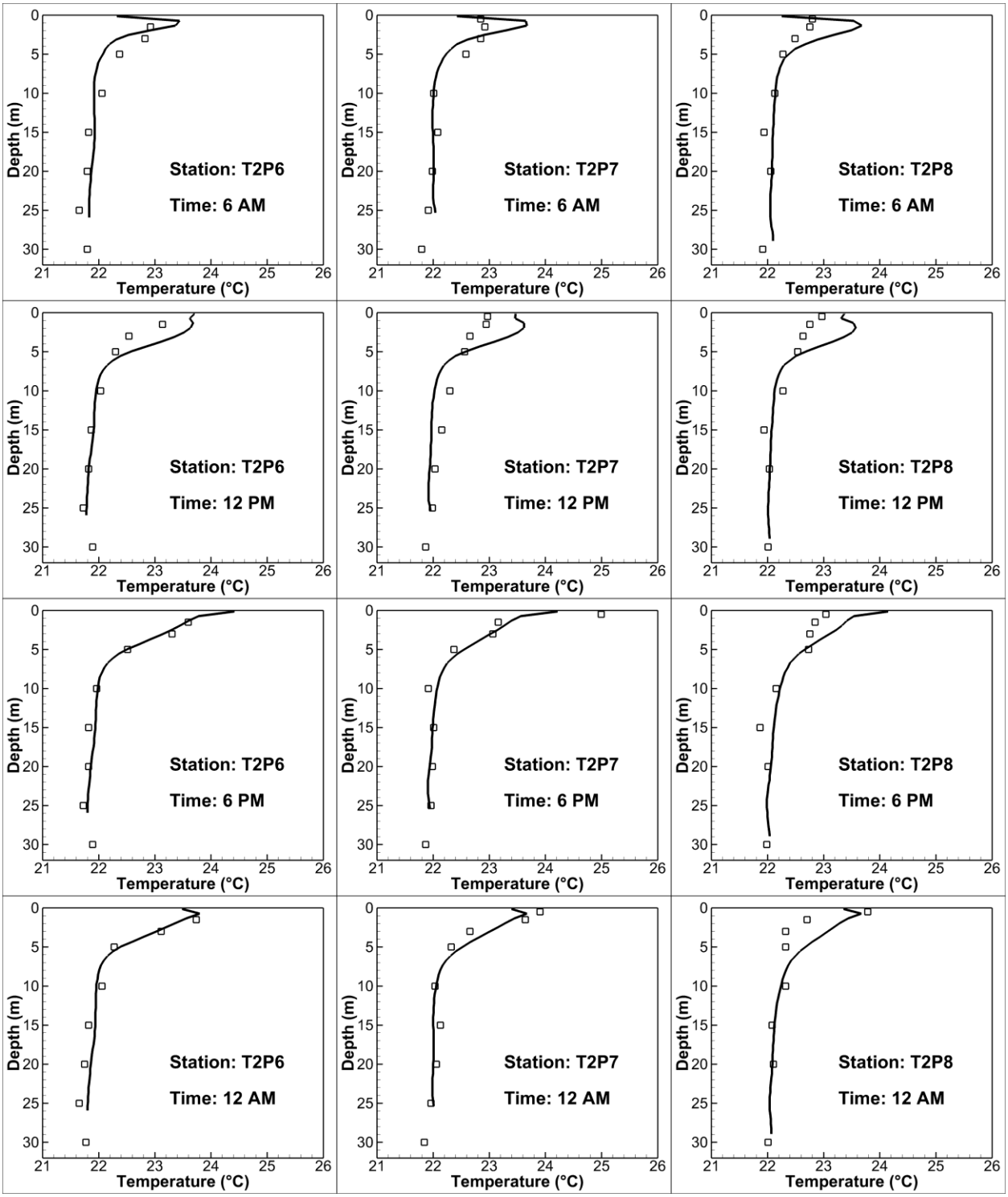

Figure 2.18 Predicted and measured temperature profiles at 6 AM, 12 PM, 6 PM, and 12 AM at stations T2P6, T2P7, and T2P8

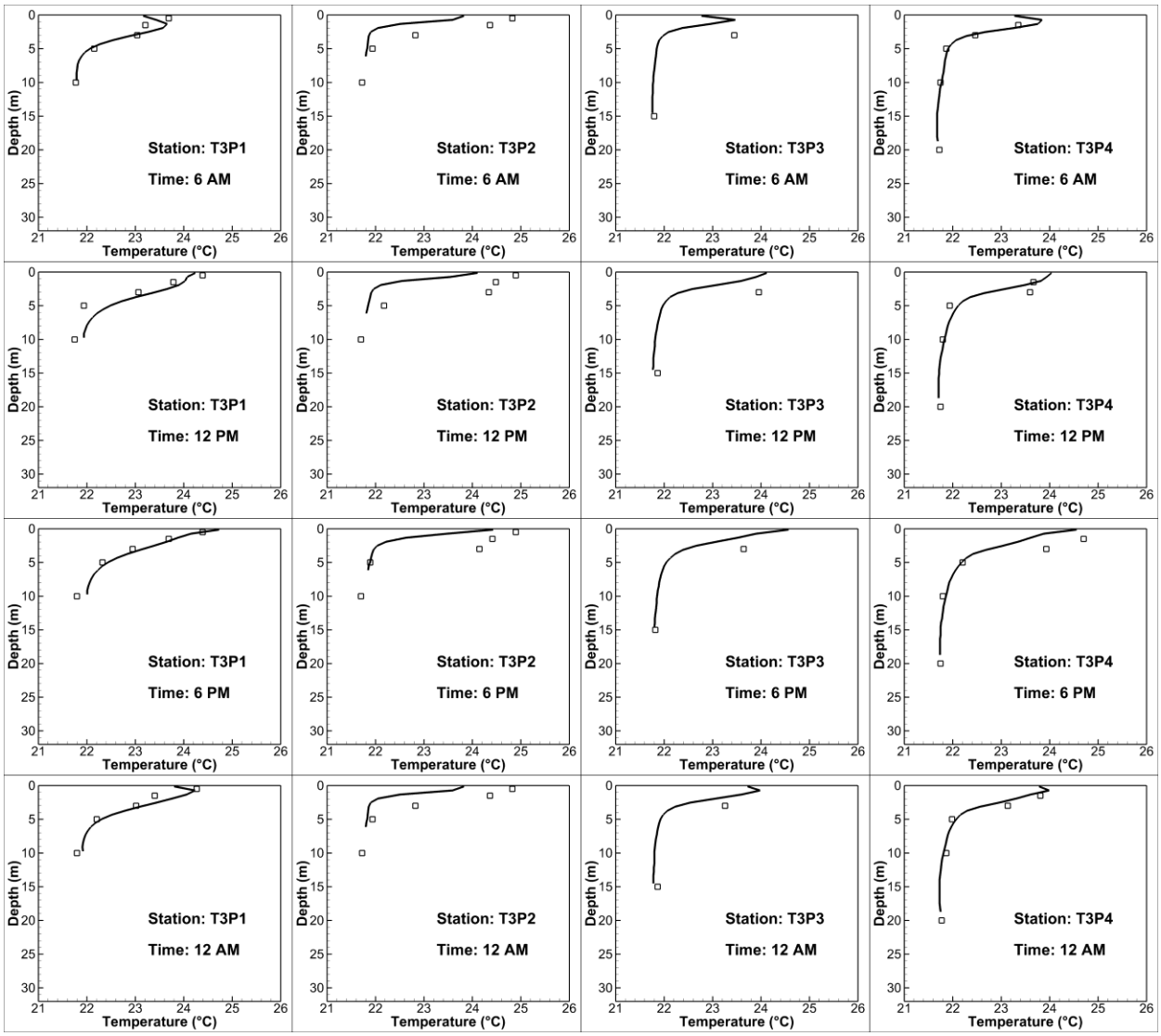

Figure 2.19 Predicted and measured temperature profiles at 6 AM, 12 PM, 6 PM, and 12 AM at stations T3P1, T3P2, T3P3, and T3P4

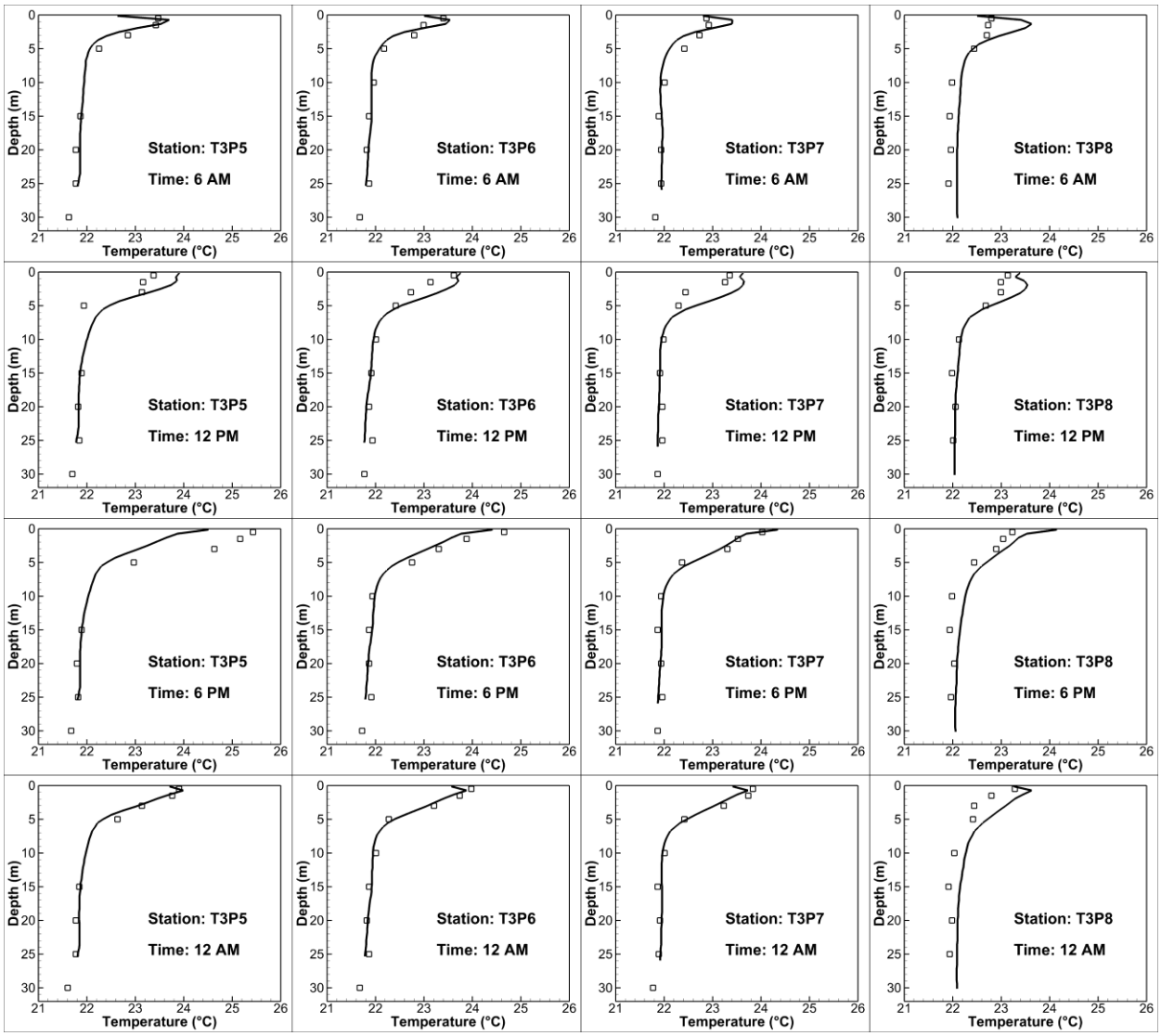

Figure 2.20 Predicted and measured temperature profiles at 6 AM, 12 PM, 6 PM, and 12 AM at stations T3P5, T3P6, T3P7, and T3P8

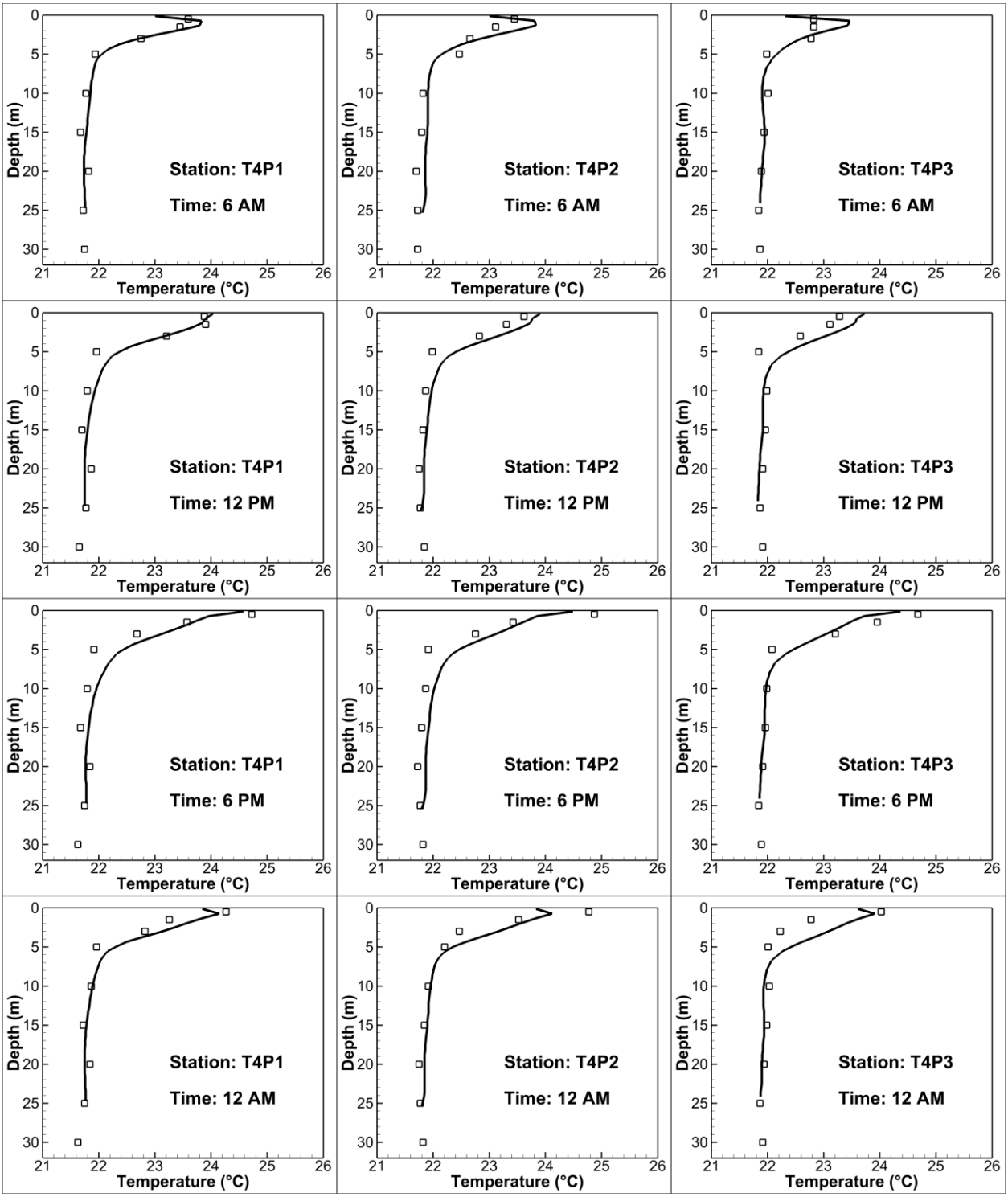

Figure 2.21 Predicted and measured temperature profiles at 6 AM, 12 PM, 6 PM, and 12 AM at stations T4P1, T4P2, and T4P3

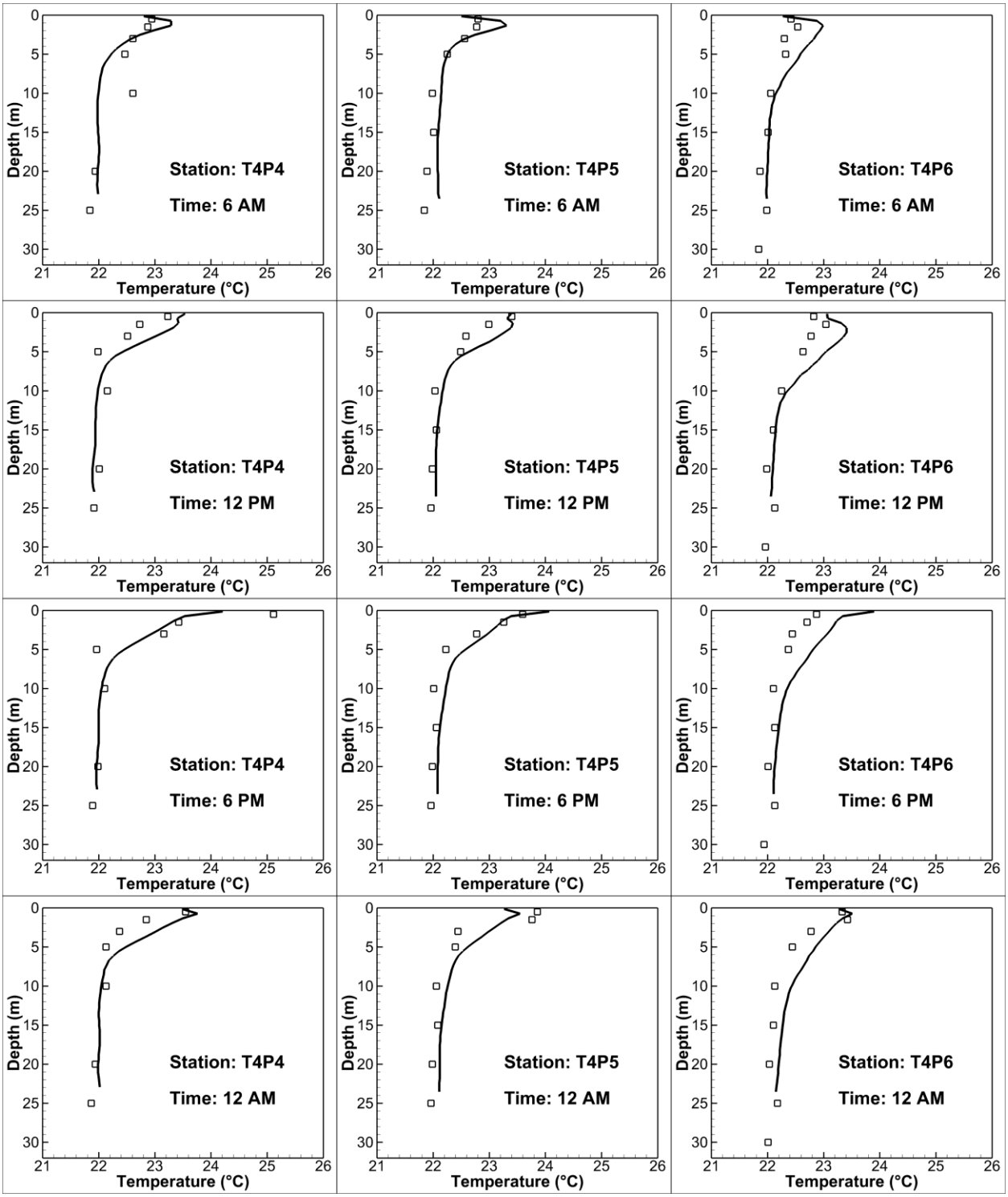

Figure 2.22 Predicted and measured temperature profiles at 6 AM, 12 PM, 6 PM, and 12 AM at stations T4P4, T4P5, and T4P6

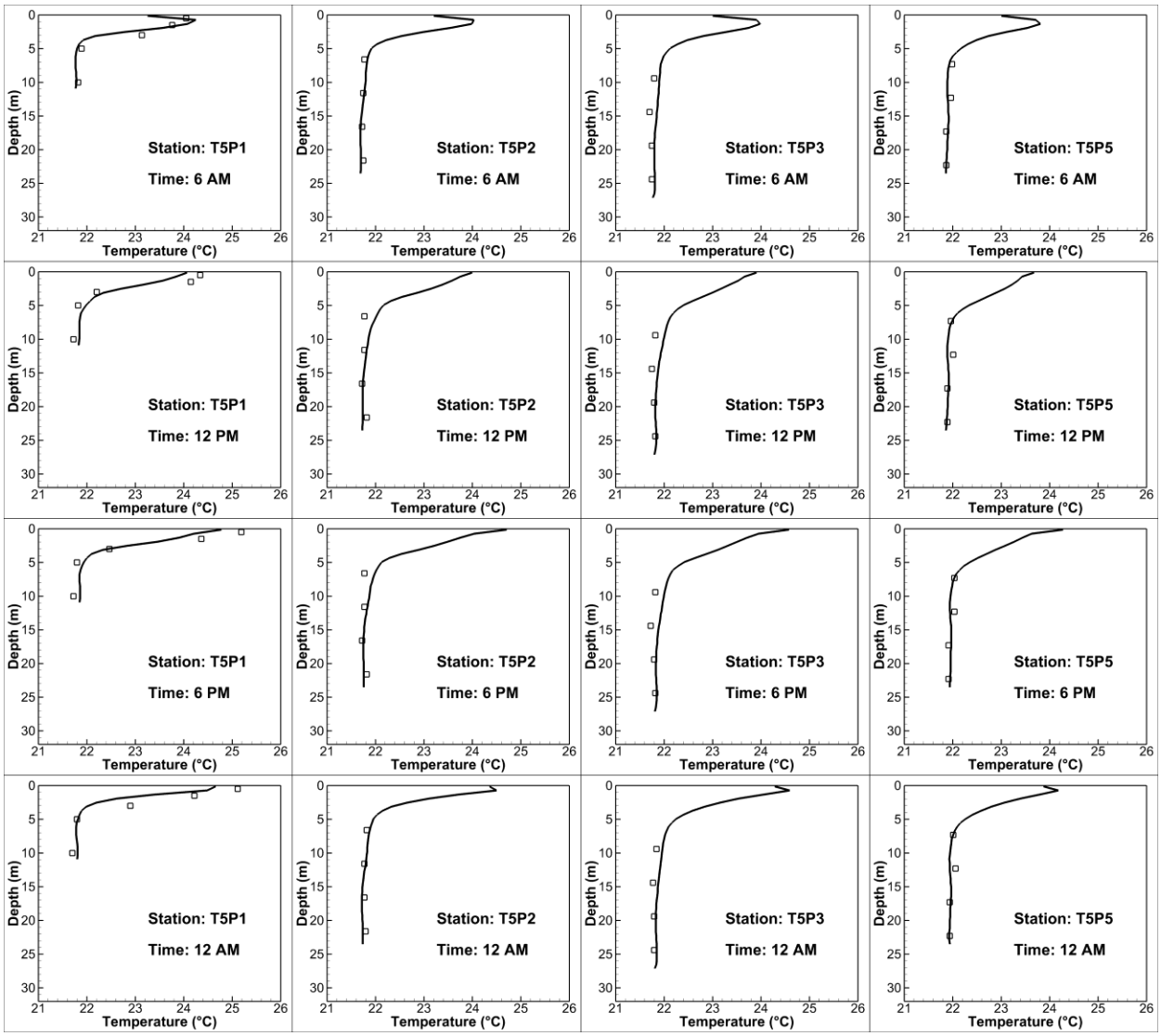

Figure 2.23 Predicted and measured temperature profiles at 6 AM, 12 PM, 6 PM, and 12 AM at stations T5P1, T5P2, T5P3, and T5P5

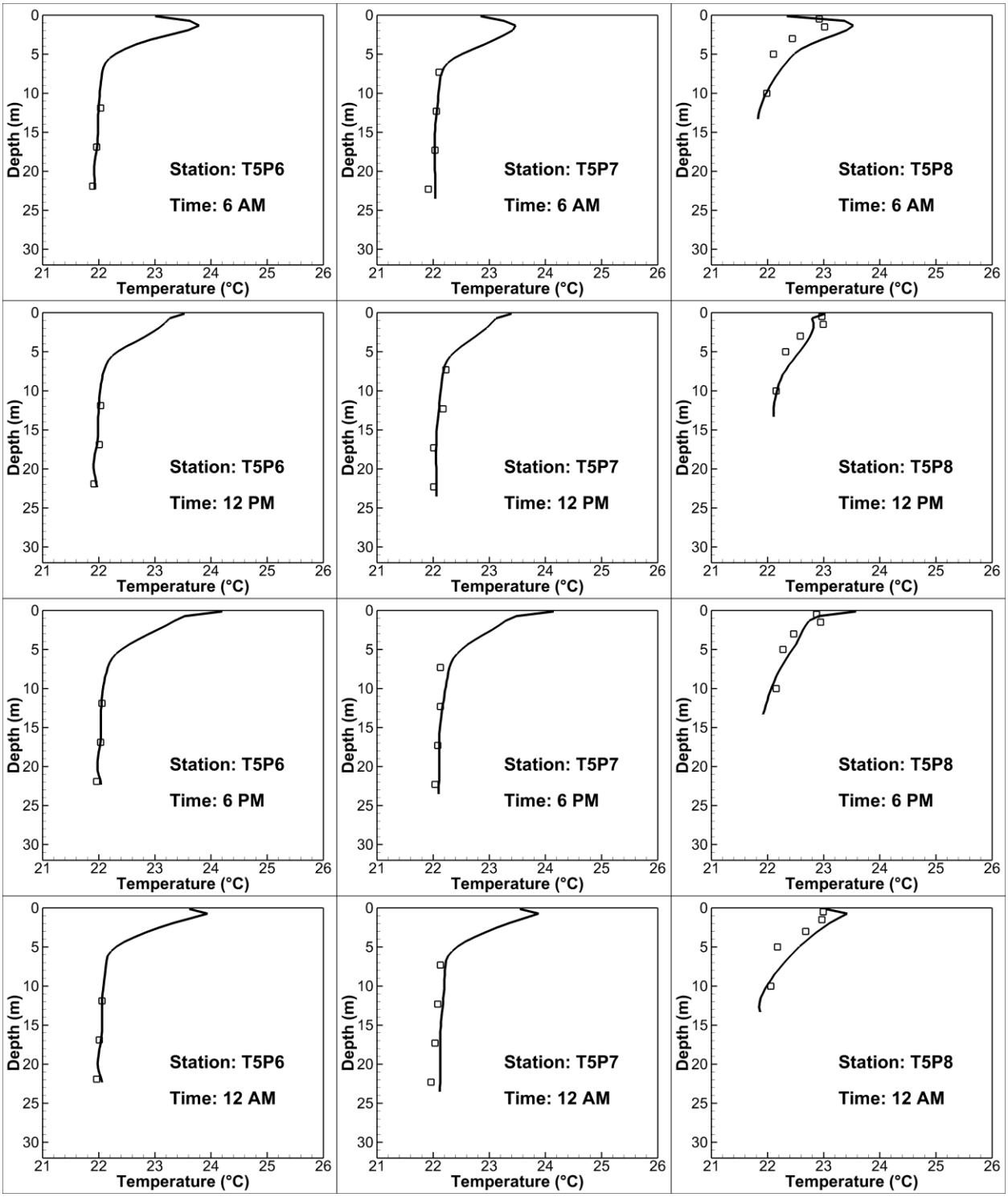

Figure 2.24 Predicted and measured temperature profiles at 6 AM, 12 PM, 6 PM, and 12 AM at stations T5P6, T5P7, and T5P8

CHAPTER III

MCNARY DAM SPILLWAY MODEL

The level of total dissolved gas (TDG) indicates the amount of gases dissolved into the water. In a natural riverine environment, the saturation of dissolved gases in water is usually referred to "normal equilibrium" at standard atmospheric pressure. Gas supersaturation can occur both as a natural phenomenon, such as at falls, and due to hydraulic structures. The primary source of TDG supersaturation in the Columbia and Snake River Basin is the spill from hydroelectric dams. During spillway or sluiceway releases, highly aerated flows are generated. Bubbles are entrained along the spillway face and at the location where spillway flow plunges into the tailrace. These bubbles collectively have a large total surface area, facilitating mass transfer between air and liquid. The dissolution rate increases with bubble depth. If entrained bubbles are carried by plunging flows deep into the stilling basin, supersaturation with respect to the equilibrium at atmospheric pressure occurs.

Elevated TDG concentrations negatively impact fish and many other invertebrates. Substantial mortality associated with high TDG levels have been reported (Elston 1997; Tan 2006). To meet water quality standards for TDG, USACE has conducted laboratory and field investigations to support TDG management and fish passage designs for their dams in the Columbia River Basin. Numerical TDG models can be very useful in devising means to prevent flow conditions leading to TDG supersaturation.

3.1 Goals and Objectives

The main goals of this chapter are:

1) Develop an unsteady, three-dimensional, multi-phase numerical model capable of:
    a. Predicting the spillway jet regimes under different spillway flowrates and tailrace elevations.
    b. Predicting the TDG distribution and degassing processes in the tailrace region of a dam.

2) Determine the required mesh resolution for the presented numerical model.
3) Compare predicted flow patterns against observed flow regimes in a reduced-scale laboratory model.
4) Evaluate spillway flow regimes predicted at prototype and reduced-scale laboratory models.
5) Compare predicted TDG distributions against field measurements in the McNary Dam tailrace.

3.2 Outline of this Chapter

The outline of this chapter is as follows. Section 3.3 presents a literature review of free-surface flow modeling, TDG modeling, and TDG impacts on fish. Section 3.4 presents and describes in detail mathematical and computational methodologies used in the numerical model of the McNary Dam spillway. Boundary conditions are also thoroughly explained. Section 3.5 presents simulation results for the reduced-scale spillway model. The capability of the current model to predict spillway regimes downstream of a dam is validated and discussed. Numerical results for TDG distribution in the prototype McNary Dam tailrace spillway model are presented in Section 3.6. Model parameter influences are evaluated and discussed. Section 3.7 summarizes the modeling effort presented in this chapter.

3.3 Previous and Related Studies

3.3.1 TDG

Spillway operations significantly impact the amount of dissolved gases in the tailrace of a hydraulic dam. Dominant mechanisms contributing to dissolved gas production/reduction downstream of a spillway can be divided into two main processes. Near the spillway, air bubbles are entrained along the spillway face and carried into the stilling basin by plunging spillway jets. Air-to-water mass transfer is increased by the elevated total air-water surface area as well as the high pressures deep in the stilling basin (Geldert et al. 1998). In the downstream river channel,

dissolved gas concentrations diminish through degasification at the free surface and mixing with adjacent waters.

Supersaturation of TDG downstream of a spillway was first documented as an environmental concern in Ebel and Raymond (1976). It has been established that fish exposed to high TDG levels while migrating through a hydropower dam might suffer gas-bubble disease (Ebel 1969; Beiningen and Ebel 1970; Meekin and Allen 1974; Arntzen et al. 2009). In response, regulations and laws have been enacted and enforced to control TDG generation downstream of hydropower plants. The US Environmental Protection Agency (EPA) established the water quality standard for TDG saturation at 110% in 1972 (EPA 1987). However, the extreme structural and operational measures necessary to reduce TDG supersaturation often come into conflict with efforts to protect fish and restore natural river conditions. In the Columbia River System, spills required for fish passage frequently result in exceedance of the TDG standard at many dams. Based on a further review of the most recent studies by the National Oceanic and Atmospheric Administration (NOAA) in 1995 and 2000 Biological Opinions (NOAA 1995; 2000), the TDG allowance level was increased to 115% in forebays and 120% in tailraces for Columbia and Snake River dams to allow spill of substantial volumes of water to bypass downstream migrant juvenile salmon during the spring and summer (Weitkamp 2008). To meet these standards, considerable efforts have been applied to monitoring and management of TDG concentrations over the US (e.g. Hampton 2002; Beeman et al. 2003).

3.3.2 Spillway Jet Regimes and Water Entrainment

One alternative to minimize TDG supersaturation in the tailrace is to install flow deflectors on the spillway face. The concept of the deflector is to redirect spilling jet horizontally, preventing spillway flow from plunging deep into the stilling basin, thus reducing gas dissolution (Nielsen et al. 2000). Ideally, this structural modification changes the regular plunging flow into a skimming flow, where surface jets containing most of the spilling momentum remain tangential to the free surface, transporting bubbles in a thin superficial flow

layer. Distinct flow conditions may, however, occur downstream of a spillway deflector. These regimes depend on geometry, spill flowrate, and tailwater elevation (Dierking 2001). Deflector performance is usually tested in reduced scale hydraulic model studies before installation in the field (Nielsen et al. 2000).

Spillway flow deflectors greatly influence circulation patterns in the stilling basin and tailrace. Strong vertical circulation cells are observed beneath deflected spilling jets. In addition, strong lateral flows are created and powerhouse flows can be entrained by the spill flows changing the flow patterns in the tailrace (USACE 2001). This phenomenon is called water entrainment and has been reported in both field (e.g. Schneider and Wihelms 1996) and model studies (e.g. Fuller 1997). The main mechanism causing water entrainment was studied by Turan et al. (2007). The authors recognized that consideration of anisotropic turbulence and bubble effects is required for proper modeling of the water entrainment.

3.3.3 Turbulent Free-Surface CFD Models

In recent years, considerable attention has been given to numerical simulations of two-phase free surface flows to investigate unsteady fluvial processes. A comprehensive review of mathematical and numerical models for two-phase free surface flow is found in Caboussat (2005). Among various models and numerical methods developed to simulate free surface flow, the Volume of Fluid (VOF) method and Level Set Method (LSM) are very popular and have been successfully applied to capture the free surface location in many studies. The VOF method has proven to be very useful for fluvial regimes that do not have a sharply defined interface (Brocchini and Peregrine 2001) and is used to resolve the free-surface in this study.

Calculation of free surface shape in a tailrace is a key element in the accurate approximation of jet regime and water entrainment phenomenon. The VOF method has been demonstrated as very useful for the study of free-surface flow in short river channels (Ma et al. 2002). VOF applications for large water bodies are limited by heavy computational resource requirements (Politano et al. 2009; 2012; Fu et al. 2010).

Turbulence is an important characteristic of fluids and has been actively studied in CFD related areas for several decades. Most widely used free-surface flow numerical models are based on the Reynolds-Average Navier-Stokes (RANS) equations coupled with isotropic turbulence closure models. Water entrainment caused by spillway deflectors is significantly under-predicted by isotropic RANS models (Haug et al. 2003). Further research by Turan et al. (2007) on mechanisms causing entrainment in spillway flows revealed that an anisotropic turbulence model is required to adequately capture the entrainment phenomenon and predict the flow pattern in the tailrace. The authors found that turbulence levels near the free surface were over-predicted by isotropic turbulence models. The resulting spilling surface jet was too weak to induce observed water entrainment levels in the field. The authors proposed to use a Reynolds stress model (RSM) taking into account the attenuation of the normal fluctuations at the free surface to provide anisotropic closure for the RANS equations. Their model successfully reproduced the entrainment levels measured downstream of a reduced scale laboratory model for Brownlee dam. Since implementation of the attenuation of normal velocity fluctuations at the free surface requires major changes to the structure of existing VOF method in the OpenFOAM, in the present study, a more advanced anisotropic turbulence model is adopted to improve prediction of the flow field that directly controls TDG distribution in the area of interest.

The prohibitive expense of Direct Numerical Simulation (DNS) for high Reynolds number flows prompts the enlistment of the Large Eddy Simulation (LES)/Detached Eddy Simulation (DES) technique as a practical option. In LES, large eddies are considered problem-dependent, and determined by model geometries and boundary conditions. They are resolved directly. Small eddies are assumed to be less geometrically-dependent and modeled as isotropic and universal. In the current study, the transport of momentum, mass, energy, and other passive scalars, such as bubbles and TDG, are mainly carried out by large eddies in the dam tailrace, and therefore can be adequately represented by a LES model.

The primary difficulty in the application of standard LES models to wall-bounded flows is that the cost scaling of the near-wall region is identical to DNS. As an alternative, combined

RANS and LES methodologies were developed which employing RANS model in the boundary layer while treat the rest of the flow in a LES-like manner. One example of this hybrid technique is the DES approach first proposed in Spalart et al. (1997). Their DES model was originally derived from the Spalart-Allmaras (SA) one-equation eddy-viscosity RANS model. The model reduces to RANS formulation near solid surfaces, and to a subgrid model away from the wall. This SA-DES model became widely applied due to its simplicity and reasonable accuracy. Utilization of this DES turbulence model can adequately resolve anisotropic eddies near the free surface without the implementation of the vertical velocity fluctuation attenuation at the free surface. Compared to the RANS-RSM approach employed by Turan et al. (2007), utilization of the SA-DES approach requires more computational resources. However, since the rate-controlling processes of the flow pattern and TDG production/reduction in the tailrace occur in the resolved large scales, it is expected that DES will reduce errors introduced by turbulence modeling and produce more accurate and reliable predictions in the present study (Lu et al. 2008).

Increasing computing power in recent years has led many engineers and researchers to employ the VOF method coupled with LES/DES turbulent closure in the study of free-surface related problems. Christensen (2006) performed a LES-VOF based simulation of waves approaching the shore and breaking over a beach with uniform slope. The set-up, undertow, and turbulence levels were analyzed and compared to experimental data. Satisfactory results for wave height decay and undertow were obtained on a rather coarse mesh. Lu et al. (2008) proposed a hybrid numerical model combining finite element method, LES, and VOF method to predict free-surface flow over a semi-circular obstruction. Numerical and experimental results matched well in these simulations. Wan et al. (2009) developed a hybrid finite element/volume (FE/FV) solver combining the merits of both methods. The authors incorporated the SA-DES turbulence model and VOF method to solve flows involving two immiscible fluids. The model was validated by comparing simulation results against benchmark data. Whitworth (2011) used the VOF method to analyze cavitating flow over a Delft Twist 11 foil using DES as the

turbulence model. By comparing with results predicted using RANS turbulence models, the author found that the DES turbulence model predicts better cavitation patterns in highly dynamic flows. Li et al. (2011) investigated hydraulic characteristics along the side wall for a proposed arrangement-scheme of a sudden lateral enlargement and vertical drop using DES and VOF method. The authors selected the two equations, realizable $k-\varepsilon$ model and Smagorinsky subgrid model as their DES approach. The numerical results agreed well with data obtained from an experimental study. Cataño-Lopera et al. (2012) examined flow characteristics around a partially buried short cylinder in a simulated river bed using VOF as the multi-phase model and LES as the turbulence closure model. The author found that the use of LES model allows studying of the highly unsteady coherent turbulent structures generated both by the object and the surrounding bedforms.

The LES/DES-VOF approach was also applied to study hydrodynamics in open channel flows. Keylock et al. (2005) examined the potential for using LES as a fluvial modeling tool and provided some examples of early work that used LES in a fluvial context. Recent work by Sanjou and Nezu (2010) and Huai et al. (2011) studied flow structures in a natural fluvial channel with non-submerged vegetation over mainstream and compound channel. The authors demonstrate the VOF method combined with LES approach as an effective tool in the study of open channel flows around hydraulic structures.

3.3.4 TDG Models

The TDG concentration at a given location depends on extremely complex processes involving dissolved gas transport and mass transfer across boundaries (bubble-liquid and air-liquid). In addition, the intrinsic unsteady flow field in the tailrace combined with a dynamic bubble phase leads to a strong unsteady three-dimensional TDG field, further complicating the process.

Early attempts to predict TDG downstream of dams were based on laboratory/field experiments and data fitting. Although this approach proved reasonably effective, it is relatively

expensive and time-consuming. Spillway deflectors have been designed based on laboratory experiments and tested in the field to alter flow patterns and lower TDG production in the tailraces. One primary shortcoming of these studies is that the laboratory models cannot quantitatively reproduce turbulence and many water-quality parameters, such as temperature and TDG, due to model scaling issues. No quantifiable prediction of TDG concentration can be made by laboratory experiment. A "performance curve" relating flow conditions to past experiences was commonly employed. This approach poses potential environmental and financial risks when applied to the design of TDG control structures.

On the other hand, physically based models describing gas transfer processes have been developed to quantitatively predict TDG levels downstream of a spillway. An early analytical predictive model for dissolved gas concentration was proposed by Roesner and Norton (1971). An important improvement to this model was made by Geldert et al. (1998), taking mass transfer across the free surface and at the bubble-liquid interface into account. Depth-averaged TDG levels downstream of a spillway can be determined by their model. Most of these early works rely on empirical correlations for TDG transport and are therefore limited their utilization to where specific hydrodynamic and TDG data are available. In addition, due to the multi-dimensional nature of the tailrace region, flow characteristics governing bubble behavior and mass transfer cannot be adequately represented by the above discussed models thus compromising the predictability of these models.

Limited research is found in multi-dimensional modeling of dissolved gas in the literature. Orlins and Gulliver (2000) developed a two-dimensional, laterally averaged numerical model to predict TDG generation and transport. Their model used an incompressible mass transport equation to simulate TDG accounting for convection, turbulent diffusion, and mass transfer across the interfaces. This model advanced the state of numerical modeling of TDG downstream of a spillway. However, hydrodynamic data including flow velocity, turbulent variables, and bubble distribution were required as inputs. The authors used data from a physical model and TDG field measurements, which limited the predictive capability of this model.

Weber et al. (2004) improved the model by predicting the hydrodynamics and extending the model to three-dimensions. The authors used a rigid-lid approach which did not predict spillway jet regimes. A skimming surface jet flow condition was assumed in the study and an effective penetration depth of entrained air-bubbles was estimated based on previous hydraulic model studies. Two coefficients, named the TDG production parameter and the surface exchange parameter, were calibrated and fitted to field measurements. Their model was applied to estimate TDG distribution downstream of Wanapum Dam and Hells Canyon Dam with reasonable success. Urban et al. (2008) specified three distinct flow regions downstream of a spillway. Different governing equations were applied to these regions simulating the main physical processes that affect TDG concentrations. The flow field was calculated following a relationship developed in an experimental study by Ead and Rajaratnam (2002). Good agreement between model predictions and field measurements was obtained for the Ice Harbor Dam tailrace. Note that in the models mentioned above, as the dominant source of TDG generation/reduction, bubble distributions in the tailrace were not fully simulated but calculated using parameters based on empirical correlations. This factor becomes more important with the non-uniform flow field induced by the installation of spillway deflectors.

To predict tailrace hydrodynamics and TDG distribution, Politano et al. (2007) developed an anisotropic two-phase flow model capable of predicting water entrainment caused by spillway deflectors. The author used a mixture model to predict bubble and TDG distribution. A bubble number density transport equation was introduced to account for bubble size variation due to mass transfer and compression. The free-surface shape and spillway regime were simulated using the VOF method. A rigid-lid approach was used for TDG calculations. Attenuation of normal velocity fluctuation at the free-surface was taken into account to capture tailrace water entrainment. This model has been successfully applied and quantitative agreement between the numerical results and field data for TDG concentrations were obtained at several dams (Turan et al. 2007; Politano et al. 2009a; 2009b; 2011; Arenas Amado et al. 2011).

Limitations of this mathematical model were discussed thoroughly in Politano et al. (2009c). Their model focused on the mass transfer and transport processes in the tailrace assuming a known entrainment gas volume fraction and bubble size distribution. In applying this model, the free-surface shape was fixed during bubble and TDG computation due to the difficulties in implementation of normal fluctuation attenuation at the free surface with the VOF method, and more importantly, to reduce required computational resources. This approach has been proven adequate for predicting TDG distribution in engineering applications. However, use of a fixed surface imposes limits in prediction of unsteady nature of the flow and TDG dynamics in a tailrace. First, free-surface shape downstream of a spillway is highly complex and unsteady due to spillway jets. Strong disorder patterns or even roll-over waves may occur near a dam. A degree of approximation and/or simplification needs to be applied to ensure mesh quality when fixing the free-surface in a rigid-lid approach. The effectiveness of determining free-surface shape is highly dependent on previous experience and can be time consuming. Since unique meshes need to be created for each specific simulation condition, the relative mesh quality from case to case may increase uncertainty in final solutions. Second, the tailrace flow field is highly dynamic and unsteady. Transient water surface oscillations downstream of hydraulic structures were observed in both field and numerical studies (Cook and Richmond 2001). The selection of a proper “steady state” for TDG calculation is not trivial and may hinder further studies on TDG transport under unsteady flow conditions. Despite the disadvantages, the model provides a good base for further improvement in dissolved gas production and transport modeling, which is the main focus of the present study.

In the current work, the author attempted to extend past successes of Politano et al. (2009c), in developing an unsteady TDG model based on the VOF method using the open-source code OpenFOAM. The model aims to more accurately simulate flow patterns and TDG distributions in the vicinity of a spillway. The multi-phase TDG model was developed using a one-way coupling approach, assuming the influence of the bubble field on the liquid field is negligible, to calculate the dynamic evolution of TDG distribution downstream of a dam.

3.4 Mathematical and Numerical Models

In this section, numerical models and governing equations used in this chapter are described in detail.

3.4.1 Mathematical Model

In the conventional VOF method, conservation equations for mass and momentum are solved simultaneously with a transport equation for an indicator function that represents the volume fraction occupied by one fluid.

$$\nabla \cdot \boldsymbol{U} = 0 \tag{3.1}$$

$$\frac{\partial(\rho \boldsymbol{U})}{\partial t} + \nabla \cdot (\rho \boldsymbol{U}\boldsymbol{U}) = -\nabla p + \nabla \cdot (\mu \nabla \boldsymbol{U}) + \rho \boldsymbol{f}_b \tag{3.2}$$

$$\frac{\partial \gamma}{\partial t} + \nabla \cdot (\boldsymbol{U}\gamma) = 0 \tag{3.3}$$

where $\boldsymbol{U}$ represents the velocity vector field, ρ and μ are the effective local density and viscosity, respectively, p is the pressure, $\boldsymbol{f}_b$ are body forces per unit mass including gravity and surface tension effects at the interface, and γ is the volume fraction of one phase.

The physical properties of fluid at any point in the computational domain are calculated as weighted averages based on distribution of the volume fraction as:

$$\rho = \rho_l \gamma + \rho_g (1-\gamma) \tag{3.4}$$

$$\mu = \mu_l \gamma + \mu_g (1-\gamma) \tag{3.5}$$

where subscripts l and g denote liquid and gas phases.

Governing equations for LES/DES are obtained by applying a filtering procedure to the mass and momentum conservation equations represented by equations (3.1) and (3.2) (Smagorinsky 1963):

$$\nabla \cdot \overline{\boldsymbol{U}} = 0 \tag{3.6}$$

$$\frac{\partial(\rho \overline{\boldsymbol{U}})}{\partial t} + \nabla \cdot (\rho \overline{\boldsymbol{U}}\overline{\boldsymbol{U}}) = -\nabla \overline{p} + \nabla \cdot \boldsymbol{\tau} + \nabla \cdot (\mu \nabla \overline{\boldsymbol{U}}) + \rho \boldsymbol{f}_b \tag{3.7}$$

where $\boldsymbol{\tau}$ is the subgrid-scale stress defined by

$$\boldsymbol{\tau} = \overline{\boldsymbol{U}}\overline{\boldsymbol{U}} - \overline{\boldsymbol{U}\boldsymbol{U}} \tag{3.8}$$

This extra term arises from the non-linear advection term. It cannot be resolved in the flow and thus requires to be modeled. Substituting the subgrid-scale turbulent viscosity μ_t into Equation (3.7), we obtain:

$$\frac{\partial\left(\rho\overline{\boldsymbol{U}}\right)}{\partial t} + \nabla\cdot\left(\rho\overline{\boldsymbol{U}}\overline{\boldsymbol{U}}\right) = -\nabla\overline{p} + \nabla\cdot\left(\left(\mu+\mu_t\right)\nabla\overline{\boldsymbol{U}}\right) + \rho\boldsymbol{f}_b \tag{3.9}$$

In the above procedure, fluid variables are separated into resolved and subgrid parts as $\boldsymbol{U} = \overline{\boldsymbol{U}} + \boldsymbol{U}'$. The resolvable scale part $\overline{\boldsymbol{U}}$ represents the large eddies, while the subgrid scale part $\boldsymbol{U}'$ is included through the subgrid-scale model. The line over the top of a letter indicates the resolvable scale part and will be omitted in the following text for clarity.

The SA-DES model utilized in this study is a simple derivative of the SA one-equation eddy-viscosity RANS model. The transported variable in the SA model, υ, is identical to the turbulent kinematic viscosity, except in the near-wall region. The transport equation for υ is given by (Spalart et al. 1997):

$$\frac{\partial\left(\rho\upsilon\right)}{\partial t} + \nabla\cdot\left(\rho\upsilon\boldsymbol{U}\right) = G_\upsilon + \frac{1}{\sigma_\upsilon}\left[\nabla\cdot\left(\left(\mu+\rho\upsilon\right)\nabla\upsilon\right) + C_{b2}\rho\left(\nabla^2\upsilon\right)\right] - Y_\upsilon \tag{3.10}$$

The turbulent viscosity μ_t in equation (3.9) is defined as:

$$\mu_t = \rho\upsilon f_{\upsilon 1} \tag{3.11}$$

where $f_{\upsilon 1}$ is the viscous damping function and given by $f_{\upsilon 1} = \dfrac{\chi^3}{\chi^3 + C_{\upsilon 1}{}^3}$ with $\chi = \dfrac{\upsilon}{\upsilon}$, and υ the molecular kinematic viscosity.

G_υ represents production of turbulent viscosity and is modeled as:

$$G_\upsilon = C_{b1}\rho S\upsilon \tag{3.12}$$

where $S \equiv S + \dfrac{\upsilon}{\kappa^2 d^2} f_{\upsilon 2}$, and $f_{\upsilon 2} = 1 - \dfrac{\chi}{1+\chi f_{\upsilon 1}}$. S is defined as $S \equiv \sqrt{2\Omega_{ij}\Omega_{ij}}$ with Ω_{ij} the mean rate of rotation tensor.

Y_υ is the destruction of turbulent viscosity in the near-wall region. This term expresses the confinement of eddies by the wall (inviscid) and viscous damping. It is modeled by:

$$Y_\upsilon = C_{\omega 1}\rho f_\omega \left(\frac{\upsilon}{d}\right)^2 \tag{3.13}$$

where the function f_ω is used to obtain a faster decaying behavior of destruction in the outer region of the boundary layer and is defined as $f_\omega = g\left(\frac{1+C_{\omega 3}^6}{g^6+C_{\omega 3}^6}\right)^{1/6}$ with $g = r + C_{\omega 2}\left(r^6 - r\right)$, and $r \equiv \frac{\upsilon}{S\kappa^2 d^2}$.

Constants of the model are:

$$C_{b1} = 0.1355,\ C_{b2} = 0.622,\ \sigma_\upsilon = \frac{2}{3},\ \kappa = 0.41,\ C_{\omega 1} = \frac{C_{b1}}{\kappa^2} + \frac{1+C_{b2}}{\sigma_\upsilon},\ C_{\omega 2} = 0.3,\ C_{\omega 3} = 2,\ C_{\upsilon 1} = 7.1.$$

The difference between the above SA-DES model and the standard SA model is the replacement of the distance to the nearest wall d, by $\tilde{d}$, where $\tilde{d} \equiv min\left(d, C_{DES}\Delta\right)$ with Δ the largest grid space in the x, y, and z directions, and $C_{DES} = 0.65$. For the numerical grid used in this study, wall-parallel grid spacing in most regions exceeds the boundary layer thickness. Therefore $\tilde{d} = d$ and the SA-RANS model is retained throughout the boundary layer. Away from solid boundaries where large unsteady turbulence scales play a dominant role, the one-equation model for subgrid-scale eddy viscosity works as a LES model.

The presence of bubbles changes the effective local density and viscosity of the fluid. In addition, the relative velocity between bubbles and liquid phases produces an extra force on the fluid changing the flow field. Interactions between bubbles and fluid may impact spillway jet behavior as demonstrated in two-phase, mixture model simulations by Turan et al. (2007). Cook and Richmond (2001) conducted a numerical study to investigate hydrodynamic flow fields downstream of hydraulic structures. The authors used the VOF method provided in the commercial code FLOW-3D to track the dynamic free-surface in the tailrace. Air entrainment and influences of bubbles were not included in their study. The general flow patterns and

predicted velocity vectors were compared with observations in laboratory and field. The authors found that predicted flow fields in hydraulic jump and skimming flow conditions matched observations within a reasonable error tolerance without consideration of bubbles. However, large differences between observed and predicted velocities occurred downstream of the flow jet off a cantilever outfall. The differences may result from a lack of air entrainment by the falling jet. To the author's knowledge, measurements of gas volume fractions in a tailrace are not available and therefore there is a lack of experimental data to correlate effects of bubbles on the flow field in a tailrace environment. In this study, the hydrodynamics were solved assuming that impact of the bubbles on the flow field is negligible.

A critical issue in VOF simulations is numerical diffusion at the free surface, where the phase indicator γ changes abruptly from $\gamma = 1$ in the liquid phase to $\gamma = 0$ in the air phase. In the present study, a modified approach proposed in Rusche (2002) is used. The free-surface is "compressed" by introducing an extra artificial compression term in equation (3.3) as following:

$$\frac{\partial \gamma}{\partial t} + \nabla \cdot (\boldsymbol{U}\gamma) + \nabla \cdot \left(\gamma(1-\gamma)\boldsymbol{U}_{\boldsymbol{r}}\right) = 0 \tag{3.14}$$

where $\boldsymbol{U}_{\boldsymbol{r}} = \boldsymbol{U}_{\boldsymbol{l}} - \boldsymbol{U}_{\boldsymbol{g}}$ is the vector of relative velocity. The detailed derivation of this equation can be found in Berberović et al. (2009).

The continuity and momentum equations for the bubble phase are (Politano et al. 2009c):

$$\frac{\partial \alpha}{\partial t} + \nabla \cdot (\boldsymbol{U}_{\boldsymbol{b}}\alpha) = -S \tag{3.15}$$

$$0 = -\alpha \nabla p + \alpha \rho_b \boldsymbol{g} + \boldsymbol{M}_{\boldsymbol{b}} \tag{3.16}$$

where α is the gas volume fraction for the bubble phase. $\boldsymbol{U}_{\boldsymbol{b}}$ is bubble velocity and ρ_b is bubble density calculated following the ideal gas law:

$$\rho_b = \frac{Mp}{RT} \tag{3.17}$$

with M the average molar mass of air, R the ideal, or universal gas constant, and T the temperature of the bubble. S represents the bubble-liquid mass transfer, and $\boldsymbol{M}_{\boldsymbol{b}}$ is the interfacial

momentum transfer between phases. Lift force, turbulent dispersion force, and virtual mass are considered negligible compared with drag force in the current study. Therefore, the interfacial momentum is obtained following Politano et al. (2009c) as:

$$\boldsymbol{M_b} = -\frac{3}{8}\rho\alpha\frac{C^D}{R}\boldsymbol{U_{br}}\left|\boldsymbol{U_{br}}\right| \tag{3.18}$$

with $\boldsymbol{U_{br}}$ the relative velocity of the bubble with respect to the liquid phase. Several options for the drag coefficient have been suggested in the literature (Ishii and Zuber 1979; Tomiyama 1998). In this study, the following equation is used:

$$C^D = \begin{cases} \dfrac{24\left(1+0.15Re_b^{0.687}\right)}{Re_b} & if\ D_b \geq 2e^{-4} \\ \dfrac{24}{Re_b} & D_b < 2e^{-4} \end{cases}, \tag{3.19}$$

where D_b represents the bubble diameter, and $Re_b = \dfrac{\rho_l D_b \left|\boldsymbol{U_{br}}\right|}{\mu_l}$ is the bubble Reynolds number.

The transport equation for bubble number density N is (Politano et al. 2009c):

$$\frac{\partial N}{\partial t} + \nabla\cdot\left(\boldsymbol{U_b}N\right) = 0 \tag{3.20}$$

The bubble radius is calculated from:

$$R = \left(\frac{3\alpha}{4\pi N}\right)^{\frac{1}{3}} \tag{3.21}$$

TDG concentration C can be calculated following Politano et al. (2009c). Notice that the equation for TDG transport is analogous to that of the phase indicator function. The same numerical technique can be employed to solve the TDG transport equation and adopt it into the multi-fluid formulation.

$$\frac{\partial \alpha_l C}{\partial t} + \nabla\cdot\left(\boldsymbol{U}\alpha_l C\right) + \nabla\cdot\left(\gamma\left(1-\gamma\right)\boldsymbol{U_r}\right) = \nabla\cdot\left(\left(\nu + \frac{\nu_t}{Sc}\right)\alpha_l\nabla C\right) + S \tag{3.22}$$

where ν and ν_t are the kinematic molecular and turbulent viscosity, respectively, and Sc is the Schmidt number. The rate of mass transfer between bubble and liquid phases is modeled as (Politano et al. 2009c):

$$S = 4\pi N R^2 k_l \left(\frac{p + \frac{\sigma}{R}}{H} - C \right) \tag{3.23}$$

where k_l is the mass transfer coefficient due to turbulence. The first two terms on the left hand side of equation (3.22) represent convection of TDG at the velocity of the fluid. The last term introduces the "compression" effect, similar to the phase indicator function γ in the VOF method, to avoid diffusion at the interface (Bohorquez 2008).

Bubbles are free to flow across the interface between air and liquid. For TDG concentration, the mass transfer at the interface is a function of the local TDG level and TDG saturated concentration at atmospheric pressure. This TDG flux is usually negligible in the aerated zone compared to TDG variation due to bubble dissolution, and therefore is not considered in the present study.

3.4.2 Boundary Conditions

Appropriate boundary conditions are required for computational modeling of any physical problem. In OpenFOAM, boundary conditions are setup for each flow variable as a Dirichlet, a Neumann, or a mixed condition, to represent the physical properties of a specific boundary type. This flexibility allows users to define any simulation conditions as needed. However, it does require a deeper understanding of the physical conditions being studied. The boundary conditions utilized in this study are summarized in Table 3.1 and discussed in the following text.

Inflow: the spillway sluice gates are modeled as inlet boundaries. At spillway inflows, imposing a uniform velocity profile calculated using the spillway rating curve under-predicts fluid velocity, as reported in Politano and Dvorak (2012). To take into account the contraction

downstream of spillway gates, the gate opening can be obtained assuming no energy loss at the spillway gate. The spillway inflow gate opening h is calculated from:

$$H = h + \frac{|\boldsymbol{U}|^2}{2g} \tag{3.24}$$

$$Q = hW|\boldsymbol{U}_u| \tag{3.25}$$

$$\boldsymbol{U}_u = |\boldsymbol{U}|\cos(\phi) \tag{3.26}$$

where H is the height difference between water surface elevation (WSE) at the forebay and spillway gate, W is the width of the spillway, Q is the flowrate at the gate, $\boldsymbol{U}_u$ the longitudinal velocity, and ϕ the local angle of the spillway. This approach has been widely used to study flows under sluice gates (Kim 2007). Turbulent variables are assumed to be zero at the upstream end.

Outflows: outflow boundary conditions are used to regulate flows exiting the computational domains. Pressure needs to be appropriately assigned at the outflow to control flowrate and surface elevation in the tailrace. For this study, the outflow boundary at the downstream end is split into two domains that allow only one fluid (air or water) to flow through. Pressure at the water-outflow is assumed hydrostatic. Atmospheric pressure is imposed at the air-outflow. Velocity and all other modeled variables are assigned a zero-gradient at both the water and air outflows.

Walls and River Bed: a no-slip condition (zero velocity) and zero flux for all other modeled variables are used at river banks, river beds, and walls. Although this study does not take boundary roughness into consideration, previous research by Meselhe and Odgaard (1998) demonstrated this approach to be satisfactory for deep large scale river reaches with low velocities and wide roughness variations.

Slip Wall and Symmetry: zero shear stress and zero flux conditions for all quantities across the plane are specified for the slip wall and symmetric boundary.

Pressure outlet: a pressure outlet boundary condition with atmospheric pressure is applied at the top of the computational domain to allow free flow of air and avert unrealistic pressure values. The same condition is applied at the air-outflow boundary.

3.4.3 Numerical Method

The TDG mathematical model described in the preceding section was implemented in the OpenFOAM solver. The PIMPLE algorithm was used to couple pressure and velocity. The first order implicit Euler method was applied to the unsteady terms. In a LES/DES simulation, central schemes are generally preferred. In this study, the limited linear differencing scheme was used as the discretization method for the spatial derivative terms to balance accuracy and stability. The specialized scheme proposed by Rusche (2002) was applied for the compression term in equation (3.14) which produces smoother air-liquid interfaces during simulation. Zero velocity and turbulence for the entire domain were imposed as initial conditions. Unsteady solutions were obtained using a variable time step with a fixed Courant number of 0.4.

3.5 Sectional Spillway Model at Reduced-Scale

The capability of the presented VOF-DES model to predict flow regimes downstream of a spillway is discussed in this section. Predicted flow patterns under different tailwater elevations are compared with observations from a reduced-scale laboratory model.

3.5.1 Simulation Conditions

The installation of spillway deflectors is considered to be the most expeditious and efficient method to alleviate TDG supersaturation downstream of spillways. Reduced-scale hydraulic model studies are usually conducted to determine effects of spillway deflectors on flow patterns in the stilling basin and downstream river channel. Although turbulence levels, entrained bubble sizes, and bubble residence times in the flow cannot be accurately reproduced due to the scaling issue, the flow regimes under diverse deflector geometries, TWE, and flowrates are usually determined using reduced-scale models. A performance curve combining deflector

performance and tailwater curves is generated from these hydraulic model studies. Each curve is used as an analysis tool for a deflector design specific to the project site.

A 1:25 scale laboratory model of the McNary Dam spillway was constructed by Northwest Hydraulic Consultants (NHC) in 1999 to investigate the performance of spillway deflectors. The Froude criterion was used for dynamic similitude in this study. Flow variable scaling ratios are summarized in Table 3.2. The model included the spillway, stilling basin, and a portion of the downstream channel. It was constructed in a 1.46m (wide) ×2.44m (high) ×15.5m (long) flume to simulate 36.6m of river width, and 390m of river length. One full central spillway bay and two half bays were reproduced, as shown in Figure 3.1. The flume walls were fabricated from transparent acrylic plastic, which allowed visualization of the flow patterns in the forebay and stilling basin in the half bays.

The performance curve for McNary Dam was obtained from this hydraulic model study (NHC 2001). As illustrated in Figure 3.2, this performance curve shows corresponding flow regimes with respect to different tailwater elevations and flowrates. Four categories were used to classify flow regimes in this study. When the tailwater elevation is high, the deflector is highly submerged and inundated by the spillway jet. Flow rolls back and a hydraulic roller forms on the deflector, and very few bubbles are transported deep into the stilling basin. With decreasing tailwater, the hydraulic jump becomes undular jump. The spillway jet exiting the deflector ramps up on the downstream water surface. Flow recirculation below the jet is developed as a support for surface oriented jet down the spillway. Skimming flow condition occurs when the momentum of the surface jet is deflected tangentially along the free surface. The surface of the tailwater is relatively flat with no plunging action and little downwelling. At low tailwater condition, water jet plunges deep with a weak supporting recirculation, transporting considerable amount of air deep into the stilling basin. Skimming flow is considered to be the most desirable condition in designing and testing deflector performance (NHC 2001; Dierking 2001).

Operational configurations used in the reduced-scale laboratory model to evaluate effects of stilling basin and downstream bathymetric elevations on deflector performance (test 3c-1 in

NHC 2001) were followed in this study. Deflector performance was tested by raising tailrace elevations while maintaining the spill flowrates. Based on available video and graphical data, four tailwater elevation conditions (FR 1, FR 2, FR 3, and FR 4) were selected to evaluate the numerical model in predicting flow regimes. Simulation conditions for these tests are outlined in Table 3.3. Notice that all values are documented in prototype-scale. According to the spillway performance curve (Figure 3.2), corresponding flow regimes for these tailwater conditions are hydraulic jump, undular jump, skimming flow, and plunging flow, respectively.

3.5.2 Computational Grid

The commercial grid generator Gridgen V15 was used to create numerical grids for the spillway model at both the reduced-scale and prototype-scale. Multi-block grids containing only hexahedral elements were used. Methodology for selecting the appropriate numerical meshes for DES simulations is discussed in the following text. Note that numerical meshes in this chapter were constructed intending to resolve flow characteristics and transport of scalars for the current application. The grid selecting procedure descripted in the following text may not be the best approach in other circumstances.

In the VOF-DES model applied in the present study, filter width for the governing equations is directly related to local mesh size, which indicates correlation between grid cell size and hydrodynamics (Pope 2004). A mesh sensitivity test is necessary to verify that the time-averaged flow field results do not strongly depend on the applied mesh. The turbulent integral length scale was used to identify appropriate mesh size for this study.

According to the Kolmogorov's Energy Spectrum, integral length scales are the largest scales in the energy spectrum. Eddies in these scales contain most of the energy and are highly anisotropic. Momentum, energy and other flow variables are mainly transported by these eddies. One way to estimate the turbulent integral length scale is by (Umlauf and Burchard 2003; Van Maele and Merci 2008)

$$l_I = \frac{k^{3/2}}{\varepsilon} \tag{3.27}$$

where l_I represents the integral length scale, k and ε are turbulent kinetic energy and turbulent dissipation rate obtained from a RANS simulation. To examine and determine the turbulent integral length scale and grid size needed for DES simulations, an unsteady RANS simulation was first performed. The standard $k-\varepsilon$ model was used to evaluate turbulent variables required for grid size calculation.

Numerical meshes were created for the reduced-scale spillway model for both RANS and DES simulations. The plastic flume wall was modeled as a slip wall. A symmetric plane was used to separate adjacent spillway bays. Tailwater elevation was controlled at the outflow boundary, about 15 meters downstream from the spillway crest. Details regarding boundary conditions are discussed in Section 3.4.2. A relatively coarse mesh was generated for the RANS simulation. The numerical grid with boundary conditions for the RANS simulation is shown in Figure 3.3. Refinement near the free surface is required to minimize numerical diffusion in VOF simulations. Grid points were clustered and nodes were highly concentrated near the predicted free-surface to best resolve the interface between air and fluid phases.

Although the general flow pattern is relatively consistent, the flow field in the stilling basin is highly unsteady due to the spillway jet. The free surface and flow patterns directly downstream of the deflector are oscillatory and chaotic. Figure 3.4 shows the predicted time-averaged turbulent integral length calculated by equation (3.27) using the time-averaged turbulent kinetic energy and turbulent dissipation rate. The flow time used for averaging is about 10 times the mean flow residence time. Turbulent integral length is low in high turbulence regions, indicating that smaller eddy sizes are required to be resolved in these areas. As illustrated in the figure, the predicted integral length scale between the spillway deflector and baffle piers is about 0.2 m, and about 0.4 m in the downstream channel. This suggests a finer mesh for the upstream part of the spillway model and a relatively coarse mesh in the downstream region. Obviously, near the spillway surface and stilling basin bottom, the integral length scale

becomes smaller as a solid boundary is approached. Since the flow regime downstream of a spillway depends mainly on large scale phenomenon, the mesh in this region need not be as fine as dictated by the level of l_I. This was confirmed using a mesh that was not refined near the wall and will be discussed later in this section.

Typically, over 80% of the turbulent kinetic energy (TKE) should be resolved for an LES calculation (Wang et al. 2012). The relationship between $k(l)/k$ and l/l_I given by Aleksy (2007) is plotted in Figure 3.5, and briefly summarized in Table 3.4. The vertical axis in Figure 3.5 represents the resolved versus total cumulative TKE. The horizontal axis is the ratio between grid spacing l and the length scale of eddies, or turbulent integral scale. In compliance with the 80% rule, the ratio of l/l_I should be less then approximately 42% to guarantee reliable LES results. Grid spacing l for DES simulations can be calculated based on the RANS simulation results shown in Figure 3.4. To examine the dependence of flow variables on the applied mesh, a baseline case study with average grid spacing to integral length scale ratio of 0.083 was performed. Base on previous studies (e.g. Aleksy 2007 and Van Maele and Merci 2008), the mesh size for the baseline mesh is sufficiently refined in both horizontal and vertical directions. Three coarser meshes were created by systematically coarsening in all three directions by a factor of $2^{0.5}$. A summary of the test cases (MT 1, MT 2, MT 3, and MT 4) with different ratios of l/l_I is tabulated in Table 3.5. Numerical meshes for the DES mesh sensitivity study cases MT 1 to MT 4 (Table 3.5) are shown in Figures 3.6 to 3.9. The numbers of grid points for cases MT 1 to MT 4 are approximately 1.4×10^6, 7.0×10^5, 3.6×10^5, and 1.8×10^5, respectively. Note that in the current study, the main focus is on the flow regime variation and gas transfer process near the water surface. Numerical resources were mainly concentrated near the predicted free surface to capture the water surface shape and transport of bubbles. Mesh spacing criteria and y-plus near solid surfaces were not honored in this study.

Time-averaged volume fraction contours along with the standard deviations for test cases MT 1 to MT 4 are shown in Figure 3.10. Time-averaged velocity magnitude and vectors for these cases are shown in Figure 3.11. These figures clearly show that DES results can strongly

depend on the mesh, particularly if the mesh is not sufficiently refined. It can be seen that the predicted free-surface shape and velocity contours remain similar in the two most refined meshes (MT 1 and MT 2). As the mesh becomes coarser, the large scale eddies in the stilling basin cannot be adequately resolved thus deviations between simulation solutions get larger. The predicted free-surface fluctuation downstream of the spillway deflector is lower in case MT 3, and is not captured in the coarsest mesh (MT 4). Large-scale unsteadiness and surface waves in the stilling basin enhance turbulent mixing and weaken surface jet strength. Notice that the free-surface shape is relatively flat and the surface jet remain stronger with the coarse mesh, due to the incapability of resolving the large-scale unsteadiness in the stilling basin. The simulation results indicate that when the grid is fine enough to accurately resolve the large scale unsteadiness, further refining the grid will cease to significantly influence the mean results.

The predicted velocity magnitude statistics and deviations on different meshes are given in Table 3.6. Instantaneous velocities were collected at two collection points: Point 1 (P1) located directly above the edge of the spillway deflector, where the maximum velocity is predicted. Point 2 (P2) is placed between the deflector end and the baffle piers, where high velocity gradients are expected. Data were sampled at a 0.01 s time interval for 100 s near the free-surface, assumed at $\bar{\gamma} = 0.5$, on the flume wall. 10000 data samples were obtained at each point. The averaged velocity (U_{mean}) was calculated by blanking data with $\gamma < 0.5$, which is considered as air phase. Instantaneous velocity magnitudes at P1 and P2 with blanking are shown in Figure 3.12. As shown in this figure, turbulence fluctuation is appropriately predicted by the two most refined meshes (MT 1 and MT 2). As the mesh is coarsened (MT 3), velocity fluctuation becomes less consistent. In the coarsest mesh (MT 4), only mean flow fluctuation can be captured.

The velocity uncertainty was estimated based on a 95% confidence interval using:

$$U_{mean} \pm t_{v,P} \frac{S_n}{\sqrt{n}} \tag{3.28}$$

where $t_{v,P}$ is value for Student's distribution, determined from the number of degrees of freedom. S_n is the sample standard deviation and n is the sample size. The deviations are given in terms of percentage from the numerical benchmark U_c, obtained using the Richardson extrapolation method (Xing and Stern 2010). Since solutions from the coarsest grid (MT 4) cannot correctly reproduce large scale unsteadiness, only solutions from the three fine grids were used to conduct a grid triplet study. The calculated convergence ratios at the two sampling points fall between 0 and 1, indicating monotonic convergence was achieved. The standard deviations and deviations from numerical benchmark U_c at P1 are much smaller compared to values at P2 with the same mesh. This is because the velocity at P2 is strongly affected by the predicted large scale eddies and surface fluctuations in the stilling basin. Coarsening the mesh can also significantly influence regions with high velocity gradients. It is shown that the two most refined meshes (MT 1 and MT 2) predict similar flow patterns (Figures 3.10 and 3.11) and have averaged deviations within 5%. Therefore, it can be concluded that the grid spacing in case MT 2 is sufficiently refined to resolve large scale unsteadiness and eddies in the present study.

Flow instability can occur as vortex shedding and wakes behind blunt bodies, or it can occur as a turbulent shear flow away from walls. In the latter case, the instability is initially introduced in the turbulent shear layer due to velocity discontinuity, and is advected downstream (Oertel 1990). Immediate downstream of a spillway, a high velocity spilling jet is injected into the relatively quiescent tailwater. This phenomenon creates velocity shear between the entering and ambient water, and generates unsteady waves and turbulent mixing in the stilling basin. In the present study, the large scale unsteadiness in the stilling basin does not originate from the near-wall region. Flow regime prediction is thus not strongly affected by the resolved boundary layer near the walls. In the DES turbulence model used in the present study, the unsteady SA-RANS turbulence model is employed in the boundary layer. A high quality RANS grid is sufficiently refined to be used in this region. To verify this, a numerical mesh in MT 2 with less refinement near the wall was used as a test case, MT 5. As shown in Figure 3.13, relatively large grid spacing is used near the deflector and spillway face. Grid spacing in the other part of the

mesh remain the same as MT 2. The number of grid points is reduced to about 5.6×10^5. Since the simulation time step directly relates to the local cell size. Using a coarser mesh can shorten computational time and improve the overall efficiency of this study. The predicted time-averaged volume fraction and velocity characteristics for case MT 5 are shown in Figures 3.14 and 3.15, respectively. Simulation results from case MT 5 are compared against the corresponding results in case MT 2. Free surface shapes and flow field pattern show qualitative agreement between the two cases. Flow pattern remain almost identical as the mesh becomes coarser near the wall. The instantaneous velocities are plotted in Figure 3.16. The calculated velocity statistics are listed in Table 3.6. Comparing results from simulation cases MT 2 and MT 5, it can be seen that turbulence characteristics predicted by the two meshes are similar. The large scale unsteadiness is captured in MT 5. The averaged deviation from the numerical benchmark U_c is 5.84%. These results illustrate that coarsening the mesh near the wall has only marginal influence on the overall flow field. Thus, the grid spacing in case MT 5 is used henceforth.

Based on the mesh quality criteria determined above, four numerical grids (FR 1, FR 2, FR 3, and FR 4) were created for the simulation conditions presented in Section 3.5.1 (Figures 3.17 to 3.20). Notice that for simulation cases FR 3 and FR 4, additional mesh volumes were provided above the stilling basin to allow extra space for the expected ramping surface and to avoid influence of the boundary condition on the flow pattern.

3.5.3 Numerical Results

Photos illustrating the flow pattern and entrained bubble distribution under diverse flow conditions (Table 3.3) found in NHC (2001) are shown in Figure 3.21. The photo illustrating the skimming flow regime is absent in this report. As a complement, a short video clip recording these flow patterns was obtained from USACE. Figures showing flow conditions were extracted and plotted in Figure 3.22. These two figures are used to qualitatively compare with flow patterns predicted by the numerical model.

The VOF-DES numerical model discussed in Sections 3.4 was used to predict flow regime variation corresponding to tailwater elevation changes downstream of a spillway bay. Zero velocity and turbulence were used as initial conditions for the entire domain. Figure 3.23 shows the evolution of flowrates at the downstream end of the numerical model for the four simulated conditions. As illustrated in this figure, hydrodynamics downstream of the spillway are highly unsteady due to the presence of spillway water jets and hydraulic jumps. The simulations go through an initial transient stage and reach a statistical steady state, which is identified by the convergence of the cumulative average flowrate to the target value (0.041 m^3/s) at the exit. The inherently unsteady nature of the LES/DES methodology requires a sufficiently long flow-time to obtain meaningful flow and turbulence statistics, typically a few mean flow residence time. In the present study, the time-averaged simulation results were obtained by averaging flow variables over 10 units of mean flow residence time.

The mean volume of fraction contours and iso-surfaces are shown in Figures 3.24 to 3.27 for simulation cases FR 1 to FR 4, respectively. Contours are plotted at the slip wall boundary. Iso-surfaces are extracted at $\bar{\gamma} = 0.5$ and colored by free-surface elevation. The zero free surface level represents the downstream tailrace water height in each simulation case listed in Table 3.3. The corresponding flow regimes for these tailwater levels are plunging flow, skimming flow, undular flow, and hydraulic jump, respectively. Visual comparisons of free surface shapes between numerical results and photographic laboratory model data show a qualitative agreement with the corresponding flow regimes. When the tailwater level is too low to support the jet and prevent it from plunging, the spillway jet impacts the free surface of the tailwater at a downward angle (Figure 3.24). When the tailwater elevation is high, the spillway jet begins to ramp above the water surface (Figure 3.26). If the tailrace water level is high enough, the flow rolls back onto the spillway deflector and a hydraulic jump is generated (Figure 3.27). Since the flow kinetic energy is dissipated at the hydraulic jump formed in case FR 4, the maximum free surface elevation of the ramping wave is lower in FR 4 than in FR 3. This is also shown in the laboratory model (Figures 3.21 and 3.22). The skimming regime shown in Figure 3.25 only occurs when

there is a balance between the upholding recirculation beneath the jet and plunging jet momentum. The flow jet is surface-oriented and the free surface is relatively flat in this condition.

The mean velocity magnitude contours and velocity magnitude iso-surfaces for different flow regimes are shown in Figures 3.28 to 3.31. In the plunging flow condition (Figure 3.28), the downward momentum is sufficiently strong to cause flow to plunge off the deflector. The plunging jet may carry entrained bubbles to depths increasing TDG production. In the skimming flow (FR 2) shown in Figure 3.29, the flow momentum is transported tangential to the free surface, which may greatly reduce downward bubble transport. The flow pattern in the undular jump (FR 3) and hydraulic jump (FR 4) conditions are similar. The spillway jet is deflected about 20 to 40 degrees above horizontal. An undulating surface with a standing wave is formed on the downstream water surface. However, some notable differences are apparent. A stronger recirculation is observed beneath the jet for the hydraulic jump condition. Bubbles transported from upstream can be trapped downstream near the deflector. On the contrary, the recirculation in the undulating surface jet condition is much weaker. The jet diffuses gradually and penetrates deeper in the stilling basin. Bubbles under this flow condition may tend to spread into the downstream part of the stilling basin. Moreover, the restrained surface jet and roll-over wave in the hydraulic jump condition help to transport trapped bubbles in the stilling basin to the free surface increasing degasification. According to the model, fewer bubbles may be transported to the downstream channel in the hydraulic jump condition compared with the undular jump condition. This trend is confirmed by laboratory model study (Figures 3.21 and 3.22).

In summary, the qualitative agreement between the numerical results and reduced-scale laboratory model demonstrates that flow regimes downstream of a spillway are adequately reproduced by the numerical model.

3.6 Prototype-Scale Spillway Model

The capability of the presented numerical model to predict flow regimes at prototype scale is discussed in this section. Predicted flow patterns downstream are compared against simulation results in the reduced-scale presented in the last section under the corresponding flow conditions.

To evaluate the capability of the model to predict TDG distribution, operational configurations and tailwater elevations observed at the McNary Dam during a TDG field study (Wilhelms 1997) are applied to the model. Bubble behavior and TDG distribution in the McNary Dam tailrace region under different flow conditions are qualitatively discussed. The capability of the presented numerical model to quantify dissolved gas exchange is evaluated against TDG field measurements.

3.6.1 Simulation Conditions to Predict Spillway Flow Regime at Prototype-Scale

As mentioned earlier, the geometrical similarity and the Froude number were honoured in the hydraulic model study. However, the Reynolds number and Weber number in reduced-scale model are much smaller than in the prototype-scale. Consequently, turbulence and surface tension effects cannot be appropriately scaled. As a result, flow regime predictions in the reduced scale laboratory model may not match field observations due to the model effect. In addition, hydrostatic pressures present in the model-scale are too small to induce gas supersaturation. Therefore, bubble behaviour and TDG distribution cannot be evaluated in the reduced-scale model.

Numerical simulation cases FRP 1 to FRP 4 were conducted to assess flow patterns at prototype scale under the corresponding flow conditions used in the reduced-scale (Table 3.3). The letter P following FR (flow regime) represents “prototype”. Equivalent geometric dimensions and flowrates were obtained following the relationship listed in Table 3.2.

3.6.2 Simulation Conditions for TDG Predictions

Spatial and temporal patterns of TDG concentrations were investigated downstream of the McNary spillway stilling basin by the USACE on February 11 through 13, 1997. A detailed description of this near-field study of TDG in the McNary dam can be found in Wilhelms (1997).

TDG measurements were collected directly below the spillway on a grid of instruments set on five lateral transects and three longitudinal profiles. A map representing the layout of TDG measuring instruments (not the actual locations) is shown in Figure 3.32. The station nomenclature contains a two-character profile identifier (Q1, Q2, Q3, Q4, Q5), a two-character transect identifier (T1, T2, T3), and a single-letter depth identifier (B-bottom, U-upper). Thus, station Q3T2B refers to an instrument located on profile Q3, transect 2, on the channel bottom.

The instruments were mounted along five steel cables anchored to the spillway piers between bays 1 and 2 (Q5), bays 4 and 5 (Q4), bays 11 and 12 (Q3), bays 17 and 18 (Q2), and bays 20 and 21 (Q1). Lateral transects 1, 2, and 3 were located approximately 122m (400ft), 188m (617ft), and 198m (977ft), downstream from the piers, respectively. Two instruments were installed at most locations to provide a bottom measurement and a surface-to-mid-depth measurement. The bottom and surface instruments measured TDG saturation at 15 and 5 minute intervals, respectively.

Notice that cables were initially installed perpendicular to the spillways. However, the entrained flow from the powerhouses realigned the cables on Q1 and Q2, angling the deployment toward the spillway bays. Additionally, vertical positioning of the surface-to-mid-depth instruments changed throughout the testing period in response to drag on the instruments, cables, and buoys. Vertical positions at the data acquisition sites are not available in the field report (Wilhelms 1997). Therefore, only TDG concentrations collected by the bottom instruments were used to compare TDG prediction with numerical simulations.

The TDG production and/or reduction result from gas exchanges in the stilling basin, and mixing with adjacent waters. Observed TDG saturation along profiles Q1, Q2, and Q3 were heavily influenced by powerhouse flows due to the water entrainment phenomenon and therefore

cannot be used to analyze the gas absorption and desorption in this region. On the other hand, profile Q5 extended downstream between bays 1 and 2, which are non-deflectored and used special split-leaf gates. Hydraulic actions caused by split-leaf operations are very different from those in deflectored spills or conventional stilling basins. Simulation of flows and TDG patterns under this condition is outside the scope of this study and is recommended for future work to increase the understanding of TDG processes in a dam. The measured streamwise distribution of TDG along profile Q4 is highly correlated with spillway discharge from spillway bays 4 and 5, and thus it was selected to analyze gas exchange characteristics of the McNary Dam tailrace.

The spillway deflector performance tests were conducted with the existing deflector and stilling basin geometry in Test 3e of the reduced-scale laboratory model study (NHC 2001). The resulting performance curve (Figure 3.33) was used to compare with the predicted flow regimes at prototype scale. Note that the range of the hydraulic jump formation in Figure 3.33 is more extensive than in Figure 3.2. This is mainly attributed to the lack of transition radius, since it results in more splash as the flow impinges directly on the level deflector that enhances energy dissipation. The spillway jet kinetic energy is lost in this process thus facilitates formation of the hydraulic jump (NHC 2001).

Four prototype spillway operational and tailwater elevation conditions (TD 1, TD 2, TD 3, and TD 4), corresponding to the four flow regimes described earlier, were selected to evaluate gas entrainment characteristics and TDG patterns under these flow conditions. The discharge, tailwater elevation, and flow regime for each case are summarized in Table 3.7. The tailwater elevation of a hydropower dam is mainly determined by total river discharge and forebay elevation of the downstream dam, which did not vary greatly for the simulated day. Therefore, differences in flow patterns can be mainly attributed to differences in spillway flowrates. The flow regimes change from the plunging to surface jump condition due to a decrease in spillway discharge from cases TD 1 to TD 4, as illustrated in Figure 3.33.

During the field study, each spill pattern was set for a minimum duration of 2 hours. Flow patterns and TDG concentrations fluctuated during the transient period between two flow

conditions. TDG measurements show that this transient stage usually last about 30 minutes before the steady state condition is reached where TDG values only vary within a relatively narrow range. To ensure a representative TDG saturation for each flow condition, only measurements in the second hour of each spill pattern were used in the analysis.

3.6.3 Computational Grid

To determine appropriate mesh spacing to model the spillway at prototype scale, the procedure outlined in Section 3.5.2 was followed. Since turbulence levels in the model-scale and prototype model are different, the turbulent integral length scales in the prototype were re-evaluated by conducting a RANS simulation. The time-averaged turbulent integral length is shown in Figure 3.34. The overall integral length scale pattern is similar in both model-scale (Figure 3.4) and prototype-scale. However, the levels are different indicating different eddy sizes existing in these two different scales.

Four additional meshes were created with the same grid spacing to eddy length scale ratio (l / l_I) listed in Table 3.4, with the integral length scale l_I being from the prototype-scale model (Figure 3.34). These meshes were used to evaluate the dependence of flow variables on the applied mesh for prototype-scale simulation, and denoted as MTP 1 to MTP 4. The letter P following MT (mesh test) represents “prototype”.

The simulation results for the time-averaged volume fraction contours along with the standard deviations, and the time-averaged velocity magnitude and vectors for test cases MTP 1 to MTP 4 are shown in Figures 3.35 and 3.36, respectively. Comparing these figures with the corresponding figures for the model-scale tests (Figures 3.10 and 3.11), it becomes clear that the trend of the dependence of flow variables on mesh density is consistent for model-scale and prototype-scale. The spillway jet induced large scale unsteadiness in the stilling basin that cannot be captured in the coarsest mesh (MTP 4). Flow patterns in the two most refined meshes (MTP 1 and MTP 2) look qualitatively similar. Table 3.8 provides an overview of flow statistics for the prototype-scale model. The averaged velocity magnitude, standard deviation, confidence interval,

numerical benchmark, and deviations are calculated as described in Section 3.5.2. The averaged deviation in the case MTP 2 is only about 3.44%. Therefore, the grid spacing in case MTP 2 was selected to predict the flow pattern in the prototype spillway model.

Based on the grid spacing determined in the above discussion, the estimated mesh size for the entire McNary tailrace region requires about 40 million grid points (22 spillway bays, 14 powerhouse units, and the downstream river channel). The enormous computational resources needed to conduct a study with such a huge mesh are not currently available to the author. CFD computations in this study were performed on the University of Iowa's Helium Cluster. IIHR owns 20 8-core nodes with 24 GB of memory for each node. All nodes use Intel Xeon processors. The estimated time for running the comprehensive McNary tailrace model on this cluster is approximated 500 days. Since computational capacity changes very rapidly, the lack of computational resources might be overcome in the near future.

In the present study, only part of the McNary Dam tailrace was modeled to reduce the computational resources required. The model geometry included two half spillway bays, flow deflectors, sluice gate, and measured bathymetry. Symmetric planes were used to separate the adjacent spillway bays. The tailwater elevation was controlled at the outflow boundary. The model was extended approximately 380m downstream of the dam to minimize outflow boundary effects. Numerical meshes were generated following the mesh quality criteria determined in the above discussion. Three-dimensional views of the prototype spillway mesh are shown in Figures 3.37 to 3.40, corresponding to the four simulation conditions shown in Table 3.7. Note that the geometry for the prototype-scale and model-scale spillway bays (Figures 3.17 to 3.20) is identical, except for the absence of the radius transition that joins the sloping spillway to the level deflector.

3.6.4 Numerical Results for Flow Regime Predictions at Prototype-Scale

Predicted flow patterns at reduced-scale and prototype-scale under different flow conditions are compared on the left and right frames, respectively, in Figures 3.41 to 3.44. The figures in each plot show (from top to bottom): volume fraction contours, volume fraction iso-surface colored by free surface elevation, velocity magnitude contours, and velocity magnitude iso-surface. Since the Reynolds number for the prototype-scale is 125 times larger than it is for the model-scale, the performance curves derived from laboratory model study may not accurately represent the flow characteristics at prototype. Notice that in the present study, the spillway gate openings were adjusted according to equations (3.24) to (3.26) to include the flow contraction at the gate. The energy loss was assumed negligible in this approach. However, past investigations on gate contraction (Kim 2007; Cassan and Belaud 2011) show that energy losses by friction and water surface oscillations may affect the contraction coefficient. Field observations show that the experimental values of contraction coefficients always exceed the theoretical values by 5-10% (Kim 2007). Neglecting the energy loss will result in a higher kinetic energy in the current simulations, which may affect the prediction of spillway regime and flow patterns in the tailrace area. Numerical simulation that includes the upstream reservoir is needed to accurately capture the contraction at the gate.

As illustrated in Figures 3.41 to 3.44, the predicted kinetic energy is consistently higher in prototype-scale compared to the corresponding reduced-scale results. The inflow velocity in prototype-scale is increased by 45.3% due to the contraction at the gate. As seen in Figure 3.41, the spillway jet in the prototype model impacts the free surface at a larger downward angle and plunges deeper into the stilling basin. Flow patterns for the skimming flow regime shown in Figure 3.42 are similar in both scales, with a slightly weaker surface jet for the prototype due to higher turbulent diffusion near the free surface. The upward deflected standing wave in the undular jump condition is lower due to the higher kinetic energy in prototype scale (Figure 3.43), and the transition from undular to hydraulic jump is delayed since there is enough energy in the

jet to maintain the flow pattern, as illustrated in Figure 3.44. These simulation results indicate that the flow regime variation in the stilling basin is very sensitive and highly dependent on the accurate modeling of the flow conditions at the gate and over the spillway. According to the model, the flow conditions observed in the reduced scale laboratory model may not accurately reproduce the flow regime observed in the field. Further studies are needed with validation against field data to assess the flow characteristic differences in the reduced-scale and prototype-scale.

3.6.5 Numerical Results for TDG Predictions

The flow regimes predicted by the model under selected simulation conditions at prototype scale (Table 3.7) are first compared against the performance curve obtained in the reduced-scale laboratory model (Figure 3.33). The time-averaged volume fraction contours, the free-surface iso-surface colored by elevation, velocity magnitude contours, and velocity magnitude iso-surface for simulation cases TD 1 to TD 4 are shown in Figures 3.45 to 3.49, respectively. Good agreement between the predicted and observed flow regimes is seen under different flow conditions. The flow patterns in the stilling basin and downstream channel are consistent with the observations in the reduced-scale model. A strong recirculation is observed beneath the surface jet in cases TD 1 and TD 4, which may affect downstream transport of entrained bubbles. Notice that the spillway jet dissipates rapidly due to presence of the hydraulic jump in case TD 4. The standing wave is lower and the flow jet is weaker in the hydraulic jump condition (TD 4) compared to the undular jump (TD 3). Since the tailwater elevations are relatively stable in the four flow conditions, the decreasing discharges from cases TD 1 to TD 4 result in decreasing flow velocities in the downstream channel from cases TD 1 to TD 4. Transported passive scalars, such as bubbles and TDG, travel slower under lower streamwise velocity. Although time-averaged flow patterns in the two half bays appear symmetrical with respect to the vertical axial centerplane, it should be noted that the instantaneous flow field is highly unsteady and oscillatory. Fluctuated waves and recirculation below the jet may

occasionally bring bubbles to depth or adjacent bays, which can cause TDG variations within the stilling basin.

As discussed in Politano et al. (2009c), the TDG model presented in this study lacks some effects of the dissolved gas exchange process that may be important under specific flow conditions. First, the air entrainment model is not included in the current study. Air entrainment occurs primarily during the plunging process, but also along the spillway face. The mechanisms of bubble entrainment are far from being completely understood. In the past three decades, researchers have published studies involving circular and planar plunging jets impinging vertically or at an angle with simplified or idealized geometries (Bin 1993; Ma et al. 2010; Kiger and Duncan 2012). However, significant research effort is needed to better understand air entrainment processes on the impact region of spillways with different flow regimes and complex geometries. Given the extremely complicated nature of the problem, the present model seeks to identify trends for the TDG distribution by tuning two parameters to match known flow field and TDG measurements. Since no data is currently available in the literature for bubble size or void fraction in a prototype spillway, effects of these two parameters on TDG distributions are evaluated in this study.

Breakup and coalescence of bubbles are also neglected in the model. Since the level of bubble interaction with each other may vary depending on spillway flow regimes and turbulence intensity, neglecting these processes may have significant consequences under certain flow conditions (i.e. plunging and hydraulic jump regimes). A polydisperse two-phase model, such as the one used by Politano et al. (2000), can be included when available gas entrainment measurements in the field be available.

Since only two half spillway bays of the McNary Dam tailrace are modeled, it is assumed that the flow fields and TDG distributions are not strongly affected by lateral flows and mixing from the adjacent bays. As observed in the field, flow jets from the neighboring spillway bays were entrained into each other periodically due to turbulent surging. The impact may be important when large differences in flow conditions and TDG levels exist in ambient waters.

Nevertheless, TDG measurements closer to the spillway are less affected by the flow field nearby. Since the current model cannot account for effects of lateral flow and water entrainment from the powerhouse, a fully three dimensional model for the entire McNary tailrace region is proposed as future work, once adequate computational resources are available.

To perform TDG calculations, the gas volume fraction for the bubble phase was assumed zero and measured forebay TDG was imposed over the entire tailrace as initial conditions. TDG concentrations developed gradually over a period of time and reached equilibrium in about 1500 seconds. Figure 3.49 shows the evolution of the area-weighted average TDG at the downstream outflow boundary for simulation cases TD 1 to TD 4. Notice that the convergence slowed from cases TD 1 to TD 4, due to the decreasing flowrate and increasing residence time.

Figures 3.50 to 3.53 depict the spatial distributions of time-averaged gas volume fraction for the four selected flow conditions. Due to the lack of measured data, a gas volume fraction of 3% and bubble diameter of 0.8 mm were used at the inlet for these simulations following assumptions in previous studies for other hydropower dams (Politano et al. 2007; 2011). The gas volume fraction and bubble diameter may vary at different dams due to variations in structure, air-entrainment level, and flow regime. Effects of the two parameters on predicted TDG distributions are further evaluated later in this section. As clearly shown in these figures, the transport of bubbles is significantly affected by the characteristic flow pattern of each spillway jet regime. As seen in Figure 3.50, a high gas volume fraction is observed in the stilling basin. Bubbles are transported deep to the stilling basin floor with the plunging flow and trapped by the strong recirculation below the jet. Rising bubbles in this recirculation may be sunk once again by the downwelling jet and remain in the deep region for long periods of time. A large portion of bubbles remain in the lower water column and rise slowly towards the water surface. The downward bubble transport is greatly reduced in the skimming flow condition (Figure 3.51). Bubbles are mainly carried by the horizontal surface jet near the free surface and leave the liquid phase gradually as they advance in the flow direction. The surface jet is first deflected upward and then splashes down with the remaining downward momentum in the undular and hydraulic

jump conditions (Figures 3.52 and 3.53). Some bubbles can be transported by the recirculation to the lower water column. However, the spillway jet does not penetrate deep to the spillway bottom and remains near the free surface. Rising bubbles in the flow recirculation are likely to be redirected along the surface, which favor bubbles to exit at the free surface. Compared to the skimming flow condition, the undular jump and surface jump regimes can cause bubbles to travel deeper in the upstream part of the stilling basin. However, bubbles are rapidly brought back to the surface resulting in a lower gas volume fraction in the downstream channel. This trend was also observed in a bubble entrainment study using a reduced-scale spillway (Hoschek et al. 2008). It can be noted that, as shown in Figure 3.53, a large portion of bubbles are trapped in the roll-over wave formed on the deflector. These bubbles can easily approach the free surface, resulting in less gas volume fraction in the downstream channel for the hydraulic jump condition compared to the undular jump condition.

The time-averaged bubble diameter contours are shown in Figures 3.54 to 3.57 for simulation cases TD 1 to TD 4. Air bubbles shrink at the lower elevation, and as bubbles rise toward the water surface, they grow larger in size. The reduction of bubble diameter at depth is mainly due to the high pressure found near the stilling bottom, and to the bubble dissolution. The elevated pressure facilitates mass transfer for bubble dissolution and compresses bubbles in the deep water column. On the other hand, bubbles may absorb air and become larger near the surface under low pressure and supersaturated local TDG concentrations. Comparing bubble sizes under different flow conditions, it can be seen that bubble diameters near the stilling basin floor in the skimming flow condition are smaller than in other flow conditions. This is mostly attributed to the effects of bubble dissolution in a region of very low gas volume fraction. As illustrated in Figures 3.50 to 3.53, the bubble gas volume fraction near the stilling basin bottom is much smaller in the skimming flow condition than in other conditions. Therefore, bubble dissolution has a large influence on bubble size variation with a low bubble gas volume fraction, as shown in equation (3.21).

The TDG source is an important component in the TDG transport equation (Eqn. 3.22) that governs the production and reduction of TDG concentrations. It is proportional to the difference between the local TDG level and saturation concentration at local conditions. The local bubble size also has a strong effect on the TDG source, since smaller bubbles have a longer residence time (less buoyancy force) and a larger interfacial area per unit volume. The predicted TDG source distributions for different flow regimes are plotted in Figures 3.58 to 3.61. A positive source represents areas of TDG production. Where the TDG source is below zero, gas is transferred from water to bubbles, reducing the local TDG level, also known as degasification. As shown in these figures, a high positive TDG source zone is found in stilling basin lower water columns for all spillway regimes. The TDG source levels are higher between the deflector and the first row of baffle piers, where bubbles are initially brought to depth. The TDG source values decrease a little near the end sill, though they remain high compared to the downstream channel. As illustrated in these figures, predominant TDG production occurs in the stilling basin. The degasification process starts near the free surface when water is supersaturated at local conditions and continues in the downstream channel. The plunging flow condition produces the highest TDG source level among the four flow regimes. The source is considerably smaller in the skimming flow condition than in other flow regimes.

The TDG distribution is determined by considering convective transport, dissolution of bubbles, and mixing. Figures 3.62 to 3.65 show spatial distributions of time-averaged TDG concentrations downstream of the spillway under different flow regimes. Since most air dissolution occurs within the stilling basin, TDG levels continue to increase in the stilling basin due to the positive TDG source in this region. High TDG values are observed immediately downstream of deflector and near the end sill. Flow recirculation beneath the spilling jet and downstream of baffle piers accumulate TDG that is transported from upstream. Since there is a lack of bubbles in the deep region of the downstream channel, TDG levels gradually decrease as they move away from the spillway due to the degasification near the free surface and turbulent diffusion. The highest TDG concentration is observed in the plunging flow condition. The peak

TDG level is found near the spillway end sill and reaches about 165%. The highest TDG concentrations for the skimming flow, undulate jump, and hydraulic jump conditions are approximately 143%, 153%, and 153%, respectively. The simulation results suggest that under the same air volume fraction (air entrainment) and bubble size, the plunging flow condition produces the highest TDG level, while the skimming flow condition results in the lowest TDG concentration.

As mentioned earlier, the entrained gas volume fraction and bubble size distribution can vary greatly in the tailrace impact region of spillway jets under different flow regimes. In addition, bubbles may breakup and coalesce differently due to varied shear stresses and turbulence intensities in each flow condition. Measurements at prototype of entrained air are not available in the literature. In the present model, two parameters are calibrated to match TDG measurement and achieve a reasonable solution with the smallest error. The parameters are entrained gas volume fraction and entrained average bubble size. The effects of these imposed variables were evaluated numerically. The TDG concentrations along the center line of the two neighboring spillways at the river bottom are plotted in Figures 3.66 to 3.69 for the four flow conditions. TDG measurements at Q4T1B and Q4T2B are shown in the same figure along with model predictions. The effects of the entrained gas volume fraction and average bubble diameter on the predicted TDG concentration are shown in the middle (b) and bottom (c) plots of Figures 3.66 to 3.69, respectively. The TDG contours on the stilling basin bottom and downstream river bed that correspond to predictions with minimum error in each case are shown on the top (a) in each figure.

The entrained gas volume fraction determines the amount of gas that can be released to the liquid along the spillway and in the tailrace. As revealed in equation (3.23), the TDG source is proportional to the gas volume fraction. Therefore, higher gas volume fraction results in higher TDG production. This trend is clearly seen in plot (b) of Figures 3.66 to 3.69. The general pattern of TDG variation along the longitudinal distance is similar under different gas volume fractions. The gas dissolution mainly occurs within the stilling basin. A sudden drop in TDG

concentration is found at about 85 meters downstream from the spillway piers separating adjacent spillway bays due to the presence of the stilling basin end sill. Bubbles and TDG are confined by the end sill and more likely to accumulate within the stilling basin. The TDG concentration gradually decreases downstream of the stilling basin due to the degasification near the free surface and turbulent diffusion within the water column. Reduction rates in the first 50 meters downstream from the end sill are slightly higher for large gas volume fractions, and become identical further in the downstream channel. Since the mass transfer rate between bubble and liquid is proportional to the difference between the TDG concentration at equilibrium and local TDG, the removal of TDG at low pressure is faster with high supersaturation levels produced by high entrained gas volume fractions assumed at the inlet. The standard deviation in the stilling basin is much higher than in the downstream channel, where TDG variation is strongly affected by unsteady flow patterns due to spillway jets.

Since the mechanism governing the bubble size distribution during air entrainment is not yet well understood, field measurements at specific project sites are important. These data can be used for modeling the bubble size distributions needed for the present model. The size of entrained bubble affects the distribution of bubble gas volume fraction and TDG in several aspects. Larger bubbles have higher terminal rise velocities, plunge shallower, and approach the free surface more rapidly. The residence time is shorter for larger bubbles compared to smaller bubbles. Also, the interfacial area density is smaller and bubble pressure is lower for larger bubbles with the same gas volume fraction. As shown in equation (3.23), these effects result in a smaller TDG source for large bubbles. In plot (c) of Figures 3.66 to 3.69, it can be seen that the effects of bubble size on TDG distribution are more complex and use completely different mechanisms compared to the bubble gas volume fraction. When the bubble size is large, the vertical relative velocity between bubble and liquid is large and therefore large bubbles leave the free surface before transferring important amounts of mass to the liquid phase. TDG concentrations slightly increase within the stilling basin and remain nearly constant due to the lack of bubbles in the downstream channel. If bubble size is small enough, bubbles follow

closely with the flow and plunge deep toward the river bottom. These bubbles dissolve quickly into the liquid and contribute strongly to TDG concentrations. Notice that when small bubbles are entrained, they can be transported near the bottom in the downstream channel, and bubble dissolution and TDG levels can be strongly affected by the shape of the bathymetry. River beds with local lower elevations have higher pressure, thus producing more TDG compared to elevated river beds. In general, small bubbles produce more TDG in the stilling basin and have larger impacts on TDG distribution in the downstream channel than do larger bubbles.

Figure 3.70 shows TDG concentrations predicted at different gas volume fractions and bubble sizes for the four flow conditions at Q4T1B and Q4T2B. In general, the gas volume fraction has a nearly linear effect on TDG concentration in the downstream channel. TDG levels rise as the gas volume fraction increases. The upstream station Q4T1B has a higher TDG value compared to the downstream station Q4T2B, due to degasification in the longitudinal direction. On the other hand, the dependency of TDG concentration on bubble size is more complicated. The TDG concentration rises as the bubble size gets smaller. When the bubble size is sufficiently small to allow travel to the river bottom, the TDG concentrations near the river bed become sensitive to river bed elevation and local pressure. As illustrated in Figure 3.70, the upstream station Q4T1B has a lower TDG than downstream station Q4T2B for bubbles of 0.1 mm, due to the higher river bed elevation at the former location (Figure 3.71).

Field observations and laboratory experiments suggest that the entrained bubble gas volume fraction can vary significantly under different flow regimes (Hoschek et al. 2008). On the other hand, entrained bubble size is usually within a relatively small range for varying conditions. Therefore, in the present study, the model was calibrated assuming that the bubble diameter was 0.8 mm, following previous numerical studies (Politano et al. 2007; 2011). The gas volume fractions that match better the measured TDG are 0.02, 0.0225, 0.0125, and 0.0085 for flow regimes plunging, skimming, undulate jump, and hydraulic jump, respectively, as shown in Figures 3.66 to 3.69. Notice that measured TDG reductions in the longitudinal direction are higher compared to predictions in cases TD 1 and TD 4. This is likely due to the dilution of the

lateral flow and water entrained from the powerhouse region, which is not captured by the present model.

The predicted TDG values after calibration at each data collection location along with the field measurements are summarized in Table 3.9. The model captured the trend of TDG reduction in the longitudinal direction under different flow regimes. The differences between the predicted and measured TDG are within 4%.

3.7 Summary

An unsteady, three-dimensional two-phase numerical model was developed using the open-source CFD code OpenFOAM. The model was used to study hydrodynamics and TDG distribution in the tailrace region of McNary Dam. The model utilized the VOF method combined with a DES approach to resolve the free surface and flow fields downstream of a spillway. A one-way coupling approach was used to incorporate the TDG model developed by Politano et al. (2009c) into the VOF-DES hydrodynamic model.

The adequate mesh resolution to resolve the large-scale unsteadiness in the integral scale vortices was determined for this study. It has been shown that, as the mesh becomes coarser, large scale eddies induced by the free shear flow in the stilling basin can no longer be resolved to a sufficient extent and the predicted spillway jet velocity differs strongly from the value obtained from a more refined grid.

Predicted flow regimes under varying flow conditions for the reduced-scale and prototype-scale numerical spillway models were validated against observations in a reduced scale laboratory model. The spillway jet regime depends on both spill flowrate and tailwater elevation. Simulation results demonstrated that the flow regimes downstream of a spillway can be adequately reproduced by the numerical model for both the model-scale and prototype-scale.

Bubble behaviours and TDG distributions under different flow regimes were evaluated at prototype scale by assuming the same entrained gas volume fraction and bubble size. Simulation results show that bubbles were transported deep into the stilling basin in the plunging flow

condition, producing high TDG concentrations in the river channel. On the other hand, the skimming flow condition proved to be the most favorable condition by minimizing TDG production when compared to other flow regimes.

The effects of the model inputs, gas volume fraction and bubble size, were then analyzed under different flow regimes. TDG levels increase with the gas volume fraction. In contrast, smaller bubble sizes result in higher TDG concentrations, since smaller bubbles travel deeper into the stilling basin and have larger interfacial area and residence time, facilitating gas transfer from bubbles to the liquid.

Finally, the model was calibrated and validated against measured TDG concentrations. Simulation results demonstrated that the model captured observed TDG reductions in the longitudinal direction under different flow regimes. Differences between predicted and measured average TDG values are below 4%.

The model developed in this study can be used as a predictive numerical tool to identify flow regimes and TDG production under different flow conditions in the near dam region when lateral flows are not important. However, due to computational limitations of the present study, additional validations of simulation results for the entire McNary tailrace region are needed to enable this model as a comprehensive, practical design tool for evaluating tailrace TDG mitigation measures.

Table 3.1 Summary of boundary conditions utilized in this study

	$\boldsymbol{U}$	p	γ	υ	α	N	C
Inlet	Dirichlet	Neumann	Dirichlet	Dirichlet	Dirichlet	Dirichlet	Dirichlet
Outlet	Neumann	Dirichlet	Neumann	Neumann	Neumann	Neumann	Neumann
Pressure Outlet	Neumann	Dirichlet	Neumann	Neumann	Neumann	Neumann	Neumann
Walls	Dirichlet	Neumann	Neumann	Dirichlet	Neumann	Neumann	Neumann

Table 3.2 Summary of scaling ratios for the model at reduced-scale

Parameter	Scaling Relationship	Ratio
Length	L_r	1:25
Velocity	$L_r^{1/2}$	1:5
Discharge	$L_r^{5/2}$	1:3125
Unit Discharge	$L_r^{3/2}$	1:125
Pressure	L_r	1:25

Table 3.3 Summary of simulation conditions for the model at reduced-scale

	Spillway discharge (m^3/s)	Water surface elevation (m)		Flow regime
		Forebay	Tailwater	
FR 1	255	103	79.7	Plunging
FR 2	255	103	80.8	Skimming
FR 3	255	103	83.7	Undular
FR 4	255	103	84.6	Hydraulic Jump

Table 3.4 Ratio of resolved and total cumulative TKE against ratio of resolved and integral length scale

$k(l)/k$	l/l_I
0.1	6.10
0.5	1.60
0.8	0.42
0.9	0.16

Table 3.5 Ratio of resolved and total cumulative TKE against ratio of resolved and integral length scale for cases MT 1 to MT 4

Case	l / l_I	$k(l) / k$
MT 1	0.083	0.99
MT 2	0.125	0.95
MT 3	0.17	0.9
MT 4	0.25	0.85

Table 3.6 Velocity statistics at reduced-scale for cases MT 1 to MT 5

	P1			P2			Mean Deviation (%)
	U_{mean} (m/s)	S_n	Deviation (%)	U_{mean} (m/s)	S_n	Deviation (%)	
MT 1	$3.499 \pm 2.78e^{-5}$	$1.42e^{-3}$	-0.54	$2.384 \pm 1.48e^{-2}$	$5.45e^{-1}$	1.95	1.25
MT 2	$3.477 \pm 2.80e^{-5}$	$0.95e^{-3}$	-1.17	$2.514 \pm 1.44e^{-2}$	$5.25e^{-1}$	7.51	4.34
MT 3	$3.429 \pm 6.04e^{-5}$	$3.08e^{-3}$	-2.53	$3.014 \pm 4.73e^{-3}$	$1.53e^{-1}$	28.8	15.67
MT 4	$3.340 \pm 3.90e^{-5}$	$1.99e^{-3}$	-5.06	$3.162 \pm 4.17e^{-3}$	$1.61e^{-1}$	35.2	20.13
MT 5	$3.450 \pm 9.72e^{-5}$	$4.95e^{-3}$	-1.93	$2.567 \pm 1.51e^{-2}$	$5.67e^{-1}$	9.75	5.84
U_c (m/s)	3.518			2.339			

Table 3.7 Simulation conditions for the model at prototype-scale

	Spillway discharge (m^3/s)	Water surface elevation (m)		Flow regime
	Bays 4 and 5	Forebay	Tailwater	
TD 1	385.1	103.2	81.4	Plunging
TD 2	201.0	103.1	80.8	Skimming
TD 3	155.7	103.0	81.9	Undular
TD 4	107.6	103.0	81.5	Hydraulic Jump

Table 3.8 Velocity statistics at prototype-scale for cases MTP 1 to MTP 4

	P1			P2			Mean Deviation (%)
	U_{mean} (m/s)	S_n	Deviation (%)	U_{mean} (m/s)	S_n	Deviation (%)	
MTP 1	$17.638 \pm 2.46e^{-4}$	0.109	-0.0047	$9.358 \pm 1.96e^{-2}$	6.744	1.57	0.78
MTP 2	$17.633 \pm 3.33e^{-4}$	0.109	-0.026	$9.845 \pm 1.52e^{-2}$	6.733	6.85	3.44
MTP 3	$17.383 \pm 3.31e^{-4}$	0.114	-1.44	$11.972 \pm 1.46e^{-2}$	4.756	29.93	15.69
MTP 4	$17.326 \pm 5.00e^{-4}$	0.131	-1.77	$15.030 \pm 1.08e^{-2}$	3.026	63.12	32.45
U_c (m/s)	17.638			9.214			

Table 3.9 Comparison between predicted and measured TDG in different flow conditions

Station	Predicted TDG		Measured mean TDG		Deviation (%)
	Averaged	S_n	Averaged	S_n	
TD 1					
Q4T1B	1.4671	0.0354	1.4737	0.0090	-0.45
Q4T2B	1.4225	0.0202	1.3779	0.0040	3.23
TD 2					
Q4T1B	1.2726	0.0136	1.2775	0.0033	-0.38
Q4T2B	1.2513	0.0057	1.2537	0.0019	-0.19
TD 3					
Q4T1B	1.2867	0.0103	1.2918	0.0024	-0.39
Q4T2B	1.2656	0.0066	1.2633	0.0017	0.19
TD 4					
Q4T1B	1.2109	0.0064	1.2285	0.0027	1.43
Q4T2B	1.1960	0.0019	1.1845	0.0022	-0.97

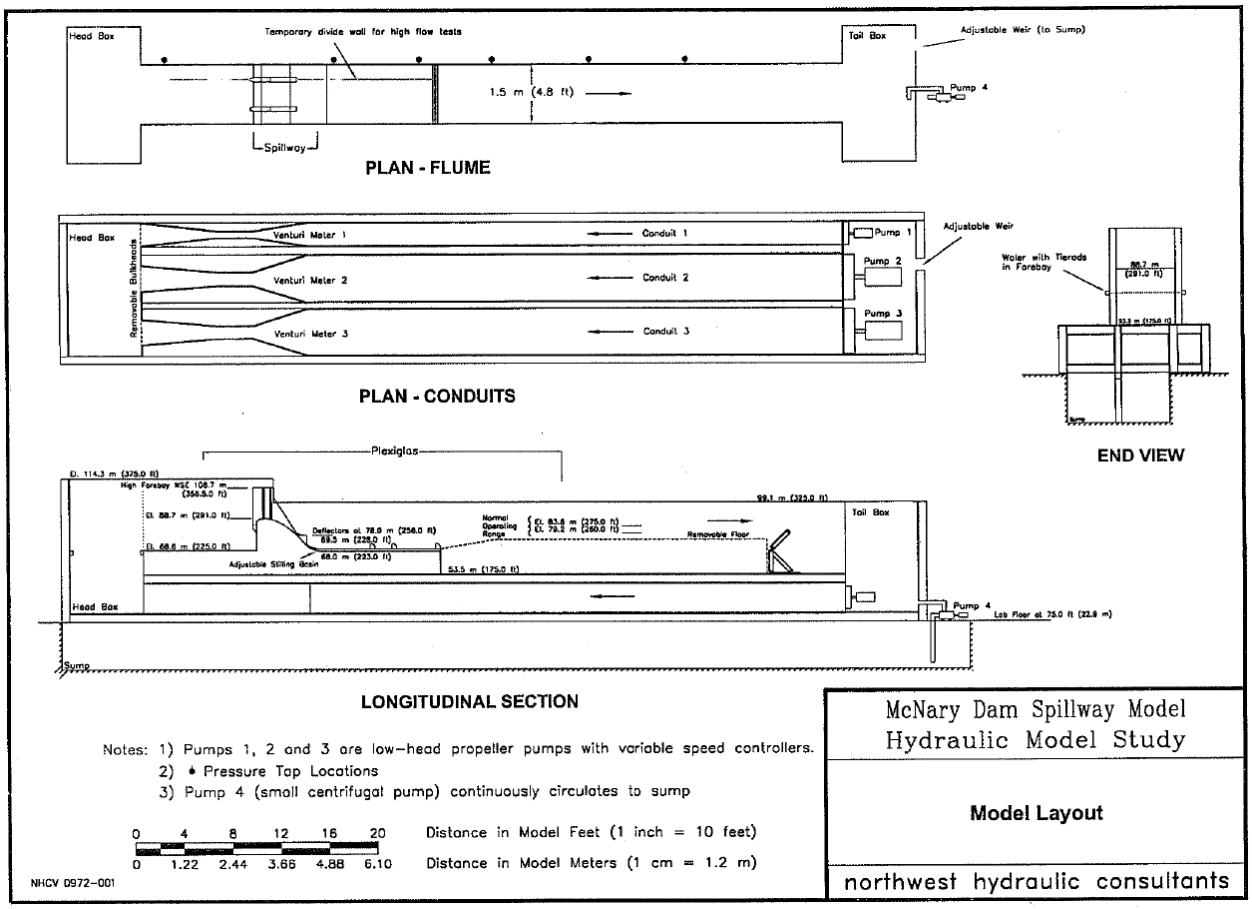

Figure 3.1 Layout of the McNary Dam reduced-scale model (NHC 2001).

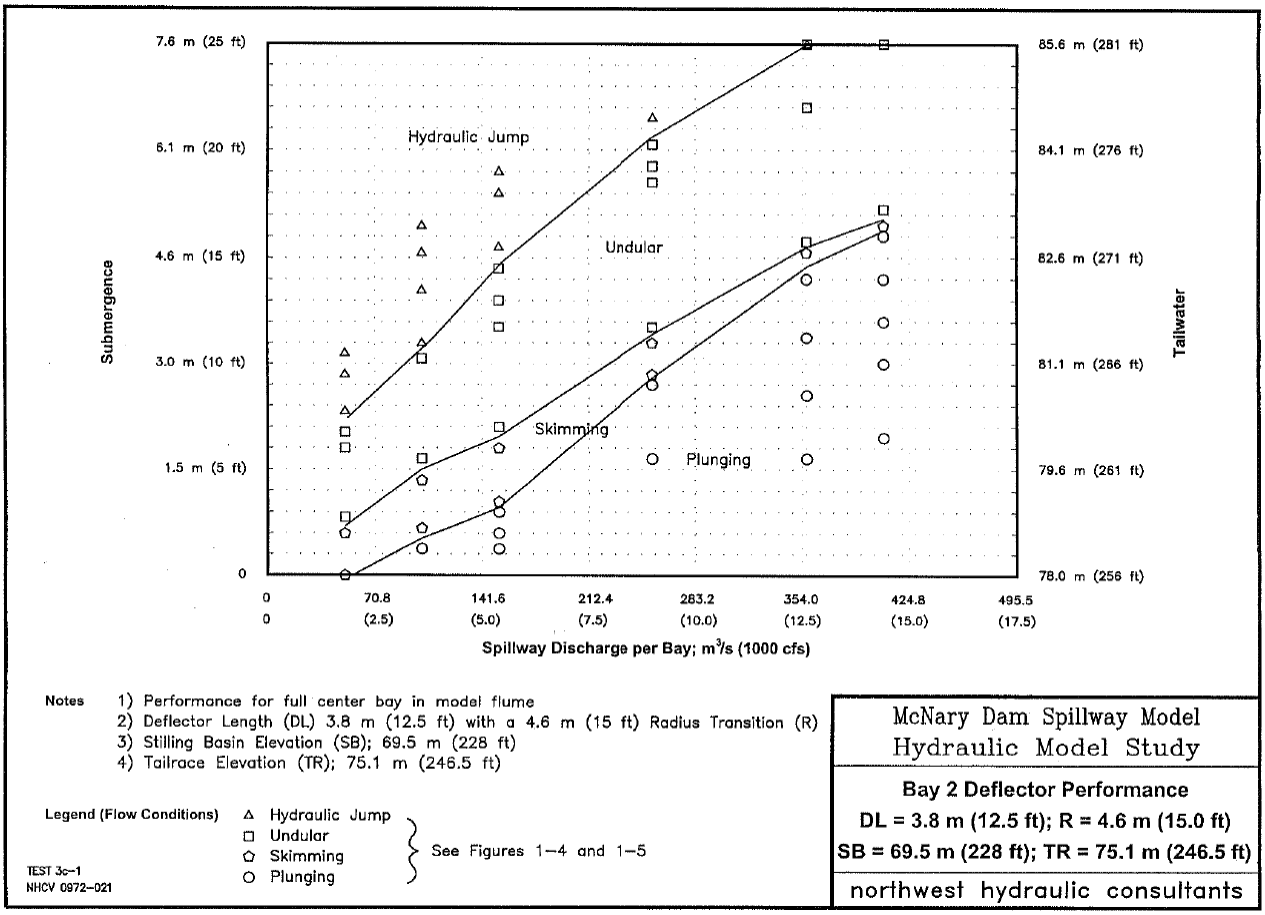

Figure 3.2 Performance curve for the reduced-scale laboratory model (NHC 2001).

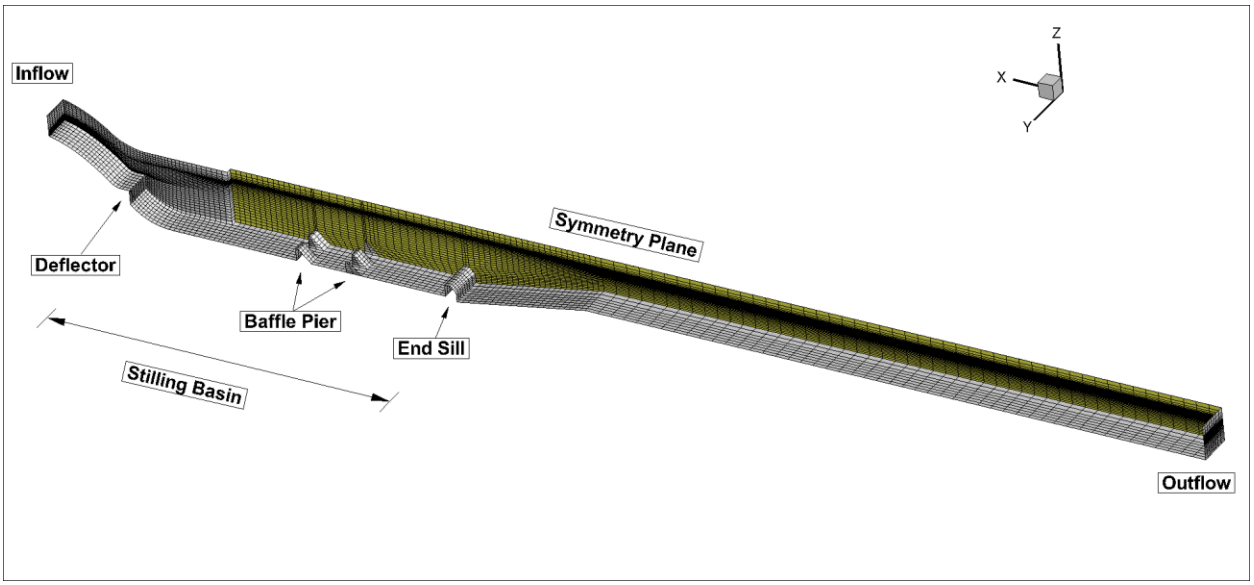

Figure 3.3 Computational mesh and boundary conditions at reduced-scale for RANS simulation.

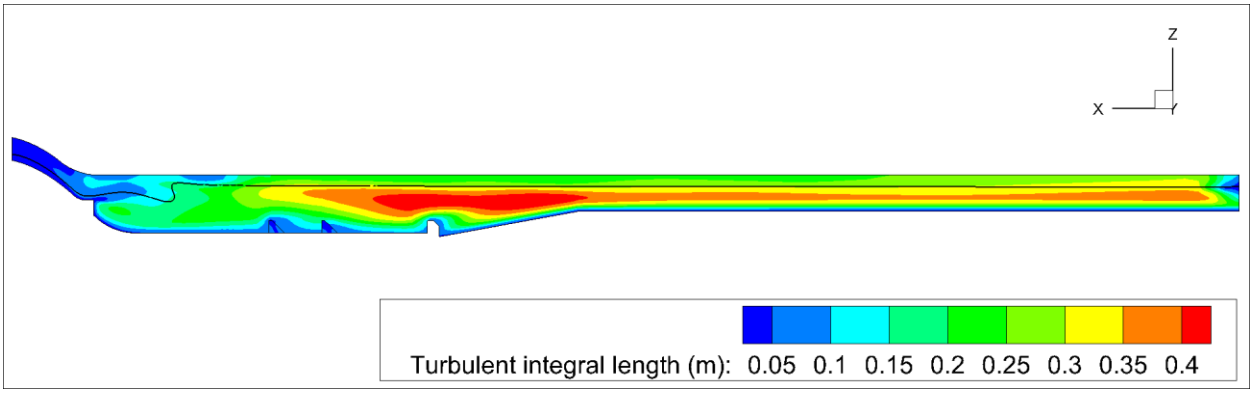

Figure 3.4 Time-averaged turbulent integral length in reduced-scale model.

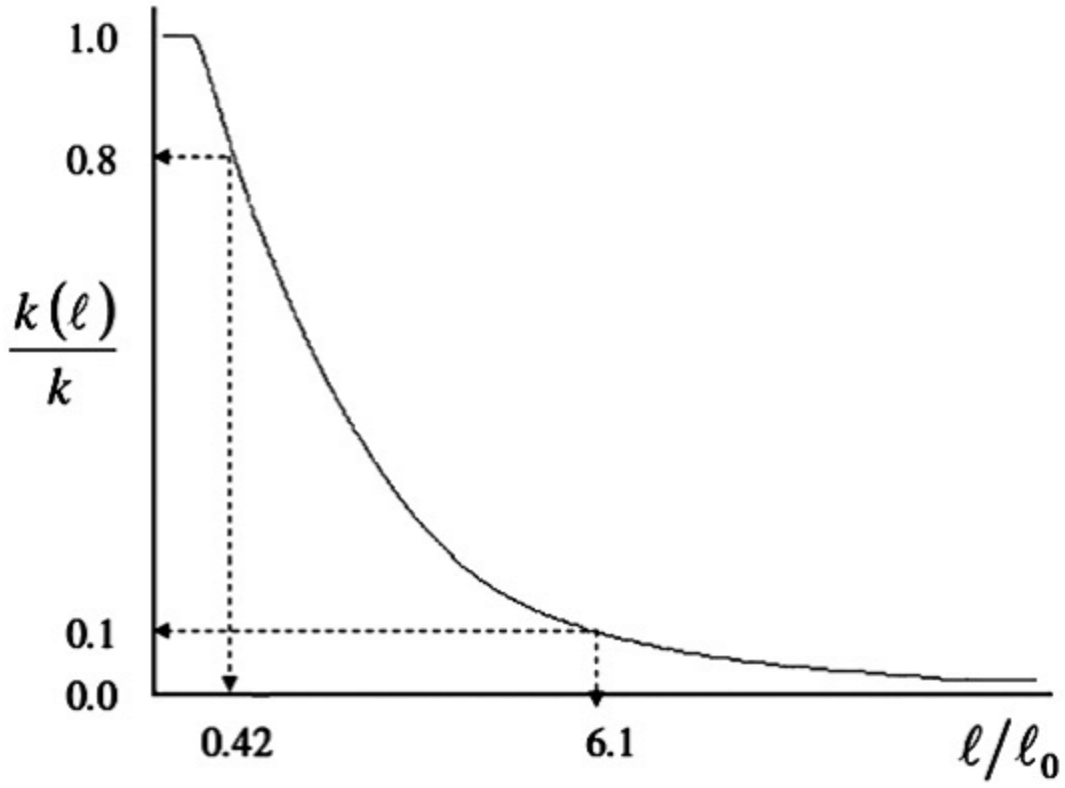

Figure 3.5 Relationship between $k(l)/k$ and l/l_I (Aleksy 2007).

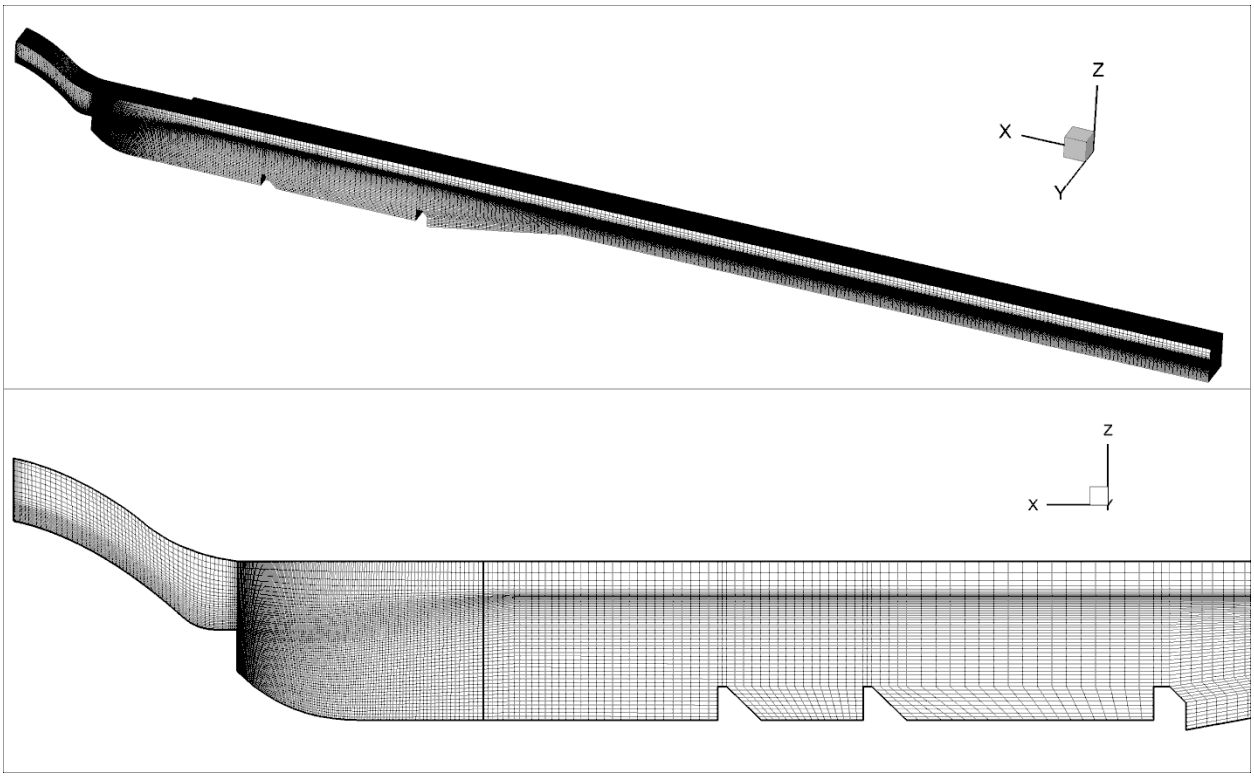

Figure 3.6 Computational mesh for the reduced-scale DES model. Case MT 1.

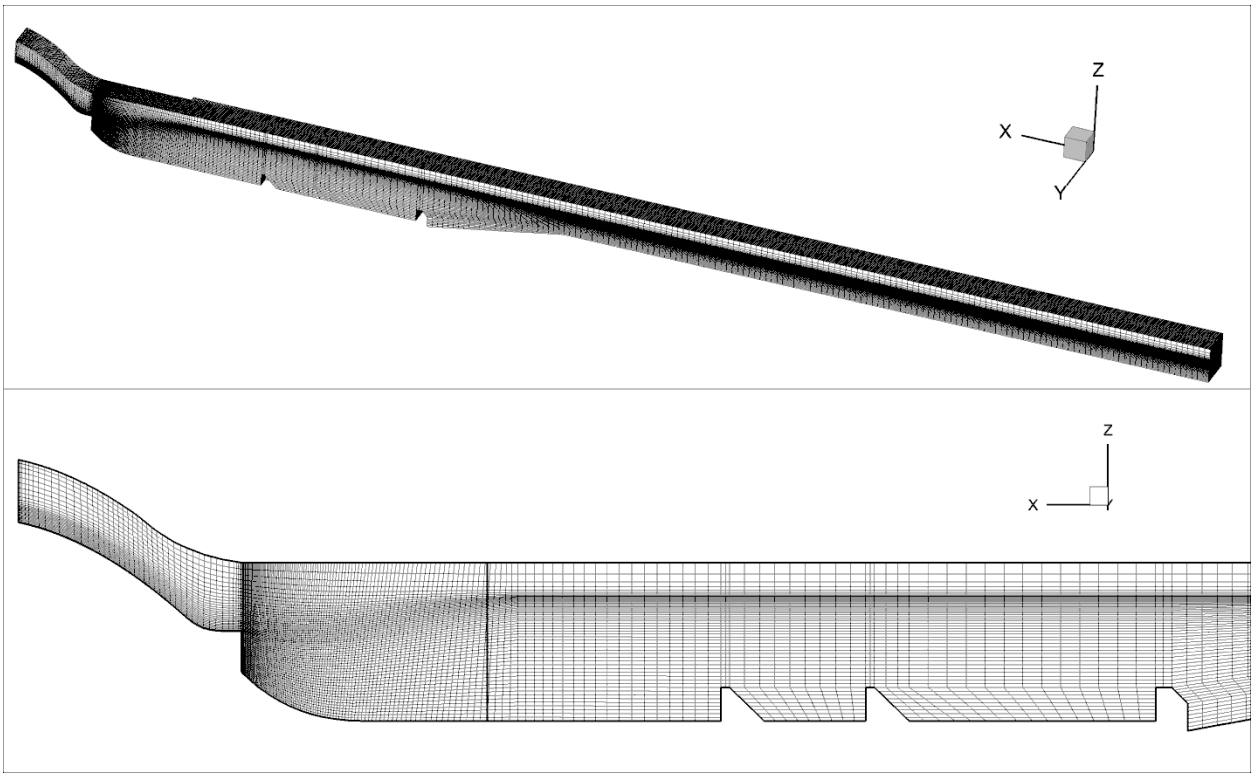

Figure 3.7 Computational mesh for the reduced-scale DES model. Case MT 2.

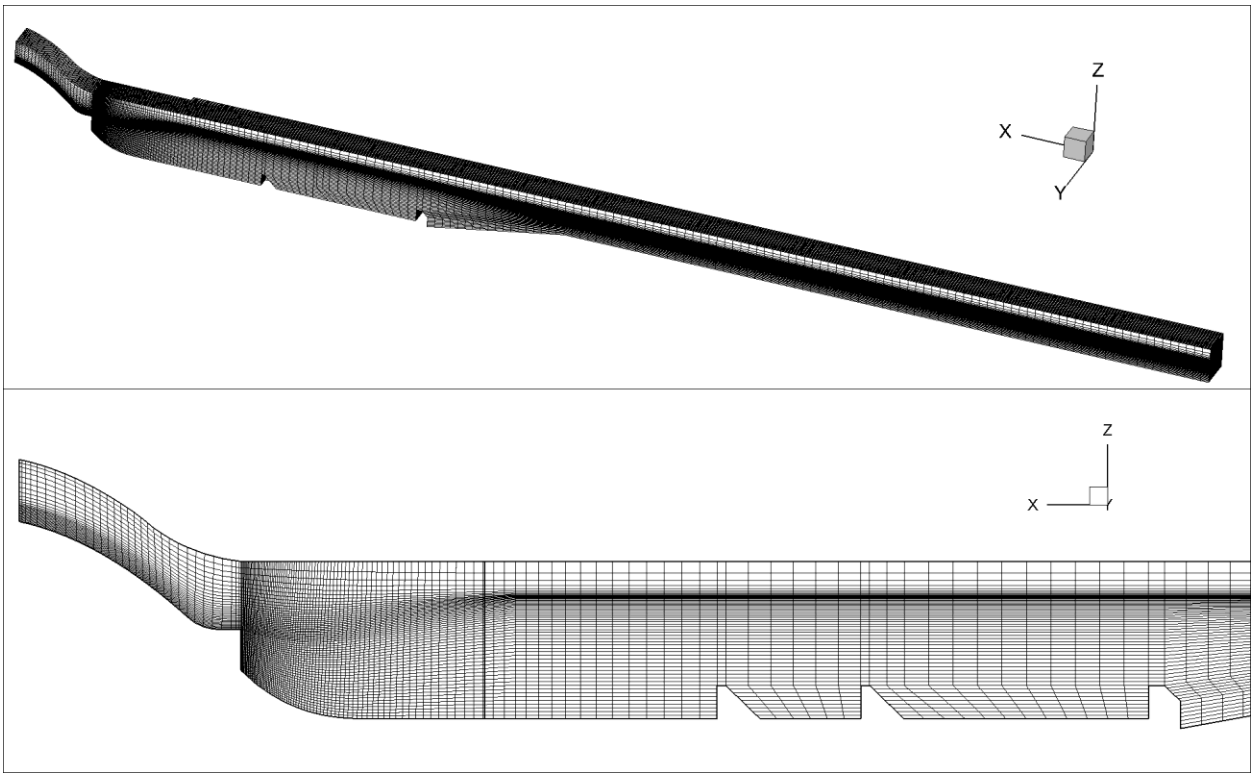

Figure 3.8 Computational mesh for the reduced-scale DES model. Case MT 3.

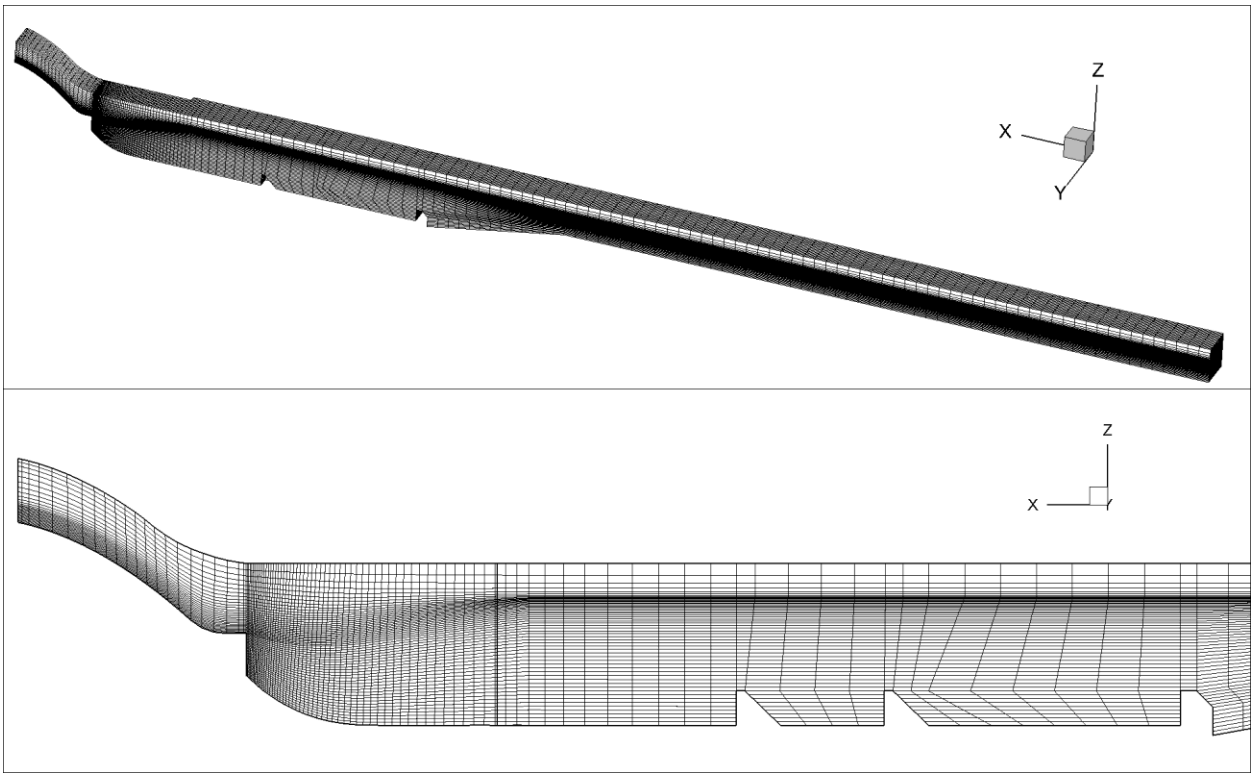

Figure 3.9 Computational mesh for the reduced-scale DES model. Case MT 4.

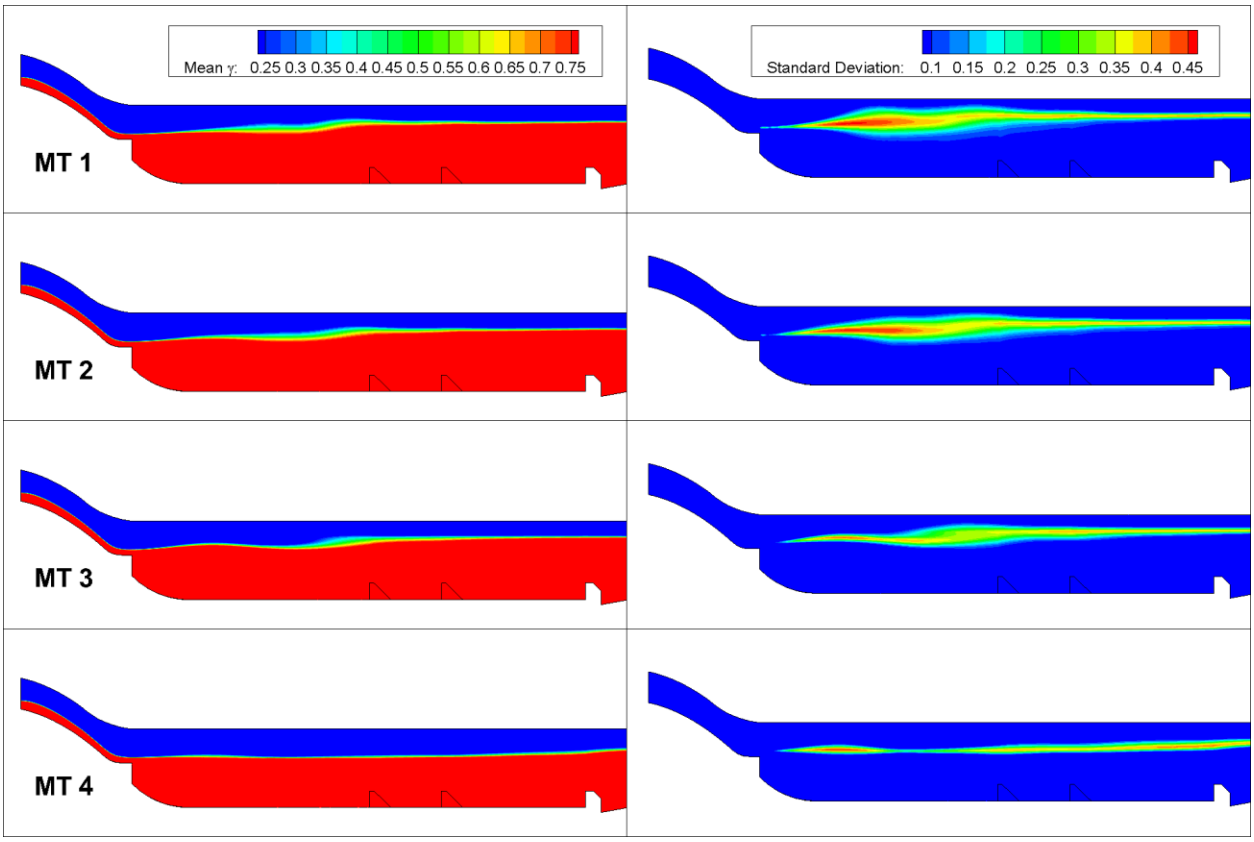

Figure 3.10 Time-averaged volume fraction contours and standard deviations at reduced-scale for cases MT 1 to MT 4.

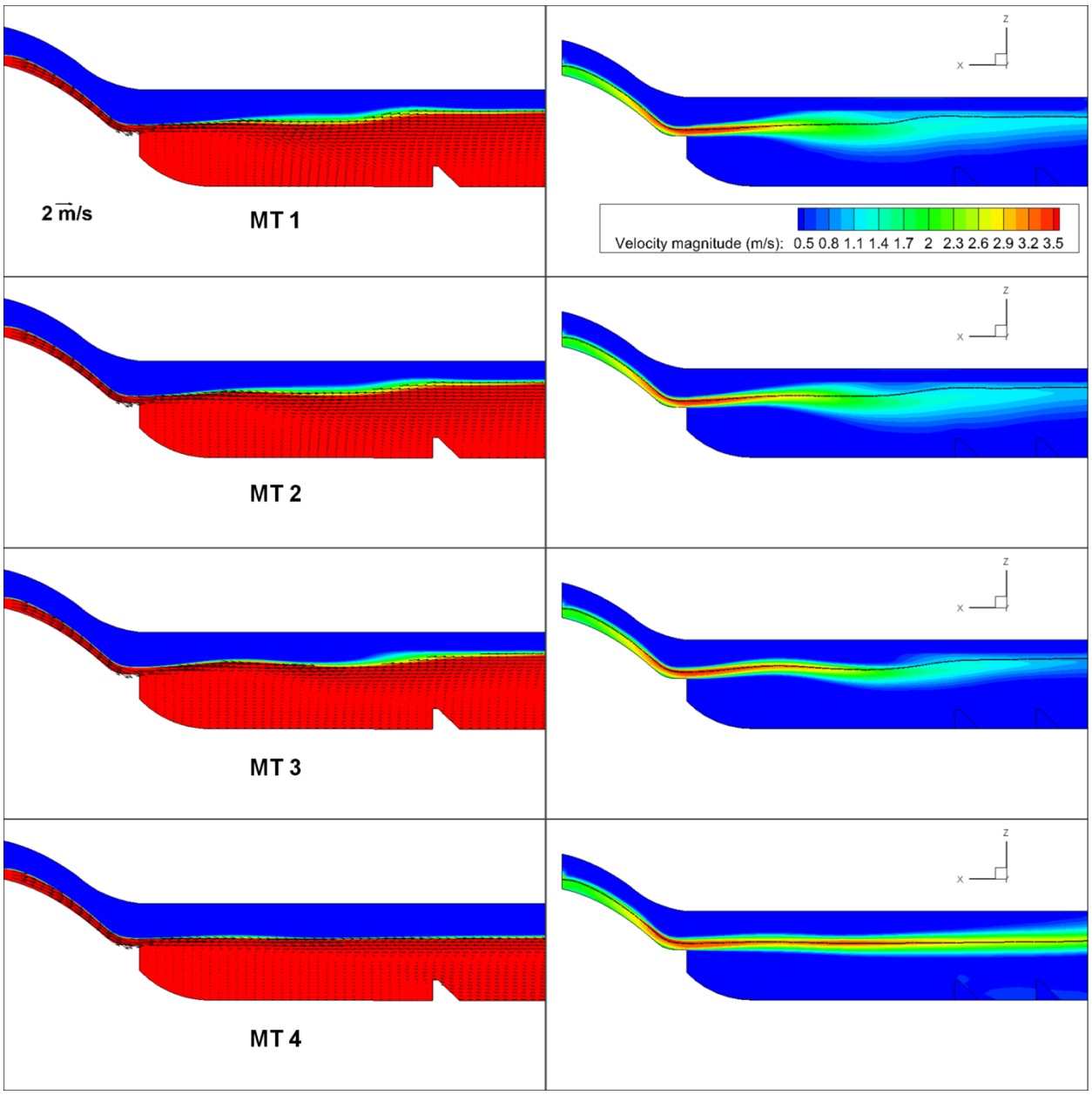

Figure 3.11 Time-averaged velocity magnitude and vectors at reduced-scale for cases MT 1 to MT 4.

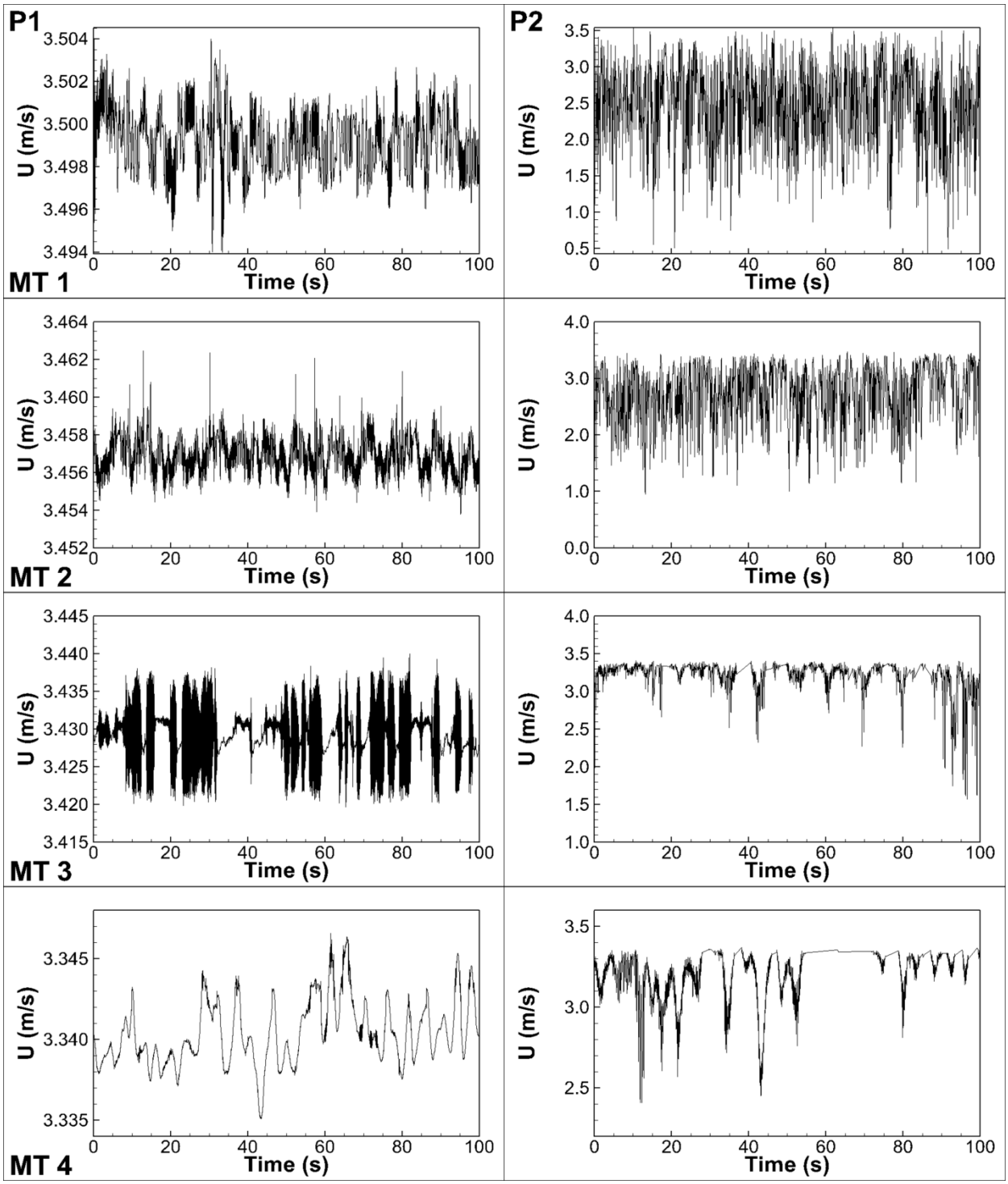

Figure 3.12 Comparison of instantaneous velocity magnitudes at P1 and P2 at reduced-scale for cases MT 1 to MT 4.

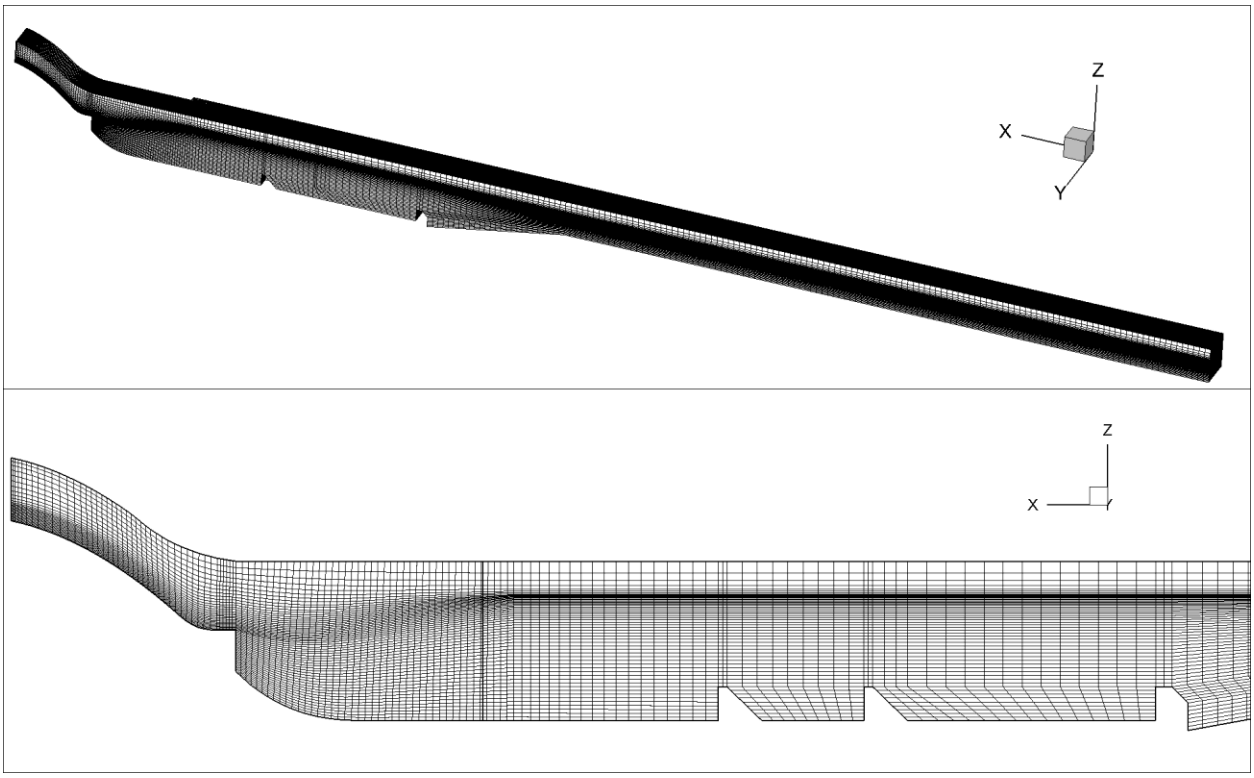

Figure 3.13 Computational mesh at reduced-scale for the DES simulation case MT 5.

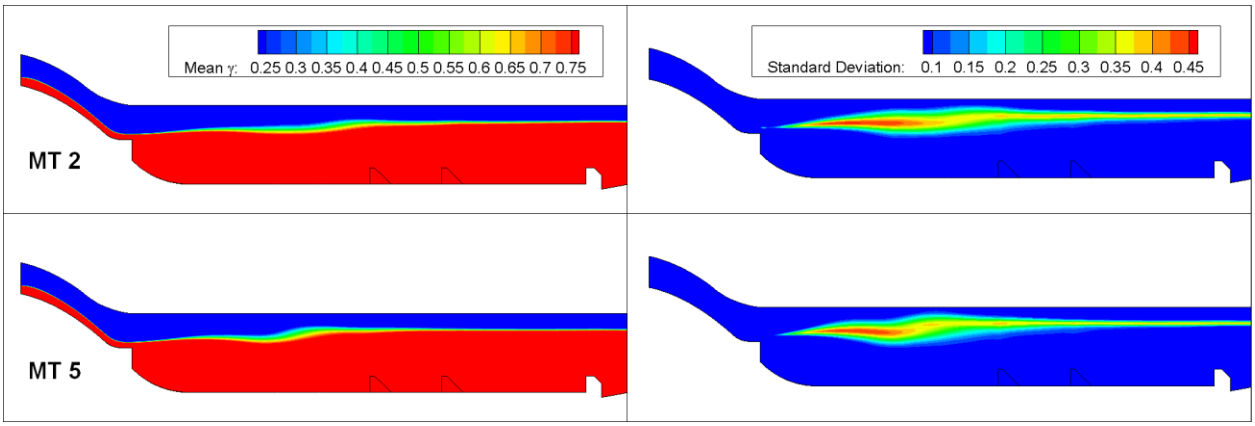

Figure 3.14 Time-averaged volume fraction contours and standard deviations at reduced-scale for cases MT 2 and MT 5

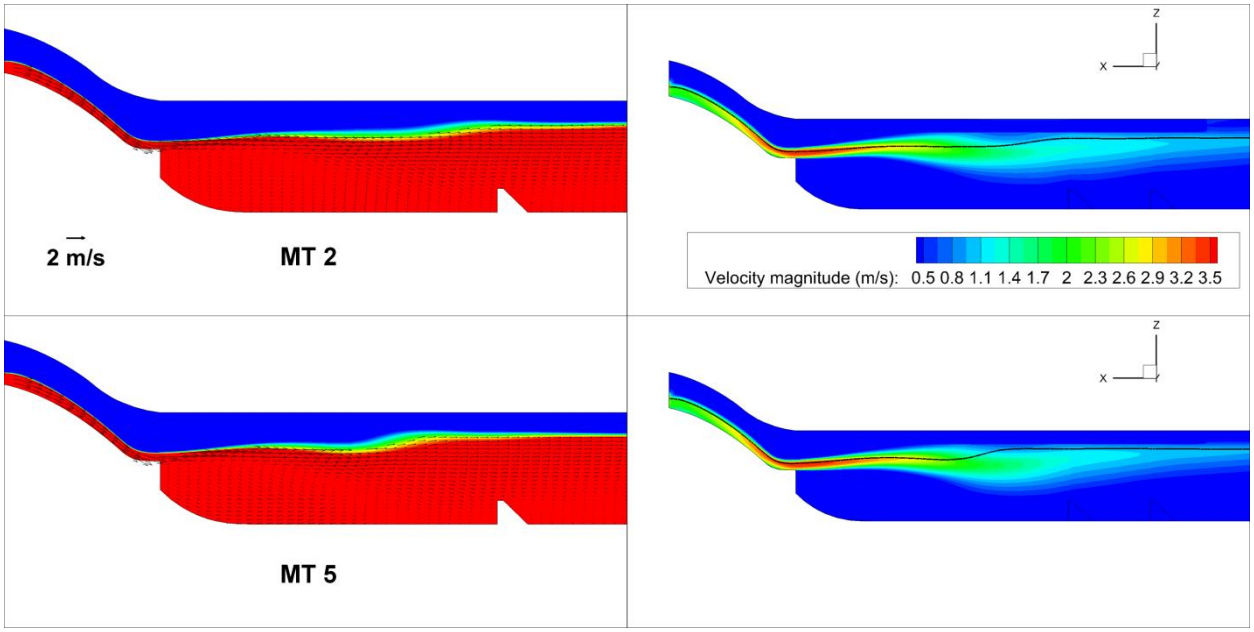

Figure 3.15 Time-averaged velocity magnitude and vectors at reduced-scale for cases MT 2 and MT 5

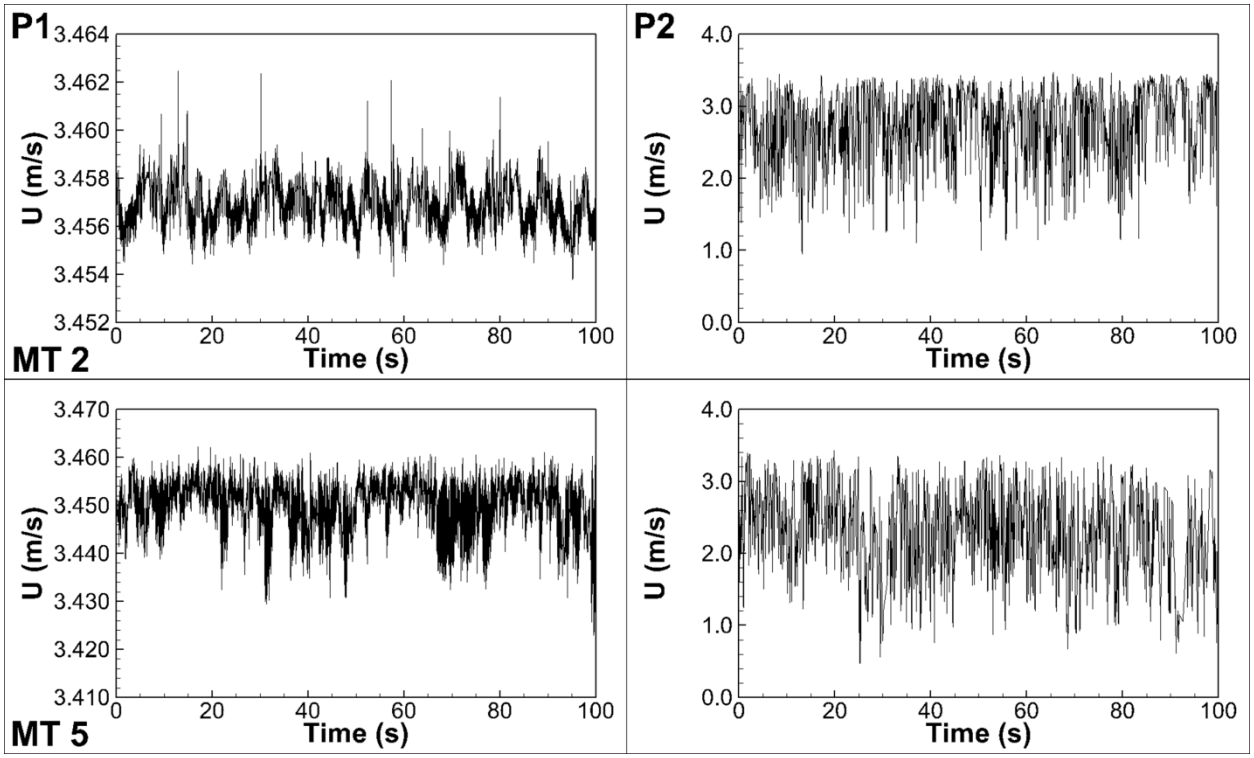

Figure 3.16 Instantaneous velocity magnitudes at P1 and P2 at reduced-scale for cases MT 2 and MT 5

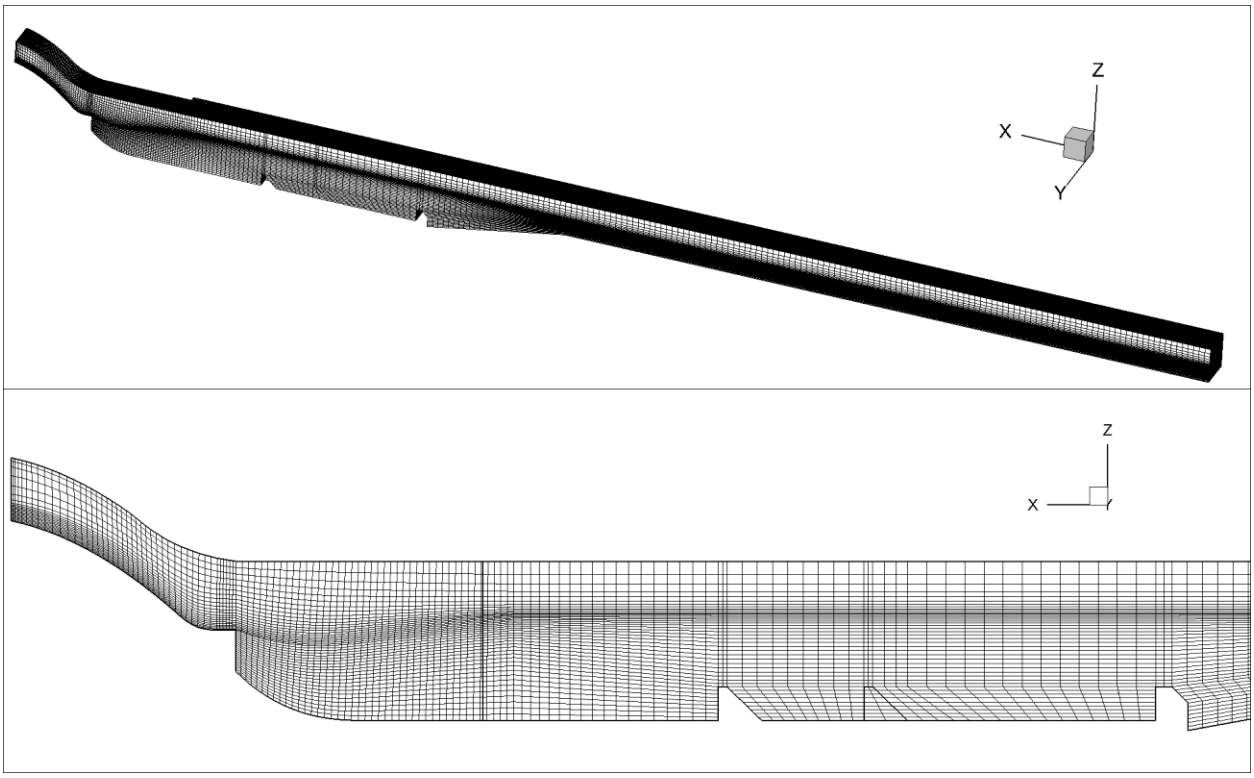

Figure 3.17 Computational mesh at reduced-scale for DES simulation case FR 1

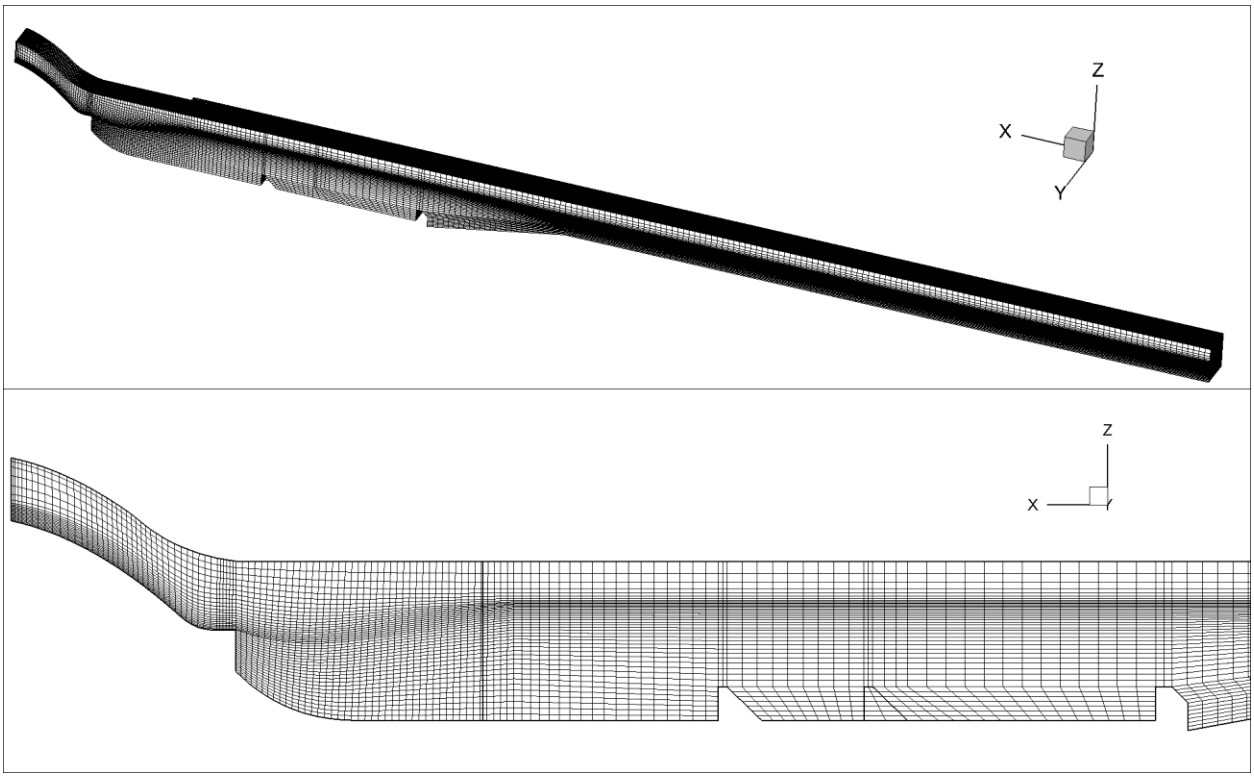

Figure 3.18 Computational mesh at reduced-scale for DES simulation case FR 2

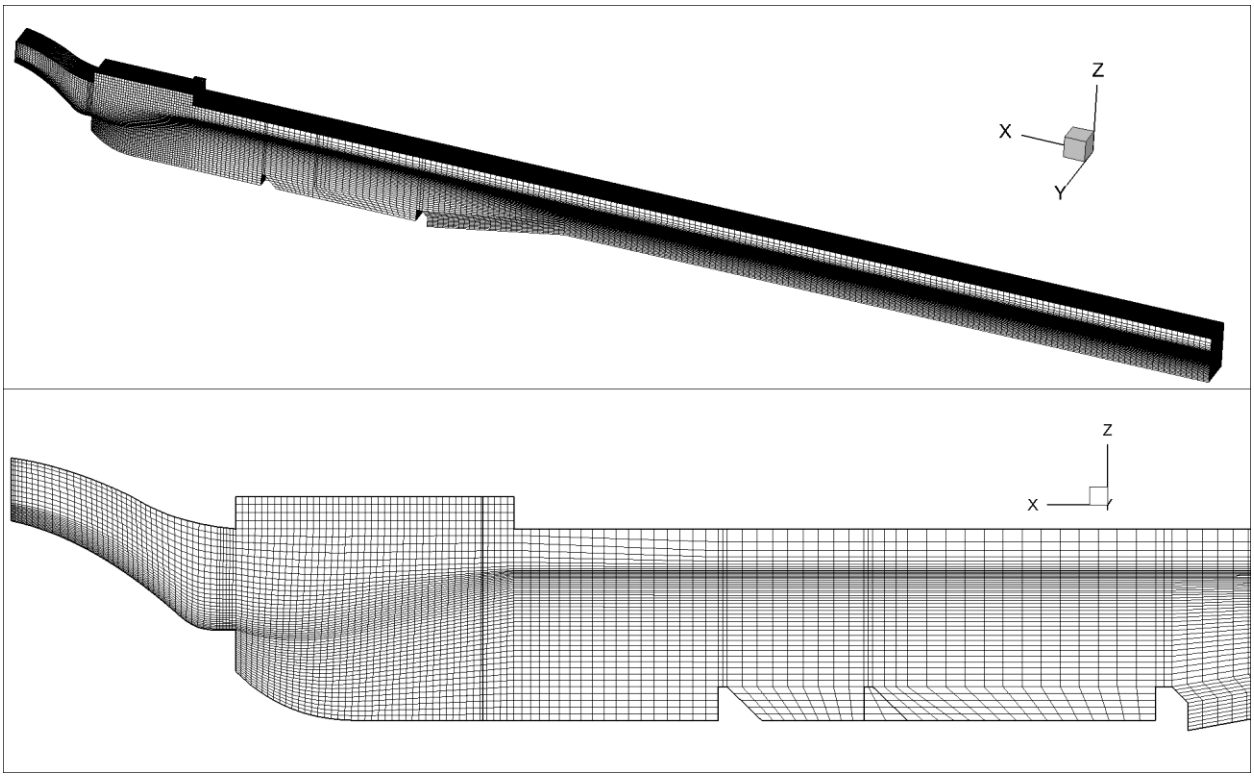

Figure 3.19 Computational mesh at reduced-scale for DES simulation case FR 3

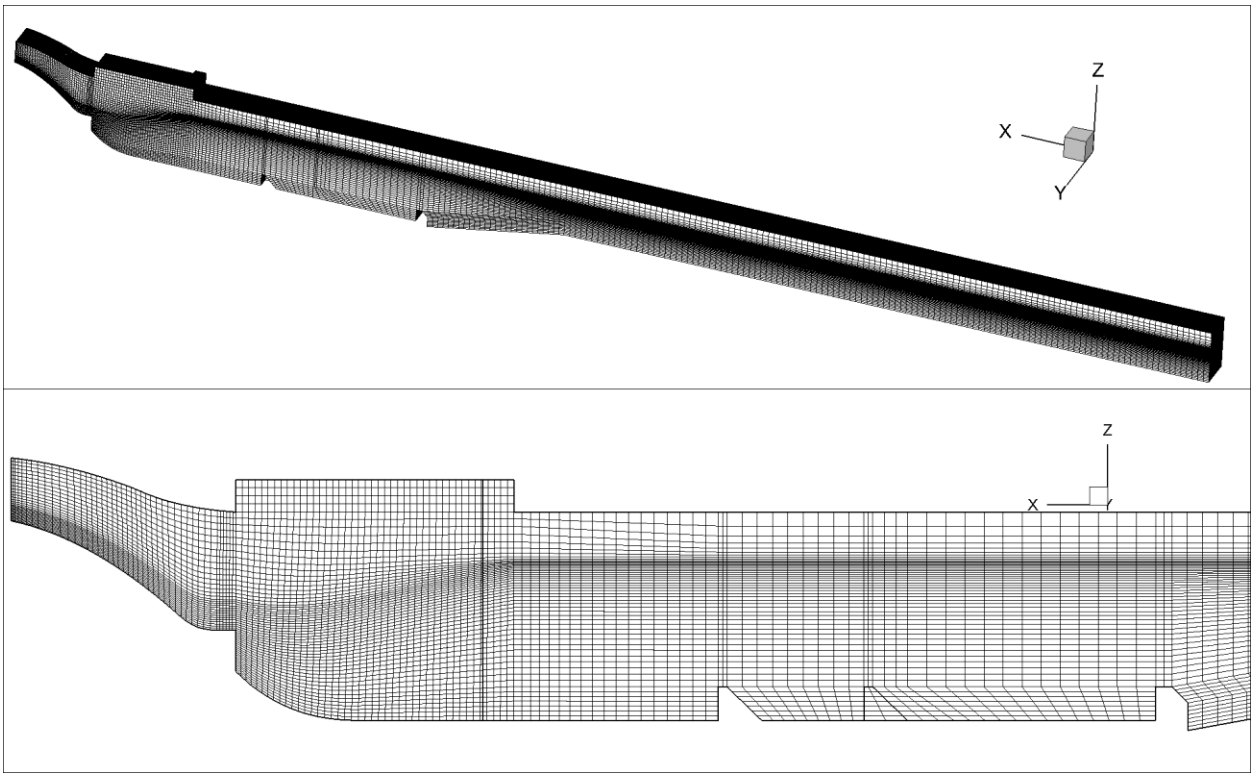

Figure 3.20 Computational mesh at reduced-scale for DES simulation case FR 4

1) Submergence 1.7 m (5.50 ft). Plunging flow.

2) Submergence 5.6 m (18.50 ft). Undular flow.

3) Submergence 6.6 m (21.50 ft). Hydraulic jump.

Bay 21 Deflector Performance; Test 3c-1
DL = 3.8 m (12.5 ft); R = 4.6 m (15.0 ft)
SB = 69.5 m (228.0 ft); TR = 75.1 m (246.5 ft)
Q = 255 m^3/s/bay (9,000 cfs/bay)

PHOTO PLATE 4-6

Figure 3.21 Photos for different flow regimes in the reduced-scale laboratory model (NHC 2001)

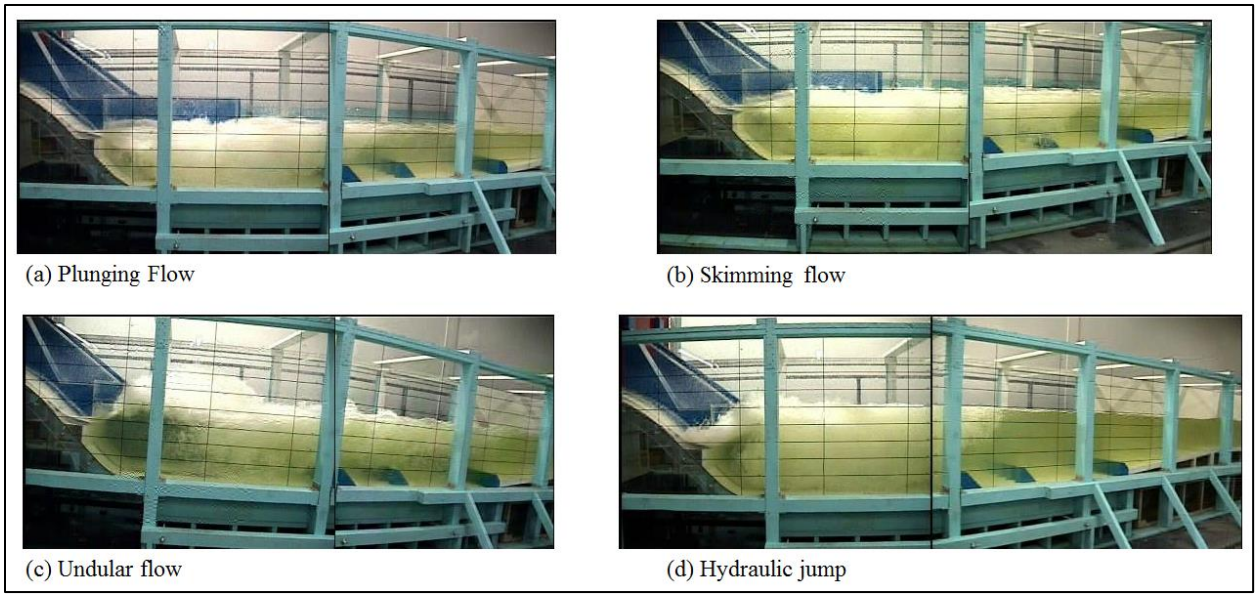

Figure 3.22 Photos for different flow regimes in the reduced-scale laboratory model extracted from video clip

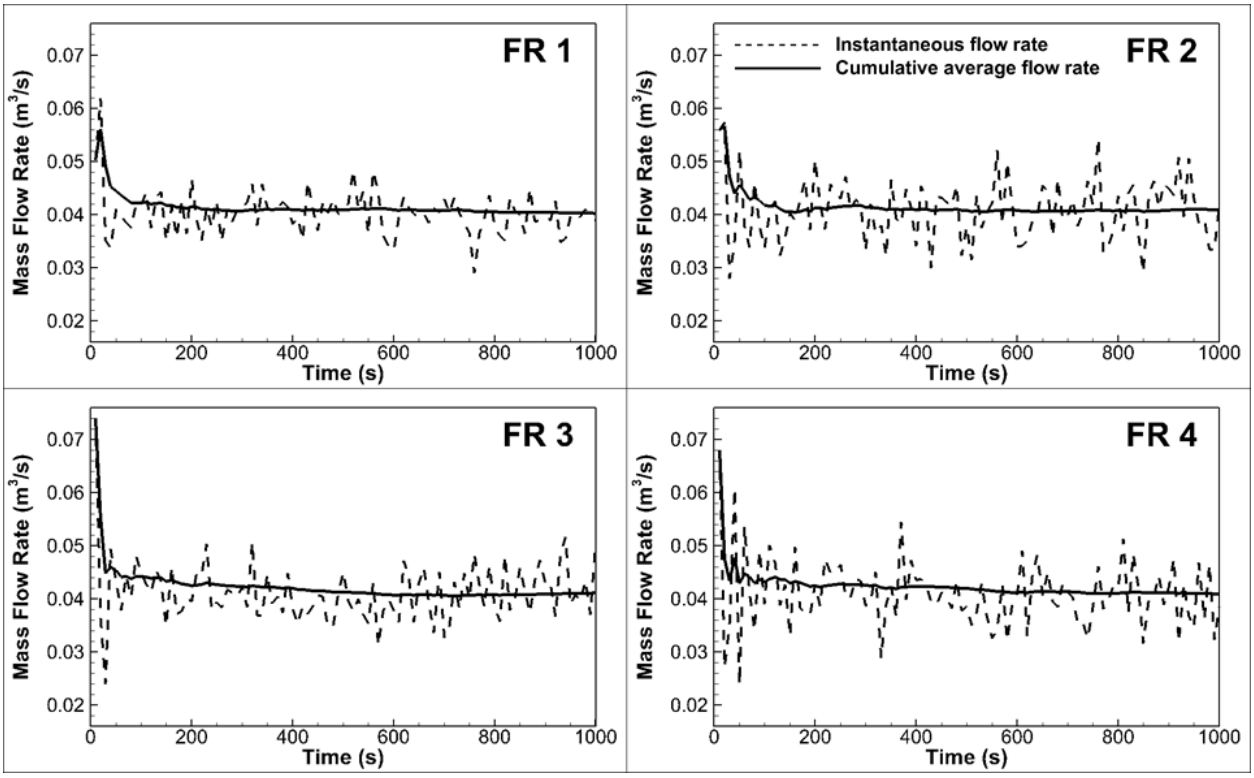

Figure 3.23 Evolution of the flow rate at the downstream end at reduced-scale for cases FR 1 to FR 4

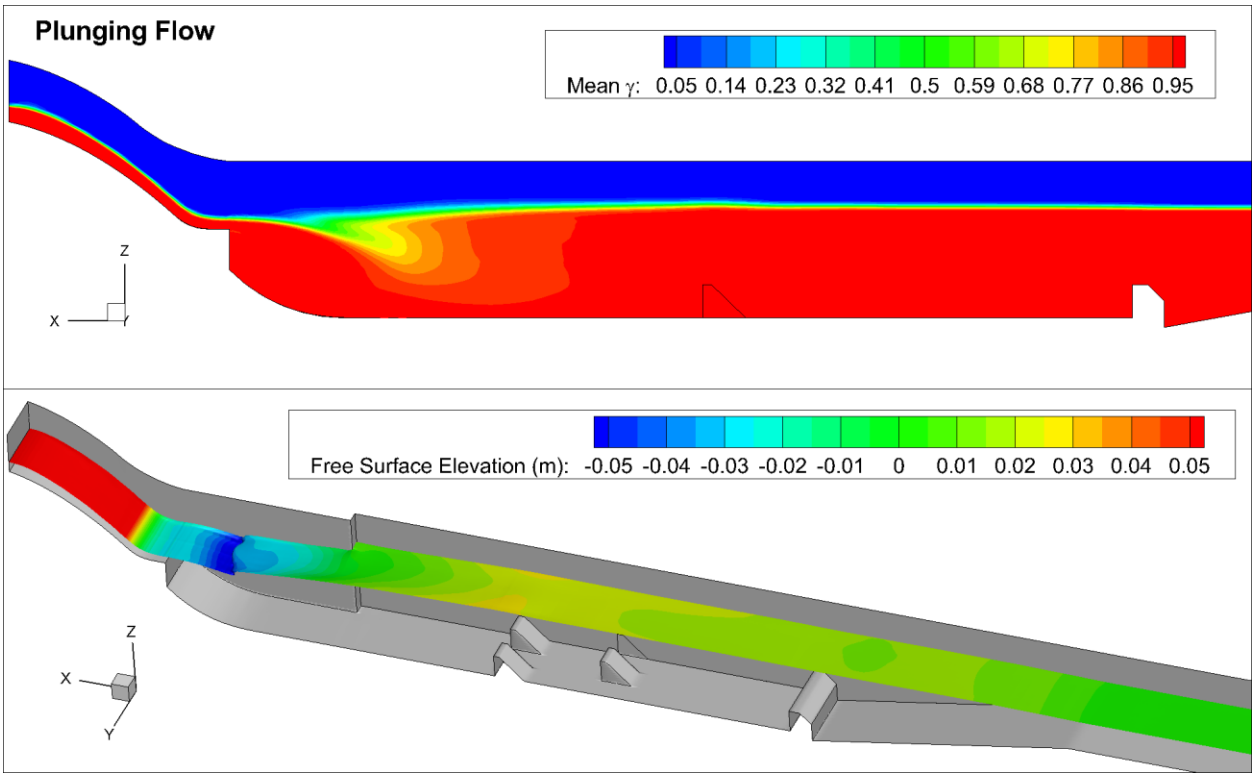

Figure 3.24 Time-averaged volume fraction contours and iso-surface colored by free surface elevation at reduced-scale for case FR 1

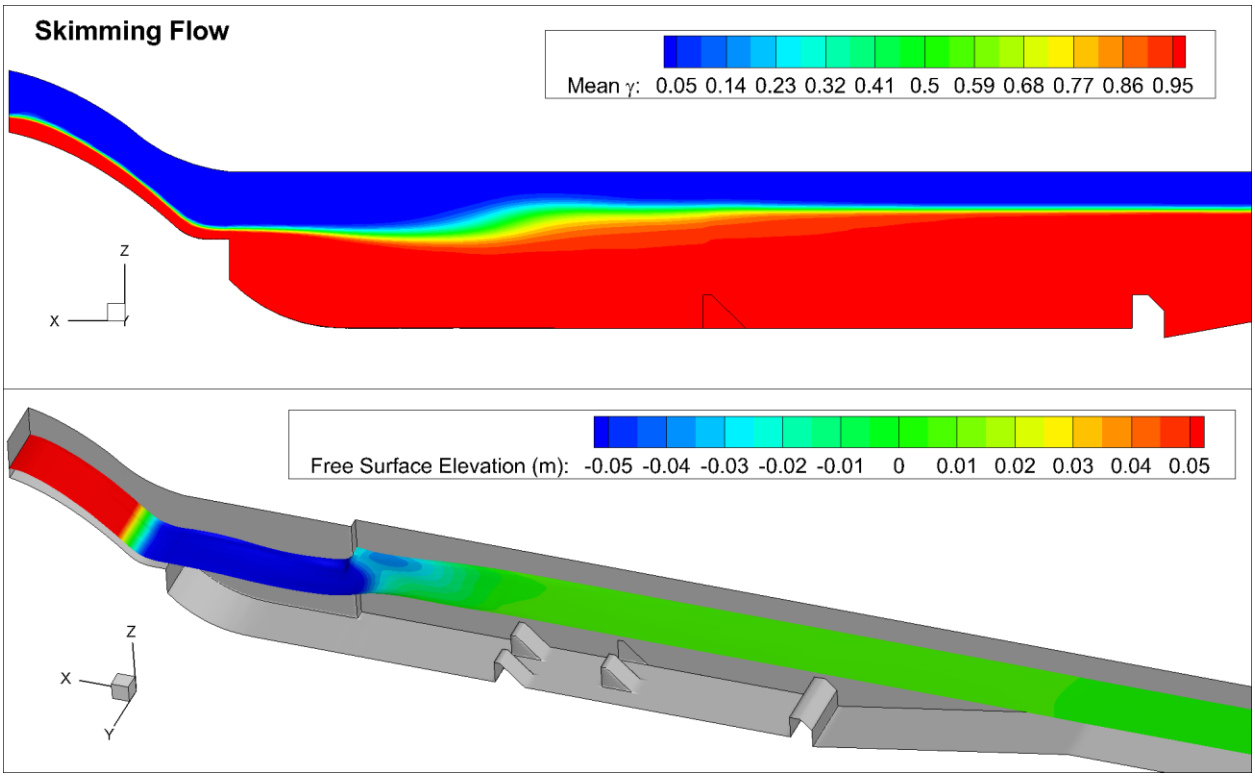

Figure 3.25 Time-averaged volume fraction contours and iso-surface colored by free surface elevation at reduced-scale for case FR 2

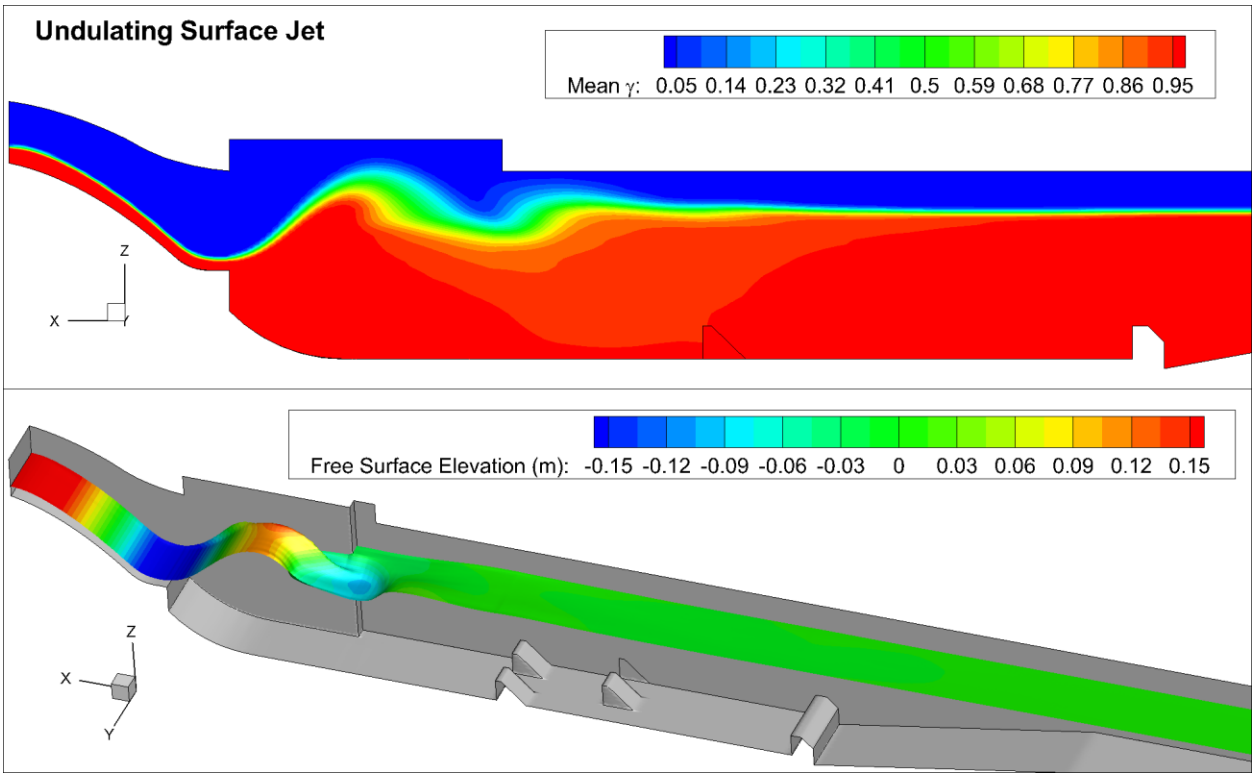

Figure 3.26 Time-averaged volume fraction contours and iso-surface colored by free surface elevation at reduced-scale for case FR 3

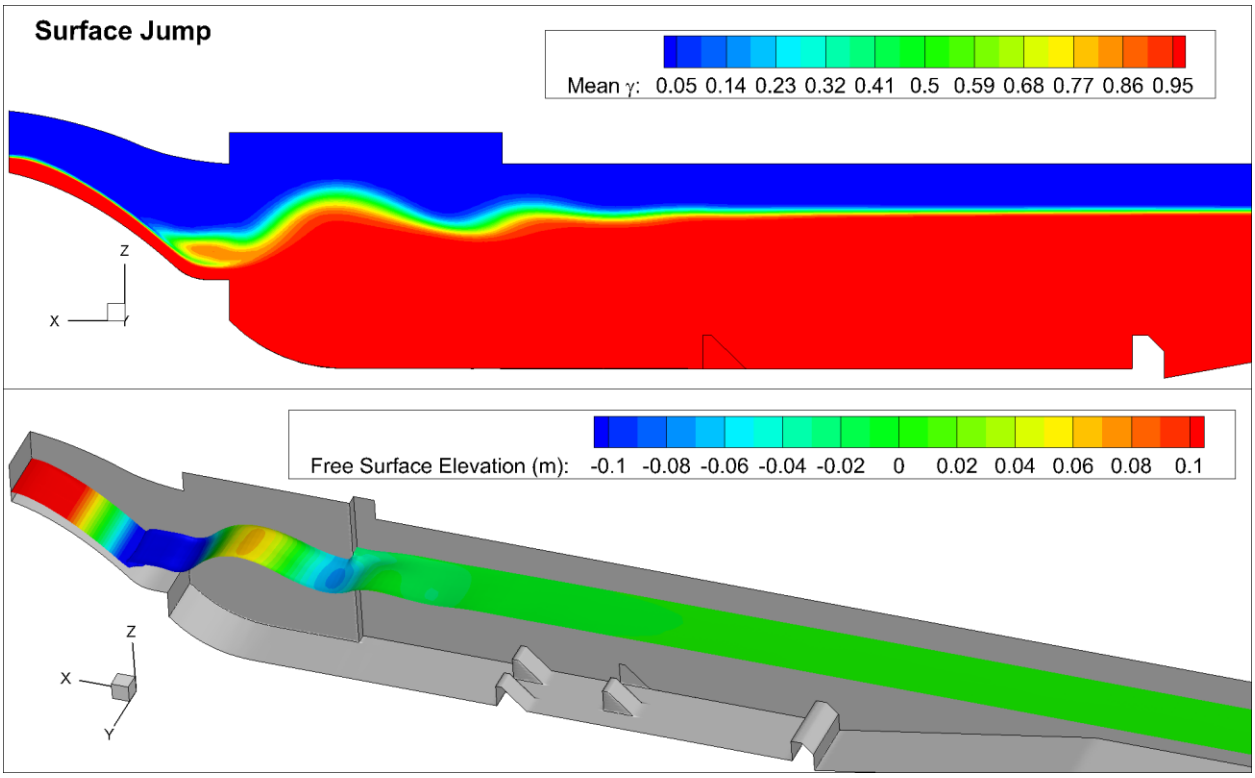

Figure 3.27 Time-averaged volume fraction contours and iso-surface colored by free surface elevation at reduced-scale for case FR 4

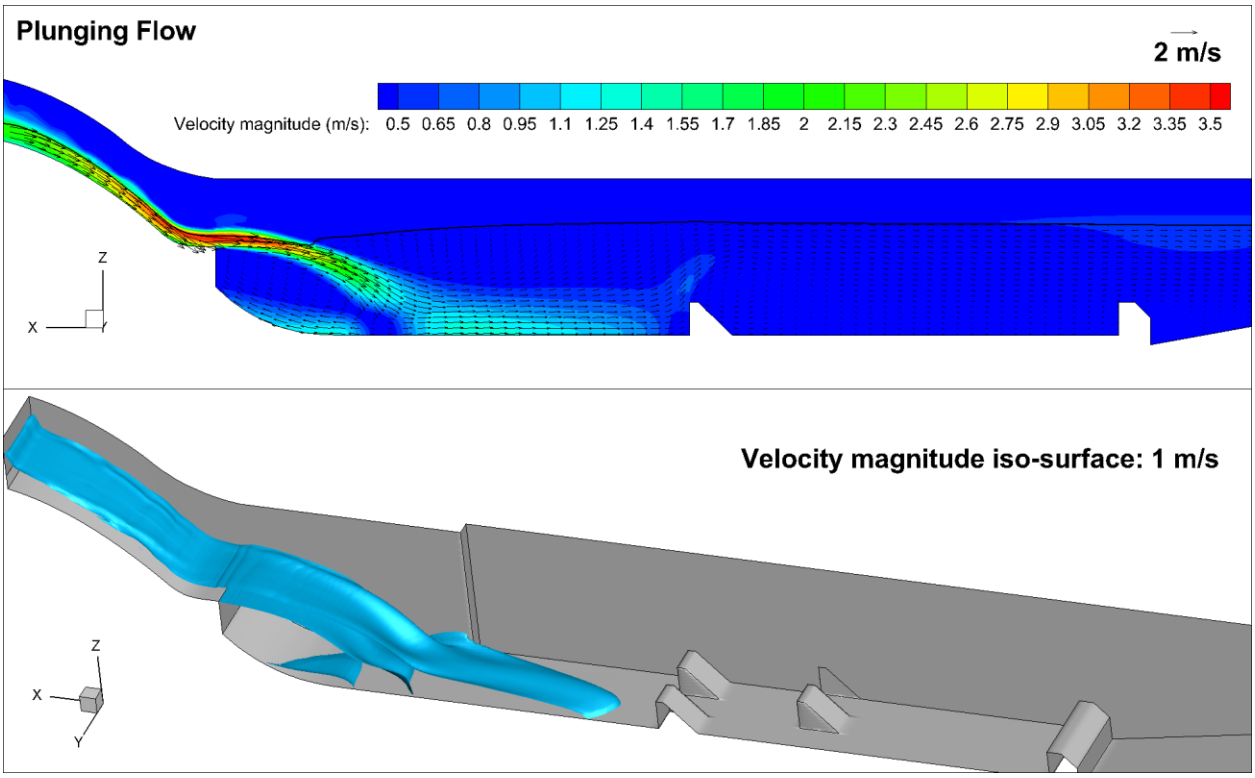

Figure 3.28 Time-averaged velocity magnitude and iso-surface at reduced-scale for case FR 1

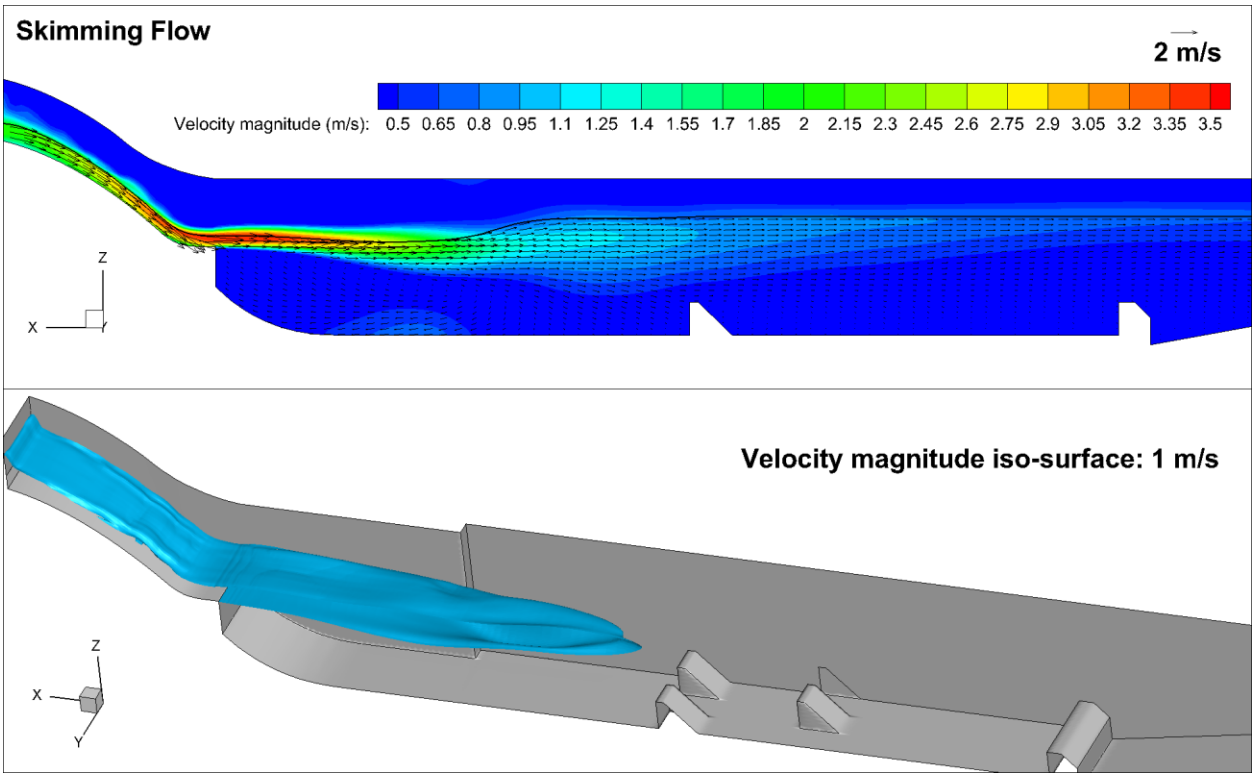

Figure 3.29 Time-averaged velocity magnitude and iso-surface at reduced-scale for case FR 2

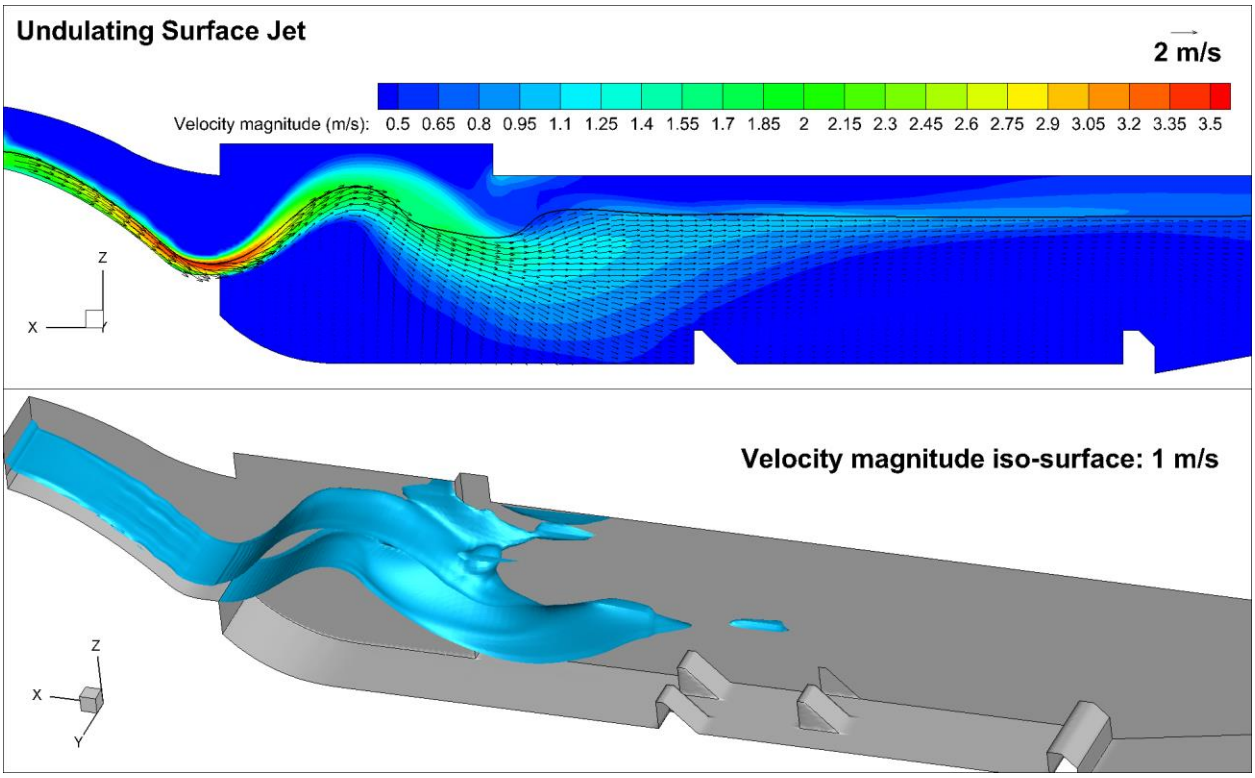

Figure 3.30 Time-averaged velocity magnitude and iso-surface at reduced-scale for case FR 3

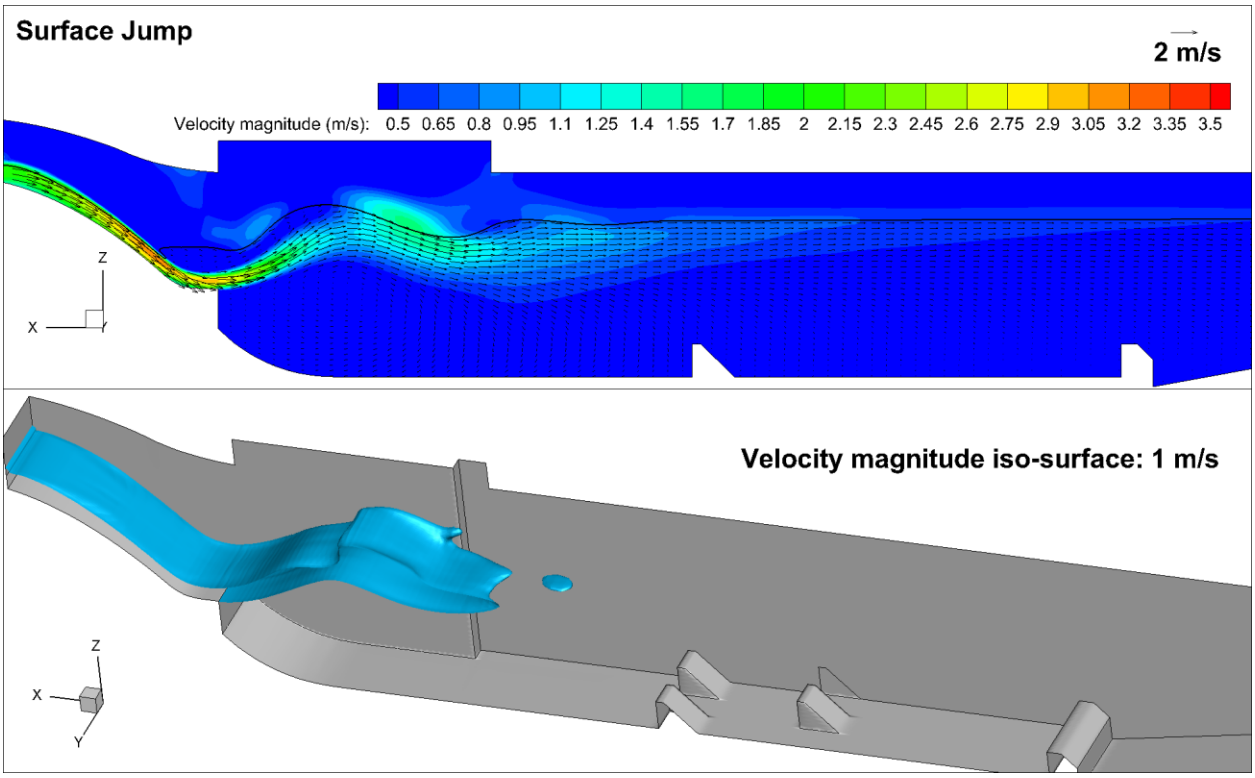

Figure 3.31 Time-averaged velocity magnitude and iso-surface at reduced-scale for case FR 4

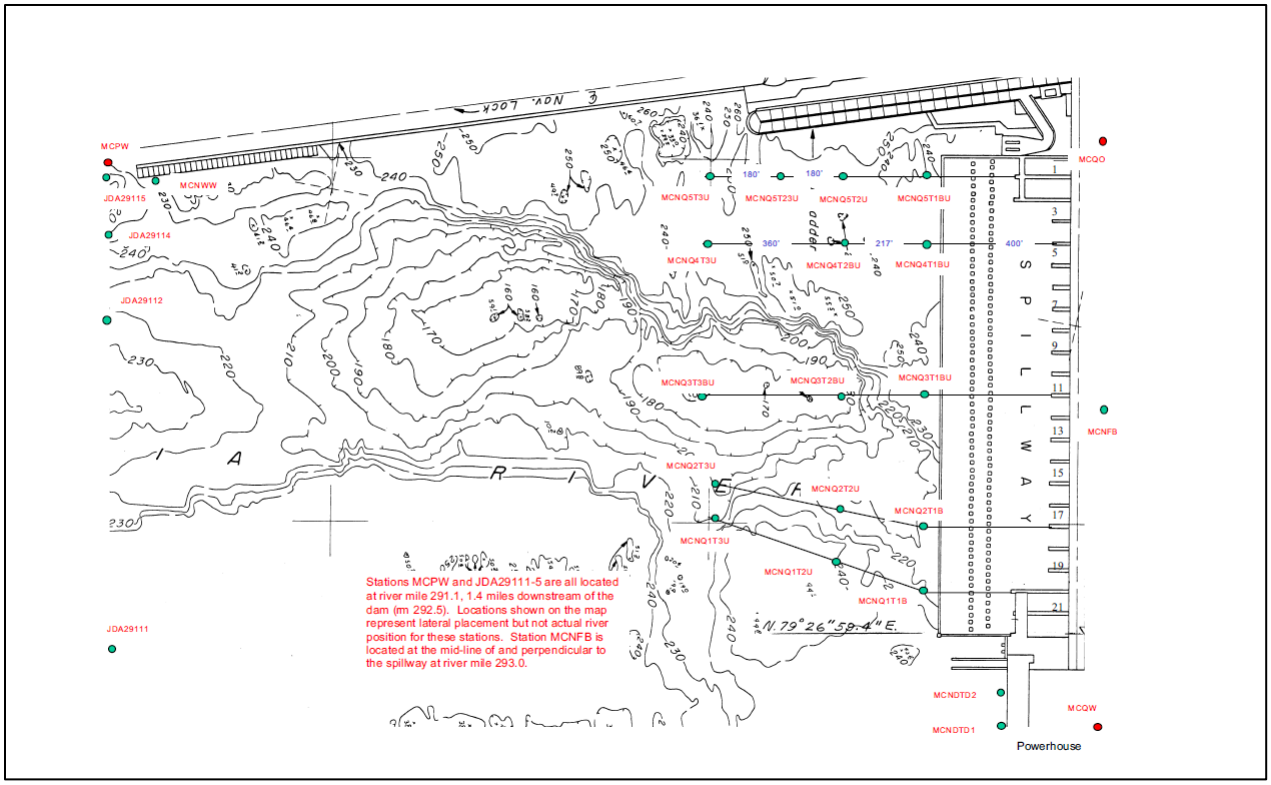

Figure 3.32 Bathymetry and TDG instrument locations during the TDG field study (Wilhelms 1997)

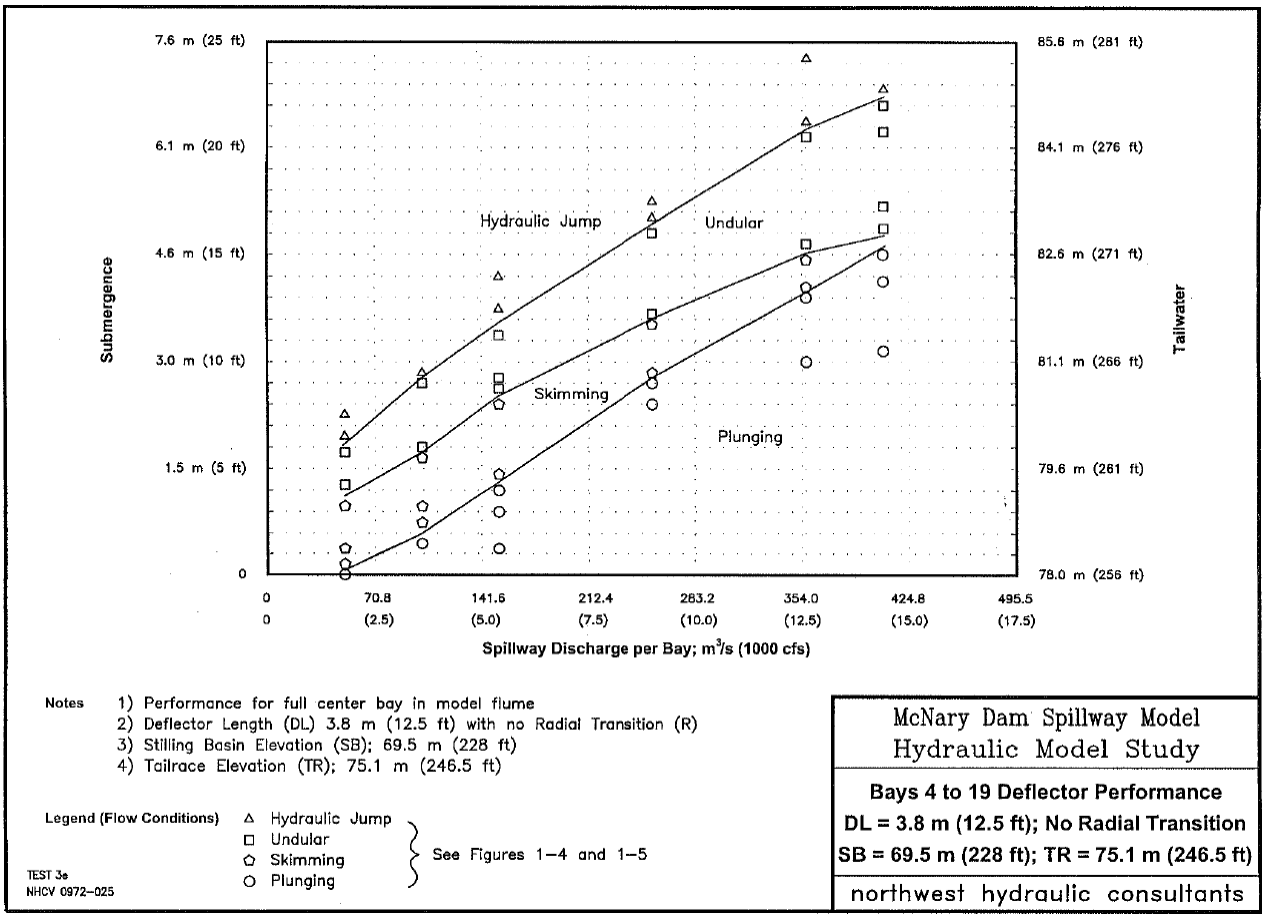

Figure 3.33 McNary Dam spillway deflector performance curve (NHC 2001)

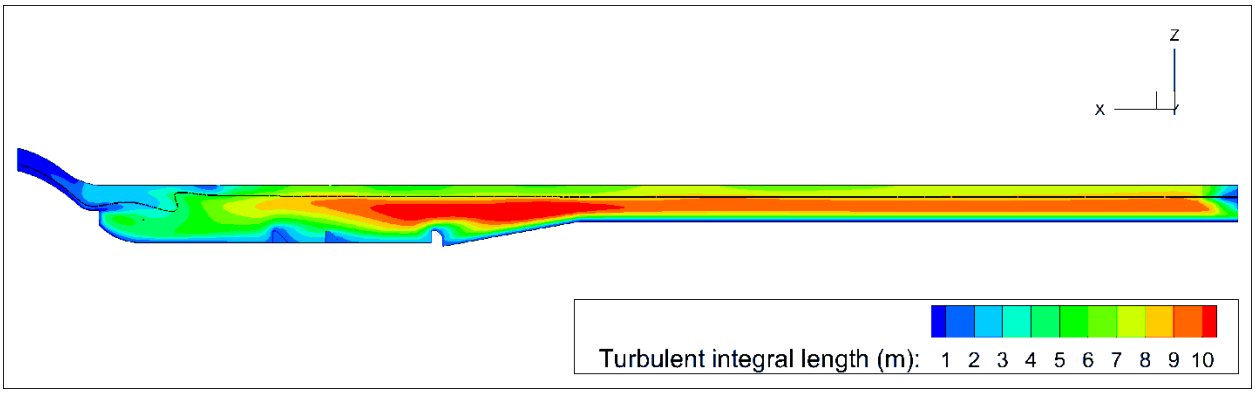

Figure 3.34 Time-averaged turbulent integral length at prototype-scale

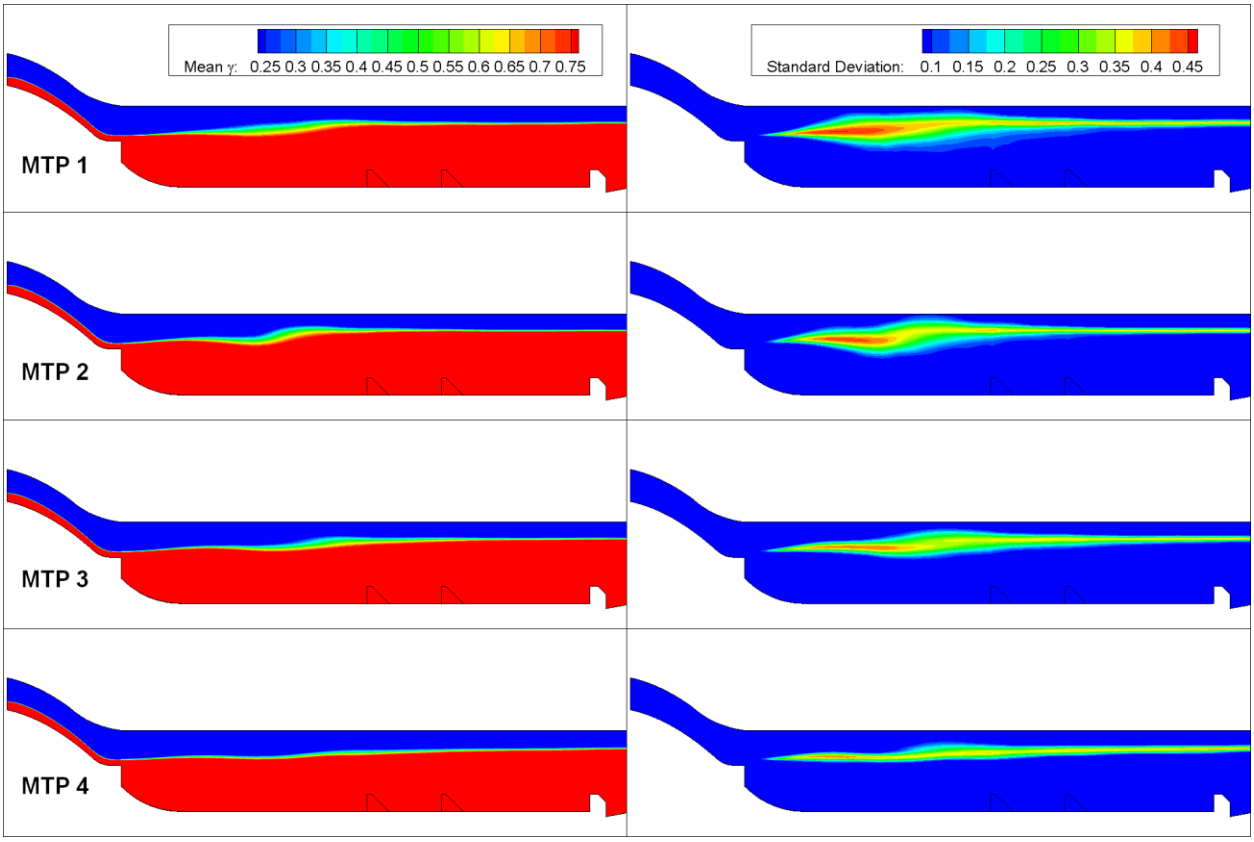

Figure 3.35 Time-averaged volume fraction contours and standard deviations at prototype-scale for cases MTP 1 to MTP 4

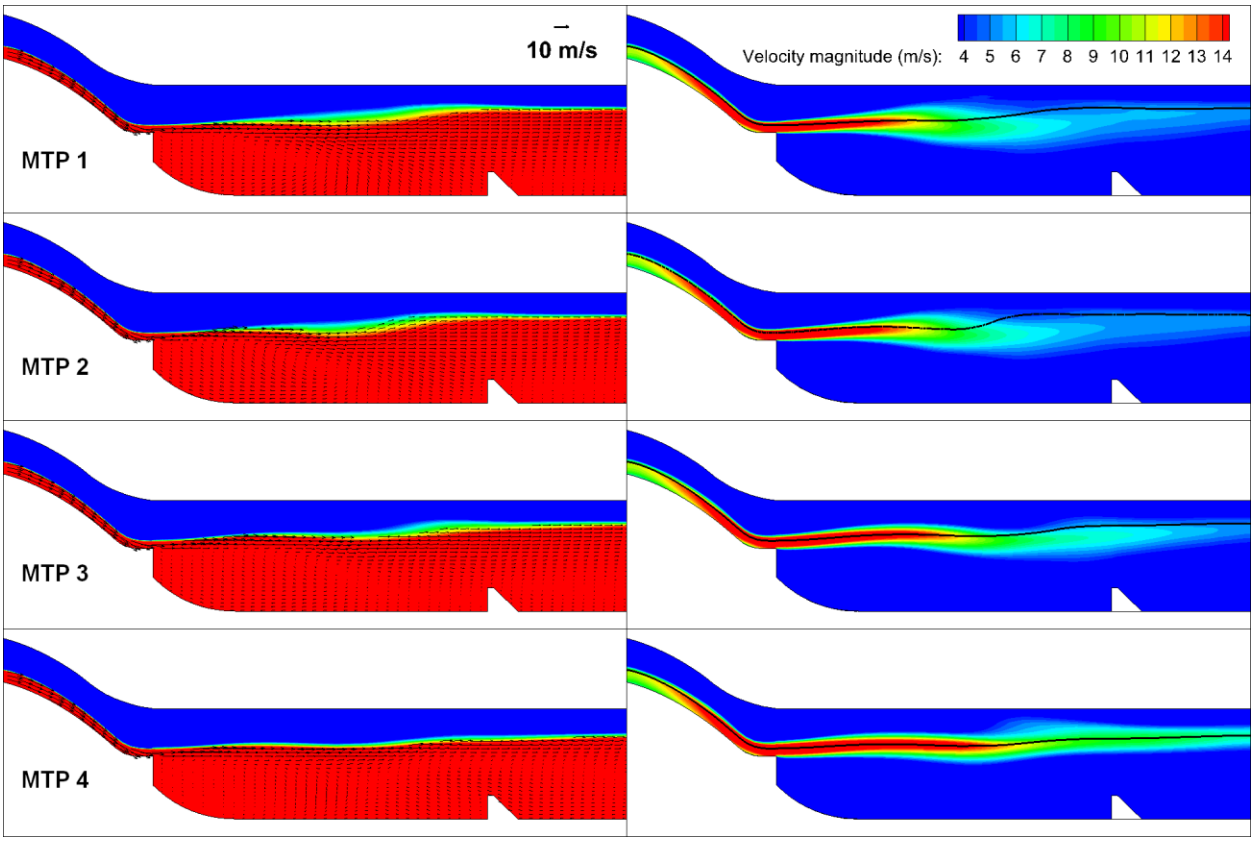

Figure 3.36 Time-averaged velocity magnitude and vectors at prototype-scale for cases MTP 1 to MTP 4

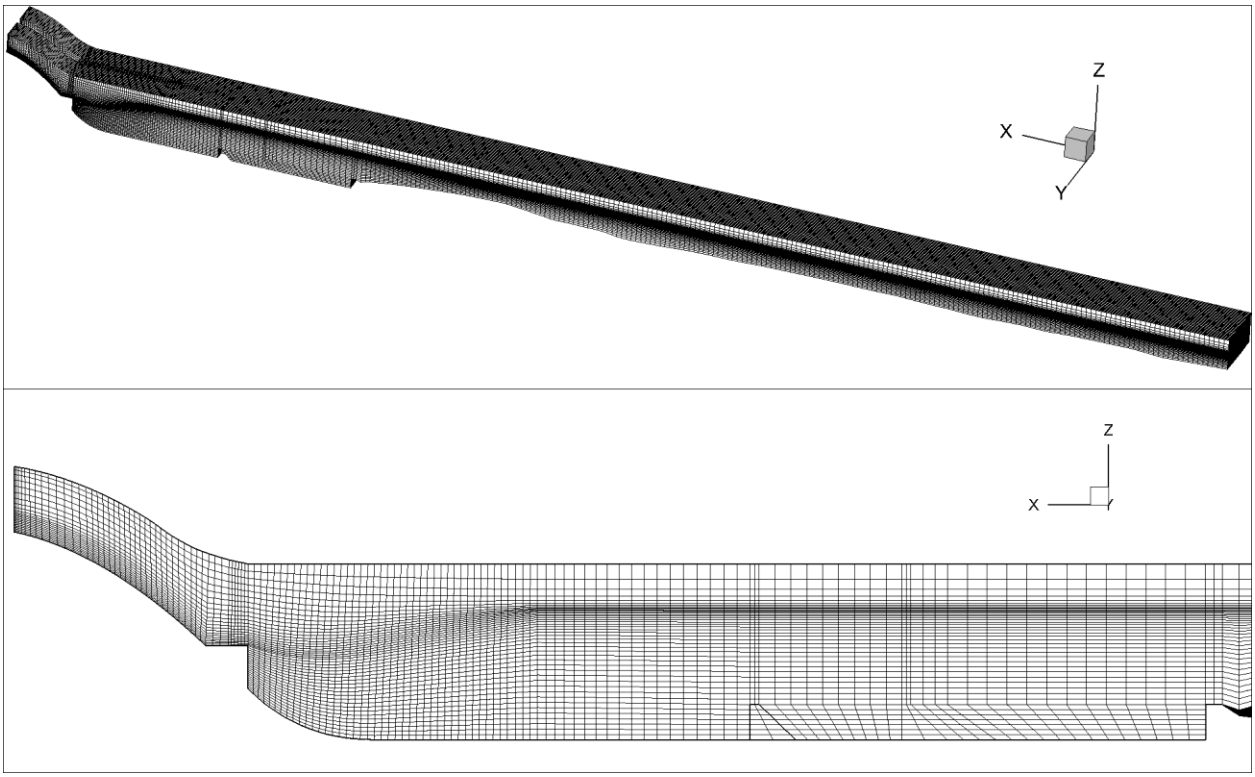

Figure 3.37 Computational mesh at prototype-scale for DES case TD 1

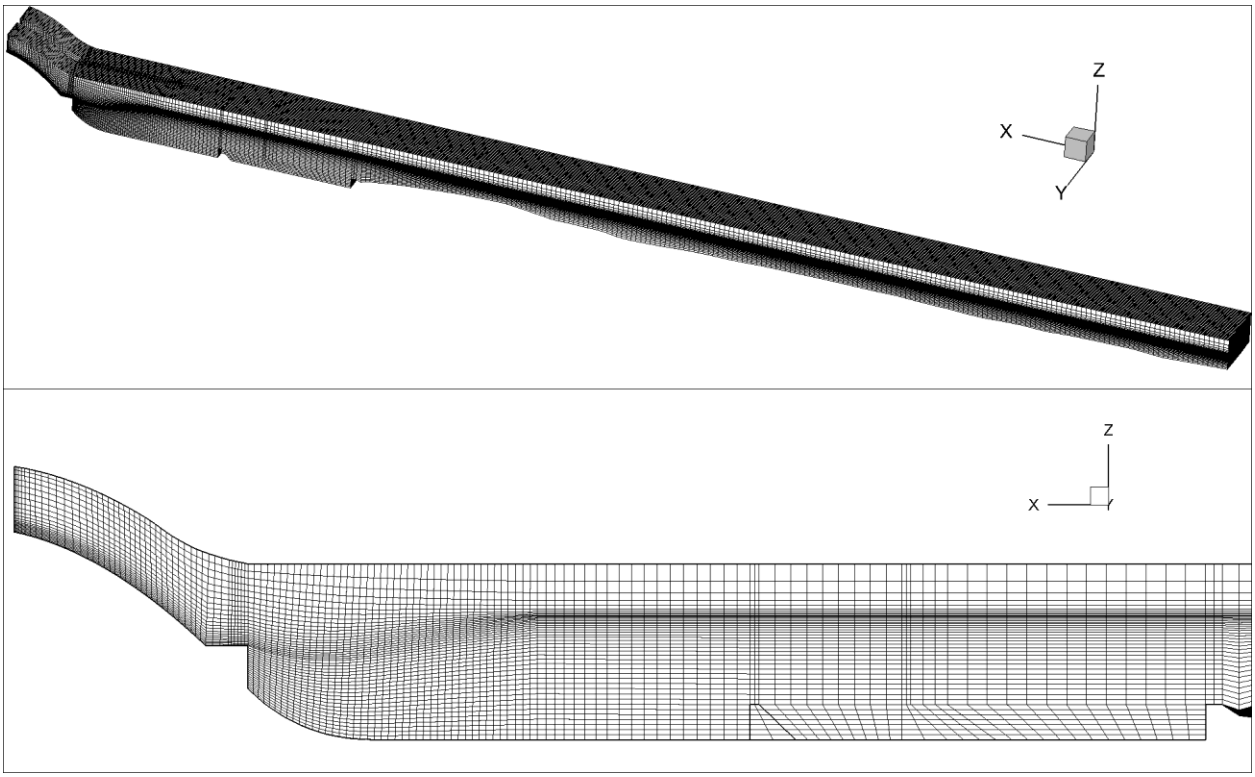

Figure 3.38 Computational mesh at prototype-scale for DES case TD 2

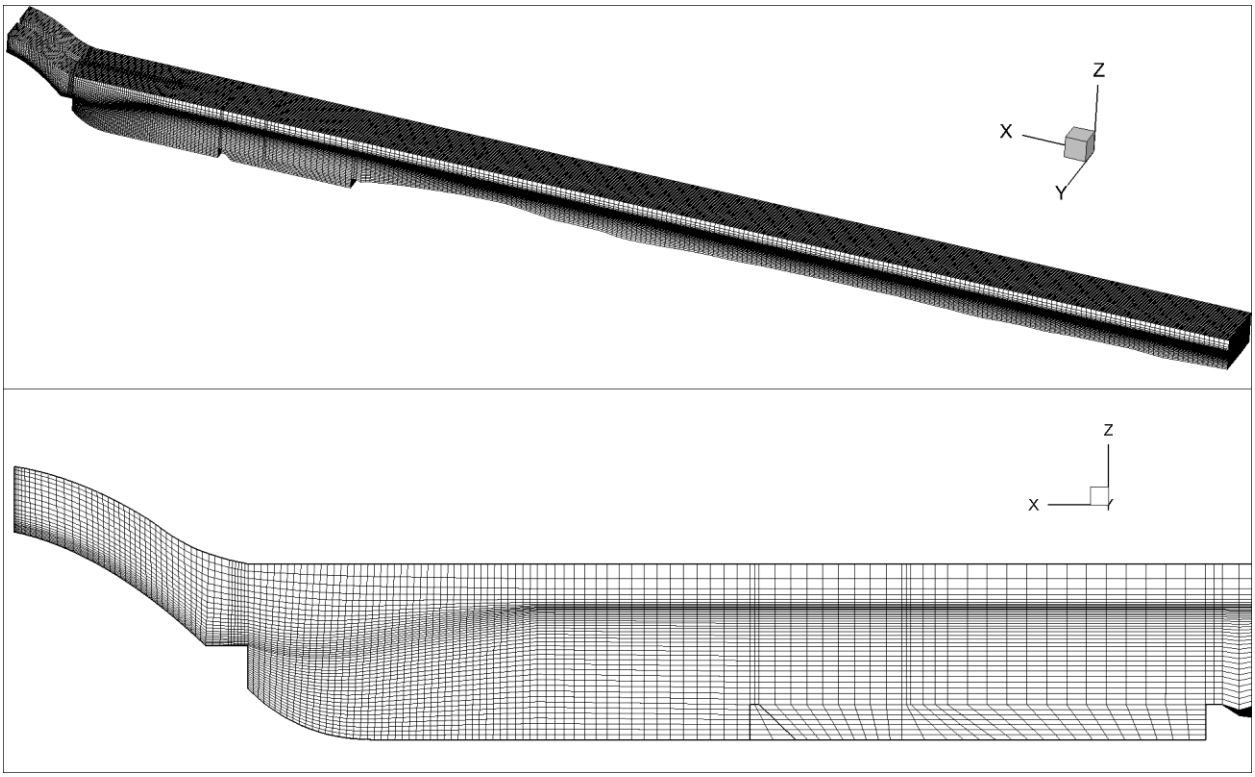

Figure 3.39 Computational mesh at prototype-scale for DES case TD 3

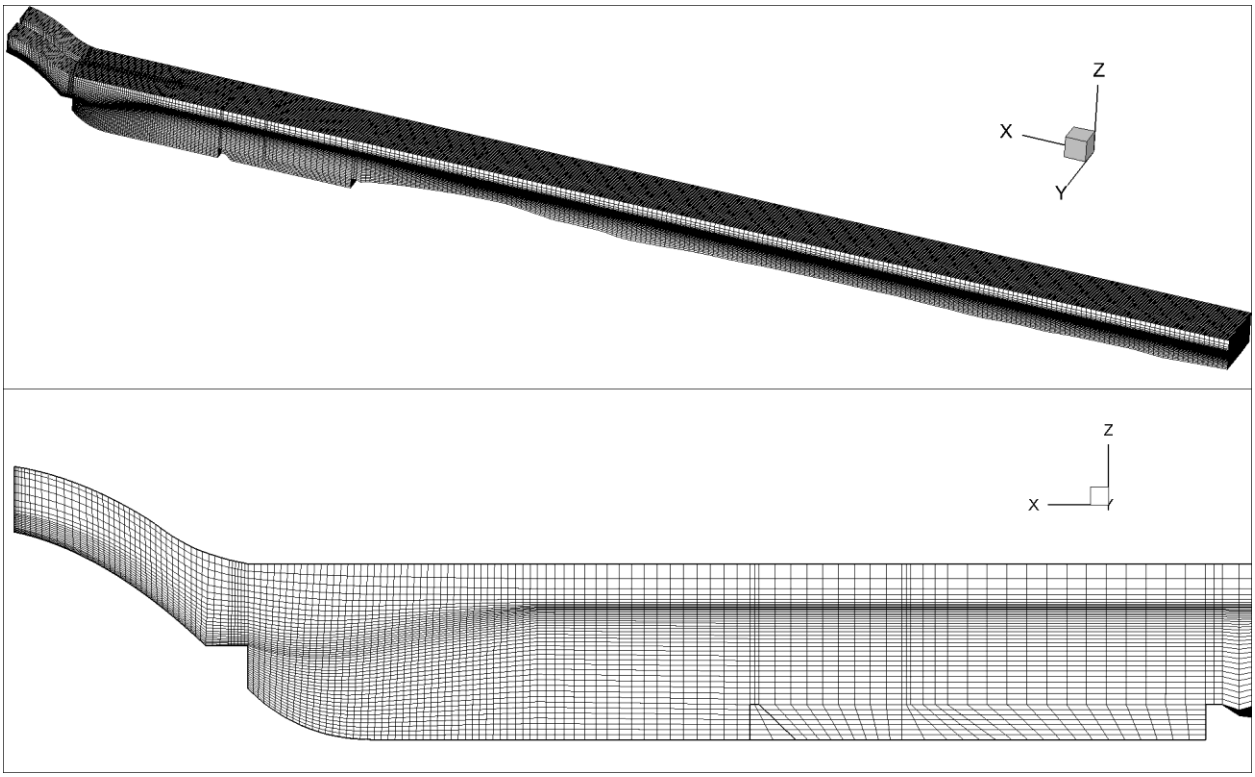

Figure 3.40 Computational mesh at prototype-scale for DES case TD 4

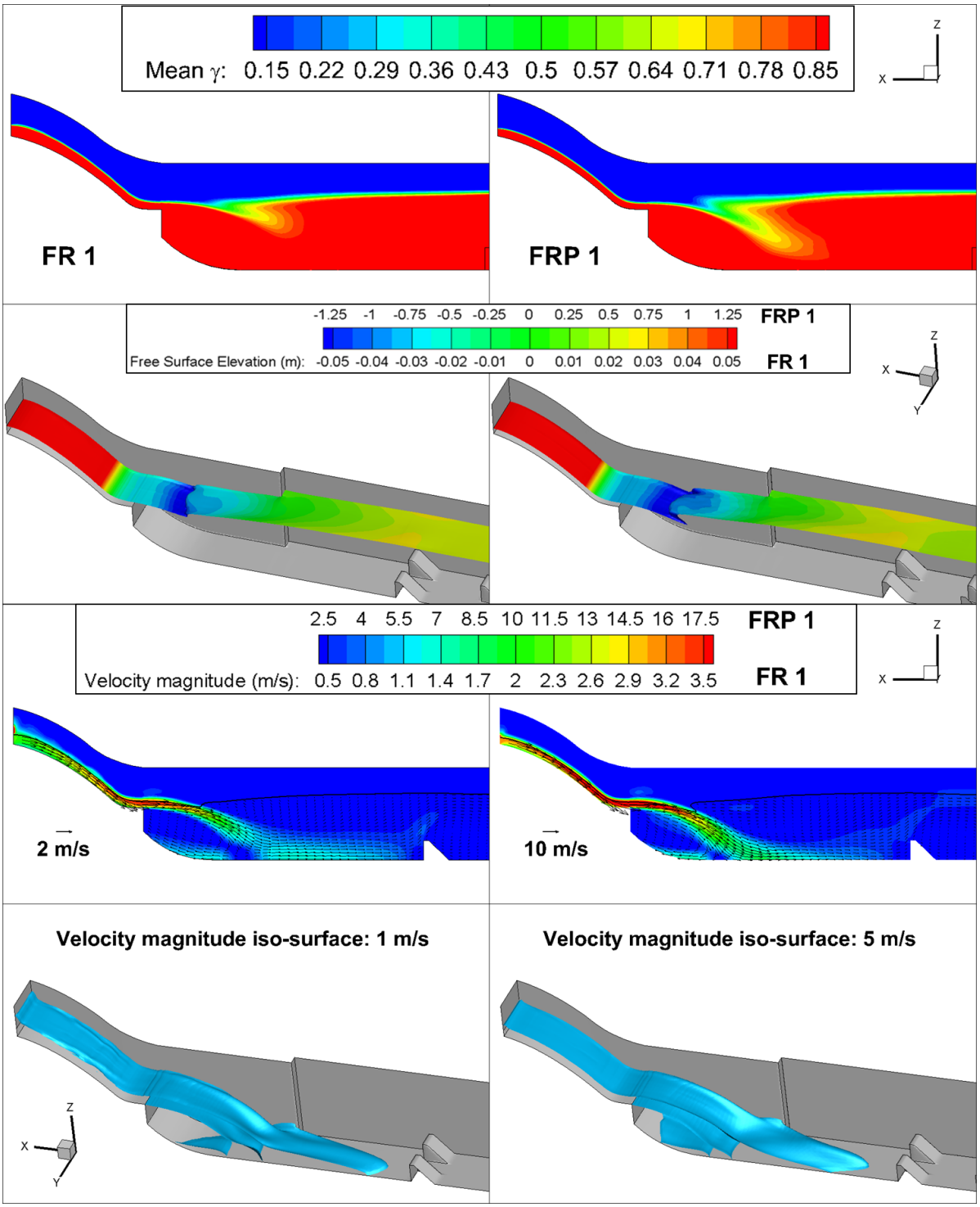

Figure 3.41 Flow patterns in reduced-scale and prototype-scale for cases FR 1 and FRP 1. Top to bottom: volume fraction contours, volume fraction iso-surface colored by free surface elevation, velocity magnitude contours, velocity magnitude iso-surface.

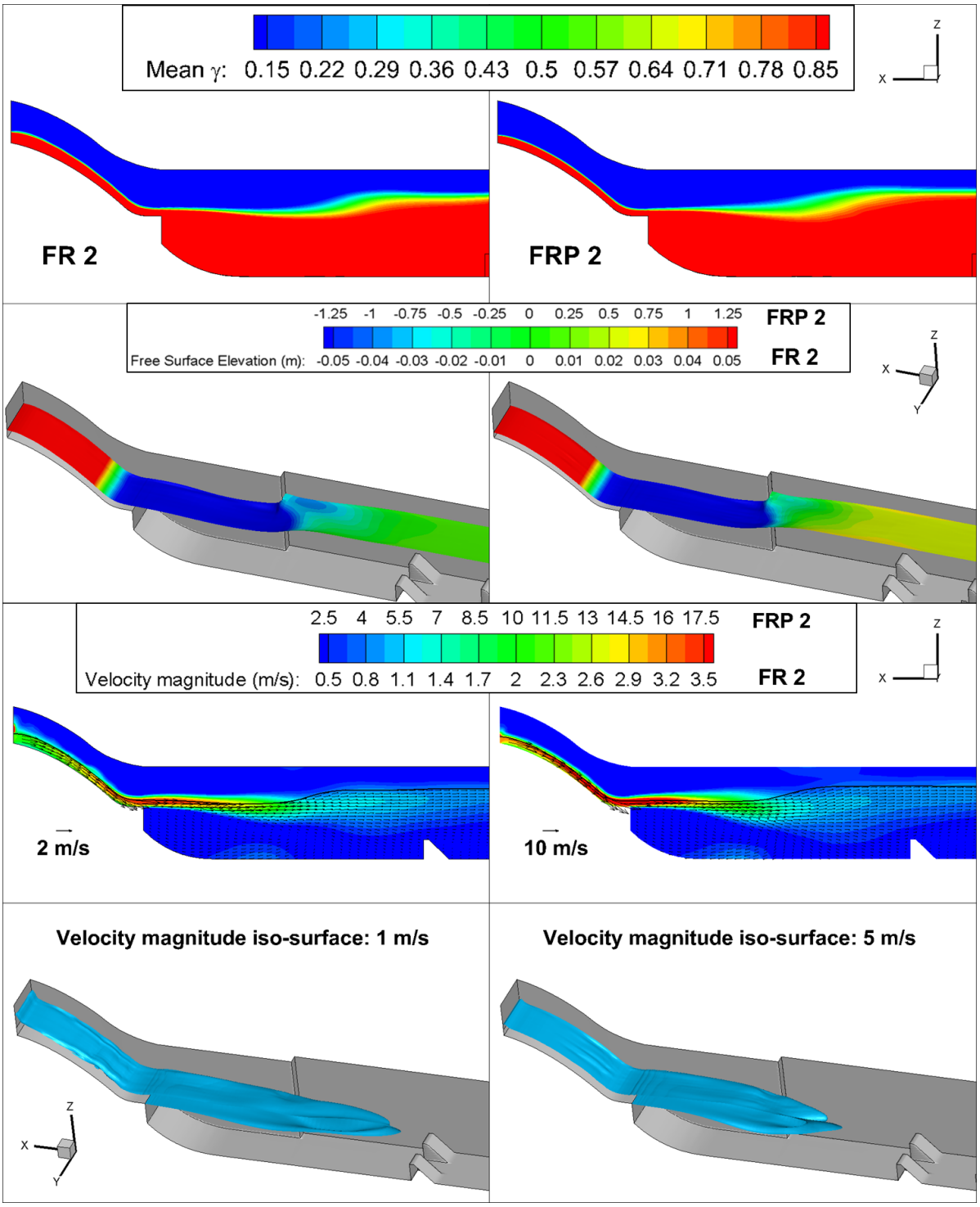

Figure 3.42 Flow patterns in reduced-scale and prototype-scale for cases FR 2 and FRP 2. Top to bottom: volume fraction contours, volume fraction iso-surface colored by free surface elevation, velocity magnitude contours, velocity magnitude iso-surface.

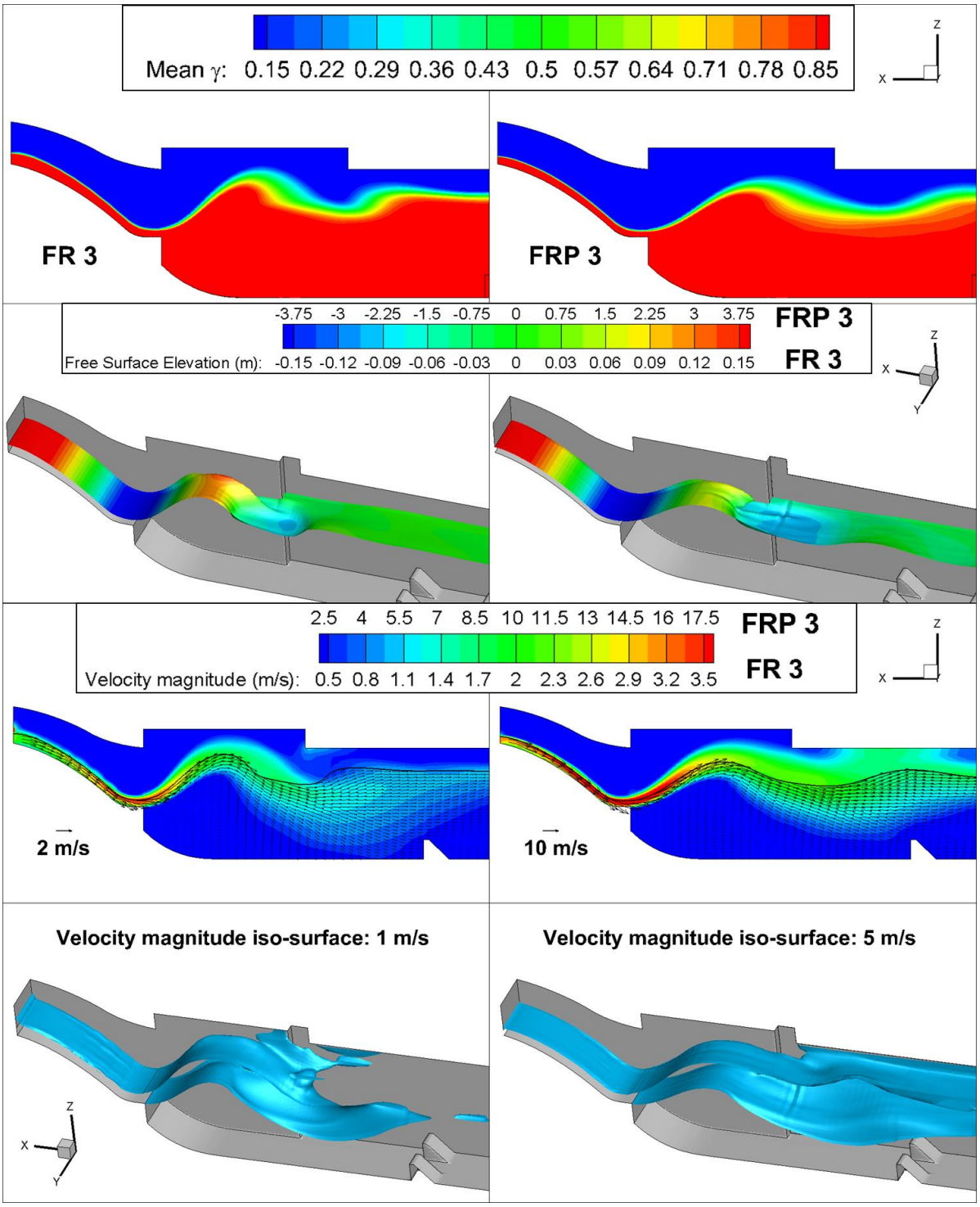

Figure 3.43 Flow patterns in reduced-scale and prototype-scale for cases FR 3 and FRP 3. Top to bottom: volume fraction contours, volume fraction iso-surface colored by free surface elevation, velocity magnitude contours, velocity magnitude iso-surface.

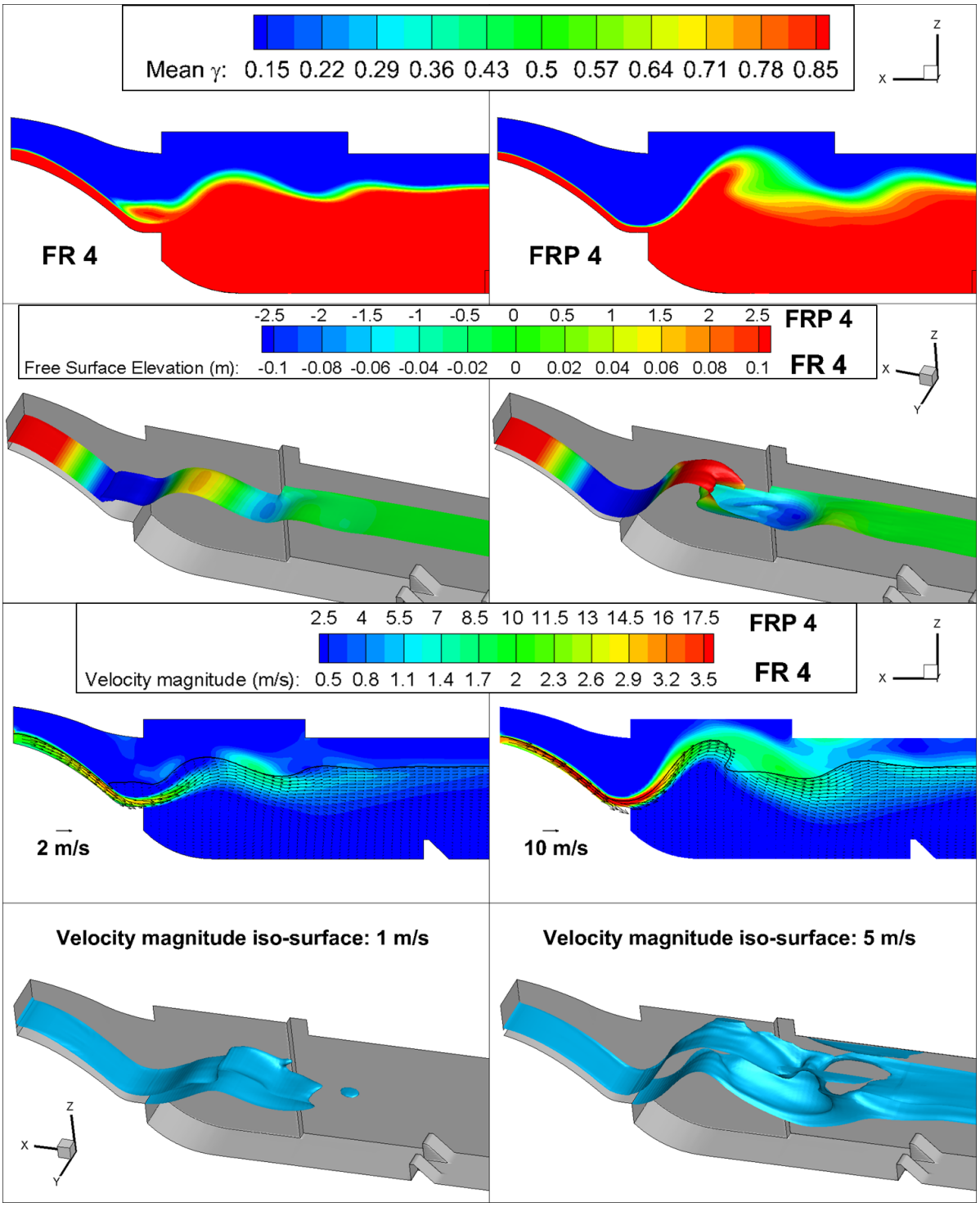

Figure 3.44 Flow patterns in reduced-scale and prototype-scale for cases FR 4 and FRP 4. Top to bottom: volume fraction contours, volume fraction iso-surface colored by free surface elevation, velocity magnitude contours, velocity magnitude iso-surface.

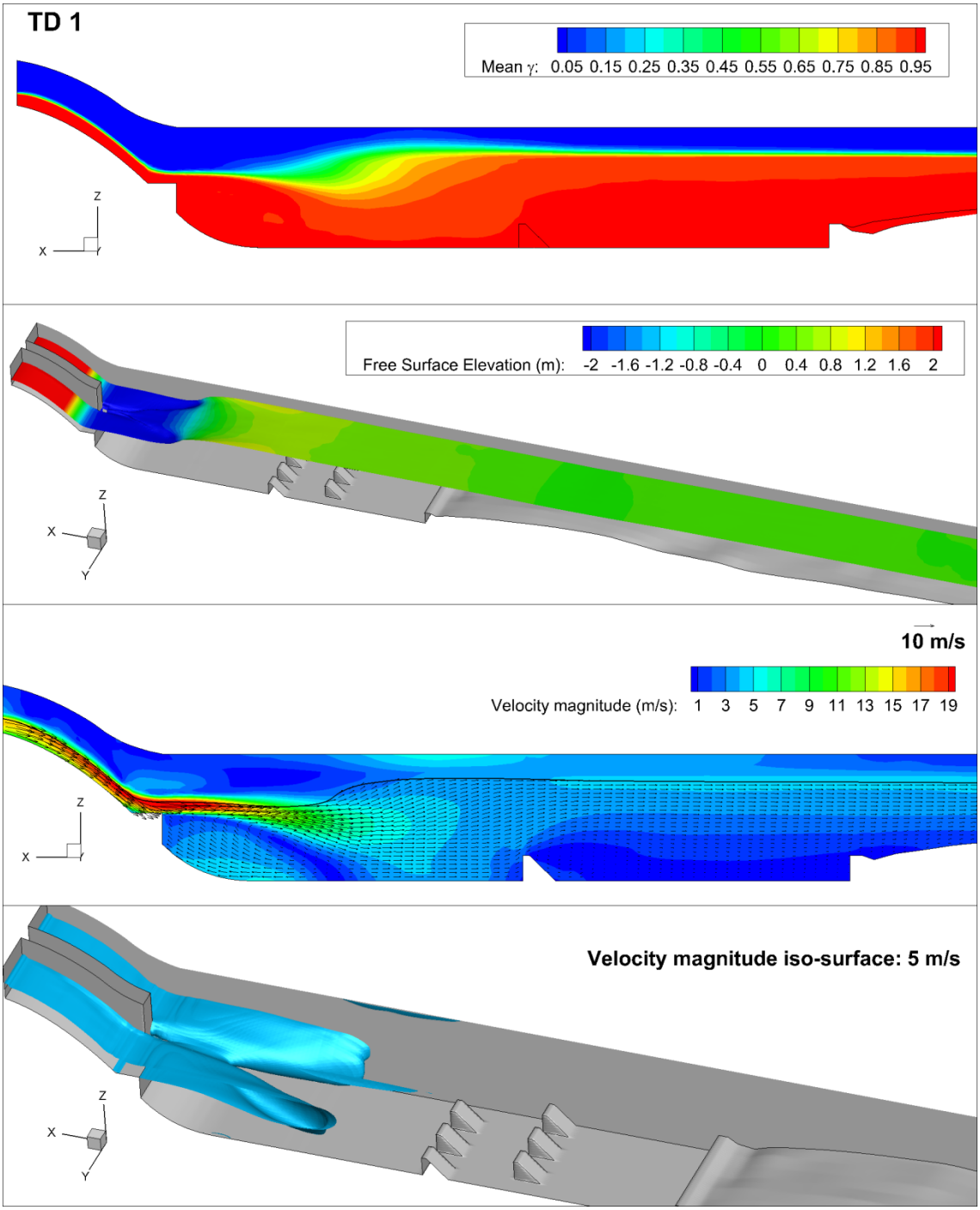

Figure 3.45 Time-averaged flow pattern for case TD 1. Top to bottom: volume fraction contours, volume fraction iso-surface colored by free surface elevation, velocity magnitude contours, velocity magnitude iso-surface.

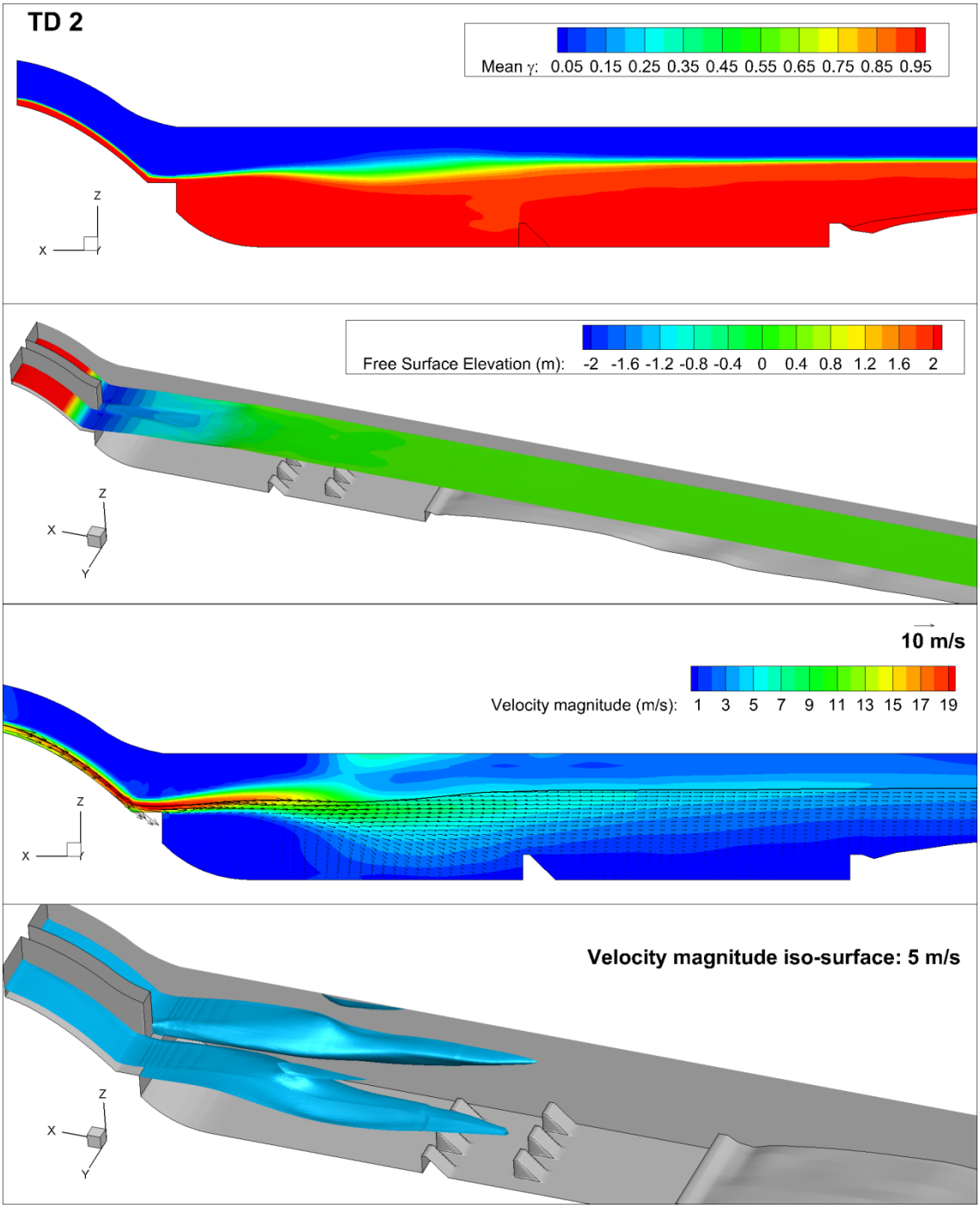

Figure 3.46 Time-averaged flow pattern for case TD 2. Top to bottom: volume fraction contours, volume fraction iso-surface colored by free surface elevation, velocity magnitude contours, velocity magnitude iso-surface.

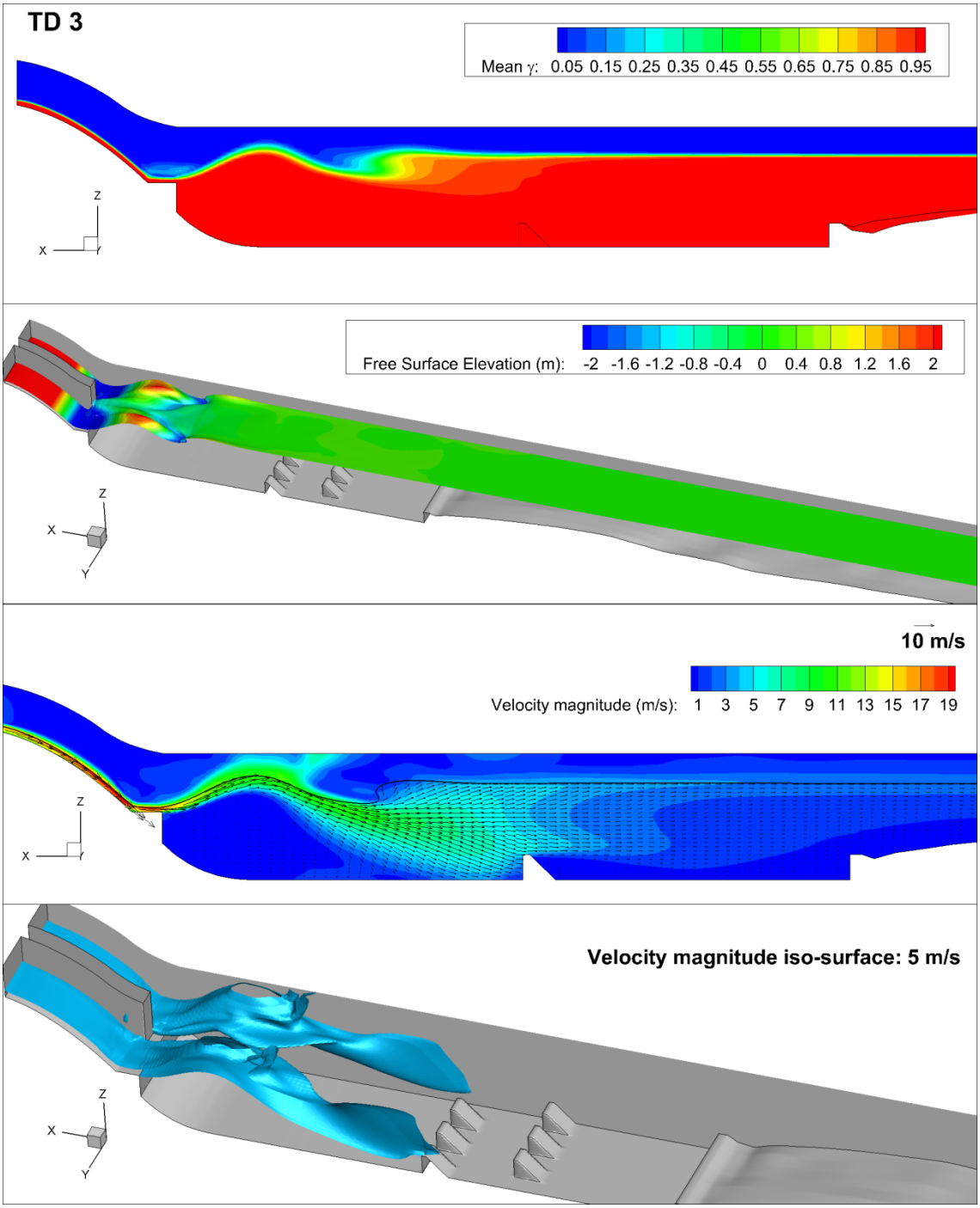

Figure 3.47 Time-averaged flow pattern for case TD 3. Top to bottom: volume fraction contours, volume fraction iso-surface colored by free surface elevation, velocity magnitude contours, velocity magnitude iso-surface.

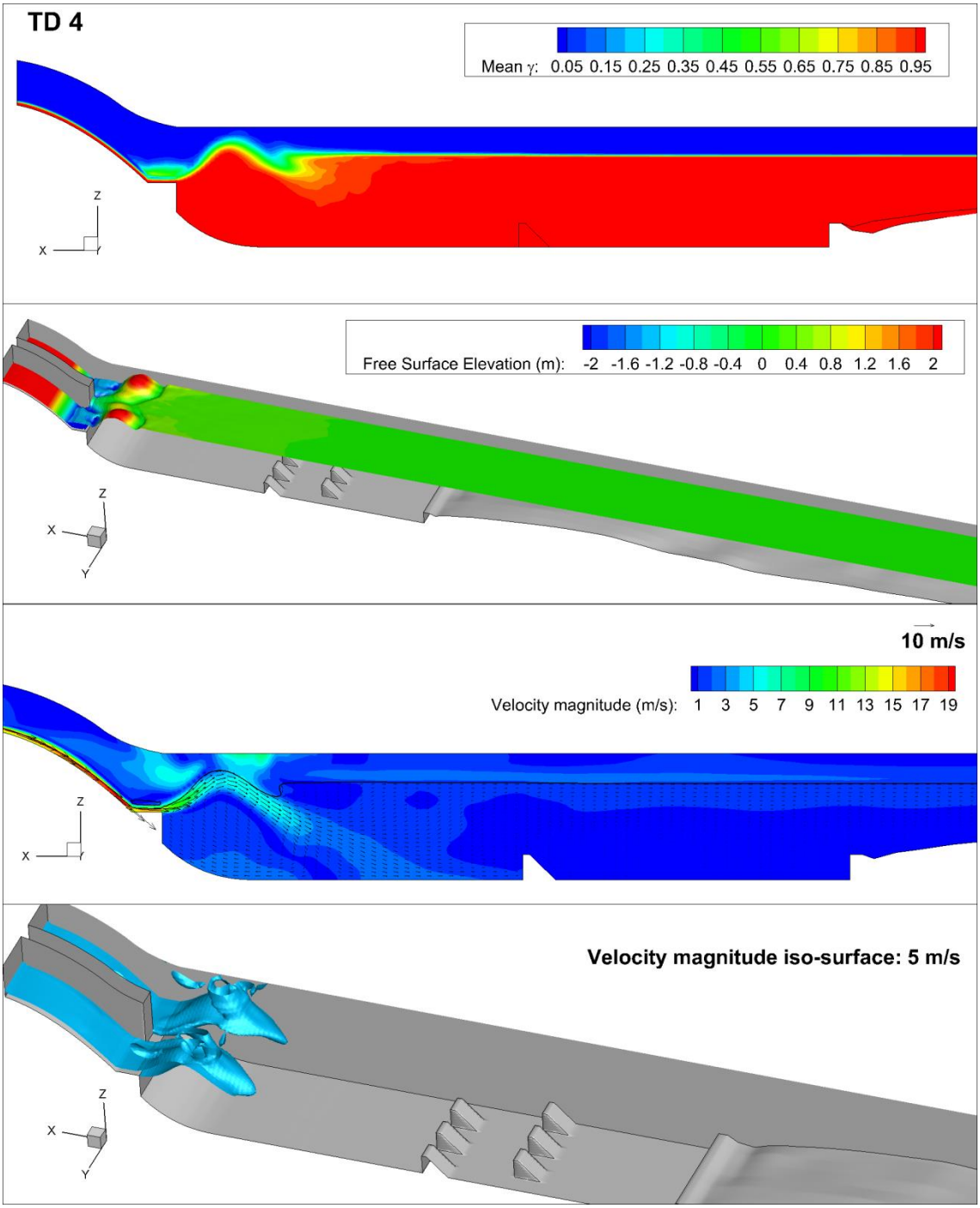

Figure 3.48 Time-averaged flow pattern for case TD 3. Top to bottom: volume fraction contours, volume fraction iso-surface colored by free surface elevation, velocity magnitude contours, velocity magnitude iso-surface.

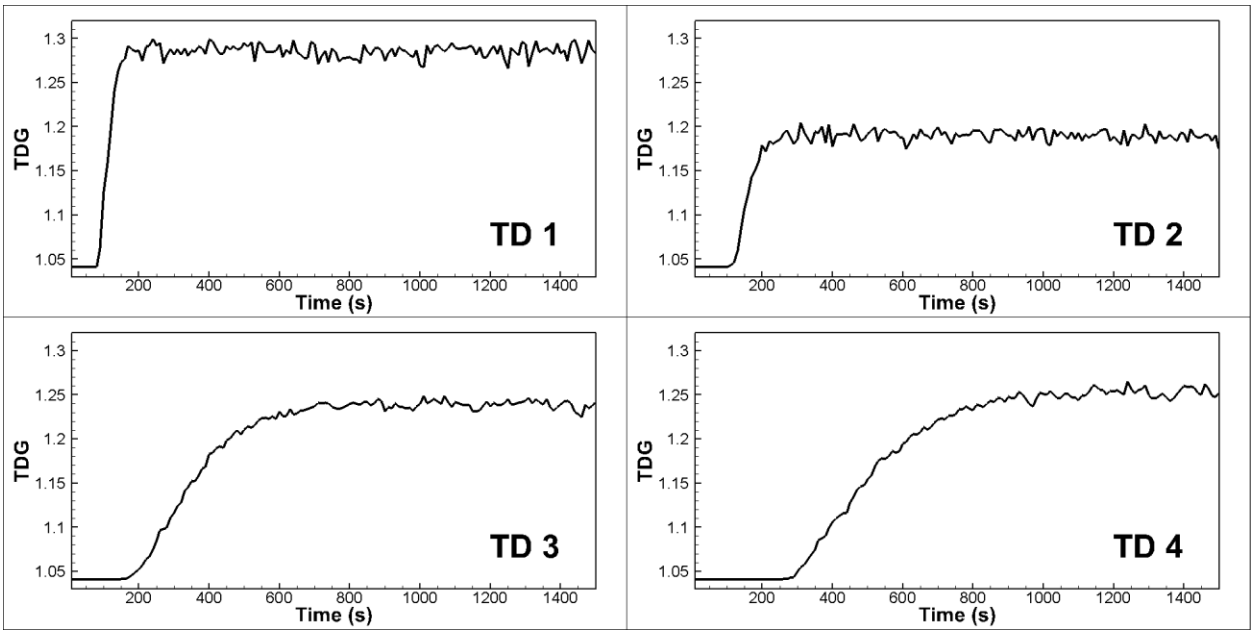

Figure 3.49 Evolution of TDG at the downstream end for prototype-scale cases TD 1 to TD 4

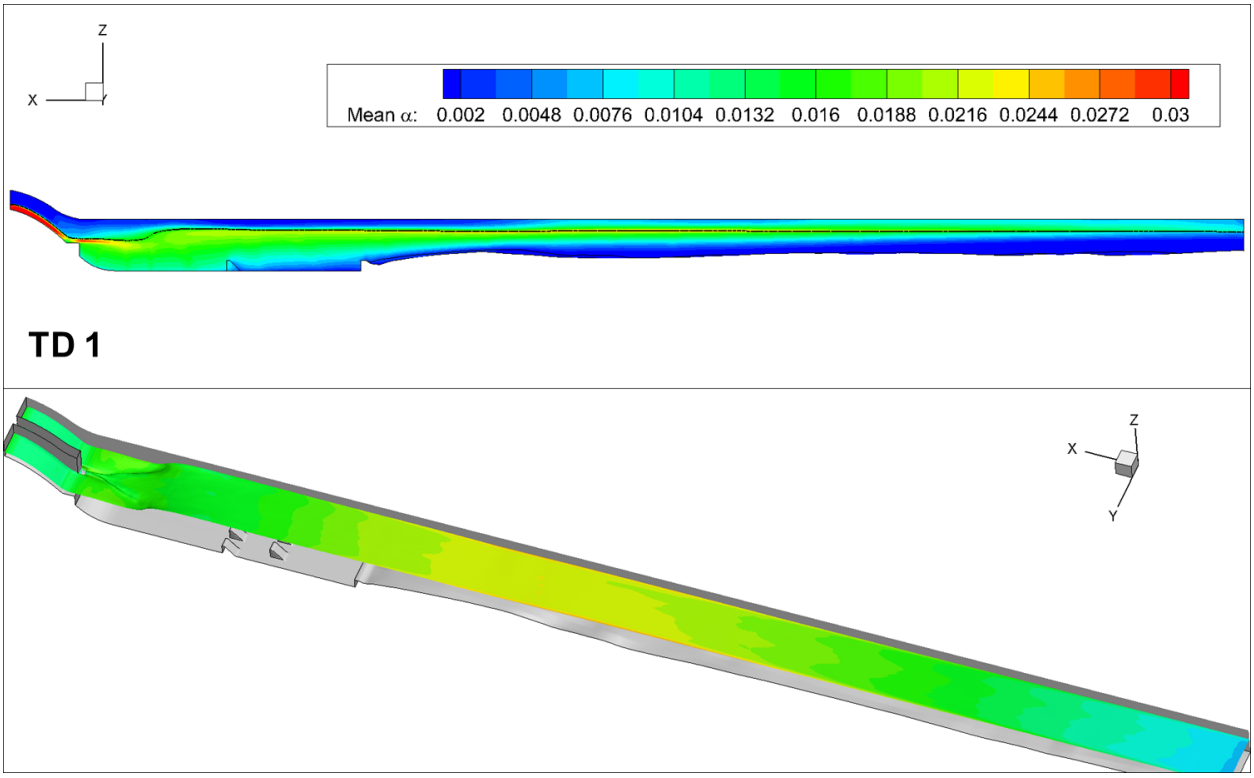

Figure 3.50 Time-averaged gas volume fraction contours for case TD 1

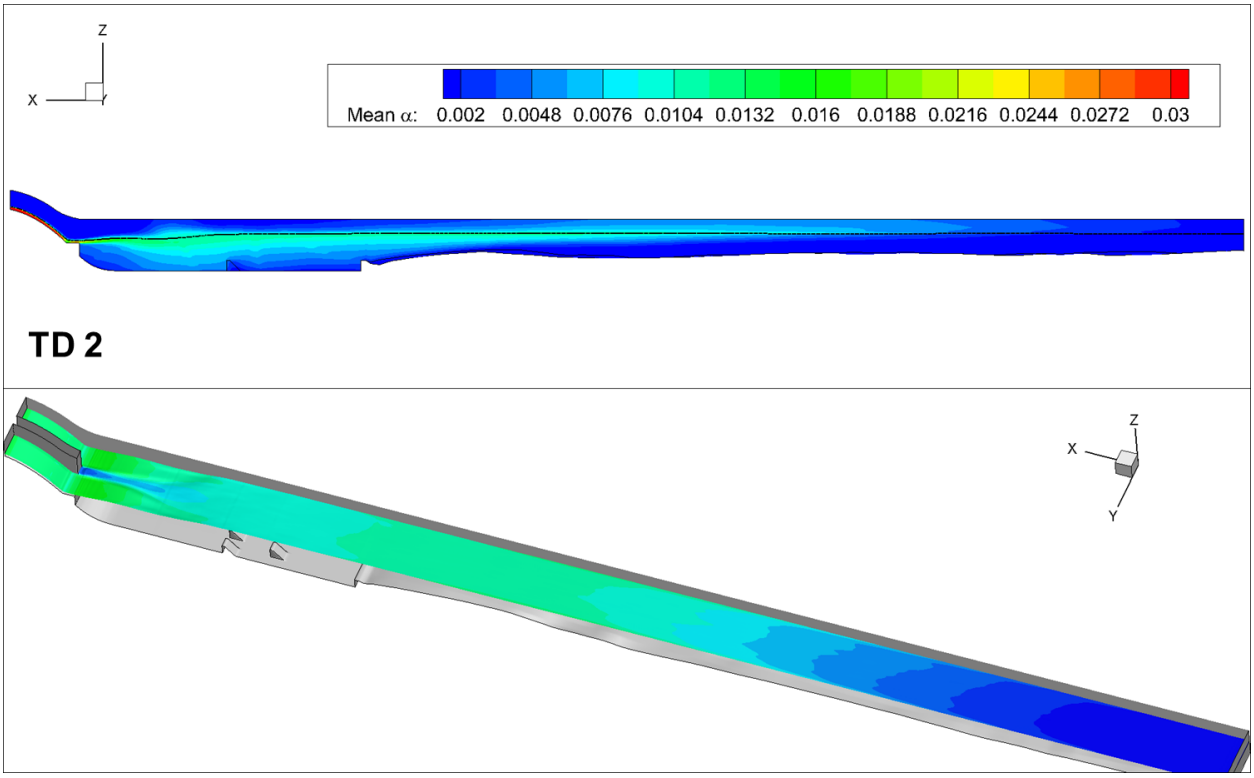

Figure 3.51 Time-averaged gas volume fraction contours for case TD 2

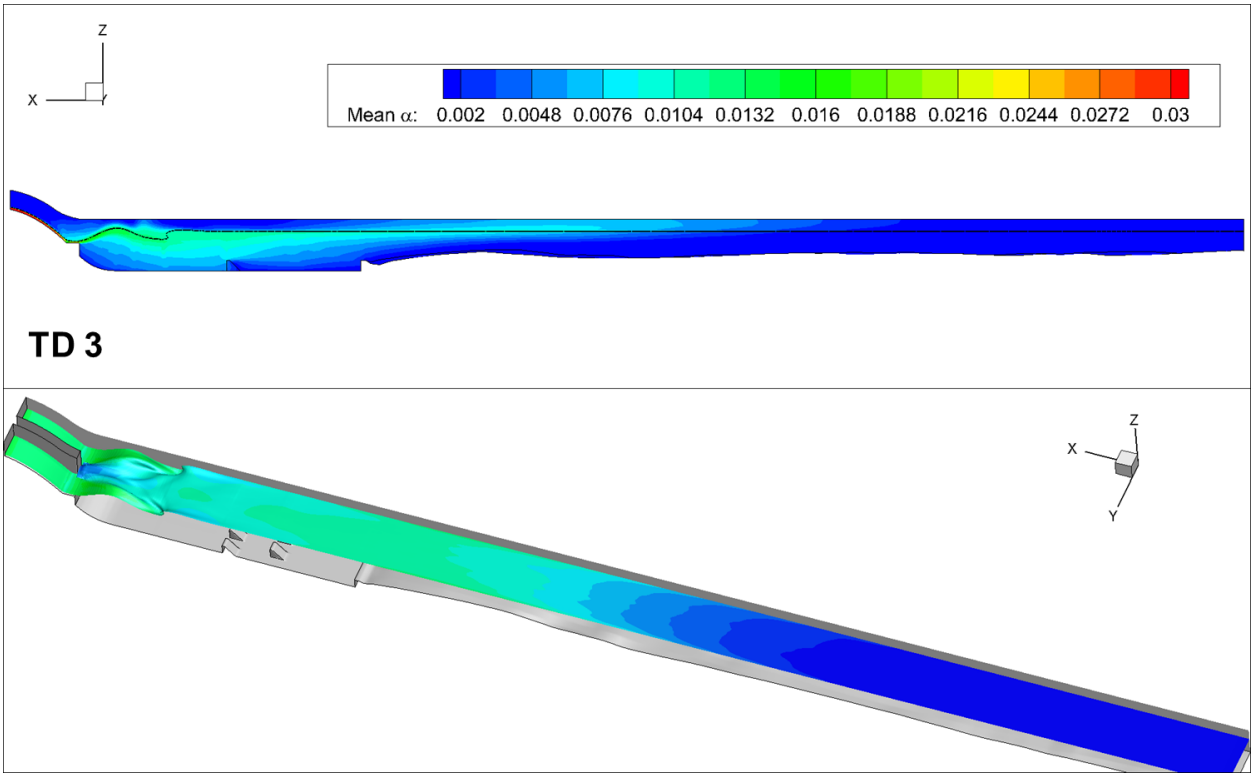

Figure 3.52 Time-averaged gas volume fraction contours for case TD 3

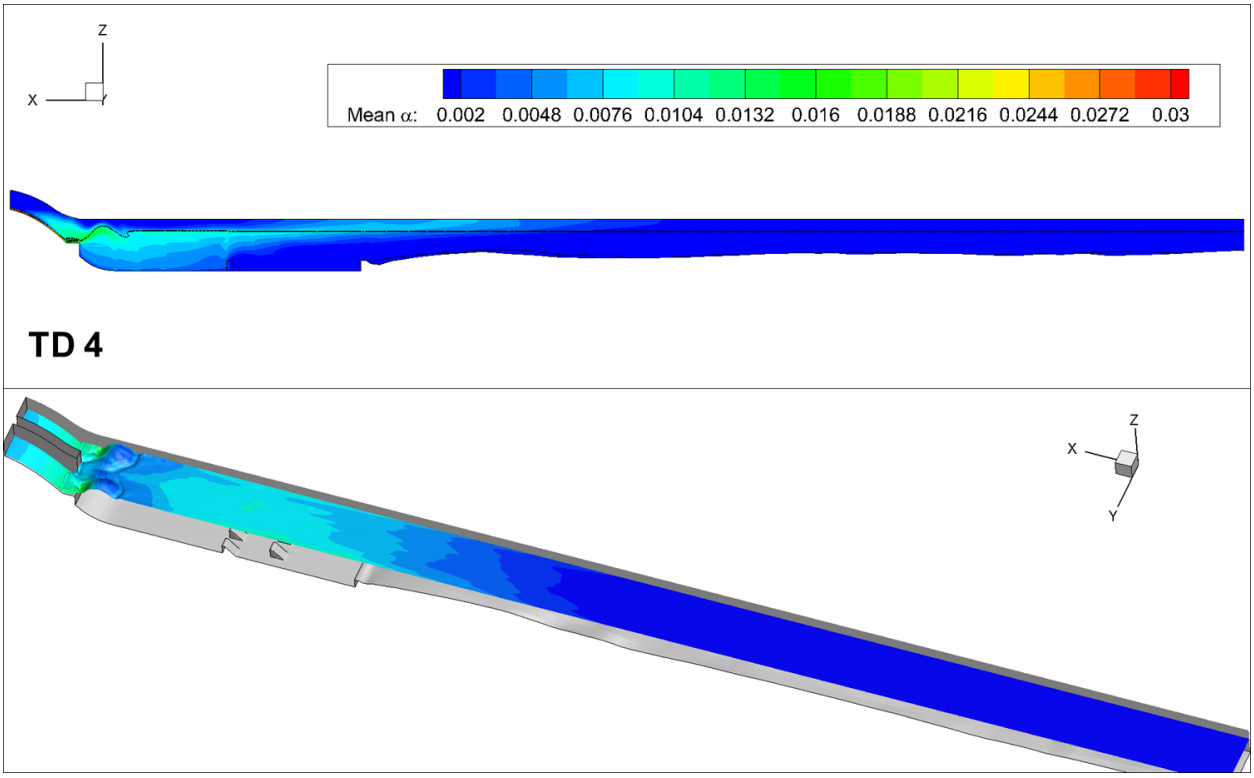

Figure 3.53 Time-averaged gas volume fraction contours for case TD 4

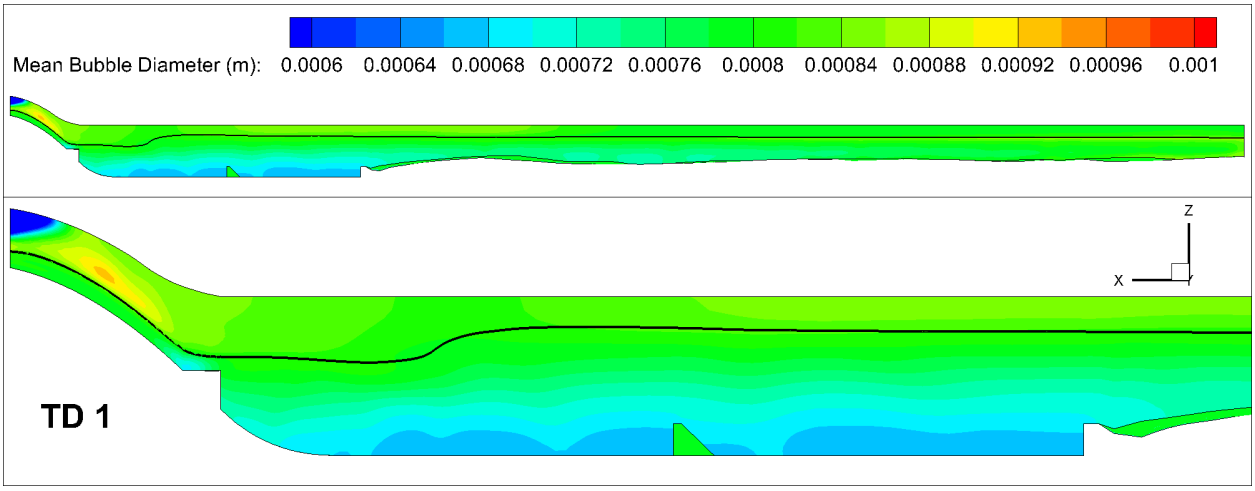

Figure 3.54 Time-averaged bubble diameter contours for case TD 1

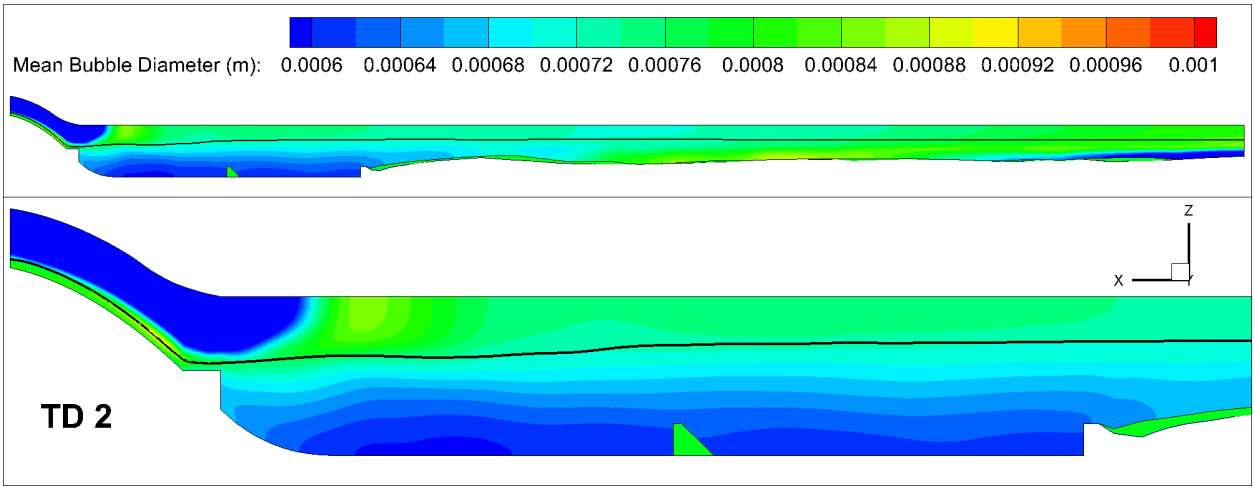

Figure 3.55 Time-averaged bubble diameter contours for case TD 2

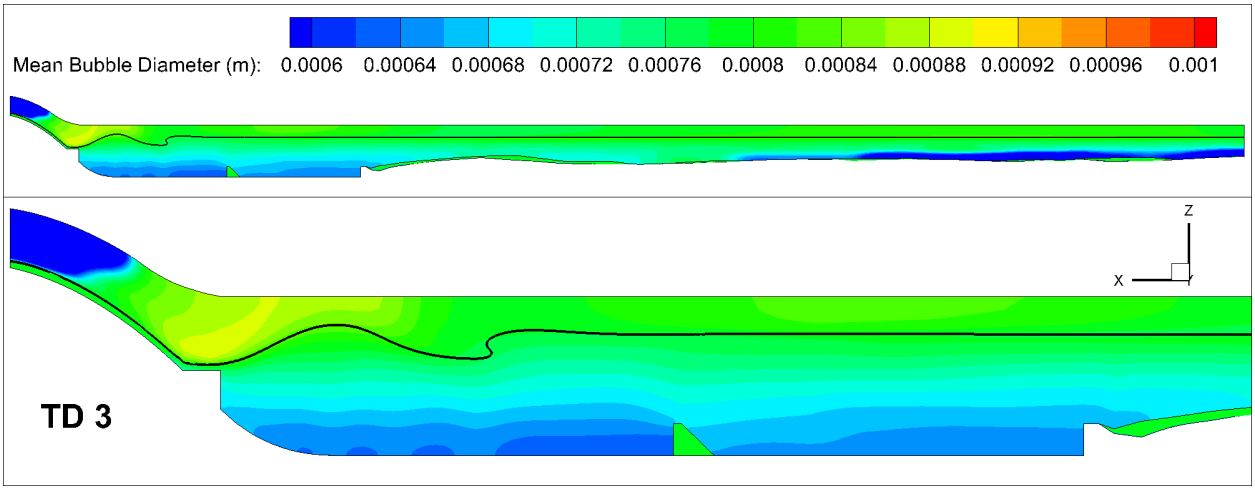

Figure 3.56 Time-averaged bubble diameter contours for case TD 3

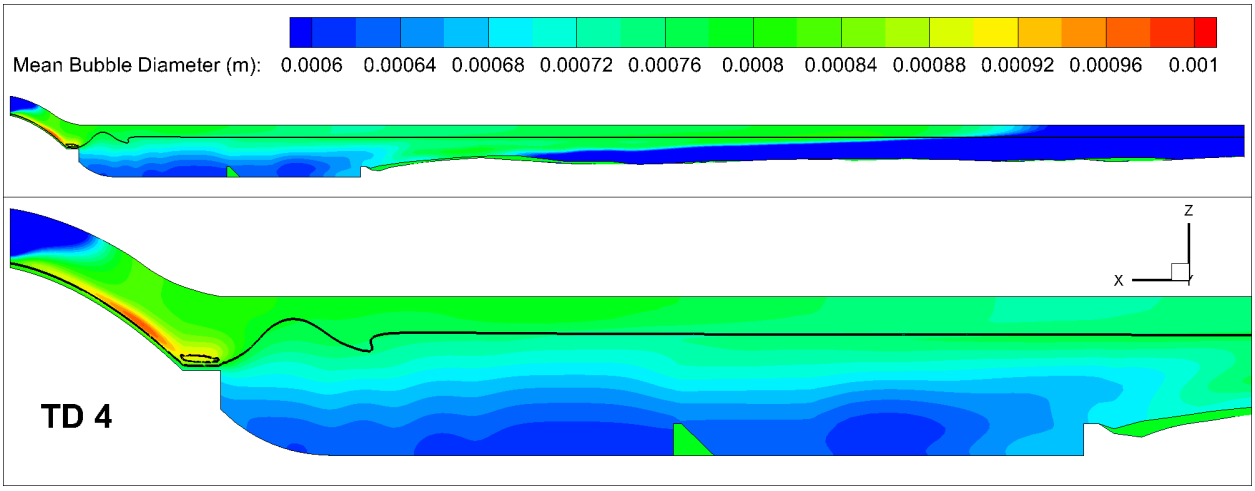

Figure 3.57 Time-averaged bubble diameter contours for case TD 4

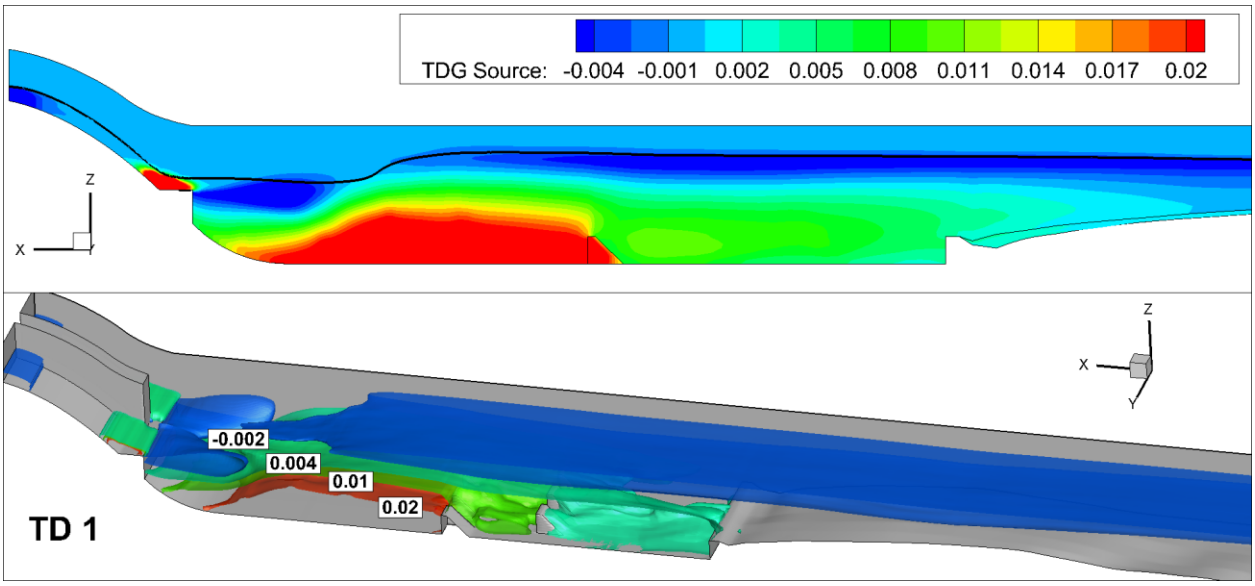

Figure 3.58 Time-averaged TDG source contours and iso-surfaces for case TD 1

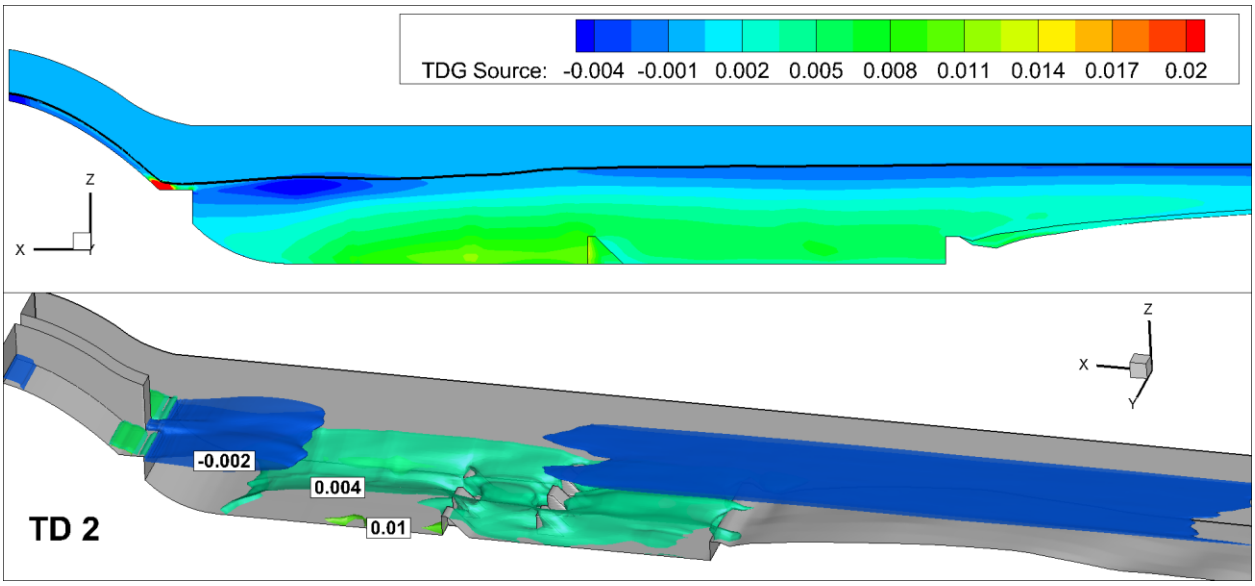

Figure 3.59 Time-averaged TDG source contours and iso-surfaces for case TD 2

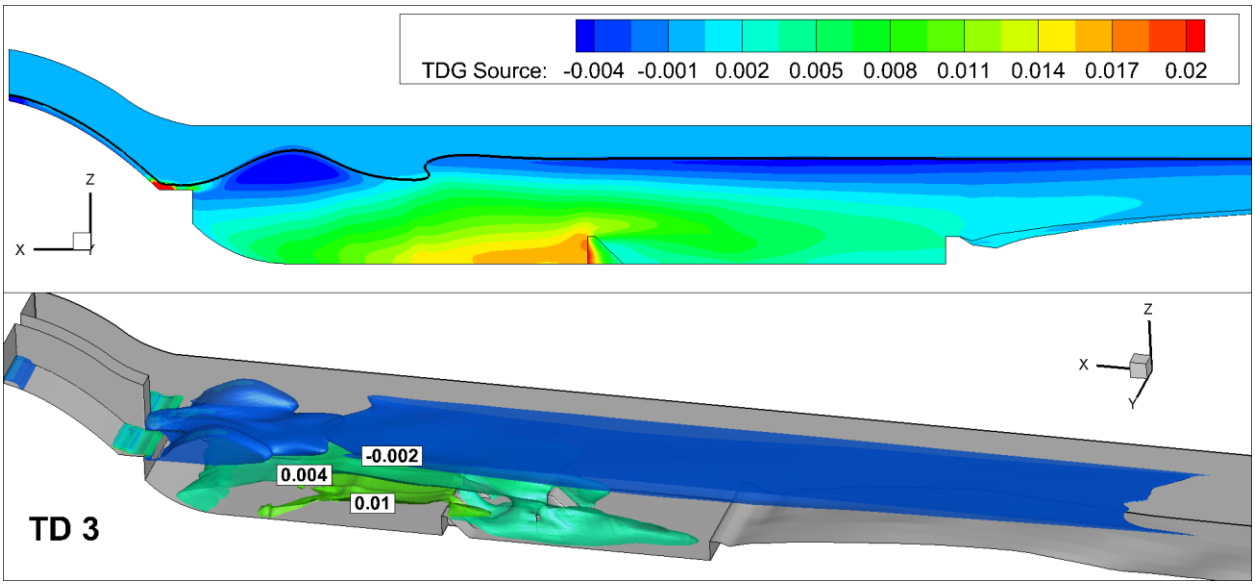

Figure 3.60 Time-averaged TDG source contours and iso-surfaces for case TD 3

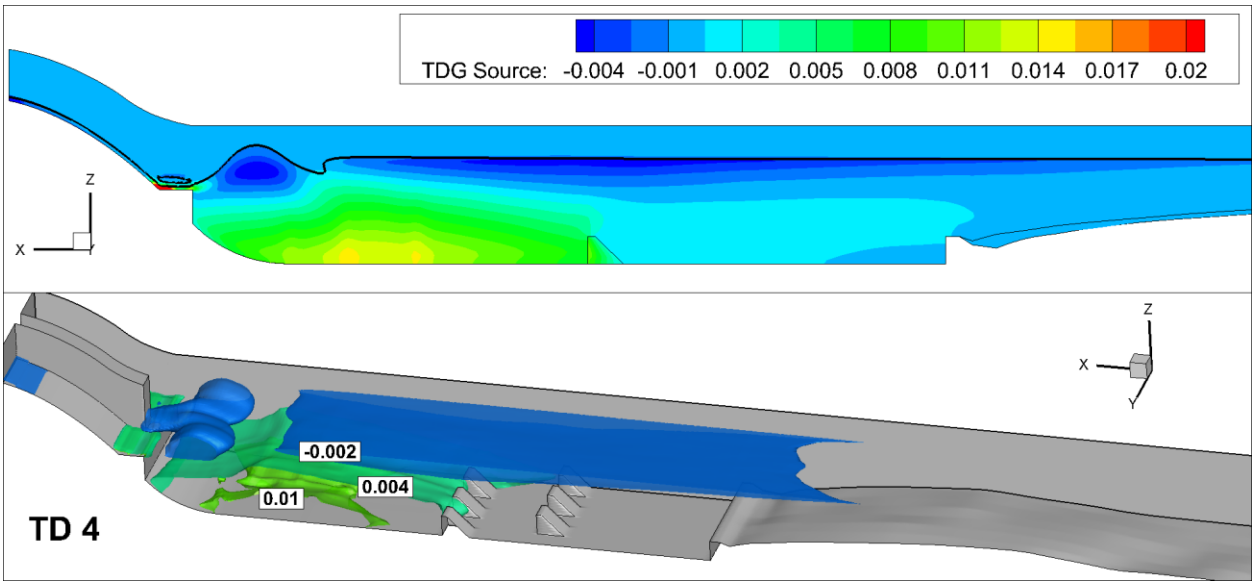

Figure 3.61 Time-averaged TDG source contours and iso-surfaces for case TD 4

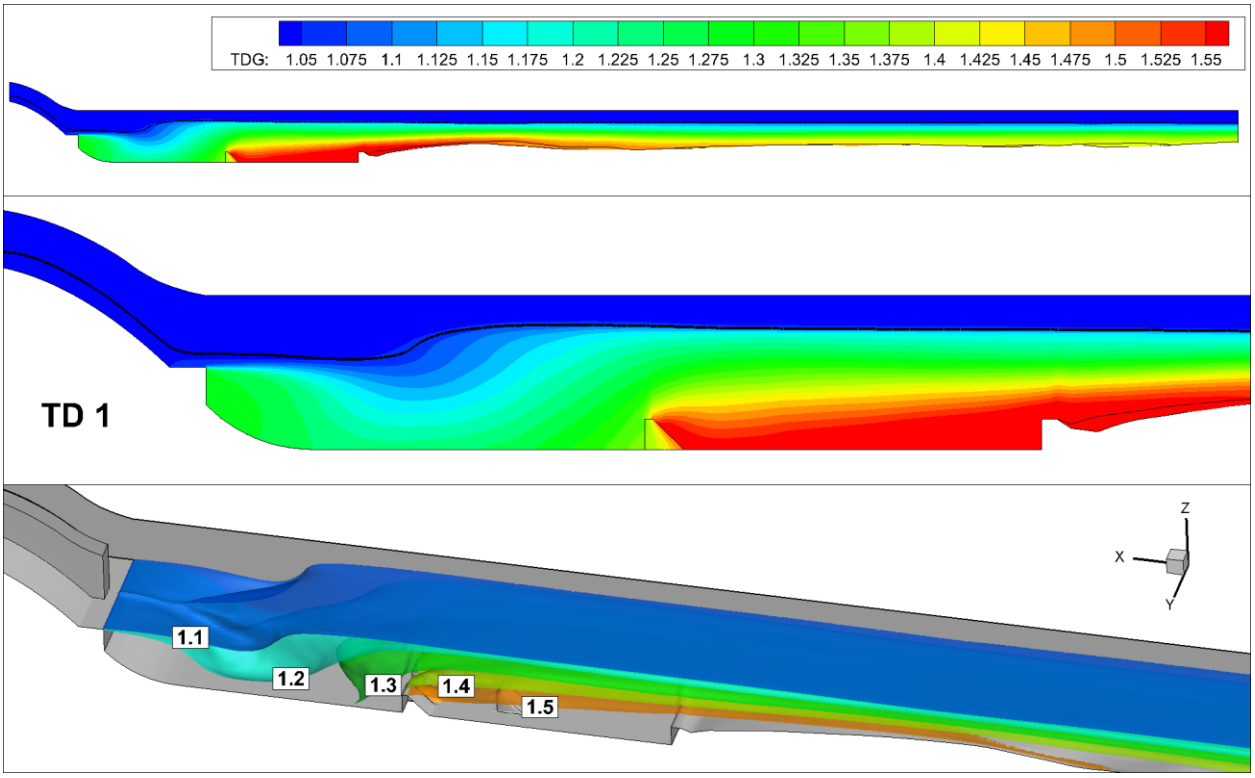

Figure 3.62 Time-averaged TDG contours and iso-surfaces for case TD 1

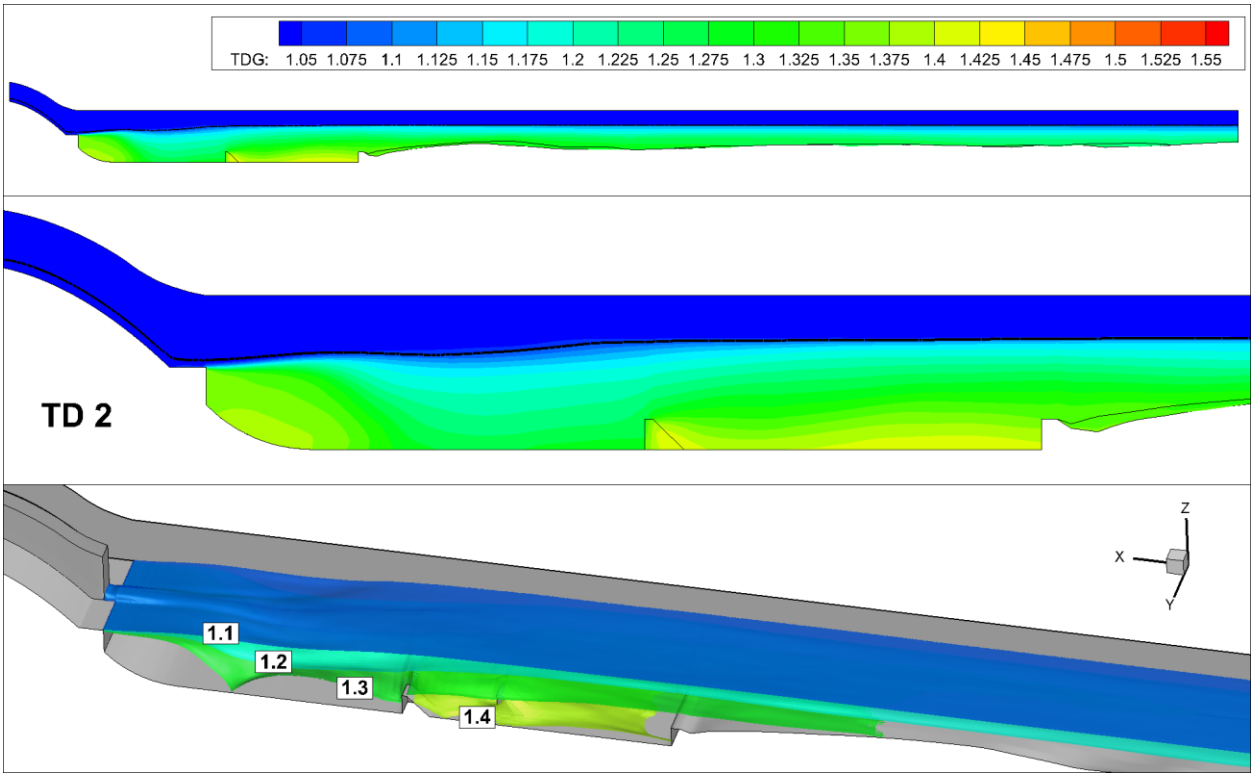

Figure 4.63 Time-averaged TDG contours and iso-surfaces for case TD 2

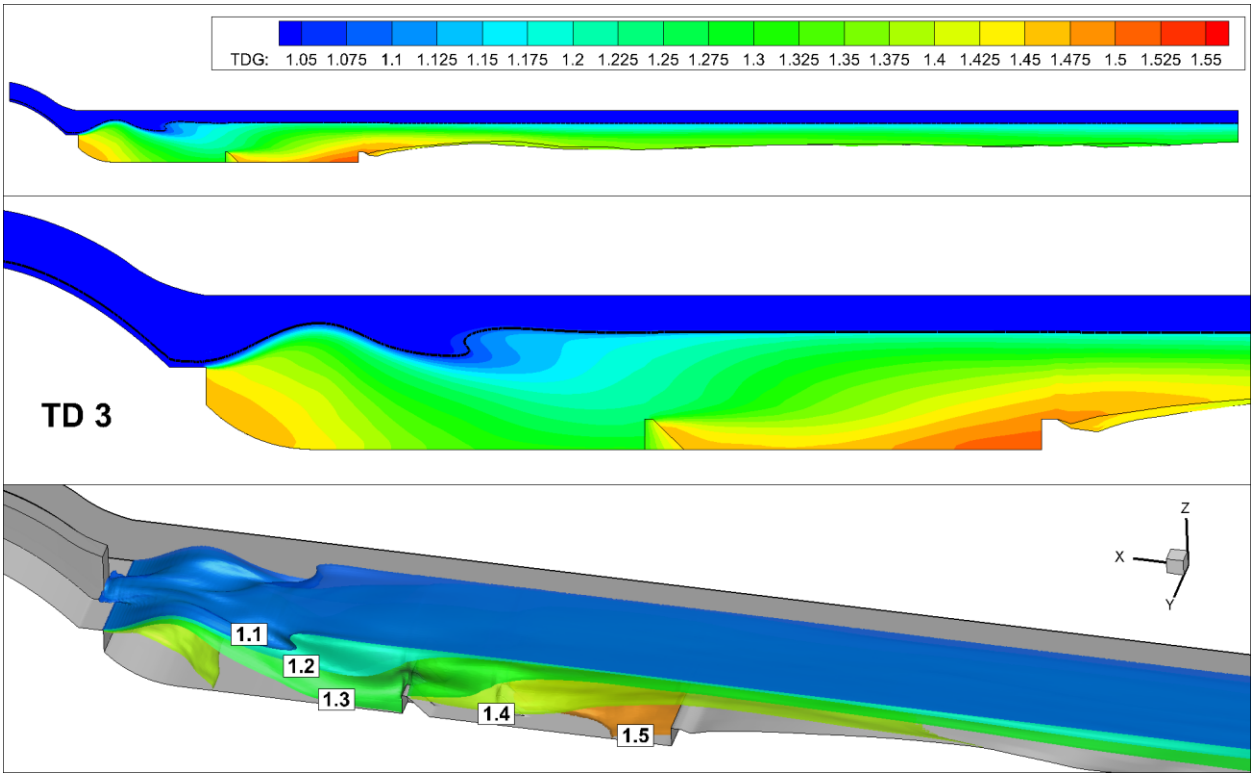

Figure 3.64 Time-averaged TDG contours and iso-surfaces for case TD 3

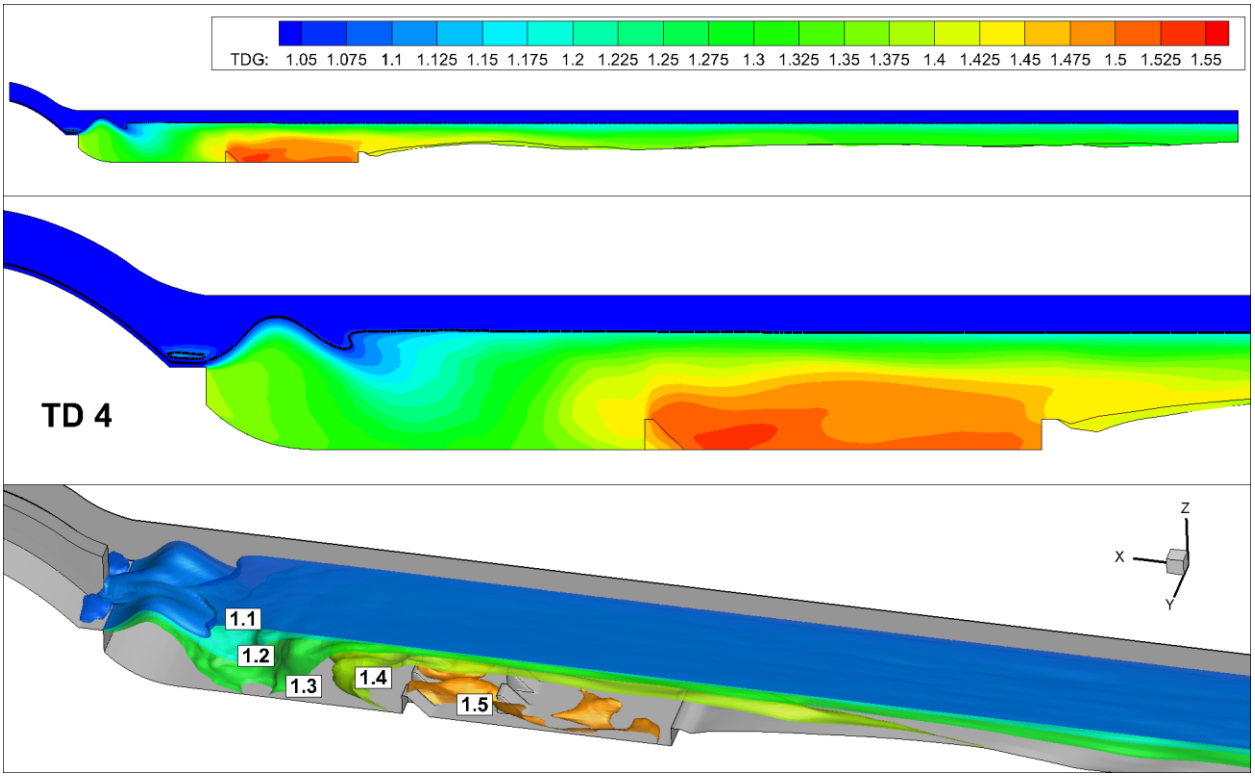

Figure 3.65 Time-averaged TDG contours and iso-surfaces for case TD 4

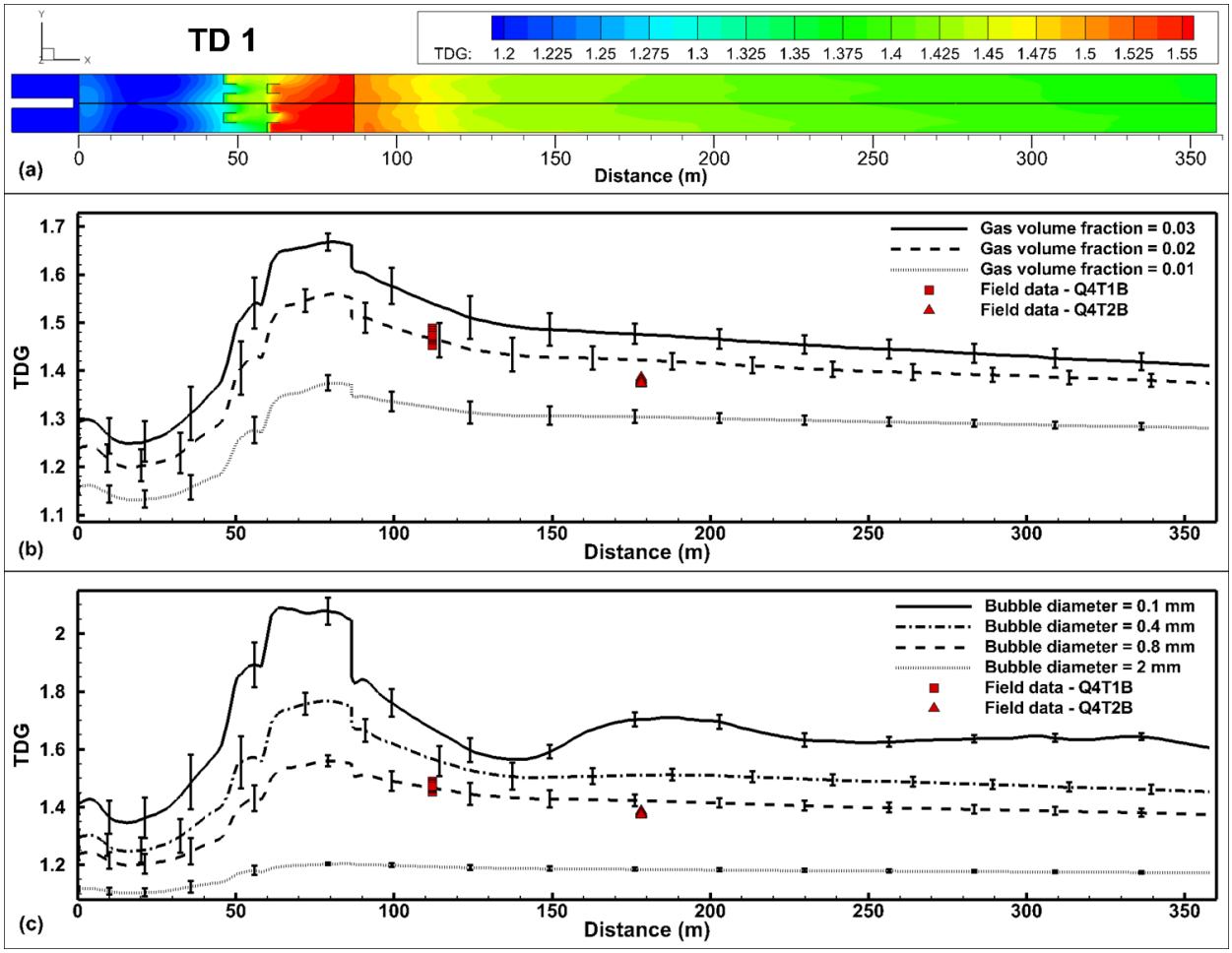

Figure 3.66 TDG concentration as a function of distance from spillway pier for case TD 1. Top to bottom: TDG contours on the stilling basin bottom and downstream river bed, TDG concentration at different gas volume fraction, TDG concentration at different bubble diameters.

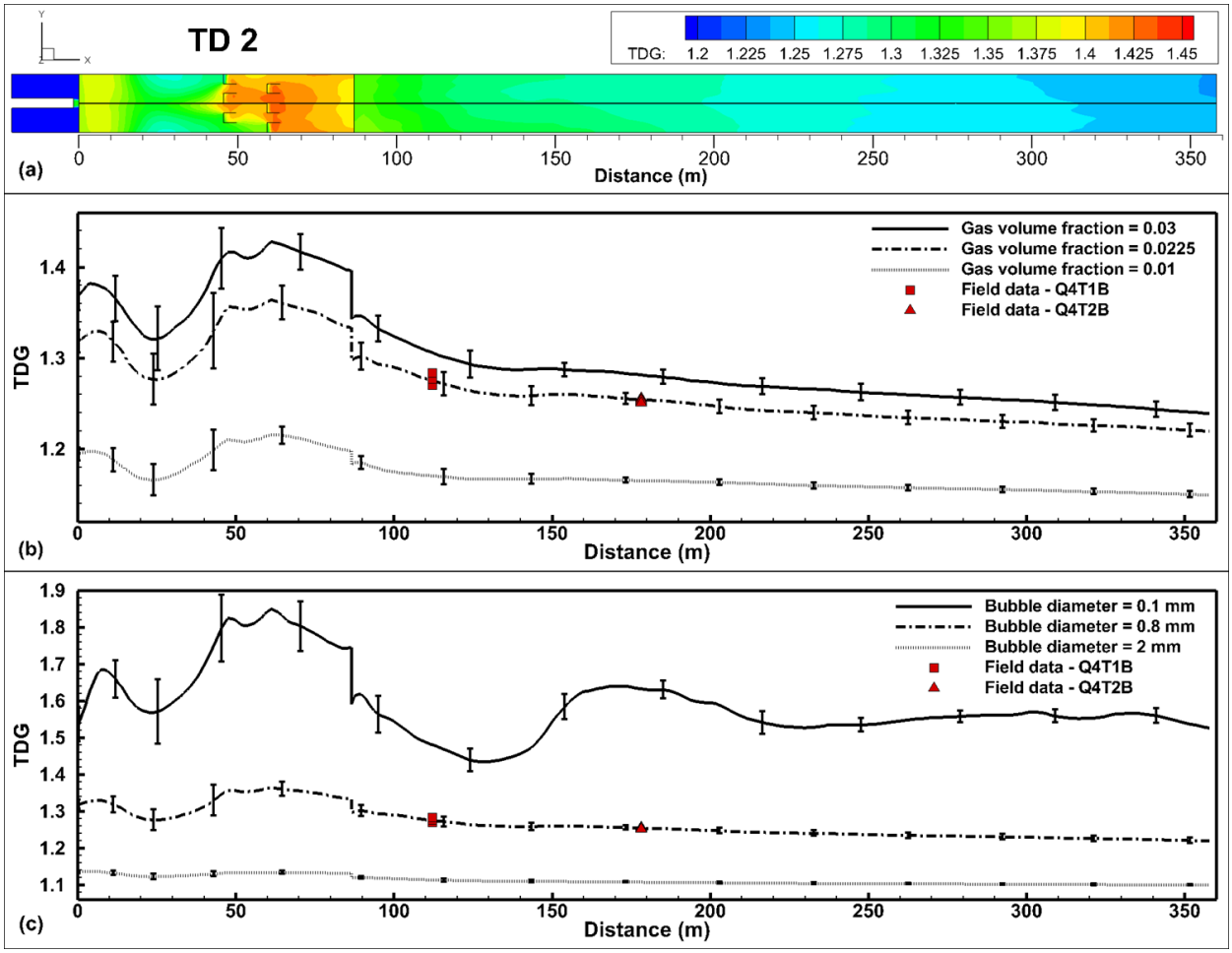

Figure 3.67 TDG concentration as a function of distance from spillway pier for case TD 2. Top to bottom: TDG contours on the stilling basin bottom and downstream river bed, TDG concentration at different gas volume fraction, TDG concentration at different bubble diameters.

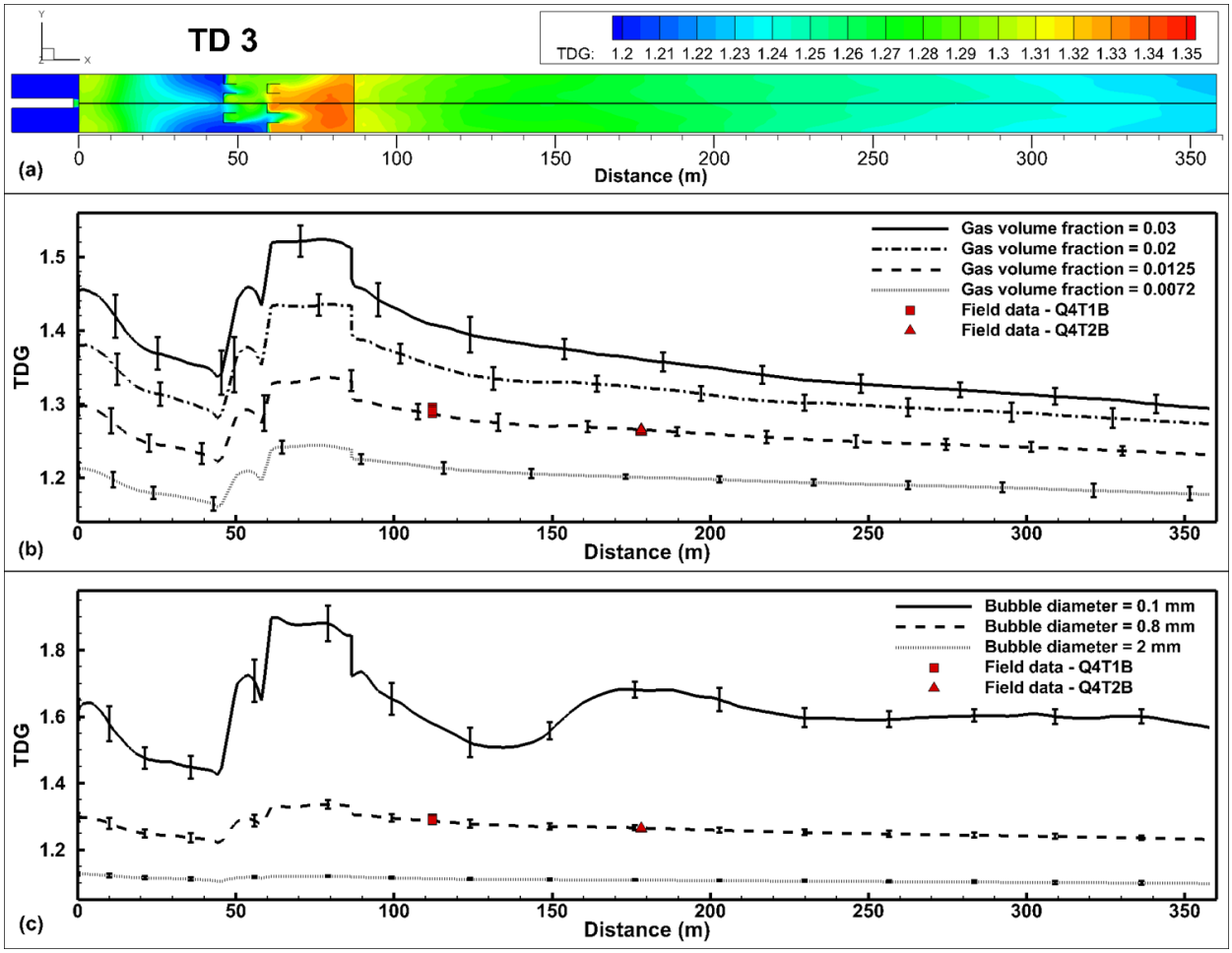

Figure 3.68 TDG concentration as a function of distance from spillway pier for case TD 3. Top to bottom: TDG contours on the stilling basin bottom and downstream river bed, TDG concentration at different gas volume fraction, TDG concentration at different bubble diameters.

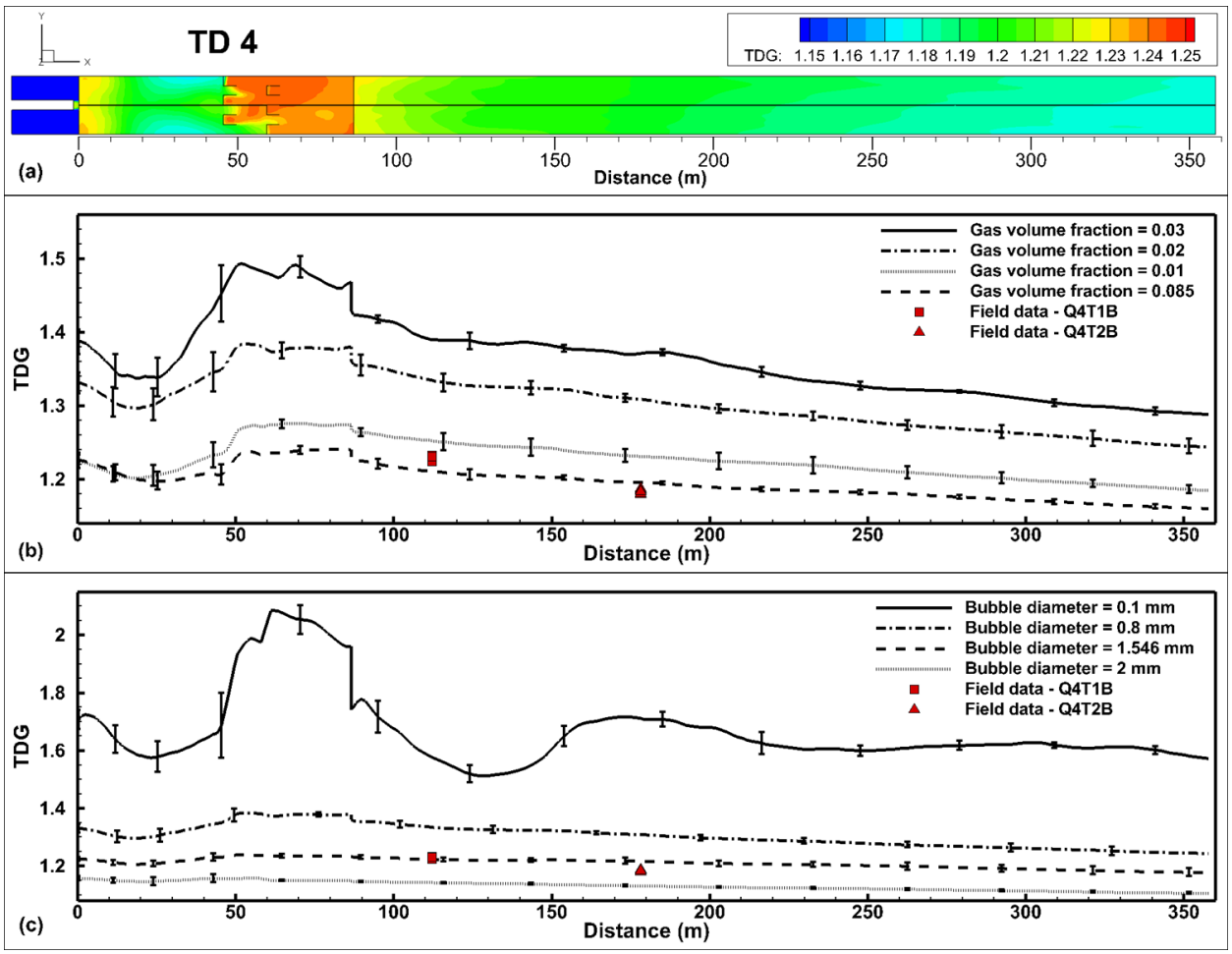

Figure 3.69 TDG concentration as a function of distance from spillway pier for case TD 4. Top to bottom: TDG contours on the stilling basin bottom and downstream river bed, TDG concentration at different gas volume fraction, TDG concentration at different bubble diameters.

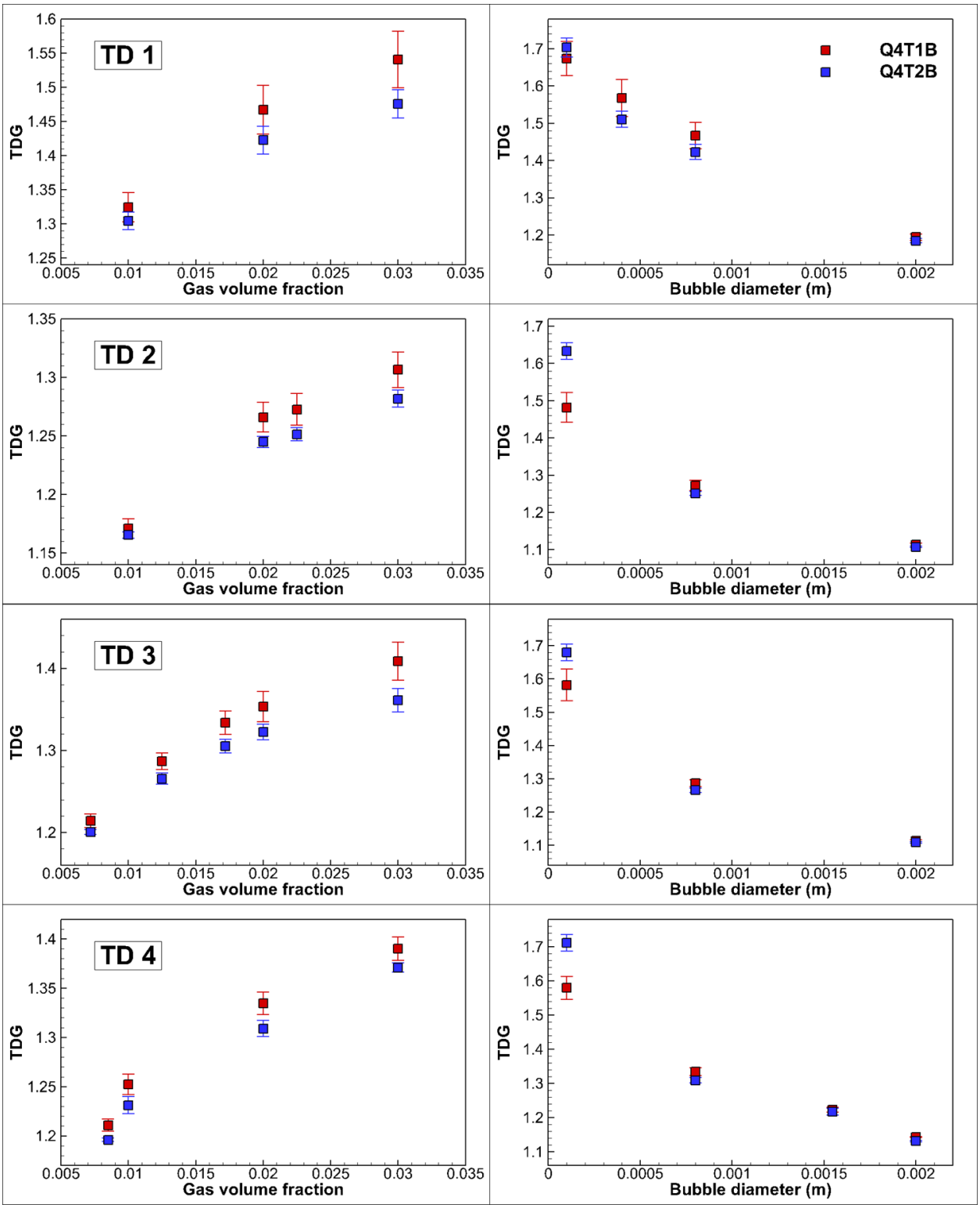

Figure 3.70 TDG concentration as a function of gas volume fraction (left column) and bubble diameters (right column) for simulation cases TD 1 to TD 4

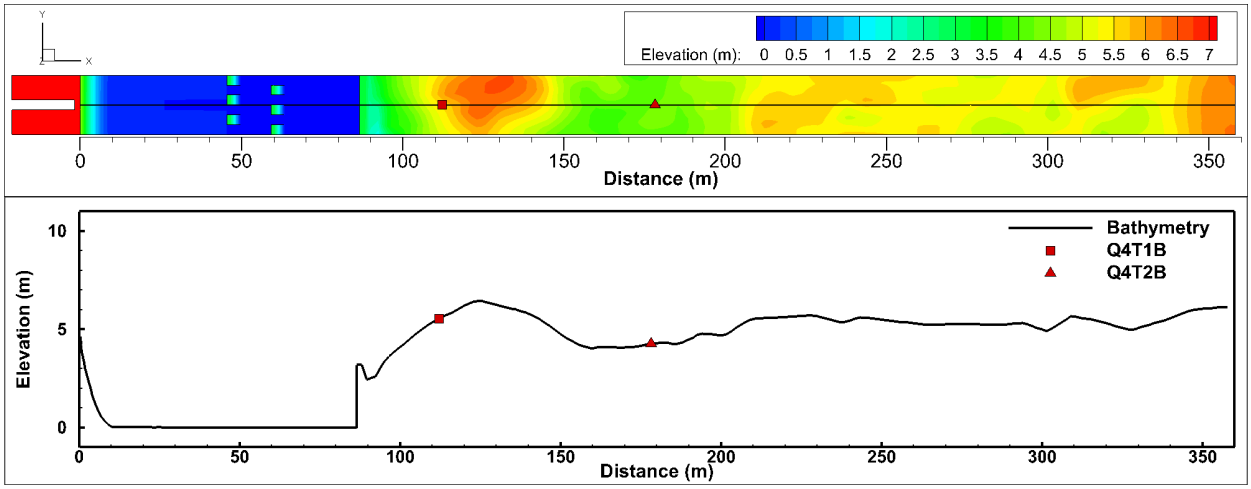

Figure 2.71 The stilling basin bottom elevation and downstream bathymetry contours (top), and along the center line of the two neighboring spillways (bottom)

CHAPTER IV

SUMMARY, CONCLUSIONS, AND RECOMMENDATIONS

4.1 Summary

This thesis documents the development and application of unsteady, three-dimensional computational fluid dynamics models to simulate the flow pattern and water-quality parameters within the forebay and tailrace area of a hydropower dam. Current numerical models for temperature and TDG prediction are improved and implemented into the open-source CFD code OpenFOAM.

The hydrodynamics and temperature dynamics in the forebay are evaluated by solving the incompressible RANS equations with the Boussinesq approximation. A realizable $k-\varepsilon$ model that accounts for the production of wind turbulence is developed. Solar radiation and convective heat transfer at the free surface are included. Model results are compared with field data collected on August 18, 2004 at McNary Dam. Observed vertical and lateral temperature distributions are accurately captured.

A numerical model to predict spillway jet regimes is developed using the VOF method coupled with a DES turbulent model. A one-way coupled multi-phase TDG model is included. Criterion for the local mesh size of the DES grid has been verified based on the integral turbulent length scale. The model accurately simulates the effect of spill flowrate and tailrace elevation on the spillway jet regime. The numerical model qualitatively agrees with jet regime obtained in a 1:25 scale laboratory model of McNary Dam. A simplified model including a small region of the tailrace at prototype scale was developed. Predicted TDG concentrations quantitatively agree with field measurements in the tailrace of McNary Dam.

4.2 Conclusions

The research presented herein demonstrates the viability of numerically modeling the complex hydrodynamic and water-quality parameters found in hydropower flows using the open-source CFD code OpenFOAM.

The application of the developed model to the McNary forebay has led to the following observations and conclusions:

1) The flow pattern in the McNary Dam forebay near the dam is primarily determined by the operational configuration of the hydropower facility. An unsteady and highly three-dimensional flow field is predicted by the model due to the influence of dam structures, reservoir bathymetry, and dynamic heat transfer processes. The predicted vertical velocity profile is not uniformly distributed.
2) The temperature dynamics and distribution in the McNary Dam forebay is a consequence of both transport from the upstream river and atmospheric heat transfer processes. The surface layer of the reservoir is warmed by solar radiation and air convection during the day, and chilled after sunset due to the long wave radiation and cooler air temperature. The incorporation of the wind-induced turbulence improves the temperature prediction near the free surface.
3) The observed temperature lateral gradient is captured by the numerical model. Comparison between predicted and measured vertical temperature profiles shows satisfactory agreement. The daily temperature variation due to heat transfer is reproduced by the model.
4) This study demonstrates the potential for using the numerical model to assess structural and operational alternatives to redirect and reduce the forebay temperature, and ultimately alleviate high local temperature impacts on fish.

CFD models are developed to study the spillway jet regimes for both reduced and prototype scales. Upon validation, the model is used to analyze transport of entrained bubbles and TDG distribution under various flow conditions at prototype scale. The tailrace model led to the following conclusions:

1) Spillway jet regime and transport of TDG downstream of a spillway depend mainly on large scale phenomenon. DES results are heavily dependent on the mesh density; if the mesh is not refined sufficiently, the spillway regime is not properly predicted.

As the mesh becomes coarser, the large scale eddies are no longer resolved and the predicted flow velocity strongly differs from that obtained on a more refined grid.

2) Flow regimes downstream of a spillway can be adequately reproduced by the numerical model in model-scale. Spillway flow regimes vary with tailwater elevation and spillway flowrate. A plunging flow occurs when the tailrace level is low or the spilling flowrate is high. The flow regime alternates from plunging flow to skimming flow, undulate jump, and hydraulic jump conditions with either increasing tailrace elevation or decreasing flowrate.
3) The transport of entrained bubbles is significantly affected by the spillway flow regimes. Bubbles are transported deep into the stilling basin floor for the plunging flow regime, while the skimming flow condition effectively prevents bubbles from traveling to depth.
4) The predicted TDG concentration depends on convective transport, dissolution of bubbles, and turbulent mixing. For the same entrained gas volume fraction and bubble size, more TDG is produced by the plunging flow due to increased dissolution of bubbles at high pressure near the bottom of the stilling basin. On the other hand, the skimming flow regime minimizes TDG production by concentrating the bubbles near the free surface. This regime produces the lowest TDG levels among all flow regimes.
5) Both TDG concentration and distribution are strongly affected by the entrained gas volume fraction and bubble size. TDG increases with the gas volume fraction. Smaller bubbles, with higher interfacial area, travel deeper into the stilling basin and produce higher TDG in the tailrace. TDG near the bottom also depends on river bathymetry. If bubbles are small enough to fill up the lower water column of the river channel, more TDG is produced.
6) The presented simulation results improve our understanding of bubble transport and TDG production under diverse flow conditions. Quantitative agreement between

predicted and measured TDG concentration at prototype scale demonstrates the potential of the model to be used as a predictive numerical tool to identify flow regimes and TDG production under various operational alternatives or structural options.

4.3 Recommendations

The present study provides a framework for using an open-source CFD model to simulate large scale complex flows of engineering interest. The author offers the following recommendations for enhancing the forebay temperature model:

1) The present study assumed a constant flow rate and wind velocity during the simulated period. The effect of variable flow and wind conditions on the temperature distribution can be investigated using the present model.
2) The present study did not take into consideration wave-affected boundary layer effects on temperature. Studies show that turbulent kinetic energy dissipation is significantly enhanced below surface waves (Terray et al. 1996). The enhancement factor can be estimated as a function of the wave height and water depth. The influence of this energetic zone can be incorporated into the current model to further improve temperature prediction in the surface layer.
3) The numerical model developed in the present study became unstable when simulating buoyancy-driven flows with strong buoyancy contributions. More research, involving the development of more stable numerical techniques, is needed to improve robustness of the present method.

The limitations of the presented McNary spillway TDG model have been extensively discussed in Chapter III. Recommendations for future work regarding this model include the following:

1) The present study employed the VOF method coupled with DES turbulent closure to simulate flow patterns downstream of a spillway. Other anisotropic turbulence

models, such as the Reynolds stress transport models (RSTM) implemented in Turan et al. (2007), can also be utilized to investigate the influences of turbulent model on predicted flow field. The attenuation of normal fluctuations at the free surface can be implemented using VOF based interface tracking technique (e.g. Barkhudarov 2004), or implementing a Level Set method in OpenFOAM. Computational resource requirements can be significantly reduced by this approach.

2) The numerical TDG model developed in the present study is based on a one way coupling approach. The influence of the gas phase on the liquid phase might play an important role in predicting spillway jet regime and water entrainment observed in the field. More research is required to fully couple the hydrodynamic and the multi-phase TDG model.
3) Preliminary simulations of the spillway jet regime at reduced and prototype scales suggest that the regime observed in the laboratory may not accurately reproduce the regime at the prototype due to scaling issues. Further comparison between flow patterns in the reduced and prototype scales is needed. Incorporation of proper flow contraction at the gate or inclusion of the forebay is recommended.
4) When computer resources are available and the entire tailrace can be modeled, the capability of the model to capture three-dimensional effects present in the tailrace needs to be evaluated. Additional validation is needed against flow field measurement in the tailrace region before the present model can be used as a practical design tool.

REFERENCES

Aleksey, G., 2007. LES & DES in FLUENT. ANSYS training material.

Amado, A., Politano, M., and Anderson, K. 2011. A CFD Model to Evaluate the Effect of Sluiceway Deflectors on the Hydrodynamics and TDG Field in the Tailrace of Hells Canyon Dam. In *Proceedings of the 34th World Congress of the International Association for Hydro-Environment Research and Engineering: 33rd Hydrology and Water Resources Symposium and 10th Conference on Hydraulics in Water Engineering* (p. 3183). Engineers Australia.

Anis A, Moum J. N., 1995. Surface wave-turbulence interations. Scaling ϵ (z) near the Sea Surface. *J. Phys. Oceanogr*. 25:2025-45

Arntzen, E. V., et al. 2009. *Total Dissolved Gas Effects on Incubating Chum Salmon Below Bonneville Dam*. Pacific Northwest National Laboratory.

Barkhudarov, M. R. 2004. Lagrangian VOF advection Method for FLOW-3D®. Flow Science Inc Technical Note FSI03TN63R, 1, 1-11.

Batchelor, G. K. 1953. Homogeneous Turbulence. Cambridge Univ. Press

Beeman, J. W., Vanderkooi, S. P., Haner, P. V., and Maule, A. 2003. Gas bubble disease monitoring and research of juvenile salmonids. 1999 Annual report of US Geological Survey to Bonneville Power Administration, Portland, Oregon.

Beeman, J. W., and Alec G. Maule. 2006. Migration depths of juvenile Chinook salmon and steelhead relative to total dissolved gas supersaturation in a Columbia river reservoir. *Transactions of the American Fisheries Society*, *135*(3): 584.

Bednarz, T. P., Lei, C. W., and Patterson, J. C. 2008. An experimental study of unsteady natural convection in a reservoir model cooled from the water surface. *Experimental Thermal and Fluid Science*, *32*(3): 844–856.

Bednarz, T. P., Lei, C. W., and Patterson, J. C. 2009. Unsteady natural convection induced by diurnal temperature changes in a reservoir with slowly varying bottom topography. *International Journal of Thermal Sciences*, *48*(10): 1932–1942.

Beiningen, K. T., and Ebel, W. J. 1970. Effect of John Day Dam on dissolved nitrogen concentrations and salmon in the Columbia River, 1968. *Transactions of the American Fisheries Society*, *99*(4): 664-671.

Bellanger, B., et al. 2004. Oxic–anoxic conditions in the water column of a tropical freshwater reservoir (Pena-Larga dam, NW Venezuela). *Applied geochemistry*, *19*(8): 1295-1314.

Berberović, E., van Hinsberg, N. P., Jakirlić, S., Roisman, I. V., and Tropea, C. 2009. Drop impact onto a liquid layer of finite thickness: Dynamics of the cavity evolution. *Physical Review E*, *79*(3): 036306.

Bin A. K. 1993. Gas entrainment by plunging liquid jets. *Chem. Eng. Sci.* 48: 3585–630

Bohorquez, P. 2008. Study and numerical simulation of sediment transport in free-surface flow. Ph.D. dissertation, ETS Ingenieros Industriales, Universidad de Malaga.

Braatne, J. H., S. B. Rood, L. A. Goater, and C. L. Blair. 2008. Analyzing the impacts of dams on riparian ecosystems: a review of research strategies and their relevance to the Snake River Through Hells Canyon. *Environmental Management*, *41*(2): 267-281.

Brett, J. R. 1952. Temperature tolerance in young Pacific salmon, genus Oncorhynchus. *Journal of the Fisheries Research Board of Canada*, *9*(6): 265-323.

Brocchini, M., and Peregrine, D. H. 2001. The dynamics of strong turbulence at free surfaces. Part 1. Description. *Journal of Fluid Mechanics*, *449*(1): 225-254.

Caboussat, A. 2005. Numerical simulation of two-phase free surface flows. *Archives of Computational Methods in Engineering*, *12*(2): 165-224.

Carneiro, J. N., Kaufmann, V., and Polifke, W. 2008. Implementation of a Moments Model in OpenFOAM for Polydispersed Multiphase Flows. In *Open Source CFD International Conference*.

Cassan, L., and Belaud, G. 2011. Experimental and numerical investigation of flow under sluice gates. Journal of Hydraulic Engineering, 138(4), 367-373.

Cataño-Lopera, Y. A., and Abad, J. D. Flow Structure around a partially Buried Object in a Simulated River Bed. In *World Environmental and Water Resources Congress 2012@ sCrossing Boundaries* (pp. 1396-1405). ASCE.

Chen, Y., Qian, X., and Zhang, Y. 2009. Modelling Turbulent Dispersion of Buoyancy Regulating Cyanobacteria in Wind-Driven Currents. In *Bioinformatics and Biomedical Engineering, 2009. ICBBE 2009. 3rd International Conference on* (pp. 1-4). IEEE.

Christensen, E. D. 2006. Large eddy simulation of spilling and plunging breakers. *Coastal Engineering*, *53*(5): 463-485.

Cook, C. B., and Richmond, M. C. 2001. Simulation of tailrace hydrodynamics using computation fluid dynamics models. PNNL-13467,Pacific Northwest National Laboratory, Richland, WA.

Craig, P. B., and Banner, M. L. 1994. Modelling wave-enhanced turbulence in the ocean surface layer. *J. Phys. Ocean*, *24*(12): 2546–2559.

Dierking, P. B. (2001). Hydraulic Modeling of Hells Canyon Dam for Spillway Deflector Design (Doctoral dissertation, University of Iowa).

Ead, S. A., and Rajaratnam, N. 2002. Plane turbulent wall jets in shallow tailwater. *J. Eng. Mech.*, *128*(2): 143–155.

Ebel, W. J. 1969. Supersaturation of nitrogen in the Columbia River and its effect on salmon and steelhead trout. *Fish. Bull*, *68*(1): 1-11.

Ebel, W. J., and Raymond, H. L. 1976. Effect of atmospheric gas supersaturation on salmon and steelhead trout of the Snake and Columbia rivers. *Marine Fisheries Review*, *38*(7): 1-14.

Edinger, J. E., Duttweiler, D. W., and Geyer, J. C. 1968. The Response of Water temperatures to Meteorological Conditions. *Water Resources Research*, *4*(5): 1137-1143.

Elston, R. 1997. Fish kills in resident and captive fish caused by spill at Grand Coulee Dam in 1997: final report. Prepared by Aquatechnics Inc, Carlsborg, Washington for the Confederated Tribes of the Colville Reservation, Nespelem, Washington and Columbia River Fish Farms, Omak, Washington.

EPA (U.S. Environmental Protection Agency) 1987. *Quality criteria for water 1986*. EPA 440/5-86-001, U.S. Environmental Protection Agency, Office of Water Regulation and Standards, Washington, DC.

Etemad-Shahidi, A., Faghihi, M., and Imberger, J. 2010. Modelling Thermal Stratification and Artificial Destratification using DYRESM; Case study: 15-Khordad Reservoir. *International Journal of Environmental Research*, *4*(3): 395-406.

Fan, S. F., Feng, M. Q., and Liu, Z. 2009. Simulation of water temperature distribution in Fenhe Reservoir. *Water Science and Engineering*, *2*(2): 32-42.

Ferrari, G. E., Politano, M., and Weber, L. 2009. Numerical simulation of free surface flows on a fish bypass. *Computers & Fluids*, *38*(5): 997-1002.

Fryer, J. K., Mainord, J., Wright, H., Folks, S., and Hyatt K. 2010. Studies into factors limiting the abundance of Okanagan and Wenatchee Sockeye Salmon. *Columbia River Inter-Tribal Fish Commission Technical Report for BPA Project 2008-503-00*.

Fu, X. L., Li, D., and Zhang, X. F. 2010. Simulations of the Three-Dimensional Total Dissolved Gas Saturation Downstream of Spillways Under Unsteady Conditions. *Journal of Hydrodynamics, Ser. B*, *22*(4): 598-604.

Fuller, B. D. 1997 Data Report: Quick Lock Experiment for Raised Tailrace, Maximum Velocities, and Powerhouse Flow Entrainment. CEWES-CS-S Memorandum for Record dated 10 January 1997, US Army Engineer Waterways Experiment Station.

Geldert, D. A., Gulliver, J. S., and Wilhelms, S. C. 1998. Modeling dissolved gas supersaturation below spillway plunge pools. *Journal of Hydraulic Engineering. 124*(5): 513–521.

Gooseff, M. N., Strzepek, K., and Chapra, S. C. 2005. Modeling the potential effects of climate change on water temperature downstream of a shallow reservoir, Lower Madison River, MT. *Climate Change*, *68*(3): 331–353.

Hampton, W. M. 2002. Total Dissolved Gas Monitoring at Rocky Reach and Rock Island dams, 2002. Chelan County Public Utility District. Wenatchee, WA

Haque, M. D. M., Constantinescu, S. G., and Weber, L. J. 2007. Validation of a 3D RANS model to predict flow and stratification effects related to fish passage at hydropower dams. *Journal of Hydraulic Research*, *45*(6): 787-796.

Haug, P.E., Li, S. and Weber, L.J. 2003. Hydraulic model studies for fish diversion at Wanapum/Priest Rapids development Part XVIII: summary of hydraulic and CFD models for Wanapum Dam, IIHR- Hydroscience & Engineering Report, The University of Iowa.

Hondzo, M., and Stefan, H. G. 1996. Lake water temperature simulation model. *Journal of Hydraulic Engineering*, *119*(11): 1251-1273.

Hoschek, S. S., Carrica, P. M., and Weber, L. J. 2008. Bubble entrainment and distribution in a model spillway with application to total dissolved gas minimization. Journal of Hydraulic Engineering, 134(6), 763-771.

Huai, W. X., Wu, Z. L., Qian, Z. D., and Geng, C. 2011. Large Eddy Simulation of open channel flows with non-submerged vegetation. *Journal of Hydrodynamics, Ser. B, 23*(2): 258-264.

Huang, H. 2002. Numerical Modeling of TDG Downstream of a Spillway. Ph.D. dissertation, IIHR, the University of Iowa.

Hurford C., Schneider M., and Cowx I. 2010. *Conservation monitoring in freshwater habitats: a practical guide and case studies*. Springer.

Ishii, M., and Zuber, N. 1979. Drag coefficient and relative velocity in bubbly, droplet or particulate flows. *AIChE Journal*, *25*(5): 843-855.

Karvinen, A., and Ahlstedt, H. 2011. Comparison of turbulence models in case of three-dimensional diffuser. In *Proceedings of Open Source CFD International Conference 2008,* Berlin, Germany, 4-5 December, 2008.

Katopodis, C., and Williams, J. G. 2011. The development of fish passage research in a historical context. *Ecological Engineering*. *48*: 8-18.

Keylock, C. J., Hardy, R. J., Parsons, D. R., Ferguson, R. I., Lane, S. N., and Richards, K. S. 2005. The theoretical foundations and potential for large-eddy simulation (LES) in fluvial geomorphic and sedimentological research. *Earth-Science Reviews*, *71*(3): 271-304.

Kiger, K. T., and Duncan, J. H. 2012. Air-entrainment mechanisms in plunging jets and breaking waves. Annual Review of Fluid Mechanics, 44, 563-596.

Kim, D. G. 2007. Numerical analysis of free flow past a sluice gate. *KSCE Journal of Civil Engineering*, *11*(2): 127-132.

Kirillin, G. 2010.Modeling the impact of global warming on water temperature and seasonal mixing regimes in small temperate lakes. *Boreal Environment Research*, *15*: 279-293.

Lackey, R. T., and Holmes, D. W. 1972. Evaluation of two methods of aeration to prevent winterkill. *The Progressive Fish-Culturist*, *34*(3): 175-178.

Lei, C., and Patterson, J. C. 2002. Natural convection in a reservoir sidearm subject to solar radiation: a two-dimensional simulation. *Numerical Heat Transfer Part A*, *42*(1-2): 13-32.

Lessard, J. L., and Hayes, D. B. 2003. Effects of elevated water temperature on fish and Macroinvertebrate communities below small dams. *River Research and Applications*, *19*(7): 721-732.

Li, G. J., Dai, G. Q., Yang, Q., and Ma, X. D. 2011. Detached eddy simulation of hydraulic characteristics along the side-wall after a new arrangement-scheme of the sudden lateral enlargement and the vertical drop. *Journal of Hydrodynamics, Ser. B, 23*(5): 669-675.

Lichatowich, J. 1999. *Salmon without rivers: a history of the Pacific salmon crisis*. Washington, D.C.: Island Press

Lu, L., Li, Y., and Bin, T. 2008. Numerical simulation of turbulent free surface flow over obstruction. *Journal of Hydrodynamics*, *20*(4): 414–423.

Liu, W. C., and Chen, W. B. 2012. Prediction of water temperature in a subtropical subalpine lake using an artificial neural network and three-dimensional circulation models. *Computers & Geosciences*, *45*: 13-25.

Ma, L., Ashworth, P. J., Best, J. L., Elliott, L., Ingham, D. B., and Whitcombe, L. J. 2002. Computational fluid dynamics and the physical modelling of an upland urban river. *Geomorphology*, *44*(3): 375-391.

Ma, J., Oberai, A. A., Drew, D. A., Lahey Jr, R. T., and Moraga, F. J. (2010). A quantitative sub-grid air entrainment model for bubbly flows–plunging jets. Computers & Fluids, 39(1), 77-86

Mahmoodi, B., Nikou, M. R. K., and Bahrami, M. B. 2012. An Assessment on the Performance of Reynolds Stress Model (RSM) in Modeling Churn Fully Turbulent Flow in Bubble Column Reactors. *relation*, *24*(1): 0-15.

Marsh, D. M., Harmon, J. R., Paasch, N. N., Thomas, K. L., McIntyre, K. W., Sandford, B. P., and Matthews, G. M. (2001). *Research related to transportation of juvenile salmonids on the Columbia and Snake Rivers, 2000*. Coastal Zone and Estuarine Studies Division, Northwest Fisheries Science Center, National Marine Fisheries Service, National Oceanic and Atmospheric Administration.

Meekin, T. K., and Allen, R. L. 1974. Nitrogen Saturation Levels on the Mid-Columbia River, 1965-1971. *Nitrogen Supersaturation Investigations in the Mid-Columbia River, Washington Department of Fisheries Technical Report 12, 1974-*, 32-77.

Meselhe, E. A., and Odgaard, A. J. 1998. 3D numerical flow model for fish diversion studies at Wanapum Dam. *Journal of Hydraulic Engineering*, *124*(12): 1203-1214.

Mtada, O. S. M. 1987. The influence of thermal stratification on pelagic fish yields in Lake Kariba, Zambia/Zimbabwe. Journal of fish biology, 30(2), 127-133.

NHC (Northwest Hydraulic Consultants) 2001. McNary Dam Spillway Flow Deflectors Hydraulic Model Study–Final Report. Northwest Hydraulic Consultants, Seattle, WA.

Nielsen, K. D., Weber, L., and Haug, P. E. 2000. Hydraulic model study for fish diversion at Wanapum/Priest Rapids development, Part XVI: 1:32.5 scale sectional model of Wanapum Dam spillway deflectors. IIHR Hydroscience & Engineering, Report No. 284, The University of Iowa.

NOAA (National Oceanographic and Atmospheric Administration) 1995. Item 2. Pages 104-110 in: Endangered Species Act - Section 7 Consultation, Biological Opinion, Federal Columbia River Power System (FCRPS). National Oceanic and Atmospheric Administration, National Marine Fisheries Service, Northwest Regional Office, Seattle, WA.

NOAA (National Oceanographic and Atmospheric Administration) 2000. "Risk Assessment for Spill Program Described in 2000 Draft Biological Opinion." Appendix E in "Endangered Species Act Section 7 Biological Opinion on the Reinitiation of Consultation on Operation of the Federal Columbia River Power System, Including the Juvenile Fish Transportation Program, and 19 Bureau of Reclamation Projects in the Columbia Basin." Available at http://seahorse.nmfs.noaa.gov/pls/pcts-pub/sxn7.pcts_upload.summary_list_biop?p_id=12342 (March 30, 2006).

Oertel Jr, H. 1990. Wakes behind blunt bodies. Annual Review of Fluid Mechanics, 22(1), 539-562.

Orlins, J. J., and Gulliver, J. S. 2000. Dissolved gas supersaturation downstream of a spillway. II: Computational model. *J. Hydraul. Res.*, *38*(2): 151–159.

Panara, D., Porta, M., Dannecker, R., and Noll, B. 2006. Wall-functions and boundary layer response to pulsating and oscillating turbulent channel flows. In *Proceedings of the 5th International Symposium on Turbulence, Heat and Mass Transfer THMT06*.

Pasiok, R., and Stilger-Szydło, E. 2010. Sediment particles and turbulent flow simulation around bridge piers. *Archives of Civil and Mechanical Engineering*, *10*(2): 67-79.

Politano, M., Haque, M. M., Constantinescu, G. S., and Weber, L. 2006. A Three-Dimensional Thermal Model for McNary Dam. In *World Environmental and Water Resource Congress 2006@ sExamining the Confluence of Environmental and Water Concerns*. ASCE.

Politano, M. S., Carrica, P. M., Cagri, T., and Weber, L. 2007. A multidimensional two-phase flow model for the total dissolved gas downstream of spillways." *J. Hydraul. Res.*, *45*(2): 165–177.

Politano, M., Haque, M. D. M., and Weber, L. J. 2008. A numerical study of the temperature dynamics at McNary Dam. *Ecological Modelling*, *212*(3-4): 408-421.

Politano, M., Arenas Amado, A., and Weber, L., 2009a, An Investigation into the Total Dissolved Gas Dynamics of the Wells Project. FERC Report No 2149.

Politano, M., Fu, X., Lluellen, L., and Weber, L., 2009b, Computational Fluid Dynamics Model to Evaluate Total Dissolved Gas Field within the Tailrace at McNary Dam. IIHR Limited Distribution Report No 359.

Politano, M., Carrica, P., and Weber, L. 2009c. A multiphase model for the hydrodynamics and total dissolved gas in tailraces. *International Journal of Multiphase Flow*, *35*(11): 1036-1050.

Politano, M., Arenas Amado, A., Bickford, S., Murauskas, J., and Hay, D. 2011. Investigation into the Total Dissolved Gas Dynamics of Wells Dam Using a Two-Phase Flow Model. *Journal of hydraulic engineering*, *137*(10): 1257-1268.

Politano, M., Arenas Amado, A., Bickford, S., Murauskas, J., and Hay, D. 2012. Evaluation of Operational Strategies to Minimize Gas Supersaturation Downstream of a Dam. *Computers & Fluids, 68*: 168-185.

Politano, M. and Dvorak, J. 2012. Computational Fluid Dynamics (CFD) Modeling to support the reduction of fish passage exposure to predator habitat at McNary Dam. IIHR Limited Distribution Report No 377.

Pope, S. B. 2004. Ten questions concerning the large-eddy simulation of turbulent flows. *New Journal of Physics*, *6*(1): 35.

Pringle, J. M. 2007. Turbulence avoidance and the wind-driven transport of plankton in the surface Ekman layer. *Continental Shelf Research*, *27*(5): 670-678.

Robb, D. 2011. Hydro's fish-friendly turbines. *Renewable energy focus*. *12*(2): 16-17.

Roesner, L. A., and Norton, W. R. 1971. A Nitrogen Gas (N2) Model for the Lower Columbia River, Final Report. Prepared for the Portland District, North Pacific Division, U. S. Army Corps of Engineers, Portland, Oregon Report, (1-350), 2.

Rusche, H. 2003. *Computational fluid dynamics of dispersed two-phase flows at high phase fractions* Doctoral dissertation, Imperial College London (University of London).

Sanjou, M., and Nezu, I. 2010. Large eddy simulation of compound open-channel flows with emergent vegetation near the floodplain edge. *Journal of Hydrodynamics, Ser. B*, *22*(5): 582-586.

Schneider, M. L. and Wihelms, S. C. 1996 Near-Field study of TDG in the Lower Monumental Spillway Tailwater. CEWES-CS-S Memorandum for Record dated 6 December 1996, US Army Engineer Waterways Experiment Station.

Schneider, M. L. and Wihelms, S. C. 1996 Near-Field study of TDG Dissolved Gas in the Dalles Spillway Tailwater. CEWES-CS-L Memorandum for Record dated 16 December 1996, US Army Engineer Waterways Experiment Station.

Shih, T. –H., Liou, W. W., Shabbir, A., Yang, Z., and Zhu, J. 1995. A new $k-\varepsilon$ eddy-viscosity model for high Reynolds number turbulent flows. *Computers Fluids*, *24*(3): 227-238.

Sinha, S., Liu, X., and Garcia, M. H. 2012. Three-dimensional hydrodynamic modeling of the Chicago River, Illinois. *Environmental Fluid Mechanics*, *12*(5): 471-494

Smagorinsky, J. 1963. General circulation experiments with the primitive equations. *Monthly weather review*, *91*(3): 99-164.

Smith, C. R., and Baker, K. S. 1981. Optical properties of the clearest natural waters. *Applied Optics*, *20*(2): 177-184.

Somero, G. N., and DeVries, A. L. 1967. Temperature tolerance of some Antarctic fishes. *Science (New York, NY)*, *156*(772): 257.

Spalart, P. R., Jou, W. -H., Strelets, M., and Allmaras, S.R. 1997. Comments on the feas1ibility of LES for wings, and on a hybrid RANS/LES approach. *In: Proceedings of first AFOSR international conference on DNS/LES*, Ruston, Louisiana. Greyden Press, 4–8.

Strain, A., Politano, M. S., Lyons, T., and Weber, L. 2008. Numerical Study for the Design of a Warm Water Fish Passage. In *World Environmental and Water Resources Congress 2008@ sAhupua'A* (pp. 1-10). ASCE.

Tan, D. C. 2006. Research on the Lethal Effect of the Dissolved Gas Supersaturation Resulted from Three Gorges Project to Fish. Ph.D. dissertation, Chongqing, China, Southwest University (in Chinese).

Xing, T., and Stern, F. 2010. Factors of safety for Richardson extrapolation. *Journal of Fluids Engineering*, 132(6), 061403.

Teklemariam, E., Korbaylo, B. W., Groeneveld, J. L., and Fuchs, D. M. 2002. Computational fluid dynamics: diverse applications in hydropower project's design and analysis. *CWRA 55th Annual Conference*, Winnipeg, Manitoba, CA.

Terray, E. A., Donelan, M. A., Agrawal, Y. C., Drennan, W. M., Kahma, K. K., Williams, A. J., and Kitaigorodskii, S. A. 1996. Estimates of kinetic energy dissipation under breaking waves. *Journal of Physical Oceanography*, 26(5), 792-807.

Tomiyama, A. 1998. Struggle with computational bubble dynamics. *Multiphase Science and Technology*, *10*(4): 369-405.

Tu, S., Aliabadi, S., Patel, R., and Watts, M. 2009. An implementation of the Spalart–Allmaras DES model in an implicit unstructured hybrid finite volume/element solver for incompressible turbulent flow. *International journal for numerical methods in fluids*, *59*(9): 1051-1062.

Turan, C., Politano, M. S., Carrica, P. M., and Weber, L. 2007. Water entrainment due to spillway surface jets. *International Journal of Computational Fluid Dynamics*, *21*(3-4): 137-153.

Umlauf, L., and Burchard, H. 2003. A generic length-scale equation for geophysical turbulence models. *Journal of Marine Research*, *61*(2): 235-265.

Urban, A. L., Gulliver, J. S., and Johnson, D. W. 2008. Modeling total dissolved gas concentration downstream of spillways. *Journal of hydraulic engineering*, *134*(5): 550-561.

US Army Corps of Engineers 2001. Data summary for Wanapum Dam phase 5 total dissolved gas post-deflector spillway performance test. *Prepared for Public Utility District No. 2 of Grant County*.

Van Maele, K., and Merci, B. 2008. Application of RANS and LES field simulations to predict the critical ventilation velocity in longitudinally ventilated horizontal tunnels. *Fire Safety Journal*, *43*(8): 598-609.

Verdier-Bonnet, C., Angot, P., Fraunie, P., and Coantic, M. 1999. Three-dimensional modelling of coastal circulations with different $k-\varepsilon$ closures. *Journal of marine systems*, *21*(1): 321-339.

Vilums, R. 2011. Implementation of Transient Robin Boundary Conditions in OpenFOAM. . *In Proceedings of the Multiphysical Modelling in OpenFOAM Workshop*. Riga, Latvia. October 20-21. 2011

Wan, T., Aliabadi, S., and Bigler, C. 2009. A hybrid scheme based on finite element/volume methods for two immiscible fluid flows. *International journal for numerical methods in fluids*, *61*(8): 930-944.

Wang, S., Ingham, D. B., Ma, L., Pourkashanian, M., and Tao, Z. 2012. Turbulence modeling of deep dynamic stall at relatively low Reynolds number. *Journal of Fluids and Structures*.

Wang, Y., Politano, M., and Laughery, R. 2013a. Towards full predictions of temperature dynamics in McNary Dam forebay using OpenFOAM. *Water Science and Engineering*, 6(3): 317-330.

Wang, Y., Politano, M., and Laughery, R. 2013b. Simulation of the temperature dynamics in McNary Dam using OpenFOAM. *Proceedings of HydroVision International Conference*. Denver: HydroVision International.

Weber, L. J., Haug, P. E. and Jeske, D. M. 1999. Performance Curves for Wanapum Dam Spillway Deflectors. *ASCE Water Resources Convention*, Seattle, Washington.

Weber, L., Huang, H., Lai, Y., and McCoy, A. 2004. Modeling total dissolved gas production and transport downstream of spillways: Three-dimensional development and applications. *International Journal of River Basin Management*, *2*(3): 157-167.

Weitkamp. D. E. 2008. Total Dissolved Gas Supersaturation Biological Effects, Review of Literature 1980-2007. Parametrix, Bellevue, Washington, June 2008.

Whitworth, S. 2011. Cavitation Prediction of Flow over the Delft Twist 11 Foil. *In: Second International Symposium on Marine Propulsors smp'11*, Hamburg, Germany, June 2011

Wilhelms, S.C., J. Carroll, and M.L. Schneider, 1997. Near-Field Study of Total Dissolved Gas in the McNary Spillway TailwaterJohn. CEWES-CR-F Memorandum for Record dated 22 August 1997, U.S. Army Engineer Waterways Experiment Station.

Wilhelms, S.C. 2005. Draft data documentation for field investigation at McNary Dam. CEERD-HC-IE Memorandum for Record dated May 20 2005, Coastal and Hydraulics Laboratory.

Wüest, A., and Lorke, A. 2003. Small-scale hydrodynamics in lakes. *Annual Review of Fluid Mechanics*, *35*(1): 373-412.

Zeng, X., and Rasmussen, T. C. 2005. Multivariate statistical characterization of water quality in Lake Lanier, Georgia, USA. *Journal of Environmental quality*, *34*(6): 1980-1991.

Zhang, L. 2002. Numerical Modeling of Flow and TDG Supersaturation Downstream of Hell's Canyon Dam. Master thesis, IIHR, the University of Iowa.

Zhang, Y., and Baptista, A. M. 2008. SELFE: a semi-implicit Eulerian–Lagrangian finite-element model for cross-scale ocean circulation. *Ocean Modelling*, *21*(3): 71-96.

Zhao, L. L., Zhu, G. W., Chen, Y. F., Li, W., Zhu, M. Y., Yao, X., and Cai, L. L. 2011. Thermal stratification and its influence factors in a large-sized and shallow Lake Taihu. *Advances in Water Science*, *22*(6): 844-850.